

Squeezed Light for Gravitational Wave Astronomy

Von der Fakultät für Mathematik und Physik
der Gottfried Wilhelm Leibniz Universität Hannover
zur Erlangung des Grades

Doktor der Naturwissenschaften
– Dr. rer. nat. –

genehmigte Dissertation
von

Dipl.-Phys. Henning Vahlbruch

geboren am 29. Juli 1976 in Frankfurt am Main

2008

Referent:	Prof. Dr. Roman Schnabel
Korreferent:	Prof. Dr. Karsten Danzmann
Tag der Promotion:	28.11.2008

Abstract

During the recent years an international network of interferometric gravitational wave (GW) detectors has been commissioned and searches for various classes of GW-signals are ongoing. Although the observatories are beginning to reach astrophysically interesting sensitivity levels, extensive upgrades are aimed for the next decade bringing us into the era of gravitational wave astronomy. One approach to enhance the detector sensitivity is the injection of *squeezed* vacuum states of light replacing the vacuum fluctuations entering the detector through its antisymmetric port.

In this thesis the unprecedented generation of squeezed vacuum states with a noise power 6.5 dB below vacuum noise within the entire detection bandwidth of ground-based GW-detectors (10 Hz - 10 kHz) was experimentally demonstrated at a wavelength of 1064 nm. For the first time a coherent control scheme was employed for comprehensive phase control of the experimental setup. This scheme is directly applicable to future GW-detector topologies. In addition, parasitic interference induced by scattered light was found to be a dominant noise source degrading squeezed states in the audio band.

The compatibility of squeezed field injection into a detuned operated dual-recycled Michelson interferometer was demonstrated in a table top experiment. A detected non-classical sensitivity improvement of up to 3.0 dB within the entire detection bandwidth (5 -15 MHz) was accomplished by optimal preparation of the injected squeezing by means of a detuned locked filter cavity.

In a further experiment strongly squeezed vacuum states were generated in the MHz-regime. With a maximum measured quantum noise reduction of 11.5 dB below the shot noise limit a new benchmark was set. This was achieved by suppression of phase noise and a remarkable reduction of optical loss in the experimental setup.

Based on the squeezed light sources developed in this thesis and the experimental results achieved, a conceptual design of a compact squeezed light source was devised, allowing for a high duty cycle sensitivity improvement of GW-detectors.

Keywords: Gravitational wave detector, squeezed light generation, low frequency squeezing

Kurzfassung

Jüngst ist ein internationales Netzwerk von interferometrischen Gravitationswellen (GW) Detektoren fertiggestellt worden, und die Suche nach GW-Signalen hat begonnen. Obwohl diese Observatorien inzwischen eine Messempfindlichkeit erreicht haben, die von astrophysikalischem Interesse ist, sind für die nächsten Jahre umfangreiche Erweiterungen geplant. Eine vielsprechende Möglichkeit die Messempfindlichkeit der Detektoren weiter zu steigern, ist die Implementierung von gequetschtem Licht, das in den dunklen Ausgang des Detektors injiziert wird.

Im Rahmen dieser Arbeit wurden daher erstmals bis zu 6,5 dB gequetschte Vakuumzustände erzeugt, die den gesamten Messbereich (10 Hz - 10 kHz) erdgebundener GW-Detektoren abdecken. Für eine umfassende Kontrolle der erzeugten nicht-klassischen Zustände kam ein neuartiges kohärentes Schema zum Einsatz. Zusätzlich wurde Streulicht als eine Quetschgrad limierende Rauschquelle indentifiziert.

Die Kompatibilität von gequetschten Zuständen mit einem verstimmtten "Dual-recycling"-Interferometer wurde in einem weiteren Experiment gezeigt. Hierbei konnte eine Rauschunterdrückung von bis zu 3 dB unterhalb des Schrotrauschens im MHz-Bereich (5 - 15 MHz) gemessen werden. Diese breitbandige Steigerung des Signal-zu-Rauschverhältnisses erforderte eine optimale Präparation des gequetschten Lichts mittels eines komplementär verstimmtten Filterresonators.

In einem dritten Experiment wurden stark gequetschte Zustände bei Seitenbandfrequenzen im MHz-Bereich erzeugt. Mit einem maximal gemessenen Quetschgrad von 11.5 dB wurde weltweit ein neuer Höhepunkt gesetzt. Dieses Ergebnis konnte durch die Unterdrückung von Phasenrauschen und eine erhebliche Reduktion von optischen Verlusten im experimentellen Aufbau erzielt werden.

Abschließend wird ein Quetschlichtquellen-Design vorgeschlagen, das für den direkten Einsatz in interferometrischen GW-Detektoren geeignet ist. Durch eine Zusammenführung der oben aufgeführten Experimente konnte gezielt ein Konzept entwickelt werden, das eine langzeitstabile Erzeugung und Kontrolle von gequetschten Vakuumzuständen in einem zugleich sehr kompakten Aufbau garantiert.

Stichworte: Gravitationswellen Detektor, gequetschtes Licht, Quantenoptik

Contents

Abstract	i
Kurzfassung	iii
Contents	v
Glossary	ix
List of Figures	xiii
List of Tables	xvii
1 Introduction	1
1.1 Detection of gravitational waves	1
1.2 Gravitational wave detection with laser interferometers	2
1.3 Noise sources in interferometric gravitational wave detectors	3
1.3.1 Seismic noise	3
1.3.2 Thermal noise	4
1.3.3 Quantum noise	4
1.3.3.1 Photon shot noise	4
1.3.3.2 Quantum radiation pressure noise	5
1.3.3.3 Standard Quantum Limit	5
1.4 Quantum enhancement	6
1.5 Structure of the thesis	8
2 The Theory of Non-Classical Light	11
2.1 Field quantization	11
2.2 Quantum fluctuations	14
2.3 Quadrature operators	15

vi	Contents	0.0
2.4	Coherent states	16
2.5	Squeezed states	18
2.5.1	Photon statistics	22
2.6	Wigner function	24
2.7	Generation of quadrature squeezed light	26
2.8	Second order optical nonlinearity	27
2.8.1	Dielectric polarization	28
2.8.2	Optical parametric process	28
2.8.3	Phase matching	29
2.9	Detection of squeezed states	30
2.9.1	Balanced homodyne detection	31
2.9.2	Sideband modulation fields in quantum optics	35
3	Generation of strongly squeezed vacuum states	37
3.1	Introduction	37
3.2	Limitations to squeezing	39
3.2.1	Escape efficiency / cavity linewidth	39
3.2.2	Propagation loss	40
3.2.3	Homodyne efficiency	40
3.2.4	Detection efficiency	41
3.2.5	Phase jitter	41
3.3	Experimental setup	44
3.3.1	Second harmonic generation	44
3.3.2	Mode cleaner cavities for the fundamental and second harmonic field	49
3.3.3	Monolithic squeezed light source	53
3.3.4	Homodyne detector	57
3.4	Observation of 10 dB squeezed vacuum states of light	60
3.5	Observation of 11.5 dB squeezed vacuum states of light	62
3.6	Conclusion	68
4	Coherent Control of Vacuum Squeezing in the Gravitational-Wave Detection Band	71
4.1	Introduction	72
4.2	Coherent control theory	74
4.2.1	Coherent control field under nonlinear process	74
4.2.2	Phase control of the second harmonic pump field	77
4.2.3	Phase control of the squeezed vacuum field	78
4.3	Experimental setup	80

4.3.1	Squeezed light source cavity length control	80
4.3.2	Coherent frequency shifted control field	82
4.4	Detection of vacuum states and squeezed states of light at audio frequencies	84
4.5	Squeezed state engineering	86
4.6	Parasitic optical interference	88
4.6.1	Potential sources for scattering	90
4.6.1.1	Homodyne detector	90
4.6.1.2	Frequency shifted control beam	92
4.6.1.3	Green pump beam	93
4.6.1.4	Lab environment	93
4.7	Application of squeezed states in a Michelson interferometer	93
4.8	Conclusion	96
5	Demonstration of a Squeezed Light Enhanced Power- and Signal-recycled Michelson Interferometer	97
5.1	Introduction	98
5.2	Experimental setup	99
5.3	Results and discussion	103
5.4	Conclusion	104
6	Conceptual Squeezer-design for GEO 600	107
6.1	Optical GEO 600 squeezer setup	108
6.1.1	Laser preparation stage	108
6.1.2	Squeezed light source design	109
6.1.2.1	Pump field at frequency $2\omega_0$	109
6.1.2.2	Alignment beam at frequency ω_0	111
6.1.2.3	Squeezed light source cavity length control beam	111
6.1.2.4	Squeezing ellipse and phase control beam	112
6.1.3	Diagnostic homodyne detector	113
6.2	The GEO 600 squeezer breadboard design	113
6.3	Control electronics	115
6.3.1	Second harmonic generator control	115
6.3.2	Mode cleaner cavity for the green pump beam at frequency $2\omega_0$	116
6.3.3	Squeezed light source and coherent control fields	118
6.3.3.1	Alignment beam at frequency ω_0	118
6.3.3.2	Auxiliary Laser 1 phase locking loop and SLS cavity length control beam	119
6.3.4	Mode cleaner for the homodyne detector LO beam	121

viii	Contents	0.0
	6.3.5 Second auxiliary laser phase locking loop and squeezing ellipse and phase control loops	122
	6.3.6 Main squeezing laser frequency lock to the GEO 600 laser .	125
	6.3.7 Squeezing phase and alignment control for GEO 600	126
	6.3.8 Digital I/O channel overview	126
	6.3.9 Overview of the modulation frequencies	126
6.4	Squeezed light injection into GEO 600	128
	6.4.1 First sequence: Output mode cleaner – Faraday Rotator – Photodetector	128
	6.4.1.1 Optical loss budget	128
	6.4.2 Second sequence: Faraday Rotator – OMC - Photodetector .	130
	6.4.2.1 Optical loss budget	130
	6.4.3 Estimated squeezing strength	132
7	Summary and Outlook	135
A	Source Codes	137
	A.1 Homodyne detection	137
	A.2 Squeezing simulations	139
B	Electronics	145
	Bibliography	159
	Acknowledgments	167
	Curriculum vitae	169
	Publications	171
	Index	175

Glossary

Abbreviations

A/D	Analog/Digital
AA	Anti-aliasing
AOM	Acoustic-optical modulator
AR	Anti-reflection
BLIRA	Blue induced infrared absorption
BS	Beamsplitter
DSP	Digital signal processing
EOM	Elektro-optical modulator
EP	Error point
DBS	Dichroic beamsplitter
\mathcal{F}	Finesse
FFT	Fast fourier transform
FSR	Free spectral range
FWHM	Full width half maximum
GRIIRA	Green induced infrared absorption
HD	Homodyndetektor
HR	High-reflection
HV	High voltage
IR	Infrared
LO	Local oscillator
LSD	Linear spectral density
MC	Mode cleaner cavity
NPRO	Nonplanar ring-oscillator
ND:YAG	Neodymium-doped yttrium aluminum garnet

OPA	Optical parametric amplification
OPO	Optical parametric oscillation
PBS	Polarizing beamsplitter
PD	Photodetector
PDH	Pound-Drever-Hall
PLL	Phase-locking loop
PRM	Power-recycling mirror
PZT	Piezo-electric transducer
QCF	Quadrature control field
RF	Radio-frequency
RBW	Resolution bandwidth
ROC	Radius of curvature
SHG	Second harmonic generation
SNR	Signal to noise ratio
SQL	Standard quantum limit
SRM	Signal-recycling mirror
VBW	Video bandwidth

States

$ 0\rangle$	Vacuum state
$ n\rangle$	Fock-state with n photons
$ \alpha\rangle$	Coherent state
$ \alpha, \tilde{\zeta}\rangle$	Squeezed coherent state

Symbols

$[\hat{A}, \hat{B}]$	Commutator with \hat{A} und \hat{B}
$\mathbb{1}$	Unity-matrix
\hat{a}, \hat{a}^\dagger	Creation and annihilation operator
$\chi^{(2)}$	Second order non-linearity
$\chi^{(3)}$	Third order non-linearity
$\Delta\hat{O}, V_{\hat{O}}$	Variance from \hat{O}
$\hat{D}(\alpha)$	Displacement-operator
$\delta\hat{a}$	Fluctuations of the coherent field \hat{a}
ϵ_0	Electrical permeability
$E(x, t)$	Electric field
E_n	Energy eigenvalue
η_{PD}	Photo diode quantum efficiency
η_{det}	Detection efficiency
\mathcal{F}	Finesse
f	Frequency
f_0	Eigen-frequency
Δf	Frequency bandwidth
f_s	Sampling frequency
g	Total nonlinear gain
G	Newton gravitational constant
\hbar	Planck-constant
$H(z)$	Filter transferfunction
\hat{H}, H	Hamilton-operator, Hamilton-function
i_+	Photocurrent sum
i_-	Photocurrent difference
μ_0	Magnetic permeability
\hat{n}	Number operator
$\hat{\rho}, \hat{\sigma}$	Density operators
ν	Laser frequency
ν_0	Carrier frequency
r	Squeezing-parameter
$S(\xi)$	Squeezing-operator

$U(V_x, V_p)$	Uncertainty product
\mathcal{V}	Visibility
$W(x, p)$	Wigner-Function
ω	Angular frequency
ω_0	Angular carrier frequency
ϕ	Phase angle
p	Position
P	Laser power
\mathcal{P}	Electric polarization
q	Momentum
\hat{X}^θ	Quadrature-operator
$\hat{X}^+ = \hat{X}^{\theta=0}$	Amplitude-quadrature operator
$\hat{X}^- = \hat{X}^{\theta=\pi/2}$	Phase-quadrature operator
\hat{Y}^+, \hat{Y}^-	Rotated quadrature operator

List of Figures

1.1	Schematic of a classic Michelson interferometer	3
1.2	Quantum noise limited strain sensitivities for a Michelson interferometer in dependence of the circulating laser light power	6
1.3	Schematic of a Michelson interferometer operated at a dark fringe . . .	7
1.4	The effect of squeezing on a Michelson Interferometer when a 20 dB squeezed vacuum field is injected into the antisymmetric port	8
2.1	Illustration of the quantum noise variance in dependence of the quadrature angle ϕ	19
2.2	Illustration of squeezed states in the phase-space - I	20
2.3	Illustration of squeezed states in the phase-space - II	21
2.4	Histogram of the photon number distribution for a squeezed vacuum state	24
2.5	Wigner function of a vacuum state $ 0\rangle$	25
2.6	Wigner funktion of a squeezed vacuum state	26
2.7	Schematic of a balanced homodyne detection scheme	31
2.8	Illustration of the gain dependence for the homodyne detection efficiency	33
2.9	Illustration of the beamsplitter ratio dependence for the homodyne detec- tion efficiency	34
2.10	Amplitude and phase modulation in the sideband picture	36
3.1	Illustration of a propagation loss model	40
3.2	Simulated noise power spectra in dependence of detection efficiency - I	42
3.3	Simulated noise power spectra- II	43
3.4	Schematic of the experimental setup for the 10 dB squeezing experiment	45
3.5	Illustration of the oven design used for second harmonic generation . .	46
3.6	Measurement of the thermal transfer function of the second harmonic generator oven design	47
3.7	Open-loop gain of the second harmonic generator temperature controller	48

xiv	List of Figures	0.0
3.8	Open-loop gain of the second harmonic generator cavity length control loop	49
3.9	Schematics of the mode cleaner cavities for a wavelength of 532 nm and 1064 nm	50
3.10	Theoretical plot of the mode cleaner eigenmodes for both orthogonal polarizations	51
3.11	Open-loop gain of the MC532 mode cleaner cavity length control loop .	52
3.12	Photograph of the monolithic squeezed light source made from 7 % doped MgO:LiNbO ₃	54
3.13	Illustration of the experiment used for the absorption measurement of 7 % doped MgO:LiNbO ₃ at 1064 nm	55
3.14	Illustration of the monolithic squeezed light source	56
3.15	Photograph of the homodyne detector photo diodes	58
3.16	Measurement of the linearity of the homodyne detection system varying the local oscillator power	59
3.17	Measurement of a nonclassical noise reduction of 10.12 dB below vacuum noise	61
3.18	Squeezing and anti-squeezing levels for a parametric gain of 63 versus optical loss	62
3.19	Photograph of the Epitaxx ETX500 photodiodes and custom made high efficiency diodes made by the Fraunhofer Institut für Nachrichtentechnik, Berlin	63
3.20	Simulation of squeezing and anti-squeezing levels for two different parameter settings (optical loss and phasenoise)	64
3.21	Schematic of the updated experimental squeezing setup	66
3.22	Measurement of a nonclassical noise reduction of 11.5 dB below vacuum noise	68
3.23	Broadband squeezing measurement (3 - 10 MHz)	69
4.1	Complex optical field amplitude representing a single sideband field at a frequency $\omega_0 + \Omega$ with respect to the main carrier frequency ω_0	75
4.2	Complex optical field amplitudes. The generated outgoing field from the squeezed light source is composed of two sidebands that are equally separated by Ω from the main carrier frequency ω_0	76
4.3	Complex optical field amplitudes. The generated outgoing field from the OPO is composed of two sidebands that are equally separated by Ω from the main carrier frequency ω_0	78
4.4	Illustration of the experimental setup for the coherent control of a broadband squeezed vacuum field	81
4.5	Photograph of the low frequency squeezing experiment	82

0.0	List of Figures	xv
4.6	Measured error signal for the phase relation between the coherent control field (40 MHz shifted) and the green pump field	83
4.7	Characteristic open-loop gain measurement for the squeezing angle control locking loops	84
4.8	Noise powers (variances) of the field quadratures for a spectrum of vacuum states at different sideband frequencies	86
4.9	Squeezing measurement in the audio band	87
4.10	Measured quantum noise spectra corrupted by stray light	89
4.11	Photograph of the low frequency homodyne detector setup	91
4.12	Photograph of the low-frequency squeezing optical table.	92
4.13	Schematic of the experimental setup for the application of squeezed states in a Michelson interferometer	94
4.14	Photograph of the „Mini-Michelson-Interferometer“	95
4.15	Measurement of the a squeezing enhanced Michelson interferometer sensitivity.	96
5.1	Experimetal setup of the squeezed light enhanced power- and signal-recycled Michelson interferometer experiment	100
5.2	Four amplitude quadrature noise power spectra: (a) shot noise, (b) frequency dependent squeezing after reflection at the detuned signal-recycling cavity, (c) frequency dependent squeezing after reflection at the detuned filter cavity and (d) regained broadband squeezed light enhanced performance	102
5.3	Amplitude quadrature power spectra of the dual recycled Michelson interferometer with and without nonclassical noise reduction	103
6.1	Schematic of the general optical setup for the GEO 600 squeezing experiment utilizing four continuous wave laser beams	110
6.2	GEO 600 squeezer breadboard layout	114
6.3	Illustration of the second harmonic generator (SHG) setup for the GEO 600 squeezer	115
6.4	Detailed schematic of the required electronics for the the mode cleaner cavity length control loop	117
6.5	Schematic of the squeezed light source cavity length control loop via the alignment beam at ω_0	118
6.6	Schematic of the squeezed light source cavity length control loop suitable for the generation of squeezed states in the audio frequency band	119
6.7	Schematic of the locking loop for the mode cleaner ring cavity placed in the local oscillator beam	121

xvi	List of Figures	0.0
6.8	Schematic of the locking loops which are required for the coherent control scheme of the green pump phase and the local oscillator phase	123
6.9	Schematic of a third phase locking loop required to „synchronize“ the squeezing main laser to the GEO 600-laser frequency	125
6.10	Schematic of the optical configuration for the sequence: OMC – Faraday-Rotator – PD _{h(t)}	129
6.11	Schematic of the optical configuration for the sequence: Faraday Rotator – OMC – PD _{h(t)}	131
6.12	Degree of squeezing versus optical loss	132
6.13	Theoretical plot of the detected (anti-)squeezing strength in dependence of the sideband-frequency	133
B.1	Schematic of the 40 MHz AOM-Driver circuit	146
B.2	Schematic of a 80 MHz frequency generator plus frequency divider	147
B.3	Schematic of the generic Servo circuit (page 1)	148
B.4	Schematic of the generic Servo circuit (page 2)	149
B.5	Schematic of the generic Servo circuit (page 3)	150
B.6	Schematic of the generic Servo circuit (page 4)	151
B.7	Schematic of the modecleaner Peltier circuit	152
B.8	Schematic of the homodyne detector circuit (page 1)	153
B.9	Schematic of the homodyne detector circuit (page 2)	154
B.10	Schematic of the resonant photodiode circuit (page 1)	155
B.11	Schematic of the resonant photodiode circuit (page 2)	156
B.12	Schematic of the generic OPA/SHG temperature controller	157

List of Tables

6.1	Channel list for a digital remote control of the second harmonic generator setup	116
6.2	Required digital I/O channels for remote controlling the analog MC ₅₃₂ cavity length control locking loop	117
6.3	Required Digital I/O channels for the squeezed light source crystal temperature stabilization scheme	119
6.4	Channel list for digital remote control of the squeezer cavity length control loop and the Auxiliary Laser 1 phase locking loop	120
6.5	Channel list for digital remote control of the infrared mode cleaner cavity (MC1064) length control loop	122
6.6	Channel list for digital remote control of the green pump phase, local oscillator phase and the second laser phase locking loop (Aux 2 - Laser)	124
6.7	Channel list for a digital remote control of the main laser phase locking loop	126
6.8	Total number of required digital control and monitor channels	127
6.9	Summary of the modulation frequencies required for the GEO 600 squeezing experiment	127

Introduction

1.1 Detection of gravitational waves

The direct detection of gravitational waves will lead into a new era of astronomy. For example, a stochastic background of gravitational waves of cosmological origin would provide a unique view into the early universe and gravitational waves emitted from isolated neutron stars and from the merger of compact binary systems contain enlightening information about black holes and neutron stars.

The prediction of perturbations of space-time, caused by accelerated massive objects, were predicted by Albert Einstein as a consequence of his theory of general relativity [Einst16], [Einst18]. These ripples in space time – so-called „gravitational waves“ – travel through the universe at the speed of light.

Almost 60 years after their prediction, the first *indirect* experimental proof of the existence of gravitational waves was achieved by studying the binary pulsar system PSR 1913+16. The astronomers Russel Hulse and Joseph Taylor showed in 1974 that the oscillation period of the pulsar around its companion star decreased exactly over time as predicted by the Einstein equations [Hulse94], [Taylor94]. Further analysis determined that a part of the pulsar orbital energy is converted into gravitational radiation. In 1993 Hulse and Taylor were awarded the Nobel Prize in Physics. However, the *direct* detection of gravitational waves is one of the greatest experimental challenges today and would provide new and deep astronomical insights complementary to the electromagnetic observations.

Like electromagnetic waves, the spectrum of gravitational waves is spanned over many frequency decades. To cover a low-frequency detection band in the mHz regime, which is inaccessible for earth-based detectors due to seismic noise, the development

of a detector in space has already started. In cooperation with the European Space Agency (ESA) and the American National Aeronautics and Space Administration (NASA), the detector „LISA“ will be launched after 2018 [ESA].

On earth the first detection design was based on cylindrical aluminum bars for length measurements. A gravitational wave should excite a resonant mode of the bar whose movement is detected with a piezoelectric transducer. This technique was pioneered by Joe Weber almost 40 years ago at the University of Maryland and Argonne National Laboratory [Weber69] and is still used in today’s resonant bar and sphere detectors like AURIGA, EXPLORER, NAUTILUS, Mario Schenberg, and MiniGRAIL [AURIGA], [EXPLO06], [Mario06], [GRAIL06]. Unfortunately, these detectors are most sensitive only at a narrow bandwidth around their resonant frequency, which is approximately at 900 Hz.

A more broadband detection bandwidth is provided by earth-based kilometer-scale laser-interferometric detectors. Their current technology has been developed to a point where detection sensitivities of astrophysical interests can be reached.

1.2 Gravitational wave detection with laser interferometers

Today there is an international network of interferometric detectors in operation aiming for the first *direct* detection of gravitational waves in the frequency band from 10 Hz up to several kHz. The Laser Interferometer Gravitational wave Observatory (LIGO) consists of three long-baseline interferometers: a 4 km instrument „L1“ in Livingston, USA, and a 4 km and 2 km instrument („H1“ and „H2“) in Hanford, USA [LIGO]. In Europe there is the British-German GEO 600 detector located close to Hannover, Germany, with an armlength of 600 m [GEO600], and the French-Italian 3 km long VIRGO detector based at Cascina, near Pisa in Italy [VIRGO]. Another instrument is the Japanese TAMA 300 detector, with an armlength of 300 m [TAMA].

To achieve target sensitivities these observatories are based upon improved topologies of the classic Michelson interferometer. Basically, the strain field from a gravitational wave acts on the interferometers by effectively shortening the distance of one test mass (suspended mirror) relative to the beamsplitter while extending the distance to the perpendicular test mass (see Figure 1.1). For a classic Michelson interferometer, which compares the relative phase of two light fields that have travelled in opposite interferometers arms, this means that an output signal is produced. Since their interaction with matter is extremely weak, the emitted gravitational waves reach the earth almost undisturbed. This is the reason why the analysis of gravitational



Figure 1.1 — **Left:** A classic Michelson interferometer consists of a laser, a 50/50 beamsplitter, two test mass mirrors and a photodetector. One can think of the gravitational wave as modulating the effective refraction index of the vacuum, thereby shortening the length of one arm while expanding the length of the other. **Right:** Photograph of the French-Italian VIRGO detector with an armlength of 3 km.

wave signals can reveal new insights, which are not accessible from the study of electromagnetic waves. This advantage is, on the other hand, a handicap for their detection. In order to reach meaningful detection probabilities, gravitational wave detectors must be sensitive enough to be able to measure differential length variations of less than 10^{-18} m.

1.3 Noise sources in interferometric gravitational wave detectors

In order to reach such exceptional measurement precision it is necessary to consider noise sources that can limit the sensitivity to gravitational wave signals. Of the many noise sources, there are some prominent ones in different frequency regions: seismic and radiation pressure noise at low frequencies, thermal noise at intermediate frequencies and photon shot noise at high frequencies. Depending on the interferometer topology the coupling of these noise sources into the detected signal varies.

1.3.1 Seismic noise

At frequencies below 40 Hz, the coupling of seismic noise into the interferometer test masses positions limits the interferometer sensitivity. The coupling is reduced by using multiple-cascaded pendulum stages for the suspension of the test masses together

with active control systems. At frequencies above the pendulum eigenfrequency each pendulum stage suppresses the test mass motion due to seismic noise with $1/f^2$. At frequencies below approximately 40 Hz the motion of the test masses produces a signal that cannot be distinguished from a gravitational wave signal.

1.3.2 Thermal noise

At intermediate frequencies thermally induced movement of the test masses is expected to be a sensitivity limiting noise source - even for advanced detector designs [Rowan05] [Bragi99]. Thermal noise includes, for example, the thermorefractive noise, which describes fluctuations of the refraction index for e.g. transmissive optics [Bragi01], as well as the thermally induced motion of the reflecting test mass due to thermally excited modes of vibration and coating thermal noise [Liu00] [Crook04]. Therefore, materials with low mechanical loss (a high Q-factor) are being used for the test masses and their suspensions so that the thermal energy is stored in a few discrete vibration modes which have large amplitude but are at frequencies outside the detection band. The choice of adequate materials is limited by the requirement for excellent optical properties like high transparency for the optical wavelength used, for example.

Another approach to reduce thermally induced movement is to cool test masses and suspension. This method is under investigation at the Japanese LCGT project [Kurod06]. However, issues like heat input to the test masses from the laser, low power absorption, high thermal conductivity and cooling specific material properties have to be considered.

1.3.3 Quantum noise

Ultimately, the detector sensitivity is limited by photon quantum noise due to the Heisenberg uncertainty principle. Both, the photon shot noise as well as the quantum radiation pressure noise, originate from vacuum noise impinging on the interferometer dark port and are manifestations of the two quadratures of the vacuum field.

1.3.3.1 Photon shot noise

The shot noise contribution to the detector strain amplitude is given by [Goda07b]:

$$h_{shot}(\Omega) = \frac{1}{L} \sqrt{\frac{\hbar c \lambda}{2\pi P}}, \quad (1.1)$$

where L is the detector armlength, λ the laser wavelength and P the total light power inside the interferometer. Since the interferometer signal increases linearly with the

circulating power, but the shot noise power increases as the square root of P , the shot noise limited signal to noise may be improved by increasing P (for a given armlength).

1.3.3.2 Quantum radiation pressure noise

For high circulating light power inside the interferometer, radiation pressure noise limits the detector sensitivity. This noise source is due to the statistical variations in the photon number of the vacuum field, thereby imparting a fluctuating momentum to the interferometer mirrors. This displacement noise can be understood by relating the imparted momentum to the change of velocity of the mirror

$$\Delta p = m\Delta v = m \frac{\Delta x}{\Delta t}. \quad (1.2)$$

With the measurement interval related to the measurement bandwidth via $\Delta t = 1/2\Omega$ the contribution of the radiation pressure noise to the linear spectral noise density of the GW-strain amplitude (for a simple Michelson interferometer) is given by [Bragi92]

$$h_{rad}(\Omega) = \frac{1}{2m\Omega^2 L} \sqrt{\frac{8\pi\hbar P}{c\lambda}}, \quad (1.3)$$

and hence significant at low frequencies. Please note, that the radiation pressure noise increases with increasing P and can be compensated by increasing the mirror mass m . Currently seismic noise is the dominant noise source at lower frequencies but for Advanced LIGO the radiation pressure noise is expected to limit the sensitivity.

1.3.3.3 Standard Quantum Limit

The quadrature sum of the shot noise and the radiation pressure noise becomes the total quantum noise of a Michelson interferometer

$$h_{total} = \sqrt{h_{shot}^2(\Omega) + h_{rad}^2(\Omega)}. \quad (1.4)$$

Minimizing the total quantum noise with respect to the light input power P , the resulting minimal noise is called the standard quantum limit (SQL), which is given by [Bragi92], [Goda07b]

$$h_{SQL} = \sqrt{\frac{4\hbar}{m\Omega^2 L^2}}, \quad (1.5)$$

when the interferometer is operated with the optimal light input power for the frequency being measured

$$P_{opt} = \frac{c\lambda m\Omega^2}{4\pi}. \quad (1.6)$$

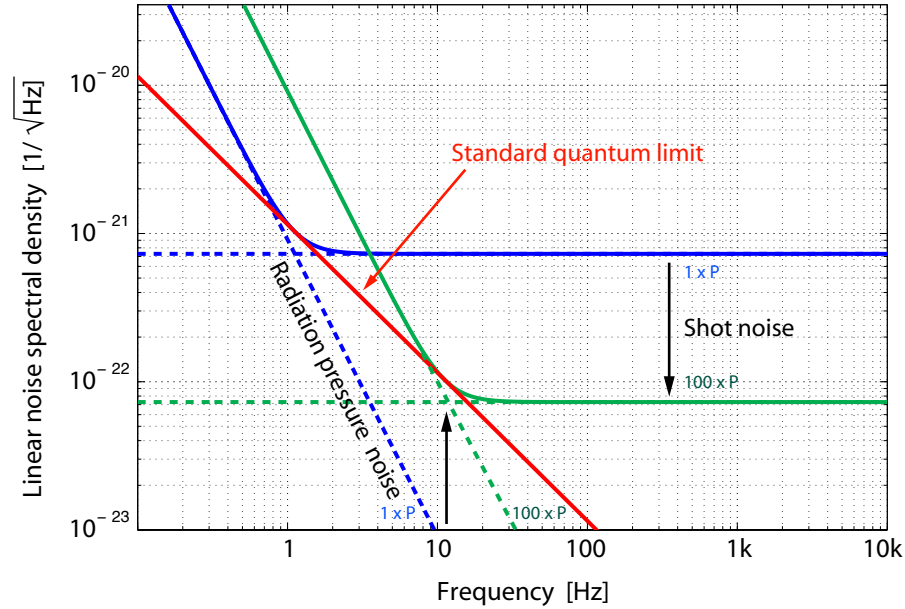


Figure 1.2 — Quantum noise limited strain sensitivities for a Michelson interferometer in dependence of the circulating laser light power [Param]. An intensity increase by a factor of 100 reduces the shot noise contribution at the expense of a higher radiation pressure noise level. The standard quantum limit is the minimized sum of both quantum noise sources for an optimal light power.

1.4 Quantum enhancement

One approach to reduce the sensitivity limiting shot noise level, is to increase the circulating laser light power inside the detector. For this reason the advanced LIGO detectors are proposed to store close to a megawatt of laser light inside the interferometer in order to reach their sensitivity goal. But optical waveform distortion due to absorption and the excitation of parametric instabilities both have a risk to limit the maximum light power [Dambr03], [Shaug04].

Using non-classical states of light (squeezed states) has the potential to achieve similar performance with less laser power. It was first proposed in 1981 by Caves [Caves81] that the quantum limit in interferometric gravitational wave detectors can be surpassed by the injection of squeezed states into the antisymmetric port of the interferometer. A squeezed state is a state whose uncertainty in *one* of the field quadratures (amplitude and phase) is reduced compared to a vacuum state.

Following this approach the uncorrelated vacuum fluctuations, entering the detec-

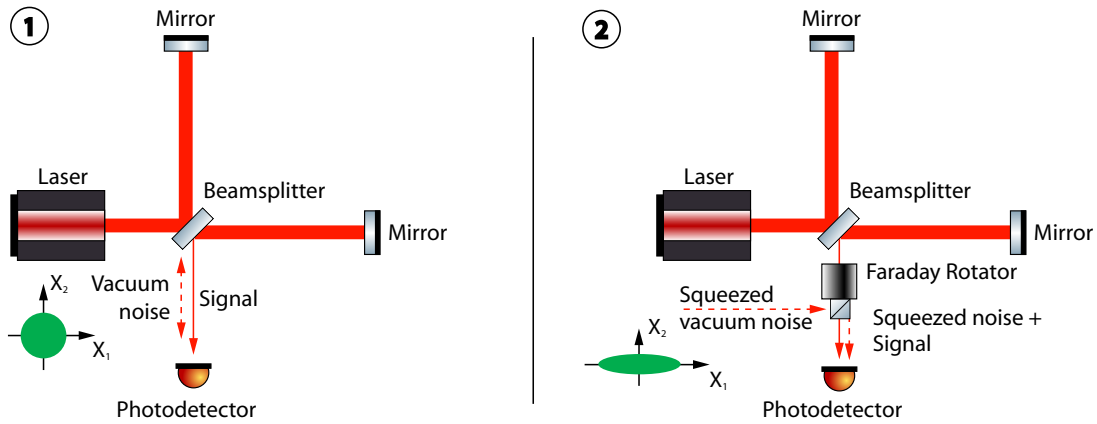


Figure 1.3 — Schematic of a Michelson interferometer operated at a dark fringe. **Left:** Vacuum fluctuations entering the antisymmetric port of the interferometer are leading to a quantum noise limited sensitivity. **Right:** A Faraday Rotator is used to inject squeezed vacuum states into the antisymmetric port, thereby substituting the ordinary vacuum fluctuations. The squeezed light enhanced interferometer output field (with a possible gravitational wave signal) is detected with a photodetector placed at the dark port.

tor through its antisymmetric port, will be replaced by correlated squeezed vacuum states. As shown in Figure 1.3 these can be injected into the interferometer using a Faraday Rotator.

In Figure 1.4 the quantum noise (blue trace) for a given Michelson interferometer is shown. Injecting a 20 dB (factor of 100) squeezed vacuum state, whose noise is squeezed in the phase quadrature X_2 , the detected shot noise level is reduced by a factor of 10. Unfortunately, due to the Heisenberg uncertainty principle, the noise in the X_1 quadrature is increased by the same factor. Thus, the interferometer quantum noise is enhanced at lower frequencies. The resulting quantum noise budget is comparable to an increase of laser power by a factor of 100, as described above. But when the squeezed vacuum states are rotated in a certain frequency band by means of a filter cavity e.g. (so called frequency dependent squeezing) [Kimbl01] then the interferometer sensitivity can be improved over the complete detection bandwidth, which is illustrated with the green trace in Figure 1.4. Using these „optimal prepared“ squeezed vacuum states even the standard quantum limit can be beaten in a certain bandwidth.

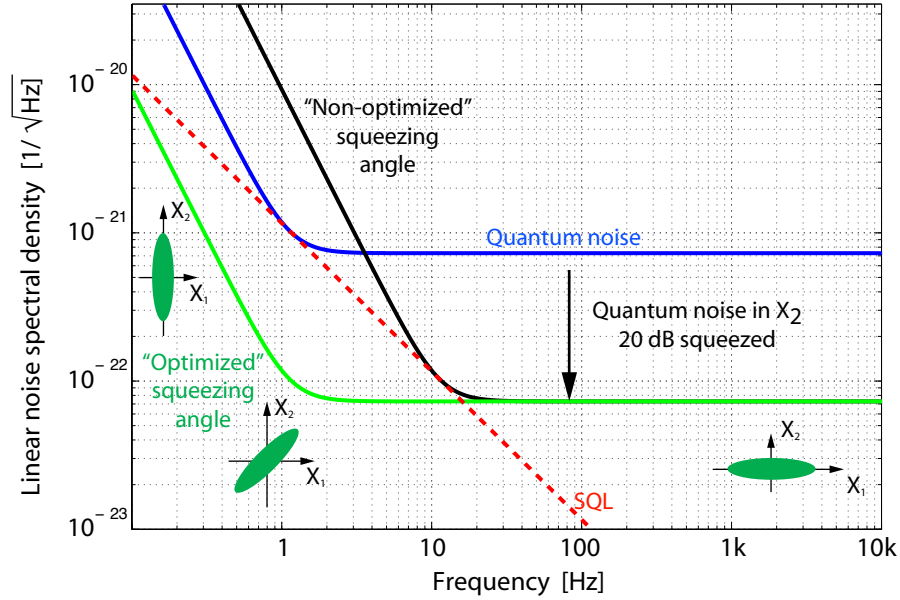


Figure 1.4 — The effect of squeezing on a Michelson Interferometer when a 20 dB squeezed vacuum field is injected into the antisymmetric port [Param]. The detector quantum noise (blue trace) gets reduced in the shot noise limited regime by a factor of 10, at the expense of a higher quantum noise at lower frequencies (black trace). The resulting quantum noise level is comparable with an increase of laser power by a factor of 100. If frequency dependent squeezed states were injected, the sensitivity can be improved over the complete detection bandwidth (green trace). In a quantum noise limited interferometer even the standard quantum level (red trace) can be beaten in that case.

1.5 Structure of the thesis

The purpose of this thesis is the study of experimental generation of squeezed vacuum states meeting the requirements for quantum enhancement in laser interferometric GW-detectors. Therefore, two main topics are addressed: First the maximal achievable squeezing strength is investigated, and second, squeezed vacuum states are generated within the GW-detector detection band based on a novel coherent control scheme.

Prior to the experimental main chapters of this thesis, Chapter 2 describes the theory of non-classical light including the generation of squeezed states and balanced homodyne detection.

In Chapter 3 the generation of strongly squeezed vacuum states at Fourier-frequencies in the MHz-regime is presented. It is shown that a quantum noise reduction

of 11.5 dB below the shot noise limit can be achieved by using a monolithic squeezed light source and reducing phase noise and optical loss.

Chapter 4 describes a coherent control scheme for squeezed vacuum states in the gravitational wave detection band. Up to 6.5 dB squeezing is measured in the frequency band from 1 Hz up to 10 kHz, thus covering the complete detection bandwidth of earth-based GW-detectors. A detailed theoretical description of the control scheme is presented and an extensive experimental section is provided.

Chapter 5 presents a peer reviewed article in the context of the first experimental description of a squeezed light enhanced dual-recycled Michelson interferometer. In this experiment a filter cavity is implemented in order to demonstrate a broadband signal-to-noise ratio improvement of the interferometer sensitivity in the MHz-regime.

A proposal of a compact squeezed light source design, optimized for the long term stable operation in GW-detectors, is reported in Chapter 6. This Chapter includes the optical layout and a detailed electronic control scheme for a low-frequency squeezer directly applicable to the GEO 600 GW-detector.

Chapter 7 provides some overall conclusions and an outlook.

In the Appendix additional information regarding computer script source codes and schematics of electronics are provided.

The Theory of Non-Classical Light

In this Chapter the essential theoretical models of quantum mechanics are presented which are required for the experimental work in this thesis. This includes the basics of quantum states of light, the description of squeezed light generation via optical parametric processes, and finally a detailed analysis of the (un-)balanced homodyne detection scheme.

2.1 Field quantization

The starting point are the Maxwell equations. Assuming a monochromatic electromagnetic field to be polarized along the x-direction, the electrical field of a standing wave cavity with perfectly reflecting mirrors can be written, in SI units, as [Gerry04]

$$E_x(z, t) = \left(\frac{2\omega^2}{V\epsilon_0} \right)^{1/2} q(t) \sin(kz), \quad (2.1)$$

where ω is the frequency of the mode and k is the wave number related to the frequency according to $k = \omega/c$. A time dependent factor having the dimension of length is given by $q(t)$. As we shall see, $q(t)$ will act as a canonical position. The pre-factors are dependent on the chosen unit system and are therefore insignificant. The magnetic field, which is polarized in y-direction, is

$$B_y(z, t) = \left(\frac{\mu_0\epsilon_0}{k} \right) \left(\frac{2\omega^2}{V\epsilon_0} \right) \dot{q}(t) \cos(kz). \quad (2.2)$$

Here, $\dot{q}(t)$ will play the role of a canonical momentum for a „particle“ of unit mass, i.e. $p(t) = \dot{q}(t)$. From Equation 2.1 and 2.2 one can derive the Hamiltonian H

$$H(q, p) = \frac{1}{2}(p^2 + \omega^2 q^2). \quad (2.3)$$

Having identified the canonical variables q and p for the classical system, we simply use the correspondence rule to exchange them by their operator equivalents

$$q \rightarrow \hat{q}, \quad p \rightarrow \hat{p} \quad \text{with} \quad [\hat{q}, \hat{p}] = i\hbar. \quad (2.4)$$

Then the electric and magnetic fields become the operators $\hat{E}_x(z, t)$ and $\hat{B}_y(z, t)$, and the Hamiltonian becomes

$$\hat{H} = \frac{1}{2}(\hat{p}^2 + \omega^2 \hat{q}^2). \quad (2.5)$$

Now the annihilation (\hat{a}) and creation (\hat{a}^\dagger) operators can be introduced through the combination

$$\hat{a} = (2\hbar\omega)^{-1/2}(\omega\hat{q} + i\hat{p}) \quad \text{and} \quad (2.6)$$

$$\hat{a}^\dagger = (2\hbar\omega)^{-1/2}(\omega\hat{q} - i\hat{p}). \quad (2.7)$$

Unlike the operators \hat{q} and \hat{p} , these new operators are non-Hermitian and therefore non-observable. The operators \hat{a} and \hat{a}^\dagger satisfy the commutation relation

$$[\hat{a}, \hat{a}^\dagger] = 1 \quad (2.8)$$

and the Hamiltonian operator can be written as

$$\hat{H} = \hbar\omega \left(\hat{a}^\dagger \hat{a} + \frac{1}{2} \right). \quad (2.9)$$

Now the number operator \hat{n} can be introduced, which is given by the operator product of $\hat{a}^\dagger \hat{a}$. We let $|n\rangle$ denote an energy eigenstate with the energy eigenvalue E_n such that

$$\begin{aligned} \hat{H} |n\rangle &= \hbar\omega \left(\hat{a}^\dagger \hat{a} + \frac{1}{2} \right) |n\rangle \\ &= E_n |n\rangle. \end{aligned} \quad (2.10)$$

If we multiply the left side by \hat{a}^\dagger we obtain a new eigenvalue equation

$$\hbar\omega \left(\hat{a}^\dagger \hat{a}^\dagger \hat{a} + \frac{1}{2} \hat{a}^\dagger \right) |n\rangle = E_n \hat{a}^\dagger |n\rangle. \quad (2.11)$$

Using the commutation relation $[\hat{a}, \hat{a}^\dagger] = 1$ we can rewrite this as

$$\hat{H}(\hat{a}^\dagger |n\rangle) = (E_n + \hbar\omega)(\hat{a}^\dagger |n\rangle), \quad (2.12)$$

which is the eigenvalue problem for the eigenstate $\hat{a}^\dagger |n\rangle$ with the energy eigenvalue $E_n + \hbar\omega$. Now the name „creation operator“ becomes clear for \hat{a}^\dagger : it creates a quantum of energy. Likewise we obtain

$$\hat{H}(\hat{a} |n\rangle) = (E_n - \hbar\omega)(\hat{a} |n\rangle) \quad (2.13)$$

if we multiply Equation 2.10 by the operator \hat{a} and use the commutation relation. Here it becomes clear that the operator \hat{a} annihilates one quantum of energy ($\hbar\omega$), the eigenstate $(\hat{a} |n\rangle)$ possessing the energy eigenvalue $E_n - \hbar\omega$. But the energy of the harmonic oscillator cannot be negative, therefore there has to be a lowest-energy state („ground state“ or „vacuum state“), which is defined by the annihilation operator \hat{a}

$$\hat{a} |0\rangle = 0. \quad (2.14)$$

The eigenvalue problem for the ground state is

$$\begin{aligned} \hat{H} |0\rangle &= \hbar\omega \left(\hat{a}^\dagger \hat{a} + \frac{1}{2} \right) |0\rangle \\ &= \frac{1}{2} \hbar\omega |0\rangle, \end{aligned} \quad (2.15)$$

so that the lowest energy eigenvalue is the so-called „zero-point energy“ and is not $E_0 = 0$ but has the energy $\hbar\omega/2$. Since we know that the creation operator \hat{a}^\dagger creates each time a quantum with energy $\hbar\omega$ ($E_{n+1} = E_n + \hbar\omega$), the energy eigenvalues are

$$E_n = \hbar\omega \left(n + \frac{1}{2} \right), \quad n = 0, 1, 2, \dots \quad (2.16)$$

If one compares this with Equation 2.10 the number operator $\hat{n} = \hat{a}^\dagger \hat{a}$ can be defined as

$$\hat{n} |n\rangle = n |n\rangle. \quad (2.17)$$

The number operator does therefore not change the state but gives as the eigenvalue the number of quanta, measured in multiples of $\hbar\omega$.

For the state $\hat{a} |n\rangle$ we have

$$\hat{a} |n\rangle = c_n |n-1\rangle. \quad (2.18)$$

For the determination of the constant c_n the inner product of $\hat{a} |n\rangle$ with itself is

$$(\langle n | \hat{a}^\dagger)(\hat{a} |n\rangle) = \langle n | \hat{a}^\dagger \hat{a} |n\rangle = n \quad (2.19)$$

$$= \langle n-1 | c_n^* c_n |n-1\rangle = |c_n|^2. \quad (2.20)$$

From this we can derive that $|c_n|^2 = n$, so we can take $c_n = \sqrt{n}$. Thus, we can summarize

$$\hat{a} |n\rangle = \sqrt{n} |n-1\rangle, \quad (2.21)$$

$$\hat{a}^\dagger |n\rangle = \sqrt{n+1} |n+1\rangle, \quad (2.22)$$

$$\hat{a}^\dagger \hat{a} |n\rangle = n |n\rangle. \quad (2.23)$$

Combining all of these results, any state $|n\rangle$ may be generated from the ground state $|0\rangle$ by the repeated action of the creation operator \hat{a} :

$$|n\rangle = \frac{(\hat{a}^\dagger)^n}{\sqrt{n!}} |0\rangle. \quad (2.24)$$

These states described in Equation 2.24 are called „Fock states“ and are especially important for single photon experiments.

2.2 Quantum fluctuations

As shown in the previous Section the number state $|n\rangle$ has a well-defined energy $E_n = (n + 1/2)\hbar\omega$. But the electric field is not well defined since [Gerry04]

$$\langle n | \hat{E}_x(z, t) | n \rangle = \mathcal{E}_0 \sin(kz) [\langle n | \hat{a} | n \rangle + \langle n | \hat{a}^\dagger | n \rangle] = 0, \quad (2.25)$$

which means that the mean field for Fock states is zero, but not the square of this field (energy density)

$$\langle n | \hat{E}_x^2(z, t) | n \rangle = 2\mathcal{E}_0^2 \sin^2(kz) \left(n + \frac{1}{2} \right). \quad (2.26)$$

The fluctuations in the electric field may be characterized by the variance

$$\Delta E_x^2 := \langle (\Delta \hat{E}_x(z, t))^2 \rangle = \langle \hat{E}_x^2(z, t) \rangle - \langle \hat{E}_x(z, t) \rangle^2. \quad (2.27)$$

For the number state $|n\rangle$ we have

$$\Delta E_x = \sqrt{2}\mathcal{E}_0 \sin(kz) \left(n + \frac{1}{2} \right)^{1/2} \quad (2.28)$$

Equation 2.28 shows that even when $n = 0$, the field has fluctuations, the so-called *vacuum fluctuations*.

2.3 Quadrature operators

Based on the annihilation and creation operators the so-called quadrature operators can be introduced

$$\hat{X}^+ = \frac{1}{2}(\hat{a} + \hat{a}^\dagger), \quad (2.29)$$

$$\hat{X}^- = \frac{1}{2i}(\hat{a} - \hat{a}^\dagger). \quad (2.30)$$

When we explicitly include the time dependence of the electric field operator we have

$$\hat{E}_x(z, t) = \mathcal{E}_0(\hat{a}e^{-i\omega t} + \hat{a}^\dagger e^{i\omega t}) \sin(kz) \quad (2.31)$$

or expressed with the quadrature operators

$$\hat{E}_x(z, t) \propto \sin(kz)[\hat{X}^+ \cos(\omega t) + \hat{X}^- \sin(\omega t)]. \quad (2.32)$$

It is evident that \hat{X}^+ and \hat{X}^- are associated with field amplitudes oscillating out of phase with each other by 90° . They satisfy the commutation relation

$$[\hat{X}^+, \hat{X}^-] = \frac{i}{2} \quad (2.33)$$

from which the Heisenberg uncertainty relation can be derived

$$\langle (\Delta \hat{X}^+)^2 \rangle \langle (\Delta \hat{X}^-)^2 \rangle \geq \frac{1}{16} \quad (2.34)$$

For a number state $|n\rangle$

$$\langle n | \hat{X}^+ | n \rangle = 0 \quad (2.35)$$

$$\langle n | \hat{X}^- | n \rangle = 0, \quad (2.36)$$

but

$$\langle n | (\hat{X}^+)^2 | n \rangle = \frac{1}{4} \langle n | \hat{a}^2 + \hat{a}^\dagger \hat{a}^\dagger + \hat{a}^\dagger \hat{a} + \hat{a} \hat{a}^\dagger | n \rangle \quad (2.37)$$

$$= \frac{1}{4} \langle n | \hat{a}^2 + \hat{a}^\dagger \hat{a}^\dagger + 2\hat{a}^\dagger \hat{a} + 1 | n \rangle \quad (2.38)$$

$$= \frac{1}{4}(2n + 1) \quad (2.39)$$

and similarly for \hat{X}^-

$$\langle n | (\hat{X}^-)^2 | n \rangle = \frac{1}{4}(2n + 1). \quad (2.40)$$

Therefore, the uncertainties in both quadratures are the same and the vacuum state ($n = 0$) minimizes the uncertainty product

$$\langle (\Delta(\hat{X}^+))^2 \rangle_{vac} = \frac{1}{4} = \langle (\Delta(\hat{X}^-))^2 \rangle_{vac}. \quad (2.41)$$

2.4 Coherent states

In the previous Chapter number states $|n\rangle$ were introduced but for the description of quantum optic experiments with laser light intensities of several watt, number states are not appropriate for the description anymore. It is often suggested that the classical limit of the quantized field is the limit in which the number of photons becomes very large such that the number operator becomes a continuous variable. But in Equation 2.25 we have shown that the mean field $\langle n | E_x | n \rangle = 0$, independent of the value of n . We know that at a fixed point in space a classical field oscillates sinusoidally in time. This does not happen for the expectation value of the field operator for a number state. For a better description of such states we seek for eigenstates of the annihilation operator. These are denoted as $|\alpha\rangle$ and satisfy the relation [Gerry04]

$$\hat{a} |\alpha\rangle = \alpha |\alpha\rangle, \quad (2.42)$$

where α is a complex number, since \hat{a} is not Hermitian. We expand α in the basis of number states $|n\rangle$

$$|\alpha\rangle = \sum_{n=0}^{\infty} C_n |n\rangle. \quad (2.43)$$

Therefore, Equation 2.42 becomes

$$\hat{a} |\alpha\rangle = \sum_{n=1}^{\infty} C_n \sqrt{n} |n-1\rangle \quad (2.44)$$

$$= \alpha \sum_{n=0}^{\infty} C_n |n\rangle. \quad (2.45)$$

Equating coefficients leads to

$$C_n \sqrt{n} = \alpha C_{n-1} \quad (2.46)$$

$$(2.47)$$

or

$$C_n = \frac{\alpha}{\sqrt{n}} C_{n-1} \quad (2.48)$$

$$= \frac{\alpha^2}{\sqrt{n(n-1)}} C_{n-2} = \dots \quad (2.49)$$

$$= \frac{\alpha^n}{\sqrt{n!}} C_0. \quad (2.50)$$

Thus, Equation 2.43 can be rewritten as

$$|\alpha\rangle = C_0 \sum_{n=0}^{\infty} \frac{\alpha^n}{\sqrt{n!}} |n\rangle. \quad (2.51)$$

The constant C_0 can be determined from the normalization requirement $\langle \alpha | \alpha \rangle = 1$ which finally leads to

$$|\alpha\rangle = \exp\left(-\frac{1}{2}|\alpha|^2\right) \sum_{n=0}^{\infty} \frac{\alpha^n}{\sqrt{n!}} |n\rangle. \quad (2.52)$$

For this *coherent state* it can be shown that the expectation value of the electric field operator does not vanish but looks like a classical field with sinusoidal oscillation. The coherent state is therefore nearly a classical-like state because it not only yields the correct form for the field expectation values but contains only the noise of the vacuum. The latter can be shown by using the quadrature operators for coherent states

$$\langle (\Delta(\hat{X}^+))^2 \rangle_{\alpha} = \frac{1}{4} = \langle (\Delta(\hat{X}^-))^2 \rangle_{\alpha}. \quad (2.53)$$

It is apparent that $|\alpha|$ is related to the amplitude of the field and thus the average photon number of the field is

$$n = \langle \alpha | \hat{n} | \alpha \rangle = |\alpha|^2. \quad (2.54)$$

To calculate the fluctuations of the photon number we need the expectation value of \hat{n}^2

$$\begin{aligned} \langle \alpha | \hat{n}^2 | \alpha \rangle &= \langle \alpha | \hat{a}^\dagger \hat{a} \hat{a}^\dagger \hat{a} | \alpha \rangle \\ &= |\alpha|^4 + |\alpha|^2 \\ &= n^2 + n \end{aligned} \quad (2.55)$$

and thus

$$\Delta^2 n = \langle \hat{n}^2 \rangle - \langle \hat{n} \rangle^2 = n, \quad (2.56)$$

which is characteristic for a Poisson process. In fact, for a measurement of the number of photons in the field, the probability of detecting n photons is

$$P_n = |\langle n|\alpha\rangle|^2 \quad (2.57)$$

$$= e^{-\bar{n}} \frac{\bar{n}^n}{n!} \quad (2.58)$$

which is a Poisson distribution with a mean of n . Note that the fractional uncertainty in the photon number is

$$\frac{\Delta n}{\bar{n}} = \frac{1}{\sqrt{\bar{n}}} \quad (2.59)$$

which decreases with increasing \bar{n} .

So far we described the coherent state via the eigenstates of the annihilation operator but another possibility for the description is given by the displacement operator \hat{D}

$$\hat{D}(\alpha) = \exp(\alpha\hat{a}^\dagger - \alpha^*\hat{a}). \quad (2.60)$$

In that case the coherent state can be written as

$$\begin{aligned} |\alpha\rangle &= \hat{D}(\alpha) |0\rangle \\ &= \exp\left(-\frac{1}{2}|\alpha|^2\right) \sum_{n=0}^{\infty} \frac{\alpha^n}{\sqrt{n!}} |n\rangle, \end{aligned} \quad (2.61)$$

which is identical to the coherent state described in Equation 2.52.

2.5 Squeezed states

From quantum mechanics it is well known that if two operators \hat{A} and \hat{B} satisfy the commutator relation $[\hat{A}, \hat{B}] = \alpha$, it can be shown for the variances that

$$(\Delta^2\hat{A})(\Delta^2\hat{B}) \geq \frac{1}{4}|\alpha|^2, \quad (2.62)$$

which describes a Heisenberg uncertainty relation. If both variances $\Delta^2\hat{A}$ and $\Delta^2\hat{B}$ are equal and also the product is $\frac{1}{4}|\alpha|^2$, a state of minimum uncertainty is described. A state is said to be *squeezed* if either

$$\Delta^2\hat{A} < \frac{1}{2}|\alpha| \quad \text{or} \quad \Delta^2\hat{B} < \frac{1}{2}|\alpha|. \quad (2.63)$$

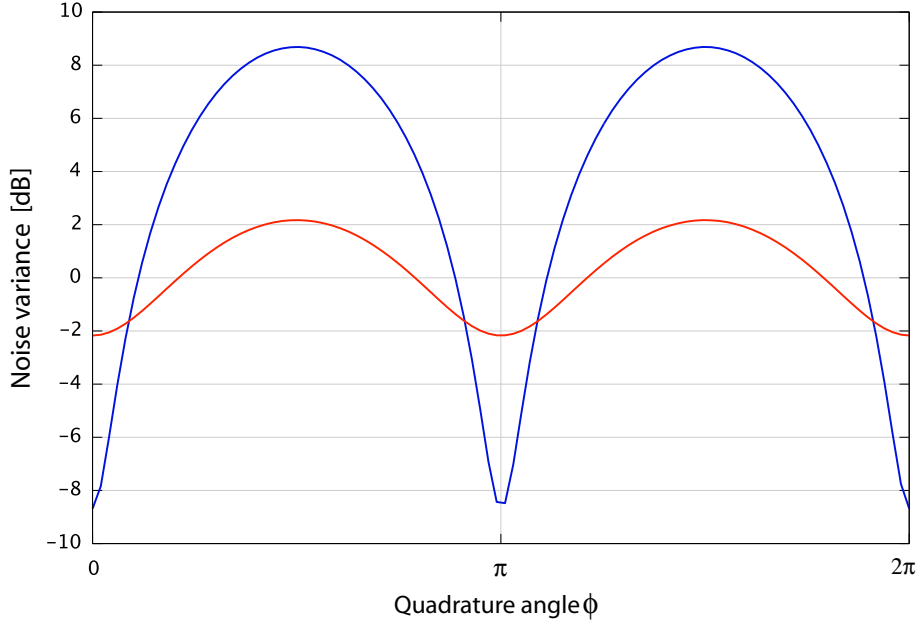


Figure 2.1 — Illustration of the quantum noise variance in dependence of the quadrature angle ϕ . The state was intended to be squeezed in the amplitude quadrature, thus the phase quadrature ($\phi = \pi/2$) is anti-squeezed. Two traces were plotted, the red trace shows a squeezed state with squeezing parameter $r = 0,25$ and in blue the squeezing parameter was $r = 1$.

Because of Equation 2.62 obviously both variances cannot be less than $1/2|\alpha|$ simultaneously. Using the amplitude and phase quadrature operators, satisfying the commutator relation in Equation 2.62, squeezing exists if

$$\Delta^2 \hat{X}^+ < 1 \quad \text{or} \quad \Delta^2 \hat{X}^- < 1. \quad (2.64)$$

We have already established that for a coherent state $\Delta^2 \hat{X}^+ = \Delta^2 \hat{X}^- = 1$. States for which one of the conditions in 2.64 holds will have less „noise“ in one of the quadratures than for a coherent state or a vacuum state. To still satisfy the uncertainty relation this means that the „noise“ in the orthogonal quadrature has to be increased. One can speak of „squeezed“ fluctuations in one quadrature and „anti-squeezed“ fluctuations in the orthogonal one.

One way of generating a squeezed state mathematically, is through the action of a *squeezing operator* defined as [Gerry04]

$$\hat{S}(\zeta) = \exp \left(\frac{1}{2} (\zeta^* \hat{a} \hat{a} - \zeta \hat{a}^\dagger \hat{a}^\dagger) \right) \quad (2.65)$$

where

$$\zeta = r e^{i\phi}. \quad (2.66)$$

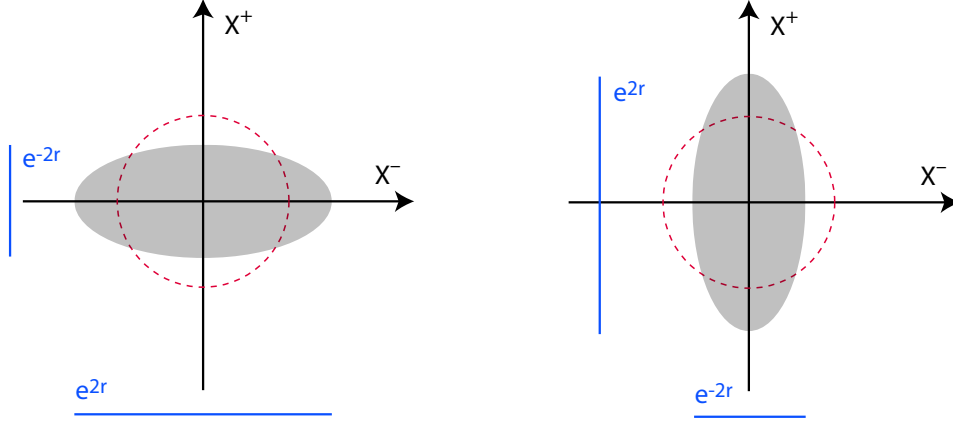


Figure 2.2 — The left picture illustrates a squeezed vacuum state where the squeezing is in the \hat{X}^+ quadrature. The dashed circle visualizes the non-squeezed vacuum noise. On the right hand a \hat{X}^- quadrature squeezed state is shown.

Here r is known as the squeezing parameter and $0 \leq r \leq \infty$ and the phase ϕ is $0 \leq \phi \leq 2\pi$. This operator $\hat{S}(\xi)$ is a kind of two-photon generalization of the displacement operator used to define the usual coherent states of a single-mode field, as previously discussed. Evidently, the operator $\hat{S}(\xi)$ acting on the vacuum would create some sort of „two-photon coherent state“ as it is clear that photons will be created and destroyed in pairs by the action of this operator [Gerry04]. Now let us consider the action of this operator $\hat{S}(\xi)$ to the state $|\psi\rangle$

$$|s\rangle = \hat{S}|\psi\rangle. \quad (2.67)$$

To obtain the variances of the quadratures we need the expectation values of the annihilation and creation operators. For the squeezing operator the following result is obtained

$$\hat{S}^\dagger \hat{a} \hat{S} = \hat{a} \cosh(r) - \hat{a}^\dagger e^{i\phi} \sinh(r), \quad (2.68)$$

$$\hat{S}^\dagger \hat{a}^\dagger \hat{S} = \hat{a}^\dagger \cosh(r) - \hat{a} e^{-i\phi} \sinh(r). \quad (2.69)$$

For the special case where $|\psi\rangle$ is the vacuum state we find for the variances of the squeezed vacuum state

$$\Delta^2 \hat{X}^+ = \cosh^2(r) + \sinh^2(r) - 2 \sinh(r) \cosh(r) \cos(\phi), \quad (2.70)$$

$$\Delta^2 \hat{X}^- = \cosh^2(r) + \sinh^2(r) + 2 \sinh(r) \cosh(r) \cos(\phi). \quad (2.71)$$

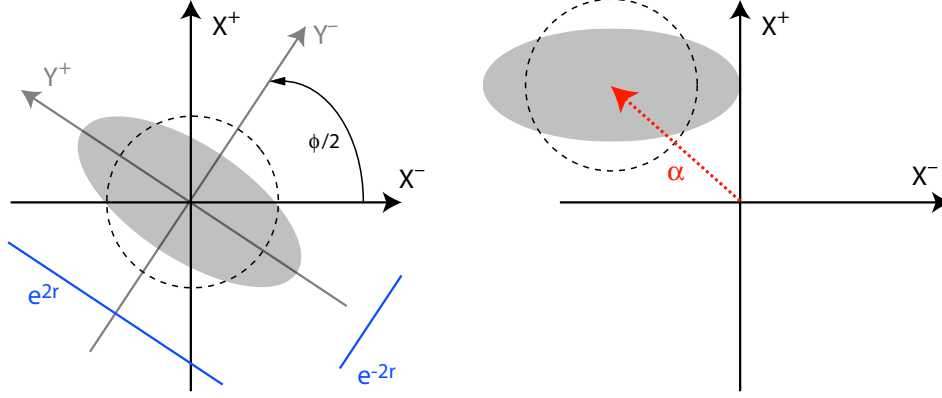


Figure 2.3 — The left picture illustrates an squeezed vacuum state where the squeezing is along the $\phi/2$ direction. On the right hand a displaced (α) squeezed state with the squeezing in the \hat{X}^+ quadrature is shown.

For $\phi = 0$, Equations 2.71 reduce to

$$\Delta^2 \hat{X}^+ = e^{-2r} \quad \text{and} \quad (2.72)$$

$$\Delta^2 \hat{X}^- = e^{2r}. \quad (2.73)$$

and evidently squeezing exists in the quadrature \hat{X}^+ . For $\phi = \pi$, the squeezing will appear in the quadrature \hat{X}^- . A useful way to illustrate squeezing graphically is the phase-space representation. Two cases of squeezing in the \hat{X}^+ - and \hat{X}^- -quadrature are shown in Figure 2.2. For other values of ϕ rotated quadrature operators \hat{Y}^+ and \hat{Y}^- can be defined

$$\begin{pmatrix} \hat{Y}^+ \\ \hat{Y}^- \end{pmatrix} = \begin{pmatrix} \cos(\phi/2) & \sin(\phi/2) \\ -\sin(\phi/2) & \cos(\phi/2) \end{pmatrix} \begin{pmatrix} \hat{X}^+ \\ \hat{X}^- \end{pmatrix}. \quad (2.74)$$

Similarly for these operators it can be shown that

$$\Delta^2 \hat{Y}^+ = e^{-2r} \quad \text{and} \quad (2.75)$$

$$\Delta^2 \hat{Y}^- = e^{2r} \quad (2.76)$$

Therefore, squeezed or anti-squeezed noise not only appears along the amplitude and phase quadrature but also in any other orthogonal quadratures.

A more general squeezed state may be obtained by applying the *Displacement operator*

$$|\alpha, \xi\rangle = \hat{D}(\alpha) \hat{S}(\xi) |0\rangle. \quad (2.77)$$

Obviously for $\xi = 0$ we obtain just a coherent state.

It has been shown in [Yuen76] that the sequence of applying the squeezing and displacement operator can be switched, which gives

$$\langle \alpha, \xi | \hat{n} | \alpha, \xi \rangle = |\alpha|^2 + \sinh^2(r). \quad (2.78)$$

In this Equation it can be seen that in the squeezing process photons are generated because the expectation value of number operator \hat{n} is increased by $\sinh^2(r)$. Once again it can be shown for such a state that

$$\Delta^2 \hat{Y}^+ = e^{-2r}, \quad (2.79)$$

$$\Delta^2 \hat{Y}^- = e^{2r}. \quad (2.80)$$

This means that the quantum noise characteristics are not affected by the coherent amplitude α .

2.5.1 Photon statistics

We now decompose the squeezed vacuum states into the photon number states in order to examine the photon statistics. We start with a vacuum state $|0\rangle$ satisfying

$$\hat{a} |0\rangle = 0. \quad (2.81)$$

Multiplying by $\hat{S}(\xi)$ and using the fact that this operator is unitary, we may write

$$\hat{S}(\xi) \hat{a} \hat{S}^\dagger(\xi) |\xi\rangle = 0. \quad (2.82)$$

Since

$$\hat{S}(\xi) \hat{a} \hat{S}^\dagger(\xi) = \hat{a} \cosh r + e^{i\phi} \hat{a}^\dagger \sinh r \quad (2.83)$$

we can rewrite Equation 2.82 as

$$(\hat{a}\mu + \hat{a}^\dagger\nu) |\xi\rangle = 0, \quad (2.84)$$

where $\mu = \cosh r$ and $\nu = e^{i\phi} \sinh r$. Thus the squeezed state is an eigenstate of the operator $\hat{a}\mu + \hat{a}^\dagger\nu$ with eigenvalue zero.

For the squeezed vacuum state we can now write

$$|\xi\rangle = \sum_{n=0}^{\infty} C_n |n\rangle \quad (2.85)$$

which, upon substituting into Equation 2.84, leads to the recursion relation [Gerry04]

$$C_{n+1} = -\frac{\nu}{\mu} \left(\frac{n}{n+1} \right)^{1/2} C_{n-1}. \quad (2.86)$$

Note that this relation connects only every other photon state. There are two distinct solutions, one involving only even photon states and a second involving only odd photon states. For vacuum states only the even solution is relevant. The solution of the recursion relation is [Gerry04]

$$C_{2m} = (-1)^m (e^{i\phi} \tanh r)^m \left[\frac{(2m-1)!!}{(2m)!!} \right]^{1/2} C_0 \quad (2.87)$$

where C_0 can be determined by normalization

$$\sum_{m=0}^{\infty} |C_{2m}|^2 = 1. \quad (2.88)$$

This leads to

$$|C_0|^2 \left(1 + \sum_{m=0}^{\infty} \frac{[\tanh r]^{2m} (2m-1)!!}{(2m)!!} \right) = 1. \quad (2.89)$$

From the mathematical identity

$$1 + \sum_{m=0}^{\infty} z^m \frac{(2m-1)!!}{(2m)!!} = (1-z)^{-1/2} \quad (2.90)$$

we obtain $C_0 = \sqrt{\cosh r}$. Using the following identities

$$(2m)!! = 2^m m! \quad (2.91)$$

$$(2m-1)!! = \frac{1}{2^m} \frac{(2m)!}{m!} \quad (2.92)$$

gives the most common form of the expansion coefficients for the squeezed vacuum state

$$C_{2m} = (-1)^m \frac{\sqrt{(2m)!}}{2^m m!} \frac{(e^{i\phi} \tanh r)^m}{\sqrt{\cosh r}}. \quad (2.93)$$

Thus, the squeezed vacuum state is

$$|\xi\rangle = \frac{1}{\sqrt{\cosh r}} \sum_{m=0}^{\infty} (-1)^m \frac{\sqrt{(2m)!}}{2^m m!} e^{im\phi} (\tanh r)^m |2m\rangle. \quad (2.94)$$

The probability of detecting $2m$ photons in the field is

$$P_{2m} = |\langle 2m | \xi \rangle|^2 \quad (2.95)$$

$$= \frac{(2m)!}{2^{2m} (m!)^2} \frac{(\tanh r)^{2m}}{\cosh r} \quad (2.96)$$

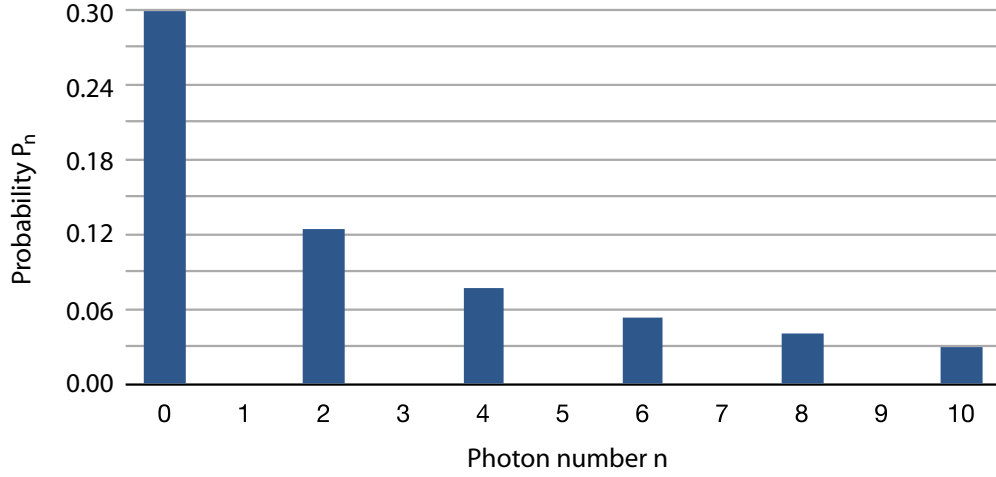


Figure 2.4 — Histogram of the photon number distribution for a 10 dB squeezed vacuum state.

while for detecting $2m+1$ states it is

$$P_{2m+1} = |\langle 2m+1 | \xi \rangle|^2 \quad (2.97)$$

$$= 0. \quad (2.98)$$

This means that the photon probability distribution for a squeezed vacuum state is oscillatory, vanishing for all odd photon numbers. In Figure 2.4 a characteristic distribution for a (pure) squeezed vacuum state is shown.

Note that, aside from the oscillatory nature of the distribution, the shape of it resembles that of thermal radiation. Remember that the squeezed vacuum is a pure state whereas the thermal state is a mixed one.

2.6 Wigner function

In 1932 Eugene Wigner introduced the „Wigner function“ which is a phase-spaced quasi-probability distribution. It is defined, for an arbitrary density operator $\hat{\rho}$, as

$$W(X^+, X^-) = \frac{1}{2\pi\hbar} \int e^{iX^-x/\hbar} \left\langle X^+ + \frac{x}{2} \left| \hat{\rho} \right| X^+ - \frac{x}{2} \right\rangle dx. \quad (2.99)$$

But $W(X^+, X^-)$ itself is not a true probability distribution since it can take on negative values for some non-classical states. However, the projection on an arbitrary quadrature X^ϕ in phase-space leads to a probability distribution in this quadrature.

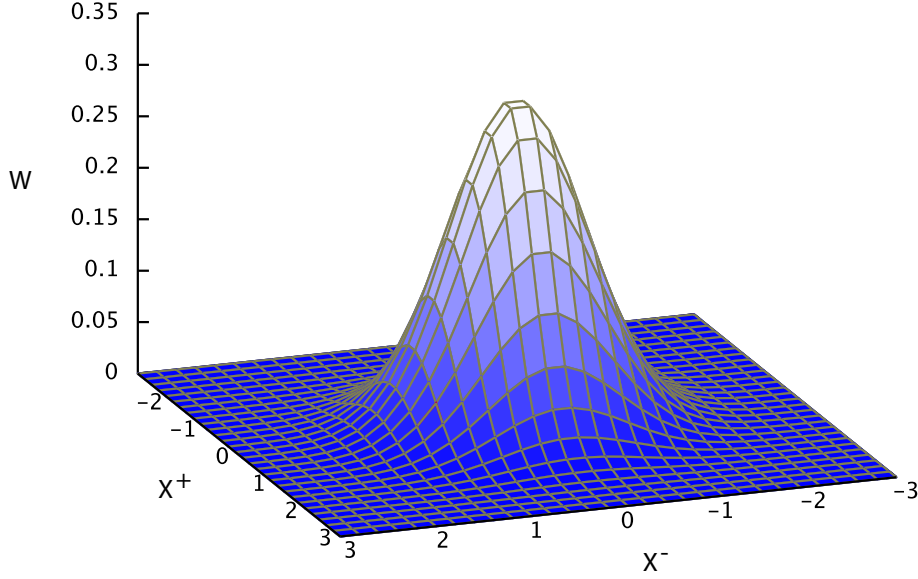


Figure 2.5 — Wigner function of a vacuum state $|0\rangle$.

For example, if the state in question is a pure state $\hat{\rho} = |\Psi\rangle\langle\Psi|$ then the integration over the phase quadrature X^- gives the probability density for the amplitude quadrature X^+

$$\begin{aligned}
 \int W(X^+, X^-) dX^- &= \frac{1}{2\pi\hbar} \int \int e^{iX^-x/\hbar} dX^- \left\langle X^+ + \frac{x}{2} \left| \hat{\rho} \right| X^+ - \frac{x}{2} \right\rangle dx \\
 &= \frac{1}{2\pi\hbar} \int \int e^{iX^-x/\hbar} dX^- \Psi \left(X^+ + \frac{x}{2} \right) \Psi^* \left(X^+ - \frac{x}{2} \right) dx \\
 &= \int \Psi \left(X^+ + \frac{x}{2} \right) \Psi^* \left(X^+ - \frac{x}{2} \right) \delta(x) dx \\
 &= \Psi(X^+) \Psi(X^+) \\
 &= |\Psi(X^+)|^2.
 \end{aligned} \tag{2.100}$$

Likewise, integrating over X^+ we obtain

$$\int W(X^+, X^-) dX^+ = |\Psi(X^-)|^2. \tag{2.101}$$

For Gaussian states (vacuum, coherent and squeezed) the Wigner-function is positive and visualizes the probability distribution in phase-space. In Figure 2.5 the Wigner-

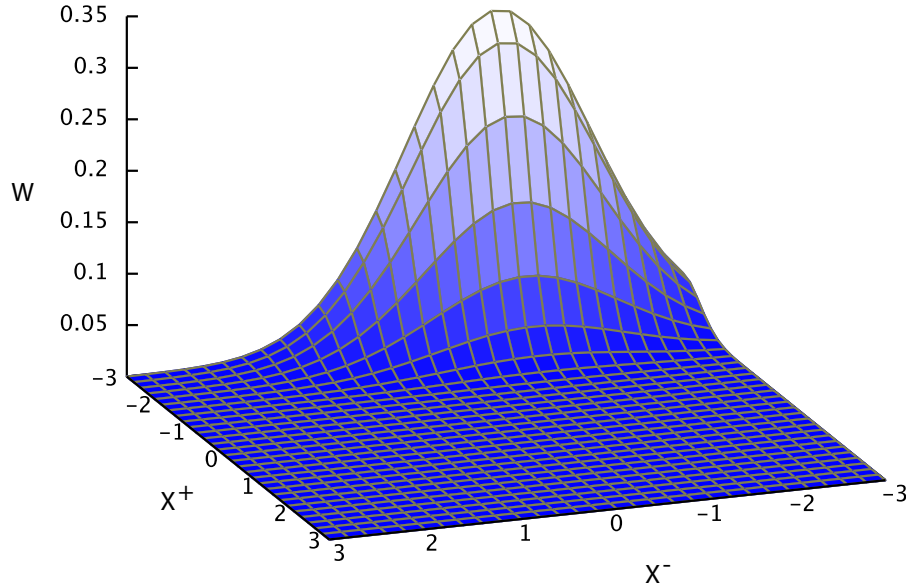


Figure 2.6 — Wigner function of a displaced 3 dB squeezed state. A projection of the Wigner-function would illustrate the squeezing ellipse in the X^+, X^- plane.

function of vacuum state is shown, which function is given by

$$W(X^+, X^-) = \frac{1}{\pi} e^{-(X^+)^2 - (X^-)^2}. \quad (2.102)$$

Since any coherent state can be generated by applying the displacement operator on the vacuum state, the Wigner-function is analog only displaced from the phase space origin. For comparison a 3 dB displaced squeezed state is shown in Figure 2.6.

Finally, it is possible to reconstruct the Wigner-function from experimental data, a procedure known as quantum-state tomography.

2.7 Generation of quadrature squeezed light

The experimental generation of squeezed states, described in this thesis, is based on the degenerate parametric down-conversion process inside a nonlinear optical device. This means that a nonlinear medium is strongly pumped by a field of frequency

ω_p and some photons of that field are converted into pairs of identical photons, of frequency $\omega = \omega_p/2$. A more detailed description of this nonlinear process can be found in the next Chapter.

However, the Hamiltonian for this process can be written as [Gerry04]

$$\hat{H} = \hbar\omega\hat{a}^\dagger\hat{a} + \hbar\omega_p\hat{b}^\dagger\hat{b} + i\hbar\chi^{(2)}(\hat{a}\hat{a}\hat{b}^\dagger - \hat{a}^\dagger\hat{a}^\dagger\hat{b}), \quad (2.103)$$

where \hat{b} is the pump field and \hat{a} is the *signal field* at half the frequency ω . The expression $\chi^{(2)}$ describes the second-order nonlinear susceptibility of the pumped medium. We assume that the pump field is a strong coherent classical field, whose intensity is insignificantly attenuated by the parametric process. Thus, the coherent state is $|\beta e^{-i\omega_p t}\rangle$ and the operators \hat{b} and \hat{b}^\dagger can be classically approximated by $\beta e^{-i\omega_p t}$ and $\beta^* e^{i\omega_p t}$. Now the parametric approximated Hamiltonian is

$$\hat{H} = \hbar\omega\hat{a}^\dagger\hat{a} + i\hbar\chi^{(2)}(\beta^*\hat{a}\hat{a}e^{i\omega_p t} - \beta\hat{a}^\dagger\hat{a}^\dagger e^{-i\omega_p t}). \quad (2.104)$$

Transforming Equation 2.104 to the interaction picture, we obtain the time dependent Hamiltonian

$$\hat{H} = i\hbar\chi^{(2)}(\beta^*\hat{a}\hat{a}e^{i(\omega_p-2\omega)t} - \beta\hat{a}^\dagger\hat{a}^\dagger e^{-i(\omega_p-2\omega)t}), \quad (2.105)$$

which simplifies if we take into account that $\omega_p = 2\omega$

$$\hat{H} = i\hbar\chi^{(2)}(\beta^*\hat{a}\hat{a} - \beta\hat{a}^\dagger\hat{a}^\dagger). \quad (2.106)$$

The associated evolution operator is

$$\begin{aligned} \hat{U} &= \exp\left(-\frac{i}{\hbar}\hat{H}t\right) \\ &= \exp(\beta^*\hat{a}\hat{a} - \beta\hat{a}^\dagger\hat{a}^\dagger), \end{aligned} \quad (2.107)$$

which has obviously the form of squeezing operator as introduced in Equation 2.65.

2.8 Second order optical nonlinearity

So far we assumed the nonlinearity of a medium as a given quantity. To get more into this subject, we need to study the physics of nonlinear optics. Hence, in this Chapter the general characteristics of the second order $\chi^{(2)}$ nonlinearity and the required experimental conditions are presented.

2.8.1 Dielectric polarization

When an electro-magnetic field propagates through a dielectric medium a macroscopic polarization is induced. This electric polarization \mathcal{P} inside the medium can be described by the response of the outer valence electron to an electric driving force E

$$\mathcal{P} = \epsilon_0 \left(\chi^{(1)} E + \chi^{(2)} E^2 + \chi^{(3)} E^3 + \dots \right), \quad (2.108)$$

where ϵ_0 is the permittivity of free space, and $\chi^{(i)}$ are the i^{th} order nonlinear susceptibilities of the crystalline medium. The first order term is connected to the refractive index n of the crystal by

$$n = \sqrt{1 + \chi^{(1)}} \quad (2.109)$$

so that for a typical material $\chi^{(1)} \approx 1$. A material with a high second order susceptibility has $\chi^{(2)} \approx 10^{-10} - 10^{-13} \text{ m/V}$. Significant third order susceptibilities are approximately at $\chi^{(3)} \approx 10^{-18} - 10^{-23} \text{ m}^2/\text{V}^{-2}$. At which frequency the polarization oscillates depends on the incident field strength. For weak fields, the effect is linear and hence for the Kerr effect, which is based on the $\chi^{(3)}$ susceptibility, more intense incident fields are required [Boyd92].

2.8.2 Optical parametric process

The focus throughout this thesis is on the processes based on the $\chi^{(2)}$ susceptibility, which was used for the generation of squeezed states and second harmonic generation. A common feature of these processes is that it involves the interaction of three modes of light (or photons), thus the $\chi^{(2)}$ processes are known as three-wave mixing processes.

The *parametric down conversion* process describes the $\chi^{(2)}$ interaction, where an incident pump photon at frequency ω_p is absorbed by the nonlinear medium and a „signal“ and „idler“ photon are generated at frequency ω_s and ω_i , respectively. Due to energy conservation

$$\omega_p = \omega_s + \omega_i \quad (2.110)$$

has to be satisfied. For the degenerated case, which describes the squeezed light sources used in this thesis,

$$\omega_i = \omega_s = \frac{1}{2}\omega_p. \quad (2.111)$$

In case of the second harmonic generation (SHG) two photons at frequency ω are absorbed by the nonlinear material to re-radiate a single photon at frequency 2ω . This $\chi^{(2)}$ interaction is called *up-conversion*.

2.8.3 Phase matching

The conservation of momentum in second-order nonlinear optical processes is often denoted as the phase matching condition. For the three involved modes we require within the plane wave approximation that

$$\frac{n_i\omega_i}{c_0} + \frac{n_s\omega_s}{c_0} = \frac{n_p\omega_p}{c_0}, \quad (2.112)$$

where n_x is the refractive index of the nonlinear medium experienced for the idler, signal or pump field and c_0 is the speed of light in vacuum. The phase matching condition for a SHG or degenerate squeezed light source is satisfied when

$$\frac{n_i\omega_i}{c_0} = \frac{n_s\omega_s}{c_0} = \frac{n_p\omega_p}{c_0}. \quad (2.113)$$

For Gaussian cavity modes the phase matching condition reads slightly different [Lastz07]. Since in most dielectric nonlinear media the refractive index n is a function of the optical frequency, the phase matching condition is difficult to achieve automatically. Generally any birefringent crystal shows three optical axes, where one has a lower refraction index than the other two. The latter are often referred to as the „ordinary“ axes, where the former axis is referred to as the „extra-ordinary“. In principal there are three methods to achieve phase matching in birefringent crystalline materials:

- *Type I phase matching*

The type I phase matching condition is fulfilled when the two polarizations of the lower energy fields are identical and the harmonic field is orthogonally polarized. Since the refractive index is highly temperature dependent ($dn_o/dT \approx 3 \times 10^{-6} K^{-1}$ for the ordinary axis and $dn_e/dT \approx 37 \times 10^{-6} K^{-1}$ for the extraordinary axis) the phase-matching condition can be satisfied via crystal temperature tuning. The phase mismatch parameter $\Delta k = \frac{n_i\omega_i}{c_0} + \frac{n_s\omega_s}{c_0} - \frac{n_p\omega_p}{c_0}$ depends on the temperature and wavelength and is given by the Sellmeier equation [Eckha91]

$$\begin{aligned} \Delta k &= k_{2\omega} - 2k_\omega \\ &= -8666 \left(1 - \frac{\lambda_0}{\lambda}\right)^2 cm^{-1} + 7.49(T - T_0)cm^{-1}K^{-1}, \end{aligned} \quad (2.114)$$

where $\lambda_0=1064$ nm, T_0 is the phase matching temperature, λ is the pump wavelength and T is the crystal temperature. The strength of a nonlinear

interaction is given by a nonlinear coupling function [Boyd92]:

$$g(\Delta kz) = \text{sinc}\left(\frac{\Delta kz}{2}\right) e^{i\Delta kz/2} \quad (2.115)$$

where z is the interaction (crystal) length. The use of MgO:LiNbO₃ at 1064 nm is a typical example of type-I phase matching for second harmonic and squeezed light generation.

- *Type II phase matching*

In type II phase matching the two fundamental (signal and idler) fields are orthogonally polarized and the high energy harmonic field has a identical polarization to one of the fundamental fields. Phase matching can again be achieved via temperature tuning, but since the generated signal and idler fields are orthogonal polarized this technique is not useful for quadrature squeezing in gravitational wave detectors.

- *Quasi phase matching*

In quasi phase matched material, the phase matching is done via periodical polarization of the nonlinear crystal's domains, which results in a periodically inverting sign of the effective nonlinear coefficient. This manipulates the accumulated relative optical phase

$$\Delta k = \frac{n_i \omega_i}{c_0} + \frac{n_s \omega_s}{c_0} - \frac{n_p \omega_p}{c_0} - \frac{2\pi}{\Lambda}, \quad (2.116)$$

where Λ is the crystal's grating period. Due to the additional periodic poling term it is no longer required that the refractive indices of the fundamental and harmonic field are equal. One other advantage of periodic poling is that highest effective nonlinear coefficients, thus providing greater conversion efficiencies, can be achieved by using materials where phase matching via temperature tuning can not be achieved. Since quasi phase matching does not rely on the dn/dT effect, the only parameter that needs to be stabilized is the grating period Λ . The effective FWHM temperature range of periodic poled material (e.g. PPKTP) is in the order of some Kelvin, and therefore much larger compared to MgO:LiNbO₃.

2.9 Detection of squeezed states

Since a single photodetector is only able to measure fluctuations in the amplitude quadrature or in the number of photons, respectively, it is not the most suitable device

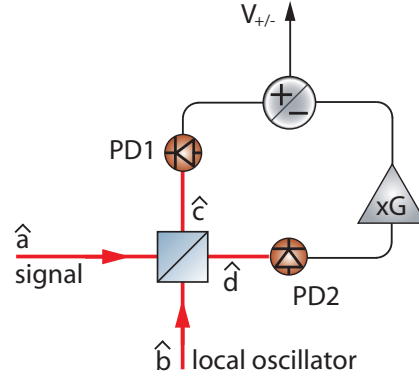


Figure 2.7 — Schematic of a homodyne detection scheme. A weak signal field (\hat{a}) is overlapped with an intense local oscillator field (\hat{b}). If the beamsplitter ratio is 50/50 and the local oscillator power is much higher than the signal power, it is a so-called balanced homodyne detector. Each beamsplitter output field (\hat{c} and \hat{d}) is detected with a photodiode (PD1, PD2) and finally the sum or difference of both photocurrents is taken. The phase relation between both input beams defines which quadrature of \hat{a} is measured.

for the characterization of squeezed states. For a more accurate description of these states, at least the squeezing and anti-squeezing level should be measured to be able to derive the states purity, or quantum-state tomography can be done, which requires the measurement of a great number of consecutive quadratures. An appropriate measuring device for this purpose is the „homodyne detector“.

2.9.1 Balanced homodyne detection

As illustrated in Figure 3.3.4 in this detection scheme the signal field of interest interferes with a strong „local oscillator beam“ on a 50/50 beamsplitter (balanced homodyne detection). Hence, both fields has to be matched in terms of frequency and spatial modes including wave fronts curvatures and polarization. Any mismatch leads to a degraded interference, which can be quantified via the *fringe visibility*

$$\mathcal{VIS} = \frac{V_{max} - V_{min}}{V_{max} + V_{min}} \quad (2.117)$$

where V_x describes the voltage of one photodiode while the relative phase between the signal and local oscillator field is dithered. The efficiency of interference or the efficiency of homodyne detection, respectively, is given by

$$\eta_{homo} = \mathcal{VIS}^2 \quad (2.118)$$

assuming no additional loss inside the detection scheme like non-perfect photodiode quantum efficiencies and absorption in optics.

Both input fields can be written as $\hat{a} = \alpha + \delta\hat{a}$ for the signal field and $\hat{b} = (\beta + \delta\hat{b})e^{i\phi}$ for the local oscillator field with an arbitrary phase between both. In the following the assumption of a fixed 50/50 splitting ratio is dropped to investigate how strong an unbalance will degrade the measured squeezing level. Experimentally such an unbalance (in the order of some percent) can easily be found since generally a non-perfect beamsplitter and non-ideal photodiodes are involved. Therefore, the first two beamsplitter output fields are:

$$\hat{c} = r\hat{a} + t\hat{b} \quad (2.119)$$

$$\hat{d} = t\hat{a} - r\hat{b} \quad (2.120)$$

where r and t is the reflectivity or the transmission of the beamsplitter, respectively. Each output field of the beamsplitter is measured with a single photodiode. Assuming a quantum efficiency of unity, the photocurrent of the first photodiode is

$$\begin{aligned} \hat{i}_c &= \hat{c}^\dagger \hat{c} \\ &= (r\hat{a}^\dagger + t\hat{b}^\dagger) * (r\hat{a} + t\hat{b}) \\ &= r^2\hat{a}^\dagger\hat{a} + rt\hat{a}^\dagger\hat{b} + rt\hat{b}^\dagger\hat{a} + t^2\hat{b}^\dagger\hat{b} \\ &= r^2 \left(\alpha^2 + \alpha(\delta\hat{a} + \delta\hat{a}^\dagger) \right) + \\ &\quad rt \left(\alpha\beta e^{i\phi} + \alpha\delta\hat{b}e^{i\phi} + \beta\delta\hat{a}^\dagger e^{i\phi} + \delta\hat{a}^\dagger\delta\hat{b}e^{i\phi} + \alpha\beta e^{-i\phi} + \beta\delta\hat{a}e^{-i\phi} + \right. \\ &\quad \left. \alpha\delta\hat{b}e^{-i\phi} + \delta\alpha\delta\beta^\dagger e^{-i\phi} \right) \\ &\quad + t^2 e^{-i\phi} e^{i\phi} \left(\beta^2 + \beta\delta\hat{b} + \beta\delta\hat{b}^\dagger + \delta\hat{b}^\dagger\delta\hat{b} \right). \end{aligned} \quad (2.121)$$

Assuming $\beta \gg \alpha$ Equation 2.121 can be simplified to

$$\hat{i}_c = rt \left(\beta(\delta\hat{a}^\dagger e^{i\phi} + \delta\hat{a}e^{-i\phi}) \right) + t^2\beta(\delta\hat{b} + \delta\hat{b}^\dagger) \quad (2.122)$$

$$= rt\beta\hat{X}_a^\phi + t^2\beta\hat{X}_b^+. \quad (2.123)$$

Likewise, we obtain for the photocurrent of the second photodiode

$$\hat{i}_d = -rt\beta\hat{X}_a^\phi + r^2\beta\hat{X}_b^+. \quad (2.124)$$

To investigate unbalanced photodiode quantum efficiencies (or electronic gains) between the two photodetectors we multiply the second photocurrent \hat{i}_d with a constant

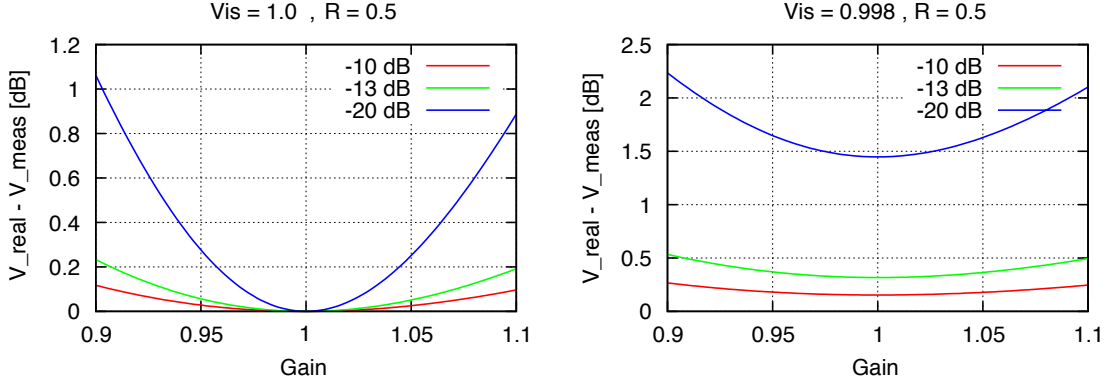


Figure 2.8 — Illustration of the gain dependence for the homodyne detection efficiency. The beam-splitter reflectivity was set to be constant at 50%. Furthermore, in the left picture the visibility between both input fields was set to 1. Depending on the initial squeezing value (10 dB, 13 dB, 20 dB) the additional detection loss due to a 10 % gain mismatch varies between 0.1 dB and almost 1.1 dB, for example. Taking a non-perfect visibility (99.8 %) into account, the additional loss is even higher, as shown in the right picture.

gain factor G . Hence, the sum of the photocurrents \hat{i}_c and \hat{i}_d is

$$\begin{aligned} I_+ &= rt\beta\hat{X}_a^\phi + t^2\beta\hat{X}_b^+ + G(-rt\beta\hat{X}_a^\phi + r^2\beta\hat{X}_b^+) \\ &= \beta\left(rt\hat{X}_a^\phi(1-G) + \hat{X}_b^+(t^2 + Gr^2)\right). \end{aligned} \quad (2.125)$$

The subtraction of \hat{i}_c and \hat{i}_d leads to

$$I_- = \beta\left(rt\hat{X}_a^\phi(1+G) + \hat{X}_b^+(t^2 - Gr^2)\right). \quad (2.126)$$

By taking the square of these two currents (I_+, I_-), the variances V can be calculated

$$V(I_+) = \beta^2\left(V(\hat{X}_a^\phi)r^2t^2(1-G)^2 + (t^2 + Gr^2)^2\right), \quad (2.127)$$

$$V(I_-) = \beta^2\left(V(\hat{X}_a^\phi)r^2t^2(1+G)^2 + (t^2 - Gr^2)^2\right), \quad (2.128)$$

where $V(\hat{X}_b^+) = 1$ was assumed. By calculating the fraction $V(I_+)/V(I_-) = V_{meas}$ one can determine the difference between the actually measured and the initial squeezing V_{real} while the parameters G (Gain) and R (beam-splitter reflectivity) are varied. In the Appendix a GNUPLOT script is attached, which was used for this calculations.

In Figure 2.8 the gain dependency for the detection efficiency is plotted, while the beam-splitter reflectivity was set to be constant at 50%. Furthermore, in the left

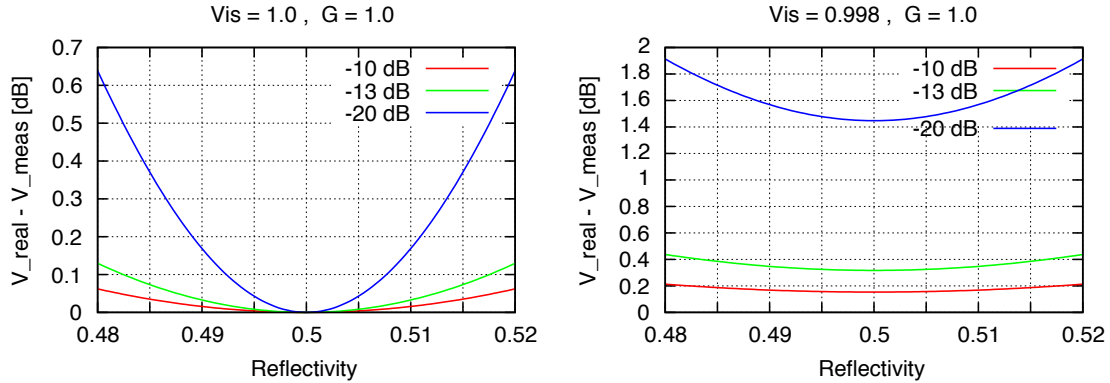


Figure 2.9 — Illustration of the beamsplitter ratio dependence for the homodyne detection efficiency. The left plot shows the calculations for a perfect fringe visibility and equal electronic gains for both photodetectors. In the range of $\pm 1\%$ splitting ratio unbalance, the additional loss for the squeezing measurement seems to be negligible since it is only in the order of 0.1%. The same is true if the fringe visibility is reduced to 99.8%, as presented the right picture.

picture the visibility between both input fields was set to 1. Depending on the initial squeezing value (10 dB, 13 dB or 20 dB) the additional detection loss due to a 10% gain mismatch varies between 0.1% and almost 1.1%, for example. Taking a non-perfect visibility (99.8%) into account, the additional loss is even higher, as shown in the right picture of Figure 2.8.

In Figure 2.9 the results regarding additional losses caused by an unbalanced beamsplitter ratio are presented. The left plot shows the calculations for a perfect fringe visibility and equal gains for both photodetectors. In the range of $\pm 1\%$ splitting ratio unbalance, the additional loss for the squeezing measurement seems to be negligible since it is only in the order of 0.1% even for very high squeezing levels. The same is true if the fringe visibility is reduced to 99.8%, as presented in the right picture.

Nevertheless, to reduce the influence of electronic components tolerances, which can cause unbalances between the two employed photodetector circuits, in most cases a self-subtraction photodetector-scheme was used for the squeezing measurements throughout this thesis. In this circuit topology the two photocurrents are directly subtracted before any further electronic signal processing is applied. Thus, any subsequent electronic component (transimpedance amplifier stage e.g.) only acts in a „common mode“ sense on both photocurrents. A schematic of the homodyne detector electronics is included in the Appendix.

2.9.2 Sideband modulation fields in quantum optics

Complementary to the illustration in the phase space, quantum states can be described (separated in Fourier-frequencies) in the *sideband picture*. In the experiments presented in this thesis light is used to transfer signals. Typically, this information transfer is done by modulating the amplitude or phase of the light at some frequency Ω . These modulation frequencies are usually in the range of several Hz up to MHz, therefore much lower than the optical light frequency (carrier), which oscillates at several THz. As shown in Figure 2.10 such modulations can be illustrated by the introduction of modulation sidebands at frequencies $\pm\Omega$ relative to the carrier frequency at ω_0 . If we now assume that the phasor of the carrier field can be represented as a fixed vector (with a given length) in a rotating frame (ω_0) of a complex plane, all modulation fields will rotate as phasors in this complex plane. To obtain the resulting light field the involved phasors have to be added vectorially. It is the phase of the sidebands with respect to the carrier that distinguishes amplitude modulation from phase modulation.

An amplitude modulation of an optical field a_0 with a modulation frequency Ω and an modulation index m can be described as

$$\begin{aligned} a_{\text{am}}e^{i\omega_0 t} &= a_0 \left(1 + m \cos(\Omega t) \right) e^{i\omega_0 t} \\ &= a_0 \left(1 + \frac{m}{2} (e^{i\Omega t} + e^{-i\Omega t}) \right) e^{i\omega_0 t} \\ &= a_0 \left(e^{i\omega_0 t} + \frac{m}{2} e^{i(\omega_0 + \Omega)t} + \frac{m}{2} e^{i(\omega_0 - \Omega)t} \right). \end{aligned} \quad (2.129)$$

Equation 2.129 supports the picture of a modulation free carrier together with two modulation sidebands. The latter ones are labeled as *upper sideband* and *lower sideband*.

Formally, a phase modulated beam $a_{\text{pm}}e^{i\omega_0 t}$ may be written as

$$\begin{aligned} a_{\text{pm}}e^{i\omega_0 t} &= a_0 e^{i(\omega_0 t + m \cos(\Omega t))} \\ &= a_0 e^{i\omega_0 t} \left(J_0(m) + \sum_{l=1}^{\infty} i^l J_l(m) (e^{il\Omega t} + e^{-il\Omega t}) \right) \\ &= a_0 e^{i\omega_0 t} \left(J_0(m) + iJ_1(m) (e^{i\Omega t} + e^{-i\Omega t}) + \mathcal{O}(l \geq 2) \right) \\ &\approx \left(e^{i\omega_0 t} + i\frac{m}{2} e^{i(\omega_0 + \Omega)t} + i\frac{m}{2} e^{i(\omega_0 - \Omega)t} \right), \end{aligned} \quad (2.130)$$

where $J_l(m)$ are the Bessel-functions and it was assumed that the modulation depth is small ($m \ll 1$). In Figure 2.10 phase modulation is illustrated in the sideband picture.

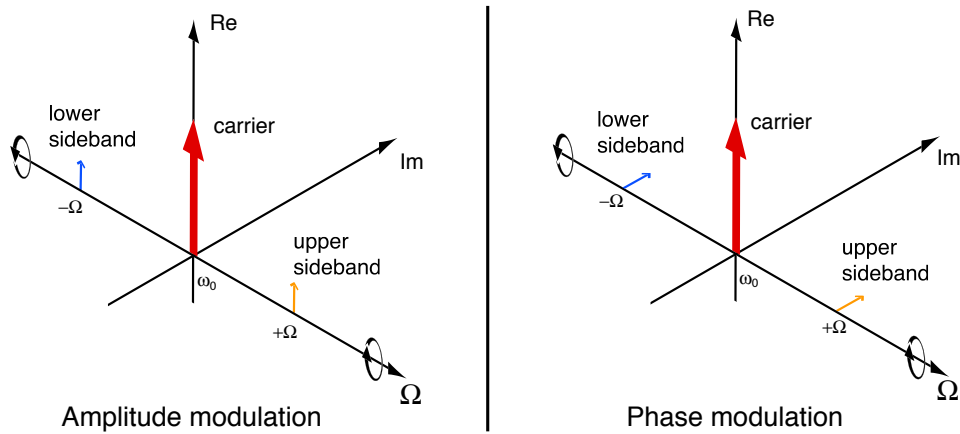


Figure 2.10 — Amplitude and phase modulation in the sideband picture. The sidebands at the modulation frequency Ω are correlated. It is the phase of the sidebands with respect to the carrier that distinguishes amplitude modulation from phase modulation.

The quantum sideband picture is derived from the classical sideband picture. Quantum noise can be understood as sidebands due to the vacuum fluctuations beating with the carrier. Therefore, these sidebands are a consequence of the harmonic oscillator ground state energy. We can think of the quantum noise as a continuum of sidebands spanning all frequencies. The result is broadband (white) amplitude and phase noise. All sidebands are uncorrelated with each other. Thus, the quantum noise is distributed equally between the amplitude and phase quadratures.

The generation of squeezed states can be thought of introducing correlations between randomly fluctuating upper and lower sideband pairs. At frequencies where squeezing can be measured, the sidebands become synchronized to some degree. For example, amplitude squeezing at a sideband frequency Ω occurs when the random quantum sidebands at Ω are converted to correlated phase sidebands. In this case the phase noise will be increased, while the quantum amplitude modulation will be reduced at this certain sideband frequency.

Generation of strongly squeezed vacuum states

3.1 Introduction

Theoretical considerations about the possible existence of light with squeezed quantum noise can be traced back to the 1920's [Dodon02]. However, only after applications for squeezed light were proposed in the 1980's squeezing was discussed in more detail [Dodon02, Yuen78, Holle79, Caves81, Walls83]. In [Caves81] it was suggested to use squeezed light to improve the sensitivity of kilometre-scale Michelson laser-interferometers for the detection of gravitational waves. Such detectors have now reached a technical standard at which squeezed light can contribute in a valuable way. For example squeezing the quantum noise can provide a sensitivity improvement equivalent to even higher laser powers, however without increasing the already problematic thermal load inside the interferometer. This is of great relevance for cryogenically cooled detectors. Proof of principle experiments have been successfully conducted [McKen02, Vahlb05] and squeezed states have been generated also in the audio signal band of ground-based detectors [McKen04, Vahlb06].

Another field of application is *continuous variable* (CV) quantum communication and information [Yuen78, Braun05, Akama04]. While *discrete variable* quantum information typically relies on single photon detectors (photon counting), which are limited in terms of detection speed and quantum efficiency, squeezed light is detected with homodyne and heterodyne detectors which reveal quantum correlations by averaging over a vast number of detected photons. Due to this, high bandwidth

and almost perfect detection efficiencies are possible. Squeezed states of light have been used to demonstrate several CV quantum information protocols. They have been used to construct entangled states of light and to demonstrate quantum teleportation [Fiura98, Bowen03, Takei05]. They are a possible resource for secure quantum key distribution protocols [Garci06, Navas06] and for generation of cluster states for universal quantum computing [Menic06]. Recently, squeezed states of light have been used to prepare Schrödinger kitten states for quantum information networks [Ourjo06, Niels06].

For all proof of principle experiments so far only modest strengths of squeezing were available. In [McKen02, Vahlb05, McKen04, Vahlb06] about 3 to 4 dB of squeezing was achieved. The first CV teleportation experiments [Fiura98, Bowen03] did not reach the so-called no-cloning limit of fidelity greater than $2/3$ [Gross01] due to the limitations in squeezing strength. Observation of much stronger squeezing indicates that high purity squeezed states can be produced for example to beat the Holevo capacity limit of quantum communication channels [Braun00]. Quite generally, the applications of squeezed light become more momentous with stronger squeezing. Although the first experimental demonstration of squeezed light succeeded in 1985 [Slush85], dedicated research in the following two decades could only achieve typical factors of 2 to 4 (3 dB to 6 dB), see also [Breite97, Treps03]. However, very recently a great step forward was achieved at the University of Tokyo and a factor of 8 (9 dB) quantum noise squeezing of a laser field at 860 nm was observed [Taken07]. This wavelength is close to atomic transitions having important implications for quantum information storage [Mthsu06]. In our experiment we generated a squeezed laser beam with a quantum noise reduction of a factor of 10 (and more) at a laser wavelength of 1064 nm which is used in current gravitational wave detectors [Aufmu05]. This Chapter refers to the following publication:

- „*Observation of Squeezed Light with 10 dB Quantum-Noise Reduction*“
H.Vahlbruch, M.Mehmet, S.Chelkowski, B.Hage, A.Franzen, N.Latstzka,
S.Gossler, K.Danzmann, and R.Schnabel,
Physical Review Letters, 100, 033602, (2008).

3.2 Limitations to squeezing

In general, the best way to characterize a squeezing experiment in terms of optical loss and the states' purity is the measurement of the anti-squeezed and squeezed quadrature noise levels for several pump powers, respectively. From this, the efficiency of the complete system, as well as the parametric gain inside the squeezer, can be determined.

In the following the most important limitations for the generation and detection of strongly squeezed states are discussed in detail and were related to data taken from the experiments.

3.2.1 Escape efficiency / cavity linewidth

The escape efficiency of a squeezed light source is given by:

$$\eta_{escape} = \frac{T}{T + L_{cav}} \quad (3.1)$$

where T is the output coupler transmission and L_{cav} is the intra-cavity round trip loss. A high escape efficiency is recommended in order to generate strong squeezing. Therefore, two approaches can be followed:

- Reducing L_{cav} : This is quite difficult, since the loss is mainly determined by the nonlinear crystal material properties. Additionally, for hemilithic cavity designs the anti-reflection coating of a crystal surface has to be taken into account.
- Increasing T : By reducing the finesse of the squeezed light source for the fundamental wavelength, a significantly more intense pump field is required since the threshold power increases quadratically: $P_{thres} \sim (T + L_{cav})^2$

For the experiment presented in this Chapter, we have chosen to increase the output coupler transmission up to a value of 12% at the expense of a much higher OPO threshold. From the parameters, which are described in full detail in Chapter 3.3.3, we derived $\eta_{escape} = 99.36\%$.

Another advantage of increasing the output coupler transmission is the broadening of the cavity linewidth of the squeezed light source. Due to the input-output coupling relations squeezed states are basically observable within this linewidth. Therefore, in our experiment linewidth considerations were unimportant since the cavity linewidth of 210 MHz (FWHM) did not significantly affect the squeezing measurement at a Fourier frequency of 5 MHz.

3.2.2 Propagation loss

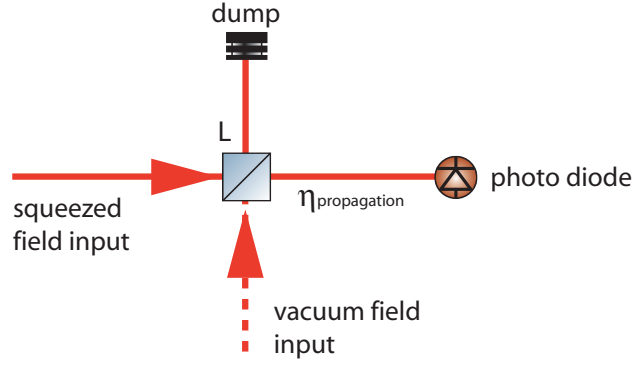


Figure 3.1 — A model for the calculation of propagation loss and non-perfect quantum efficiency of photo diodes. It implies that any loss or inefficiency can be compared to the interference of the squeezed field with an uncorrelated vacuum field.

Propagation loss due to non-perfect optics as well as a non-perfect quantum efficiency of photo diodes can be modeled as shown in Figure 3.1. Here a beamsplitter with a reflectivity of L is placed in front of a photo diode with a perfect quantum efficiency. Hence, the efficiency of propagation is defined by

$$\eta_{propagation} = 1 - L. \quad (3.2)$$

This model implies that any loss or inefficiency can be compared to the interference of the squeezed field with an uncorrelated vacuum field.

3.2.3 Homodyne efficiency

A mode mismatch between the two input fields of a homodyne detector results in a non perfect interference at the 50/50 beamsplitter, which leads to a further inefficiency in the measurement. Amongst others, this source of loss can be caused by non-identical polarization and difference in spatial modes.

A criterion for the quality of the interference between two fields with equal intensities is the fringe visibility, which can experimentally be obtained by dithering the relative phase between both input fields while measuring the fringe maximum and minimum intensities on a photodetector placed in one homodyne detector output port. The visibility \mathcal{VIS} is defined as

$$\mathcal{VIS} = \frac{I_{max} - I_{min}}{I_{max} + I_{min}}. \quad (3.3)$$

The total efficiency of the homodyne detection (assuming a photodiode quantum efficiency of unity) is given by

$$\eta_{\text{homodyne}} = \mathcal{V}\mathcal{I}S^2 \quad (3.4)$$

which means that the homodyne efficiency is dependent on the square of the interference visibility. This shows how essential a high overlap between both input fields is for the detection of strongly squeezed states.

In our experiment we achieved a fringe visibility of 99.8 %, which is equivalent to a homodyne efficiency of 99.6 %, or – in other words – an introduced loss of only 0.4 %.

3.2.4 Detection efficiency

If the quantum efficiency of the photodiodes (used for the homodyne detection scheme) is not equal to unity, the measured squeezing level will be reduced comparable to optical propagation loss. For a wavelength of 1064 nm the only so far relevant photodiode materials are silicon (Si) or indium-gallium-arsenide (InGaAs). For silicon the quantum efficiency is typically 80 % whereas InGaAs-photodiodes exhibit a quantum efficiency of up to 95 ± 2 %.

Another important issue is the clearance of the measured quantum noise from the electronic detector dark noise. If this dark noise clearance is too low, the *measured* squeezing level becomes artificially reduced. For a long time it was common to publish re-calibrated „measured“ squeezing levels by doing a mathematical dark noise correction after the measurement. However, in the last few years a general acceptance was achieved, that only the real measured squeezing levels should be presented.

In our experiment more than 26 dB of dark noise clearance was present with respect to the shot noise level generated by a local oscillator beam of 26.9 mW. For a measured 10 dB squeezed state this detector dark noise level only contributes in the order of 0.1 dB.

3.2.5 Phase jitter

With increased squeezing levels the phase jitter effect becomes an important issue. In a homodyne detection scheme, the relative phase between both input fields determines the measured quadrature of the squeezed field. Residual high frequency phase modulations as well as vibrations of reflecting surfaces at (sub-)audio frequencies cause a jitter of this phase relation. If the phase jitter period is shorter than the time required for the spectrum analyzer to measure one point, this measurement of noise will not be a pure measurement at a single quadrature angle Φ . Instead the performed

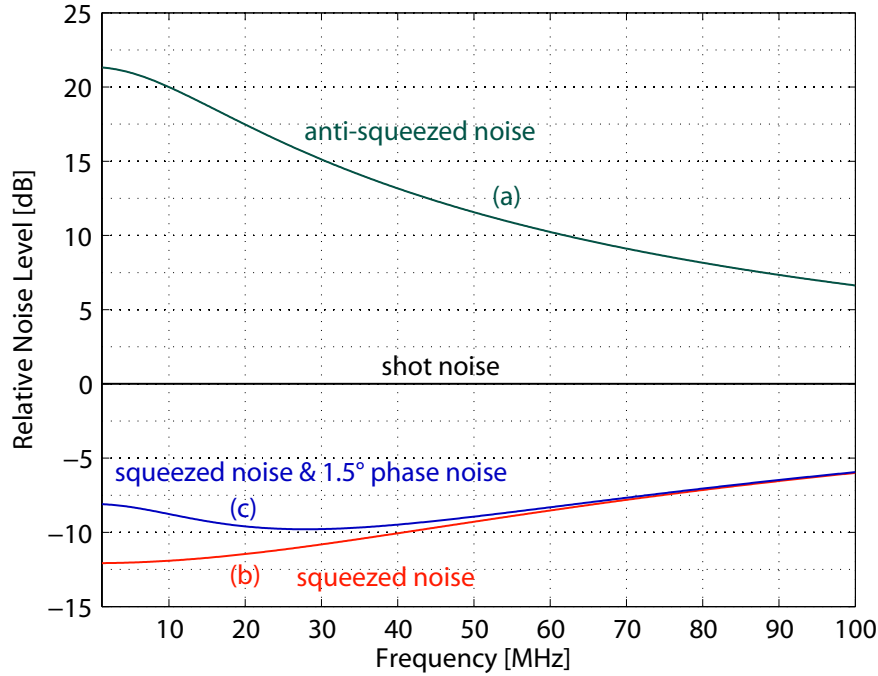


Figure 3.2 — Simulated noise power spectra for a detection efficiency of $\eta=95\%$. The green curve (trace (a)) describes the anti-squeezing level versus of the detected sideband frequency. The red trace (b) shows the corresponding squeezing level without any phase noise. While the anti-squeezing level is almost unaffected, the squeezing level gets degraded if phase noise causes a jitter of the squeezing ellipse. The blue trace (c) describes a simulated squeezing level for $\phi=1.5^\circ$ phase noise and an unaltered detection efficiency of 95%. The influence of phase jitter is reduced as the anti-squeezing level gets smaller due to the cavity linewidth.

measurement will be the integral over some span of angles $\Phi \pm \delta\Phi$. If this happens, some of the noise from the anti-squeezed quadrature is mixed into what was intended to be a measurement of the squeezed quadrature. This will reduce the observable squeezing level. As a consequence this jitter affects strongly squeezed state with a long squeezing ellipse [Franze06], [Franze08].

Two simulations, as shown in Figure 3.2 and 3.3, demonstrate that – in the presence of phase jitter – there is an optimum pump power for the highest observable squeezing level at a certain detection frequency. In Figure 3.2 an overall detection efficiency of $\eta=95\%$ was assumed. The green trace (a) describes the anti-squeezing level in dependence of the detected sideband frequency. The red trace (b) shows the squeezing level without any phase noise effects. While the anti-squeezing level is almost unaffected, the squeezing level strongly degrades if phase noise causes a jitter of the squeezing ellipse. This is shown in the blue trace (c), which describes the

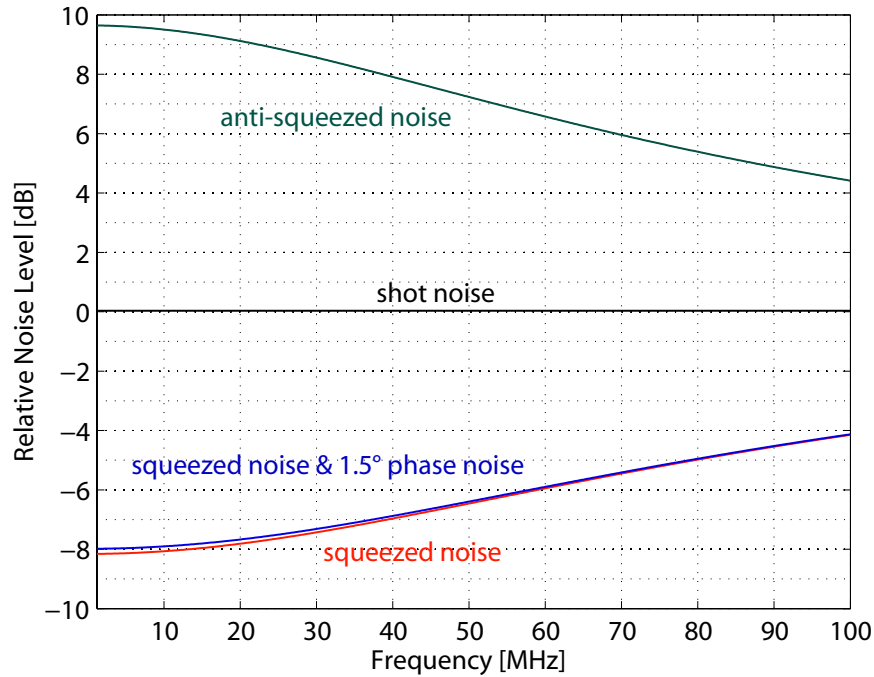


Figure 3.3 — Simulated noise power spectra with a reduced parametric gain. The influence of phase jitter decreases as the anti-squeezing level gets smaller. This can be the case due to the cavity linewidth or a reduction of initial pump power causing a reduced parametric gain inside the squeezed light source. Compared to Figure 3.2 this simulation illustrates that – for example – at a detection frequency of 5 MHz more squeezing can be achieved if the pump power is reduced. The overall detection efficiency was again $\eta=95\%$ and phase noise $\phi = 1.5^\circ$.

squeezing level for $\phi=1.5^\circ$ phase noise and a detection efficiency of still 95 %.

The influence of phase jitter gets reduced as the anti-squeezing level becomes smaller. Therefore, sometimes higher squeezing levels can be achieved if the parametric gain is reduced by either using less pump power or by measuring at sideband frequencies where the anti-squeezing level is already attenuated due to the cavity linewidth. Comparing the simulations presented in Figure 3.2 and Figure 3.3 it is illustrated that at a detection frequency of 5 MHz more squeezing can be achieved if the pump power and hence the parametric gain is reduced.

3.3 Experimental setup

In Figure 3.4 a sketch of the experimental setup is presented. The main laser source was a commercially available continuous wave Nd:YAG Laser system at 1064 nm with a maximal output power of 2 Watt (Model: Mephisto 2000 NE) [Inno]. All other parts of the experiment are discussed in detail in the following sections.

In Chapter 3.3.1 the second harmonic generator (SHG) is described. In this stage a main fraction of the initial laser light is frequency doubled providing the necessary pump field for the squeezed light source.

For the first time in a squeezing experiment the second harmonic pump field was spatially and frequency filtered by means of a travelling wave ring-cavity. This mode-cleaner cavity at a wavelength of 532 nm (MC532) is described in more detail in Section 3.3.2.

The characteristics and specifications of the monolithic squeezed light source are introduced in Chapter 3.3.3.

For the detection of the (squeezed) vacuum states a balanced homodyne detector was used. Since it is recommended to achieve a high fringe visibility between both input fields of the homodyne detector, an additional mode-cleaner cavity at the fundamental wavelength of 1064 nm was set up for spatial filtering of the local oscillator beam. This modecleaner design and the optical properties of the homodyne detector are described in Section 3.3.4.

3.3.1 Second harmonic generation

A detailed illustration of the hemilithic SHG-cavity design is shown in Fig. 3.5. The non-linear crystal was made from 7 % doped MgO:LiNbO₃ with dimensions of 2 mm × 2.5 mm × 6.5 mm. One surface of the crystal had a radius of curvature of 8 mm and was high reflection coated (R = 99.96 %) whereas the flat surface of the crystal was anti-reflection coated (R < 0.5%) for both wavelengths. The cavity was formed by an additional partial reflective outcoupling mirror (radius of curvature = 25 mm) with reflectivities of R = 90 % at 1064 nm and R < 2 % for the second harmonic field. This resulted in a finesse of the cavity at the fundamental wavelength of $\mathcal{F} = 75$ and a free spectral range (FSR) of approximately 4 GHz.

In order to maximize the conversion efficiency both fields – the fundamental as well as the second harmonic – must be phase matched inside the SHG. This was done by heating the nonlinear medium. The phase matching temperature for 7 % doped MgO:LiNbO₃ was found to be approximately 67°C.

The oven was made of aluminum housing the crystal and peltier elements. A

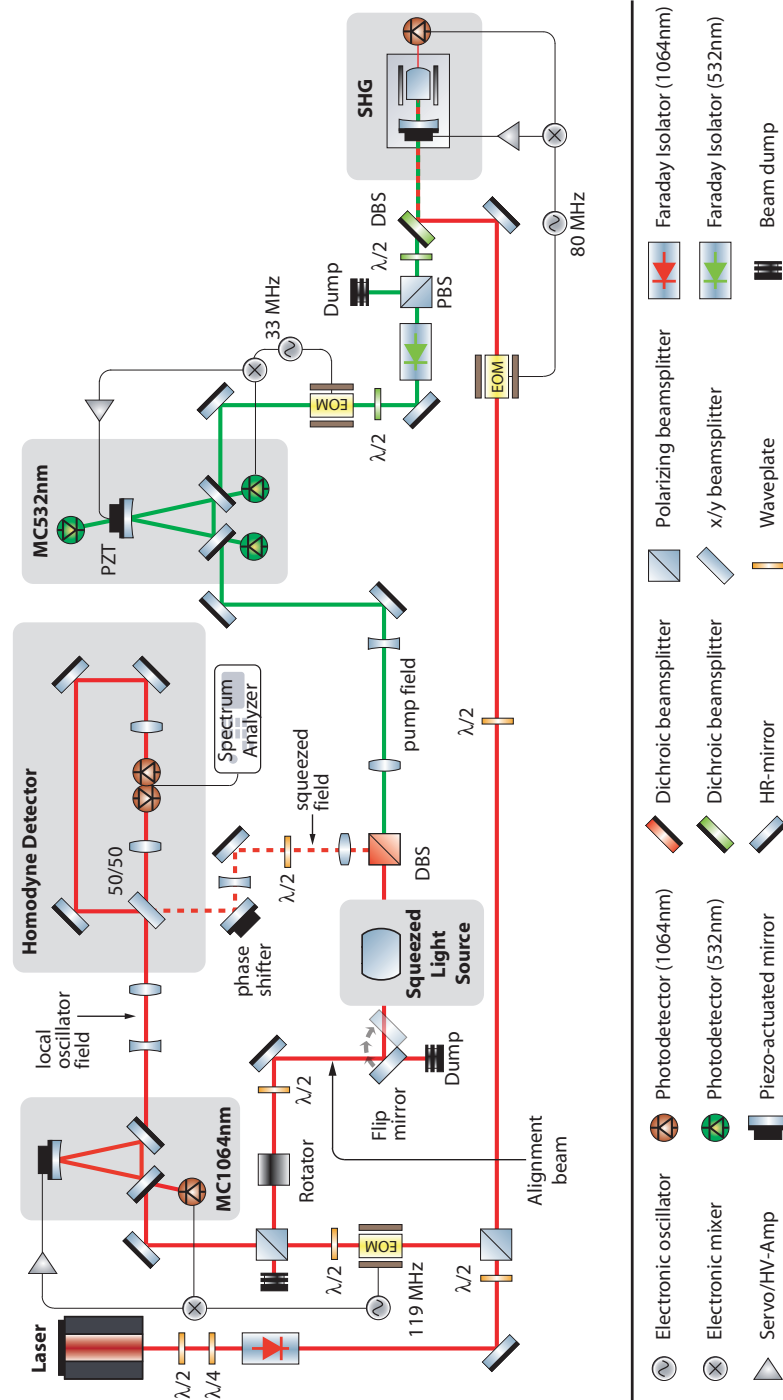


Figure 3.4 — Schematic of the experimental setup. Squeezed states of light at 1064 nm were generated inside a monolithic, standing-wave cavity by degenerated type I optical parametric oscillation (OPO) below threshold. SHG: second harmonic generation, PBS: polarizing beam splitter; DBS: dichroic beam splitter; LO: local oscillator, PD: photo diode; EOM: electro-optical modulator.

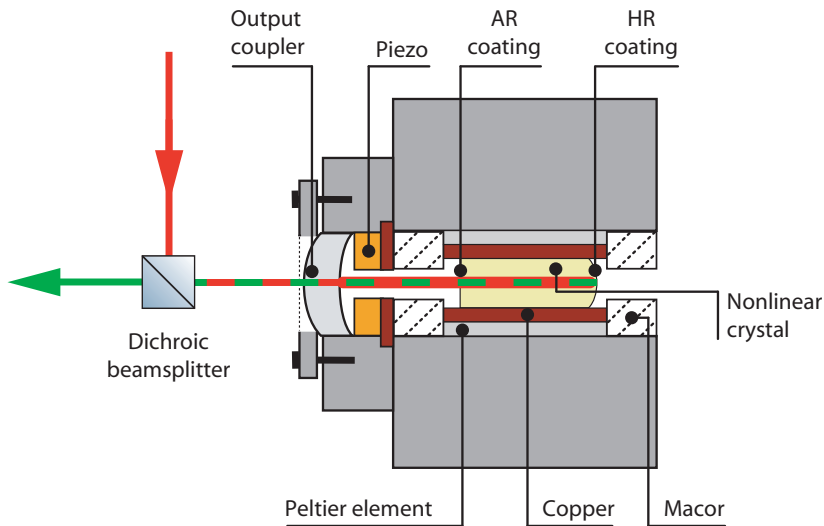


Figure 3.5 — Illustration of the oven design used for second harmonic generation. The hemilithic cavity at the fundamental wavelength is formed by the high reflection coated nonlinear crystal back surface and an additional partial reflective out-coupling mirror. Active temperature stabilization of the nonlinear crystal for type-I phase matching is realized via two peltier elements.

stack formed by the out-coupling mirror, a piezo-electric transducer (PZT) and a viton ring was clamped onto the aluminum. Small Macor blocks with drilling along the laser light propagation axis were used for thermal isolation. An active temperature stabilization of the crystal was set up by using a servo control loop. This required a negative temperature coefficient (NTC) thermistor which was embedded into the copper plates close to the crystal and peltiers. The controller electronically compared the actual NTC- resistance to a user defined set-value. This generated an error signal which was fed back onto the peltier elements after it was amplified by servo electronics. A generic schematic of custom build temperature controller can be found in the Appendix.

The measured thermal transfer function of this oven design is shown in Figure 3.6. Due to several thermal contact surfaces the transfer function shows poles at frequencies of 12 mHz, 270 mHz and 1.6 Hz. Furthermore, at frequencies of a few Hertz and even higher a differentiator characteristic was measured. This behavior originated from an electronic crosstalk between the peltier current output driver stage and the NTC input section of the controller via the common ground plane of the printed circuit board. A proper board layout reduced this crosstalk but nevertheless the residual differentiator gain had to be compensated in the servo design, otherwise the

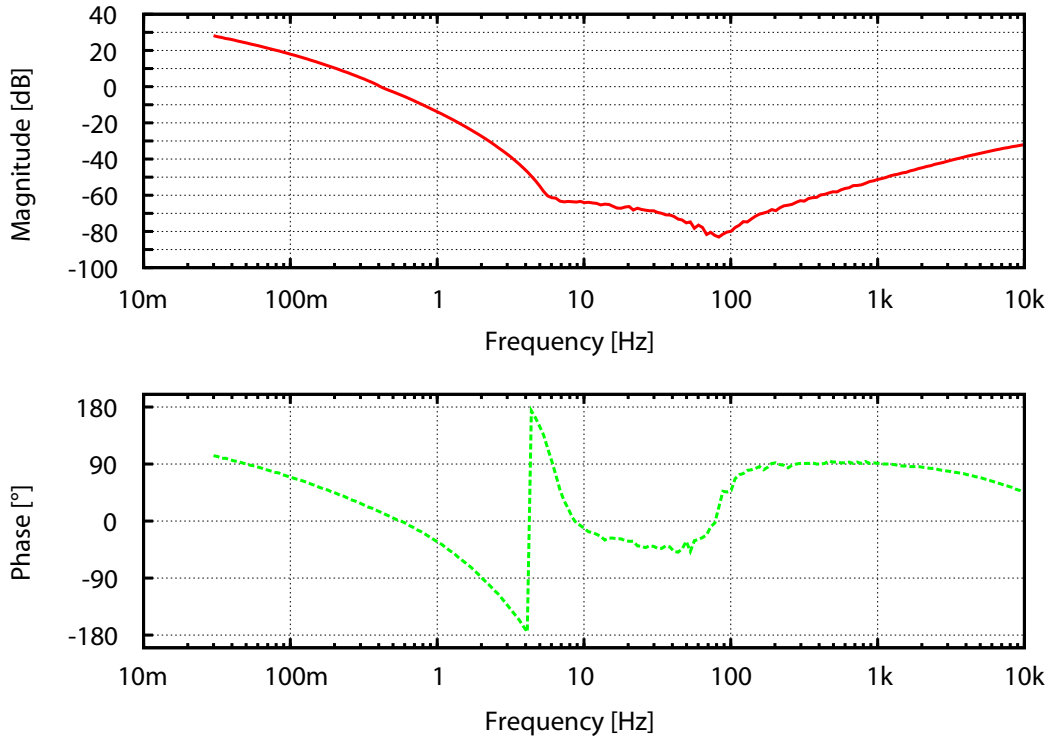


Figure 3.6 — Measurement of the thermal transfer function for the second harmonic generator oven design. Due to several thermal contact surfaces the transfer function shows poles at frequencies of 12 mHz, 270 mHz and 1.6 Hz. At frequencies above approximately 5 Hz a differential behavior is measured, which is caused by an electronic crosstalk on the temperature controller printed circuit board.

servo loop would become unstable or the unity-gain frequency would be unnecessary low. The open-loop gain of the custom build controller is shown in Figure 3.7. A unity-gain frequency of approximately 2 Hz was realized.

The SHG-cavity length had to be stabilized to be resonant for the incoming Nd:YAG laser light. This was done utilizing the Pound-Drever-Hall (PDH) technique [Drever83]. As illustrated in Figure 3.4 the incoming field at 1064 nm was phase modulated at 80 MHz using an electro-optical modulator (EOM). Since the backside of the MgO:LiNbO₃ crystal was not perfectly HR-coated ($R = 99,96\%$), residual transmitted light at 1064 nm was detected and demodulated at 80 MHz. After lowpass filtering the obtained error signal was fed back onto the piezo after being further signal processed in servo electronics.

The measured open-loop transfer function of the SHG cavity length control loop

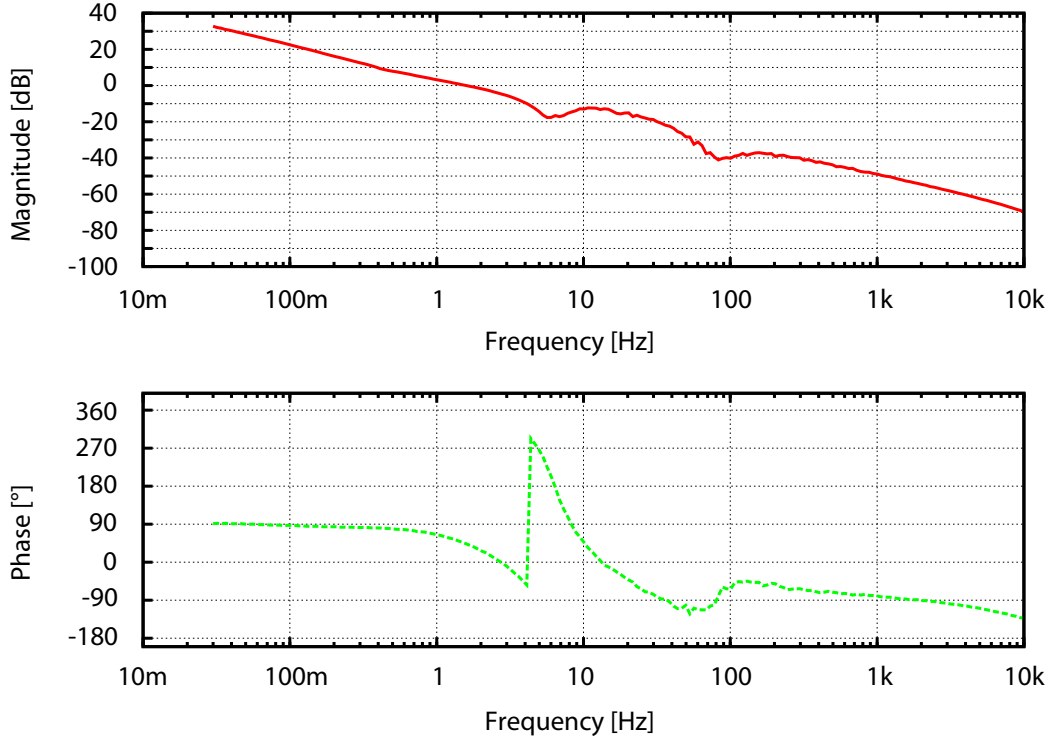


Figure 3.7 — Open-loop gain of the second harmonic generator temperature controller. A unity-gain frequency of approximately 2 Hz was realized.

is plotted in Figure 3.8. The unity gain frequency was approximately at 3 kHz and was primarily limited by several around 10 kHz.

The second harmonic generator was pumped with 1.9 Watts at 1064 nm. This input field was converted into a maximum output of 1.1 Watt at 532 nm. The conversion efficiency is defined by

$$\text{Efficiency} = \frac{(\hbar\Omega_2)B_{out}^2}{(\hbar\Omega_1)A_{in}^2} = \frac{2B_{out}^2}{A_{in}^2}, \quad (3.5)$$

where B_{out}^2 is the second harmonic output power and A_{in}^2 is the fundamental input power. Since $\Omega_2 = 2\Omega_1$, the maximal conversion efficiency was calculated to be 67 %.

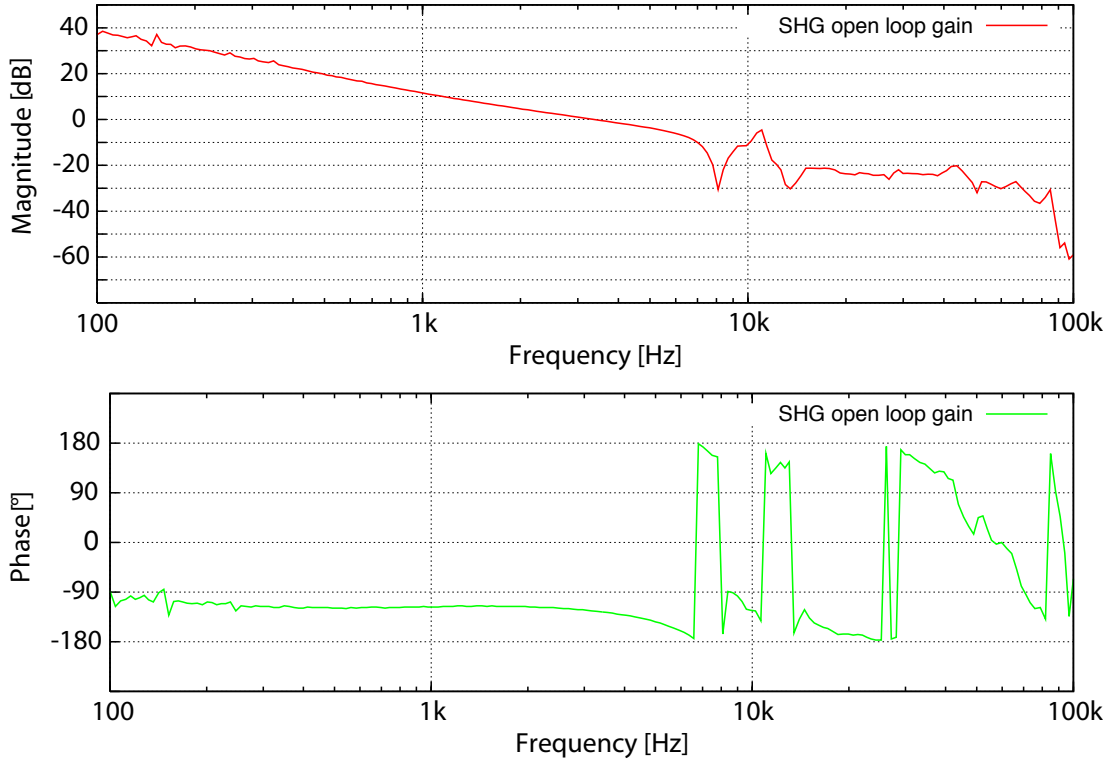


Figure 3.8 — Open-loop gain of the second harmonic generator cavity length control loop. The unity-gain frequency was approximately at 3 kHz and was mainly limited by several resonances around 10 kHz.

3.3.2 Mode cleaner cavities for the fundamental and second harmonic field

An important feature of our experiment were two travelling-wave resonators which served as optical low-pass filters for high frequency phase noise on the laser beams as well as spatial mode cleaners. These cavities were positioned in the beam path of both the fundamental and second harmonic field; one cavity close to the homodyne detector and one close to the squeezed light source. It has been shown in [Taken07, Franze06] that phase fluctuations, for example of the second harmonic pump field, can be a limiting factor for the observation of strong squeezing. Both, spatial and temporal fluctuations lead to a reduced contrast between the squeezed field and the local oscillator beam of the homodyne detector. This effect couples anti-squeezed noise into the squeezing measurement.

As illustrated in Figure 3.9 these resonators were set up as three mirror Fabry-Perot-ring-cavities. For the green mode cleaner two super-polished plano/plano

in-coupling and out-coupling mirrors were used with a transmission of $T_s = 150$ ppm for s-polarization and $T_p = 5500$ ppm for p-polarization, respectively. A highly reflective coated mirror ($T = 150$ ppm) with a radius of curvature of 1.0 m defined the eigenmoden of this ring cavity. The round-trip length was $L = 420$ mm. All three mirrors were glued onto a solid aluminium spacer, which guaranteed a quasimono-lithic mechanical stability of the cavity design. The waist size was $262 \mu\text{m}$ for the wavelength of 532 nm. The finesse can be calculated via

$$\mathcal{F} = \frac{\pi(r_1^2 r_2^2)^{1/4}}{1 - (r_1^2 r_2^2)^{1/2}} \quad (3.6)$$

to be approximately $\mathcal{F}_p = 555$ for p-polarized and $\mathcal{F}_s = 10500$ for s-polarized light. Taking the free spectral range of 714 MHz into account, the cavity linewidth (FWHM) was 1.29 MHz for p-polarization and 68 kHz for s-polarization.

For the infrared mode cleaner the transmission of the plano mirrors was 700 ppm for s-polarized and 1.1 % for p-polarized light, respectively. This results in a cavity linewidth (FWHM) of 170 kHz or 2.75 MHz depending on the polarization. In this experiment p-polarized light was used.

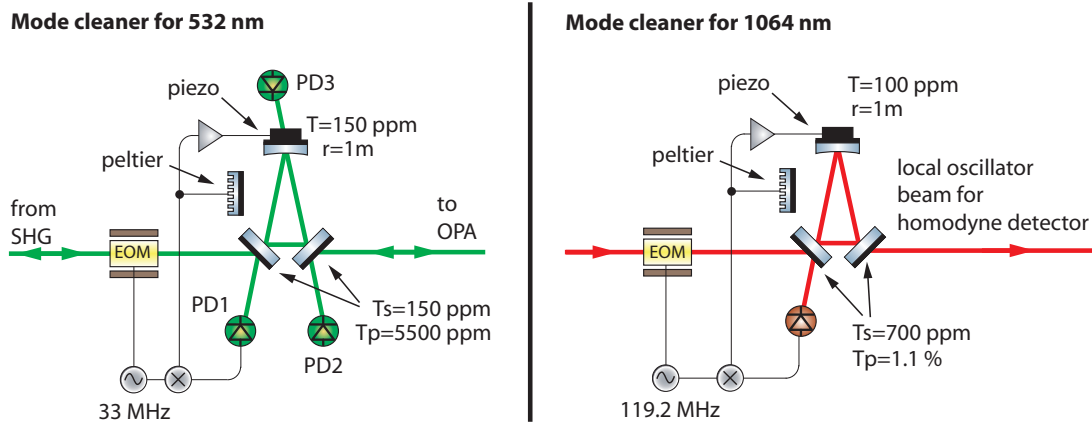


Figure 3.9 — Schematics of the mode cleaner cavities for a wavelength of 532 nm and 1064 nm, respectively. Both resonators were set up as three mirror Fabry-Perot-ring-cavities with a round-trip length of $L = 420$ mm. Each cavity was held on resonance utilizing the Pound-Drever-Hall locking technique with a modulation frequency of 33 MHz or 119.2 MHz. The cavity length stabilization was done via a split-feedback onto a piezo actuated mode cleaner mirror and onto peltier elements, which were thermally contacted to the aluminium mode cleaner spacer. The additional photodetectors PD2 and PD3 were used for alignment and intensity monitoring purposes.

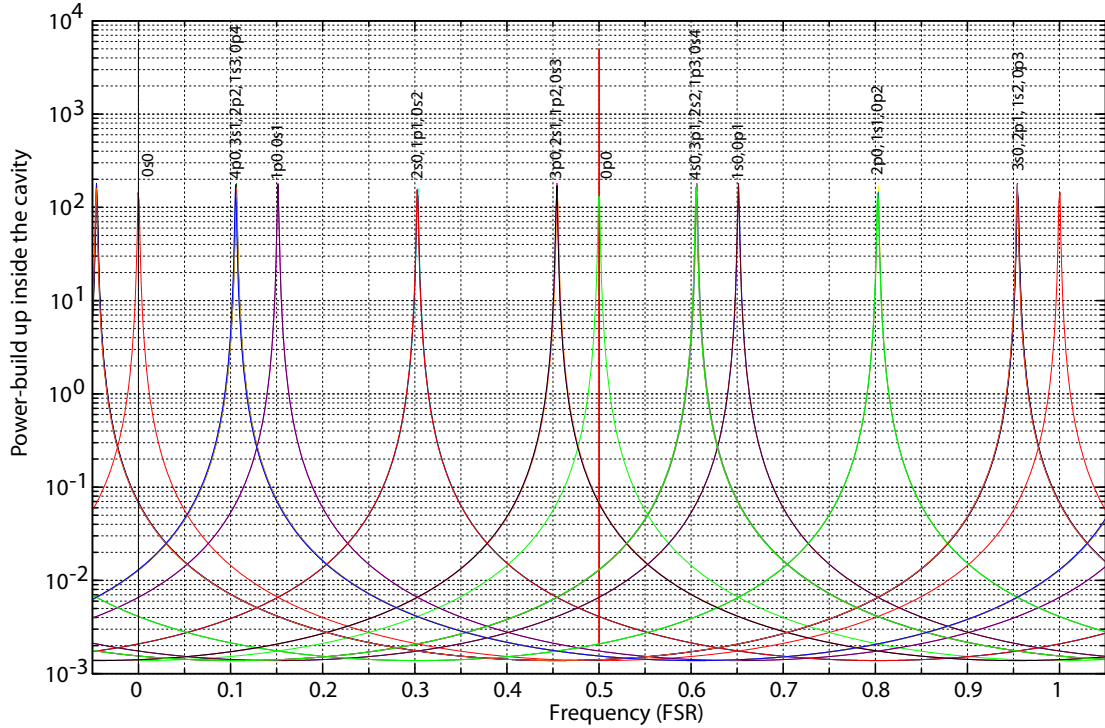


Figure 3.10 — Theoretical plot of the mode cleaner eigenmodes for both orthogonal polarizations. For various Gauss-Laguerre modes, the normalized power build up is shown versus the frequency in units of free spectral ranges. All relevant higher order modes are suppressed by at least four orders of magnitude compared to the TEM_{00} -mode.

A theoretical plot of the mode cleaner spectrum for both orthogonal polarizations is shown in Figure 3.10. For various Gauss-Laguerre modes, the normalized power build up is shown versus the frequency in units of free spectral ranges. All calculated higher order modes are suppressed by at least four orders of magnitude compared to the TEM_{00} -mode. Since only light can be transmitted through the mode cleaner cavities which fits the resonator eigenmodes, the spatial purity of the outgoing fields are high.

The mode cleaner cavity for 532 nm was held on resonance to the incoming laser light by utilizing the Pound-Drever-Hall locking scheme with a phase modulation frequency of 33 MHz. A home-made electro optical modulator made from 7 % doped $\text{MgO}:\text{LiNbO}_3$ was placed for field phase modulation between the second harmonic generator output and the mode cleaner input. As shown in Figure 3.9 the photodetector PD1, which detected the reflection of the mode cleaner input field, was employed for electronic demodulation at 33 MHz to obtain an error signal. The latter was fed

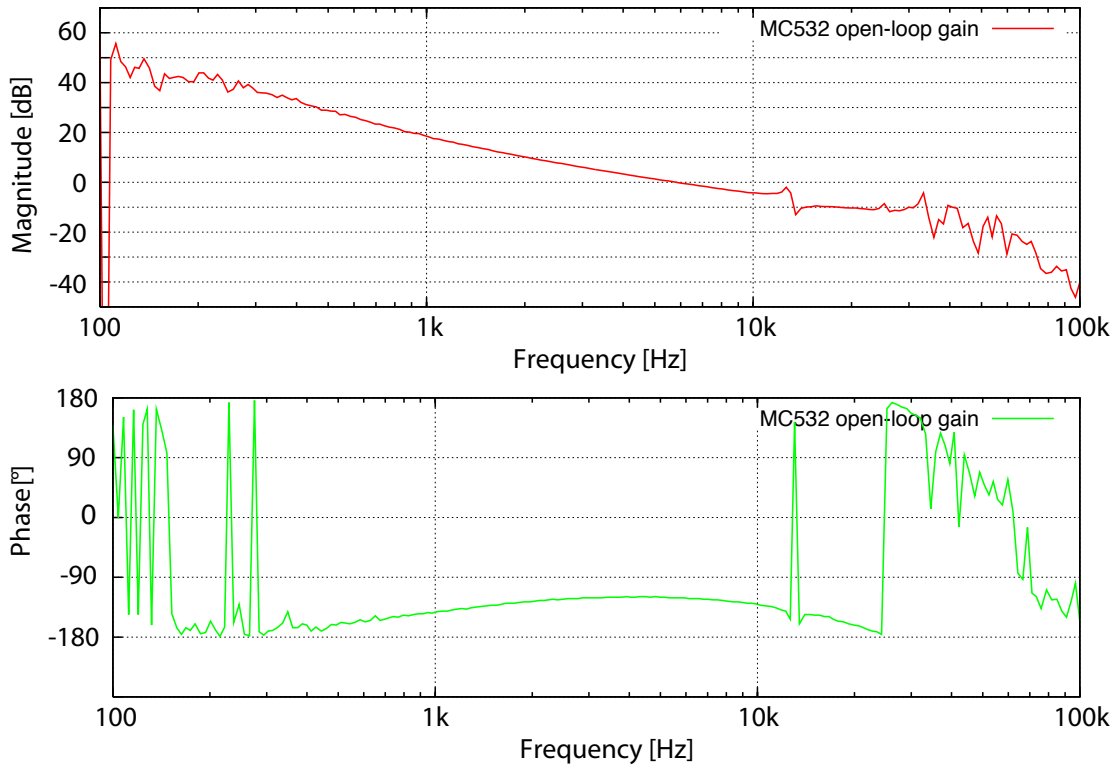


Figure 3.11 — Open-loop gain of the MC532 mode cleaner cavity length control loop. The unity-gain frequency was about 6 kHz.

back on two acutators: higher frequencies were guided onto curved ring-cavity mirror while for a slow cavity length control the two peltier elements were employed. These were thermally contacted to the solid aluminium spacer. Both feedback paths together formed a long time stable locking loop. The schematic of the peltier current driver stage can be found in Appendix.

Figure 3.11 presents the measured open-loop gain of the 532 nm mode-cleaner length control loop. A unity gain frequency of approximately 6 kHz was achieved. This control bandwidth was mainly limited by the mechanical resonances of the aluminium spacer and additional resonances of the piezo-electric-transducer. However, a more complex servo design, for example including notch filters, was not required for this experiment.

As illustrated in Figure 3.9 the light, which was residually transmitted through the curved mode cleaner mirror, was detected on an additional photo diode (PD3). This detector was used for monitoring the intra cavity light power as well as the second harmonic generator output.

Another photodetector (PD2) was set up for monitoring an important beam alignment. As we will see in more detail in Chapter 3.3.3, this port of MC532 can be used to adjust the spatial overlap between the „squeezed“-infrared eigenmode inside the squeezed light source and the green pump beam. A high mode overlap between these two fields is essential for two reasons. Firstly, a sufficiently high parametric gain inside the squeezed light source has to be reached in order to produce sufficient initial squeezing. Secondly, a perfect mode matching is recommended to reduce the overlap of the pump beam with higher order infrared modes inside the squeezed light source. This is important since other spatial modes could be squeezed or – depending on the Guoy-phase – even anti-squeezed. If this happens, an additional noise contribution to the field which was intended to be a pure squeezed TEM₀₀-mode occurs.

Therefore, an alignment beam at 1064 nm could temporarily be injected into the squeezed light source, turning the device into a second harmonic generator. Due to the strongly under-coupled squeezer cavity, only a small fraction of the injected alignment beam was frequency doubled. Hence, the photodetector PD2 was optimized for the detection of only pW's of light power at 532 nm.

The design of the mode cleaner at 1064 nm was identical to the described 532 nm mode cleaner layout. Only the modulation frequency for the Pound-Drever-Hall locking technique was chosen to be at 119.2 MHz instead of 33 MHz. For both resonators the phase modulation depth was optimized for an optimal balance between the signal-to-noise ratio of the error signal and the residual phase modulation of the transmitted light.

3.3.3 Monolithic squeezed light source

The squeezed light source was a monolithic cavity made from 7 % doped MgO:LiNbO₃ that produced squeezed states via type I degenerate optical parametric oscillation (OPO). The crystal length was 6.5 mm and both front and rear face had a radius of curvature of 8 mm. Each surface was dielectrically coated to give power reflectivities of 88 % and 99,97 % at 1064 nm, respectively. This resulted in a finesse of the resonator at 1064 nm of approximately 50. The waist size of the infrared field was approximately 28 μm. Taking the refractive index of $n = 2.23$ into account, the free spectral range was about 10.34 GHz and the cavity-linewidth was therefore 210 MHz (FWHM). The mirror coatings on the crystal also provided a second harmonic power build up by a factor of approximately 3 when the fundamental wavelength was resonant.

In a separate experiment we investigated the absorption of 7 % doped MgO:LiNbO₃-material at 1064 nm. For this experiment a high finesse cavity around a non-linear crystal was set up. The resonator was composed from a 6.5 mm long MgO:LiNbO₃ crystal, which had one high-reflection coated curved end-surface (radius of curvature = 8 mm),

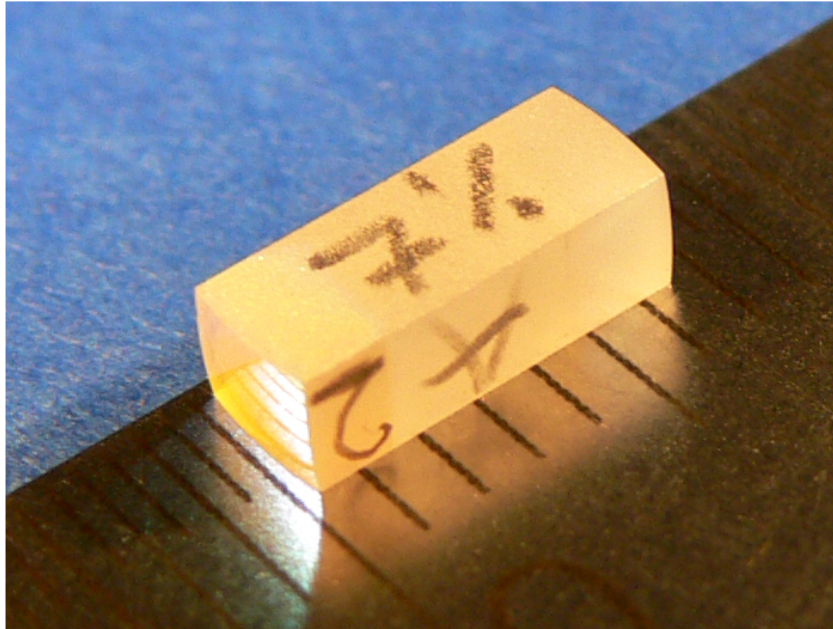


Figure 3.12 — Photograph of the monolithic squeezed light source made from 7 % doped $\text{MgO}:\text{LiNbO}_3$. The crystal length was 6.5 mm and both front and rear face had a radius of curvature of 8 mm. Each surface was dielectrically coated to give power reflectivities of 88 % or 99.97 % at 1064 nm, respectively.

and an external 25 mm curved cavity mirror. According to the manufacturers measurement protocols the power reflectivity of the HR-coated crystal surface was 99.97% and 99.92% for the external mirror, respectively. The non-curved intra-cavity surface of the $\text{MgO}:\text{LiNbO}_3$ -crystal was anti-reflection coated, with a specified residual reflection of smaller than 0.1%. Without taking the AR-coating and the crystal absorption into account the finesse of the cavity was calculated to be 5710.

In general, the finesse can be easily determined by measuring the free spectral range divided by the measured linewidth, for example. Unfortunately, in most cases this measurement procedure is only useful for low finesse cavities and often the results show a large error bar. One typical reason for this are non-linearities of a piezo-electrical-transducer which is typically used for dithering the cavity length.

To avoid these non-linearities we used an electro-optical modulator, which strongly phase-modulated the incoming light. Sidebands imprinted at a Fourier-frequency of 12 MHz served as fixed frequency markers on the detected light close to the cavity resonance frequency and therefore a cavity length scan over a complete FSR was no longer required. For this small cavity length variation the piezo actuating range could

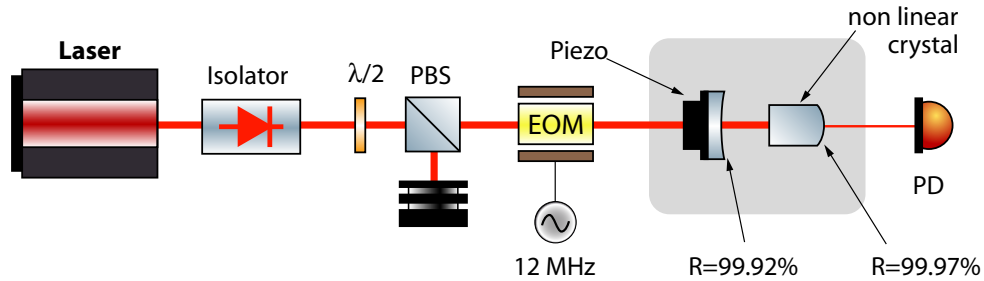


Figure 3.13 — Illustration of the experiment used for the absorption measurement of 7% doped $\text{MgO}:\text{LiNbO}_3$ at 1064 nm. A high finesse cavity was built from a HR-coated non-linear crystal and an additional piezo-actuated cavity mirror. An electro-optical-modulator generated strong sidebands which served as frequency markers for a precise measurement.

be assumed as linear. An illustration of the optical setup is shown in Figure 3.13.

A high intrinsic mechanical stability of the high finesse cavity was achieved by a construction which was comparable to the one we used for the SHG-cavity (a detailed description can be found in Chapter 3.3.1). Furthermore, we used a high bandwidth photodetector with a bandwidth of about 1 GHz and a slow cavity length scan rate ($f = 2$ Hz) to exclude bandwidth limiting effects which could distort the finesse measurement.

On average a finesse of approximately 3000 was measured. From this we could derive a cavity roundtrip loss of 0.1% or equivalent a loss of $0.077\% \text{ cm}^{-1}$. This result is indeed transferable to the monolithic squeezer cavity, since the $\text{MgO}:\text{LiNbO}_3$ material stemmed from the same manufacturing batch and went through the same HR-coating process. Please note that the measured loss of $0.077\% \text{ cm}^{-1}$ at 1064 nm in the hemilithic setup defined only an upper limit for the monolithic crystal because of the additional intra-cavity AR-coating, which quality was not measured independently. Given all relevant parameters, we obtained a minimal escape efficiency of $\eta_{\text{escape}} = 99.36\%$ for the monolithic squeezed light source, which is equivalent to a maximum loss of 0.64% for the squeezed field inside the source itself.

As described in Chapter 3.3.2 and illustrated in Figure 3.4, an auxiliary alignment beam could be temporarily injected into the squeezed light source. Due to the conversion of infrared alignment photons into a second harmonic field this infrared field was utilized for the alignment of the green pump beam in the counter direction. Additionally, this infrared auxiliary beam enabled a reliable alignment of the fringe visibility at the homodyne detector. Once the alignments were done, the auxiliary beam was switched off.

Second harmonic pump powers between 650 mW and 950 mW were mode-

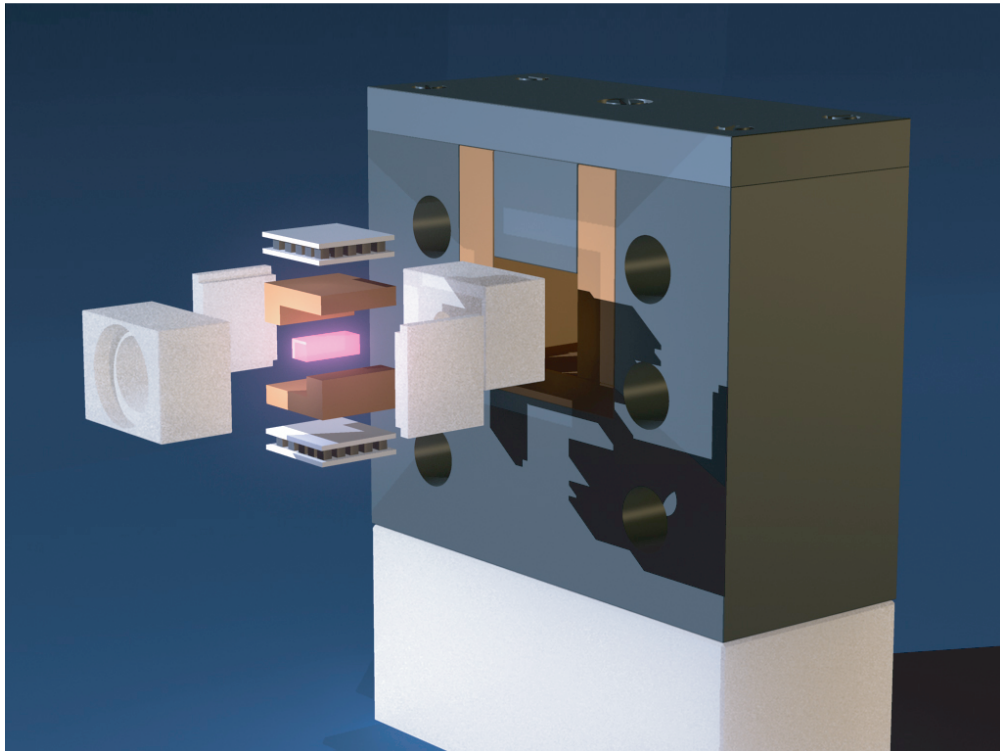


Figure 3.14 — Illustration of the monolithic squeezed light source. The nonlinear crystal is mounted between two copper plates. This sandwich was thermally contacted to a push-pull system consisting of two peltier elements. The complete stack was covered with isolation made from Macor material for passive thermal stabilization.

matched into the squeezer and parametric gains between 63 and above 200 were observed. Squeezed states of light at 1064 nm were produced when the crystal temperature was stabilized at the phase-matching temperature and the laser wavelength was tuned on resonance with the squeezed light source cavity. Due to the high stability of our setup, no servo-loop control for the laser frequency was required. The squeezed states left the source in counter direction of the pump field and were separated from the pump field via a dichroic beam splitter (DBS). This beamsplitter had a power reflectivity of $R = 99.8\%$ at 1064 nm, resulting in an additional 0.2% loss for the squeezed field.

The oven-design used for temperature stabilization of the monolithic squeezed light source is illustrated in Figure 3.14. The phase matching temperature between the infrared field and the green pump field was approximately 67°C . The nonlinear crystal was mounted between two copper plates. This sandwich was thermally contacted to a push-pull system consisting of two peltier elements. Finally, the complete stack

was covered with isolation material made from Macor ceramic for passive thermal stabilization. A NTC-thermistor (not shown in Figure 3.14) was contacted with one of the copper plates and was part of an active electronic temperature stabilization circuit, similar to the one already described in Chapter 3.3.1.

3.3.4 Homodyne detector

The observation of (squeezed) quantum noise was performed by means of a balanced homodyne detector. This is the most adequate detection scheme since both the amplitude and phase quadrature variances of the generated squeezed state needed to be measured. As presented in Figure 3.4 the homodyne detector is comprised of a 50/50 beamsplitter, a pair of photodetectors and a local oscillator field. The phase relation between the signal and the local oscillator field determines the measured quadrature of the signal field. Utilizing a piezo-actuated mirror in the squeezing path the relative path between both fields can be controlled.

Due to the high polishing quality of the MgO:LiNbO₃ monolithic crystal surfaces, the spatial mode quality of the generated squeezed field was high. As described in Chapter 3.3.2 the local oscillator beam also offered a high spatial purity because of the filtering by means of the mode cleaner cavity MC1064. These facts contributed to an extremely high homodyne detector fringe visibility of 99.8 %, which could so far not be achieved in squeezing experiments.

The two beam-splitter output fields were focused on Epitaxx ETX-500 photodiodes with beam-spot-sizes of only 10 μm . This allowed us to map out the photodiodes' surfaces to locate areas of maximum quantum efficiency. We observed quantum efficiency variations over the photodiodes' surfaces of about $\pm 1\%$. To further reduce optical loss we removed the photodiodes' protection windows and aligned the active areas at their Brewster angle. This led to an overall enhancement of the photodiode quantum efficiency in the order of 2 percent.

A maximum common mode rejection of the homodyne detector circuit, which means a high suppression of the technical laser noise carried with the local oscillator field, was achieved when both photodiodes measured the same photocurrent. Variations in both photodiodes' quantum efficiencies can be equalized in two ways. Firstly, the 50/50 homodyne beamsplitter used in this experiment was polarization-sensitive. Thus, the splitting ratio could be tuned by changing the polarizations of the input fields. Secondly, the splitting ratio also depended on the orientation of the 50/50 beamsplitter. Small rotation angles ($\pm 2^\circ$) could be used for optimizing the homodyne detection efficiency before the decreasing quality of the anti-reflection coating introduced an additional optical loss.

Figure 3.15 shows a photograph of one side of the homodyne detector electron-

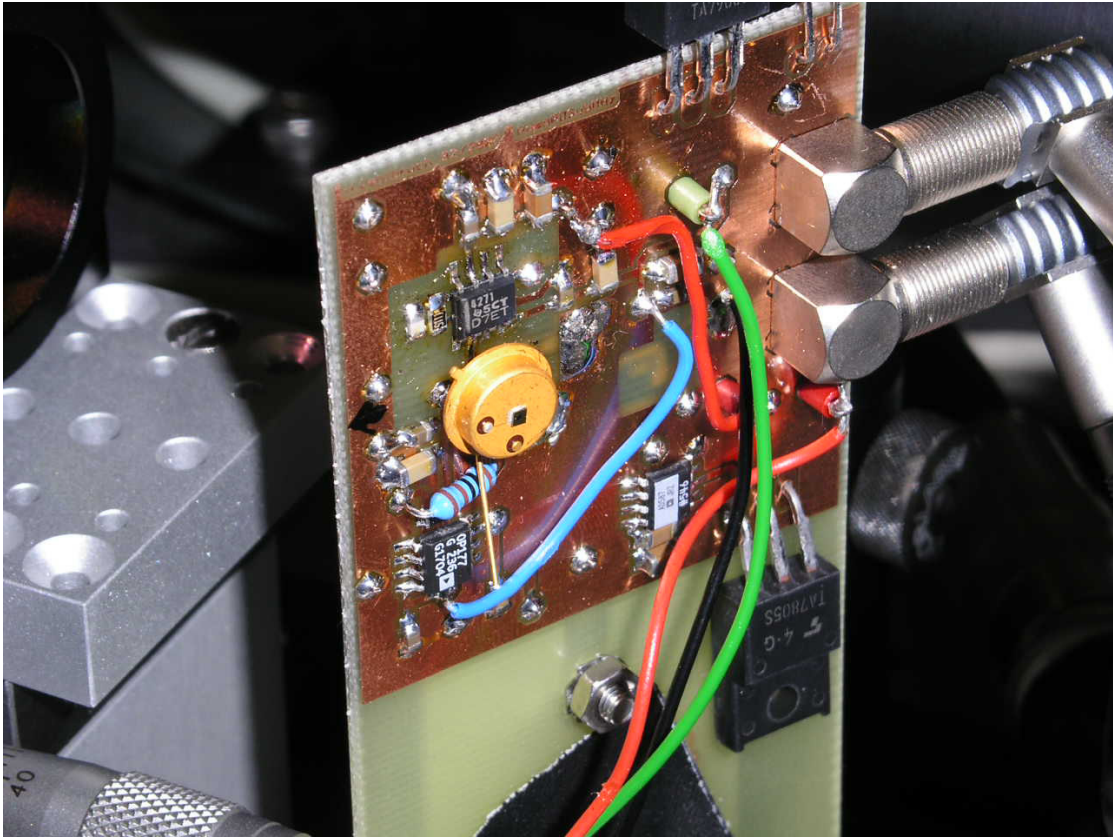


Figure 3.15 — Photograph of one side of the homodyne detector photo diodes including electronics. A photocurrent „self-subtraction“ scheme was used to directly cancel the DC component of both photocurrents. This allowed a high amplification factor at the first electronic stage (transimpedance stage), which resulted in a huge dark noise clearance. In order to keep the capacitance of the conducting paths on the printed circuit board as small as possible for both photodiodes, these were mounted back to back each on one side of the printed circuit board.

ics. A photocurrent „self-subtraction“ scheme was used to virtually cancel the DC component of each photo diode’s photocurrent. This allowed a high amplification factor at the first stage electronic amplifier stage (transimpedance stage) without any saturation. As a result, this technique offered a large signal-to-noise ratio. Using a local oscillator beam of 26.9 mW, the dark noise clearance was approximately 26 dB at a Fourier frequency of 5 MHz. A wide bandwidth of the detector was achieved by keeping the capacitance of the conducting paths on the printed circuit board as small as possible. Hence, both photodiodes were soldered back to back, each on one side of the printed circuit board.

Finally, in order to confirm the observed squeezing strength, we checked the

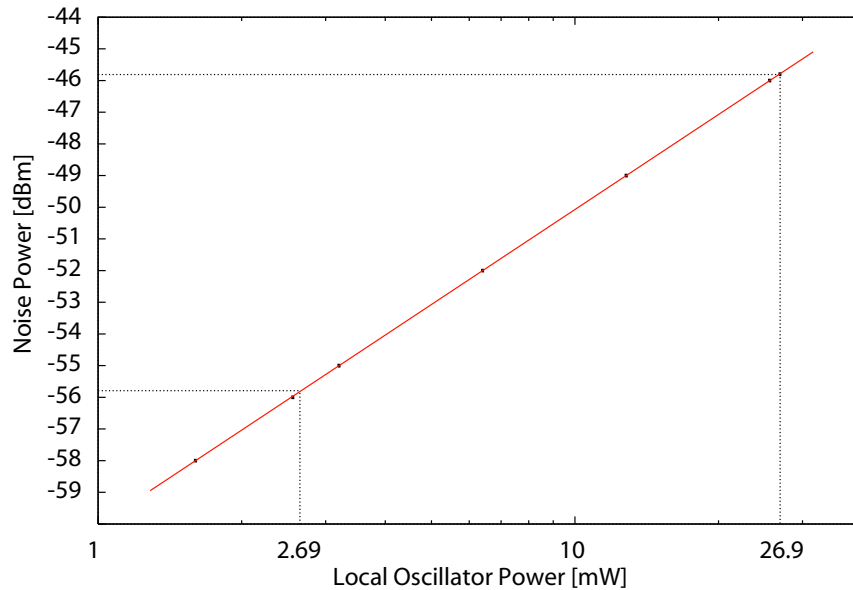


Figure 3.16 — The linearity of the homodyne detection system was validated by varying the local oscillator power. The figure shows the linear fit to seven measurement values (squares). Each square mark represents the average of 15 zero-span measurements (RBW=100 kHz, VBW=100 Hz) at 5 MHz, done with different LO powers. The sizes of the squares correspond to the measurement error bars. Note that the shot-noise of a laser beam of 2.69 mW was shown to be identical to the squeezed noise of the differential mode in our homodyne detector with ten times the light power.

linearity of the homodyne detection system including the spectrum analyser by measuring shot-noise levels versus local oscillator powers. Figure 3.16 presents seven measurement values, which are shown as square marks. Each square mark represents the average of 15 zero-span measurements (RBW = 100 kHz, VBW = 100 Hz) at 5 MHz, performed with a LO power of 1.6 mW, 2.56 mW, 3.2 mW, 6.4 mW, 12.8 mW, 25.6 mW and 26.9 mW, respectively. The sizes of the squares corresponds to the measurement error bars. In addition a linear fit to the seven measurement values is shown.

Please note, that the shot-noise level of a laser beam with an intensity of 2.69 mW is shown to be identical to the squeezed noise of the differential mode in our homodyne detector with ten times the light power.

3.4 Observation of 10 dB squeezed vacuum states of light

The first so far published direct observation of light with 10 dB squeezing is presented in Figure 3.17. Shown are noise powers at the Fourier sideband frequency of 5 MHz. Trace (a) corresponds to the shot-noise of uncorrelated photons of 26.9 mW local oscillator power and was measured with the squeezed light input blocked. In this arrangement no photons entered the signal port of the homodyne detector and the measured shot-noise could directly be linked to the vacuum noise, which corresponds to the light's quantum mechanical ground state. Trace (b) shows the quantum noise-reduction when squeezed states were injected. The directly observed squeezing level was $10.12 (\pm 0.15)$ dB. During this measurement the phase between the squeezed vacuum field and the local oscillator beam of the homodyne detector was adjusted manually via a high-voltage driven piezo-mounted mirror in the squeezing path. This enabled us to measure maximum squeezing levels as well as the maximum anti-squeezing. The detector dark noise (trace (c)) was approximately 26 dB below the vacuum noise level. Dark noise subtraction leads to a squeezing level of $10.22 (\pm 0.16)$ dB.

To further validate the observation of 10 dB squeezing we introduced a known amount of optical loss into the squeezed light beam. The observed squeezing and anti-squeezing strength should depend on this additional loss in a characteristic way. For this procedure a combination of a $\lambda/2$ waveplate and a polarizing beam splitter was placed between the 50/50 beam splitter of the homodyne detector and each photodiode (PD1, PD2). Power loss values of up to 40 % were introduced in each beam-splitter output. Since both fields – the squeezed beam and the local oscillator – suffered from the loss, the intensity of the local oscillator beam was re-calibrated to the nominal value of 26.9 mW by using a more intense beam in front of the modecleaner. With this procedure only loss for the squeezed beam was introduced without affecting the mode matching of our detector. Fig. 3.18 shows the observed amount of squeezing and anti-squeezing with additionally introduced 10 %, 20 %, 30 % and 40 % optical loss, respectively. Each square mark represents the average of 5 zero-span measurement at a sideband frequency of 5 MHz. The solid lines (b) and (c) represent the simulations for a parametric gain of $g = 63$ which was experimentally realized with 650 mW pump power. We found excellent agreement with the experimental data.

With an increased pump power of 950 mW we observed anti-squeezing of 23.3 dB whereas the squeezing was still 10 dB below vacuum noise. This observation can be used to deduce boundaries for the total optical loss in our setup. Assuming a loss free setup in which the observed squeezing strength is limited by anti-squeezing coupling into our squeezing measurement via phase fluctuations, we derived the

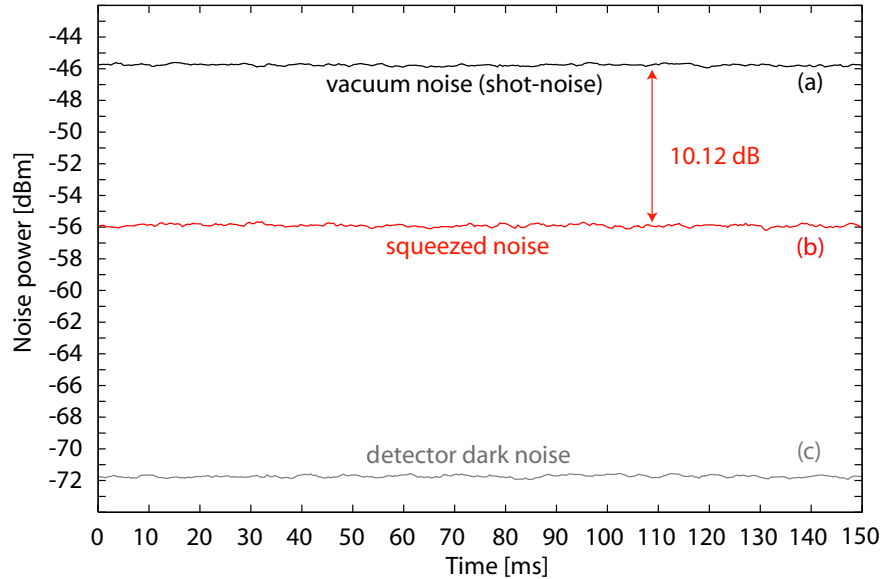


Figure 3.17 — Quantum noise powers at a Fourier frequency of 5 MHz, measured with a resolution bandwidth of 100 kHz and video bandwidth of 100 Hz. Trace (a) shows the vacuum noise level corresponding to 26.9 mW local oscillator power. Trace (b) shows the noise power of the squeezed vacuum states measured with the same local oscillator power. A nonclassical noise reduction of 10.12 dB below vacuum noise was observed. The electronic detector dark noise is shown in trace (c) and was not subtracted from the data. Each trace was averaged three times.

upper limit for phase jitter to be $\phi = 1.2^\circ$. Since ϕ is independent of the pump power we can conclude that 10 dB squeezing, as observed with 650 mW (and less anti-squeezing), was not limited by phase fluctuations but by optical loss. Even with $\phi = 1.2^\circ$ we found the minimum value for the total optical loss in our setup to be 5.6%. Secondly, we assumed phase fluctuations of $\phi \ll 1.2^\circ$. Here the observed squeezing is completely limited by optical loss, which results in the upper bound for the optical loss of 8.6%. Taking these boundaries into account, the left part of Figure 3.18 shows how much squeezing might be achieved in our setup by optical loss reduction.

The optical loss budget is composed of the following contributions: as described in Chapter 3.3.3 we determined (in independent measurements) the intra-cavity round trip loss of the squeezed light source to be less than 0.7% at 1064 nm, corresponding to an escape efficiency of the squeezed states from the source greater than 99.4%. Loss during propagation occurs due to the dichroic beam splitter (0.2% transmission loss at 1064 nm) and non-perfect anti-reflection coatings of lenses and was determined

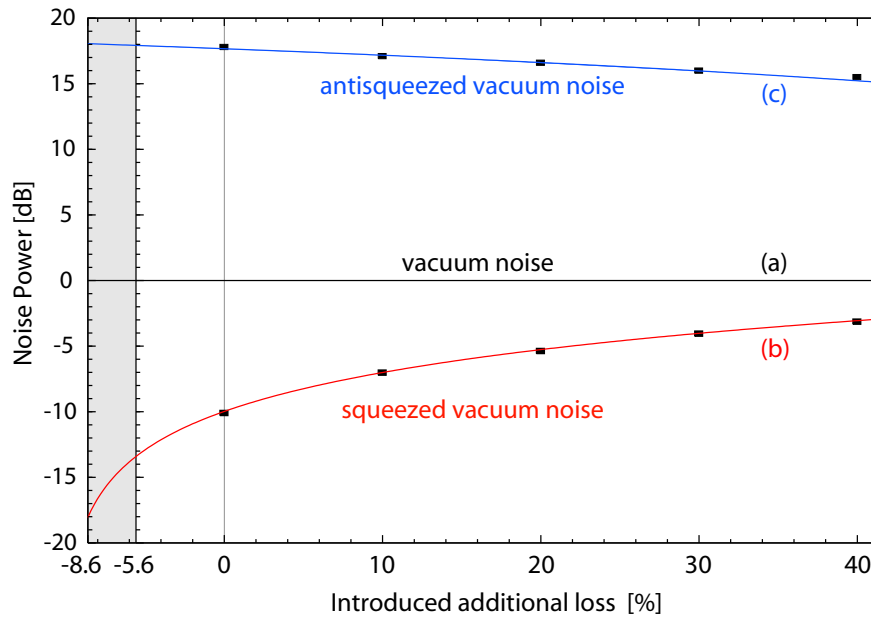


Figure 3.18 — Squeezing and anti-squeezing levels for a parametric gain of 63 versus optical loss. Solid lines show the theoretical predictions. Square boxes represent measurement values with sizes corresponding to the errors bars. Electronic darknoise was subtracted in this figure. The two vertical axis on the left corresponds to the upper and lower boundaries of how much squeezing might be achieved in our setup by further reduction of intrinsic optical loss in our setup.

to be about 1.1% in total. The non-perfect visibility at the homodyne beam splitter introduced another 0.4% of loss. Given these numbers, we estimate the quantum efficiency of the ETX-500 photo diodes to be $95(\pm 2)\%$. We note that this value is more precise than those from typical alternative measurements relying on absolute light power measurements.

3.5 Observation of 11.5 dB squeezed vacuum states of light

As concluded in the previous Chapter the dominant limitation for the measurement of even higher squeezing levels was the non-perfect quantum efficiency of the homodyne detector photodiodes. For this reason a matched pair of photodiodes with an improved quantum efficiency was custom made by the Fraunhofer Heinrich-Hertz-Institute in Berlin [HHI]. A picture of one these diodes is shown in Figure 3.19. The active area was $500\ \mu\text{m}$ in diameter and the top layer was anti-reflection coated for a wavelength

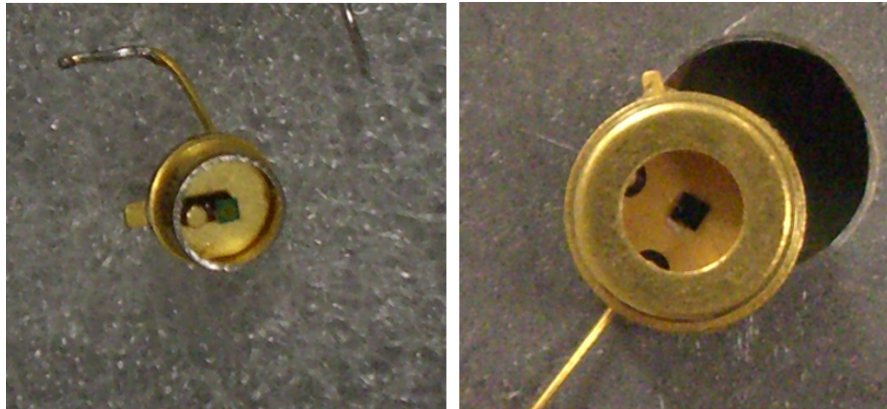


Figure 3.19 — Left: Photograph of a Epitaxx ETX500 photo diode. The protection window was removed with a can opener. Right: Picture of the custom made photo diode. The active area had a diameter of $500\ \mu\text{m}$. This diode offers a 2 % higher quantum efficiency at 1064 nm compared to the ETX500.

of 1064 nm at an incidence angle of $20^\circ \pm 2^\circ$. No window was installed for protection of the active area.

In comparison to the Epitaxx ETX500 the quantum efficiency (measured at DC) of these custom made photodiodes was 2 % higher for a wavelength of 1064 nm. Based on the manufacturers specified quantum efficiency of at least 99 % (designed, not measured), one can conclude that the ETX500 diodes could have had a quantum efficiency of 97 % (when the protection window was removed and the photodiode was aligned under brewster angle).

As illustrated in Figure 3.20 it is experimentally hard to distinguish between inherent phase noise and optical loss (for a given parametric gain). The squeezing as well as the anti-squeezing level are equally affected in both cases. The simulated red and orange traces describe a measurement in a phase-noise-free experiment with an overall optical loss of 8.6 %. These traces can hardly be separated from a measurement of noise levels corresponding to only 5.6 % loss but with an additional phase noise of 1.2° . An error bar of $\pm 0.2\%$ for the anti-squeezing level is common for almost every squeezing experiment (at high squeezing levels) and can not be used for a reliable analysis. This is due to the not intensity stabilized pump field and therefore the parametric amplification factor can easily drift from approximately 50 up to 70 due to marginal fluctuations of the conversion efficiency inside the second harmonic generator, for example.

In order to minimize the optical loss and also further reduce high frequency phase noise, which is caused by unavoidable RF-modulation for the Pound-Drever-Hall locking technique, the following experimental sections were revised:

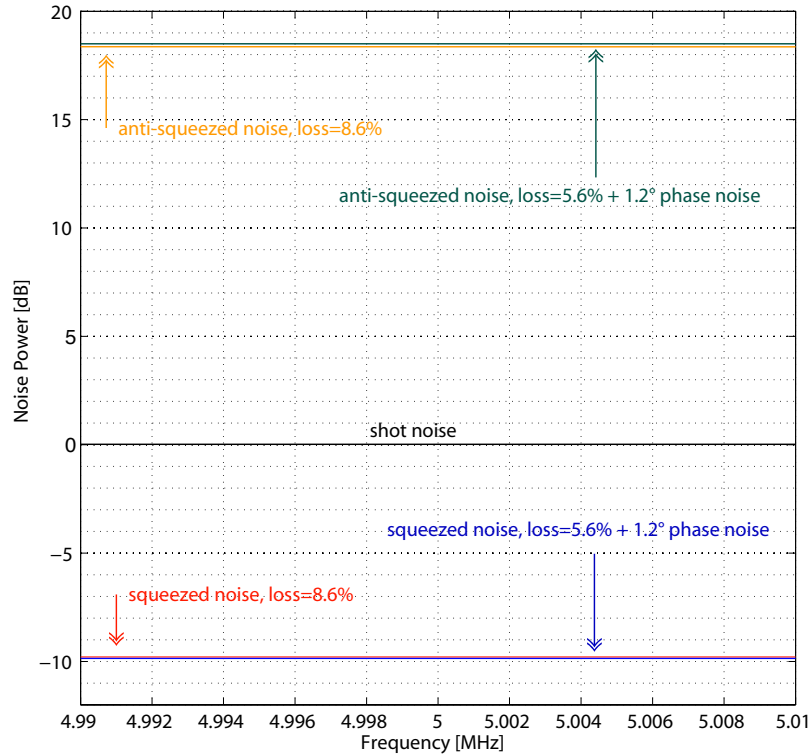


Figure 3.20 — Simulation of squeezing and anti-squeezing levels for two different parameter settings. The red and orange traces describe a phase noise free experiment with an overall optical loss of 8.6%. As one can see these traces can hardly be distinguished from a set of noise levels corresponding to only 5.6% loss but with an additional phase noise of 1.2° .

- Second harmonic generation:
 - For the 10 dB squeezing experiment the SHG-cavity length was stabilized utilizing the Pound-Drever-Hall technique with a modulation frequency of 80 MHz. A tiny fraction of the infrared intra-cavity field leaking out through the HR-coated backside of the nonlinear crystal was used for demodulation, thereby generating the desired error signal. But since the cavity linewidth of the second harmonic generator was about 50 MHz the error signal was 4 times larger if a fraction of the reflected light was used for the locking loop. Hence a 99/1 beamsplitter was inserted into the infrared input field. This allowed a significant reduction (-20 dB) of the EOM-modulation index to achieve the same error signal signal-to-noise ratio.

- Modecleaner for 532 nm:
 - Any phase noise of the green pump field leads to a jitter of the squeezing ellipse. Therefore, a high modulation frequency for the locking technique of the modecleaner cavity length is preferable, since the attenuation caused by the modecleaner linewidth gets more effective. We shifted the modulation frequency from 33 MHz up to 119.2 MHz, which is closer to half the modecleaner's free spectral range.
- Squeezing path:
 - A reduction of optical loss was achieved by removing one lens from the squeezing path. Furthermore, the dichroic beamsplitter was exchanged by a custom coated and super polished fused silica substrate. The specified reflectivity of this beamsplitter was 99.9 % for the infrared field (for s-polarization), while the transmission of the green pump beam (p-polarization) was close to unity as well. The remaining lens in the squeezing path, which was essential to handle the huge divergency of the squeezed beam due to the small waist size, was also substituted by a super polished fused silica lens. The anti-reflection coating of this component was specified to be 0.1 % (or better) for 1064 nm. Using these high quality optics also helped to minimize mode front distortion, which influences the fringe visibility with the local oscillator beam at the homodyne detector. Please note, that the loss depends quadratically on the fringe visibility. Hence, two piezo driven three axis steering mirrors, also made from super polished substrates, were inserted into the squeezing beam path for a more comfortable and sensitive visibility alignment. Finally, all polarizing optics were removed from the squeezing path, which required an exchange of the 50/50 homodyne detector beamsplitter (see next item).
- Homodyne detector:
 - The 50/50 beamsplitter was optimized for a specific polarization regarding the splitting ratio as well as the anti-reflection coating. A change of the input field's polarization required an exchange of this beamsplitter. Additionally, the orientation of the homodyne photodiodes had to be adapted for brewster angle alignment. To reduce optical loss super polished fused silica lenses (AR-coated with $R < 0.1\%$ at 1064 nm) were used instead of standard BK7 optics.

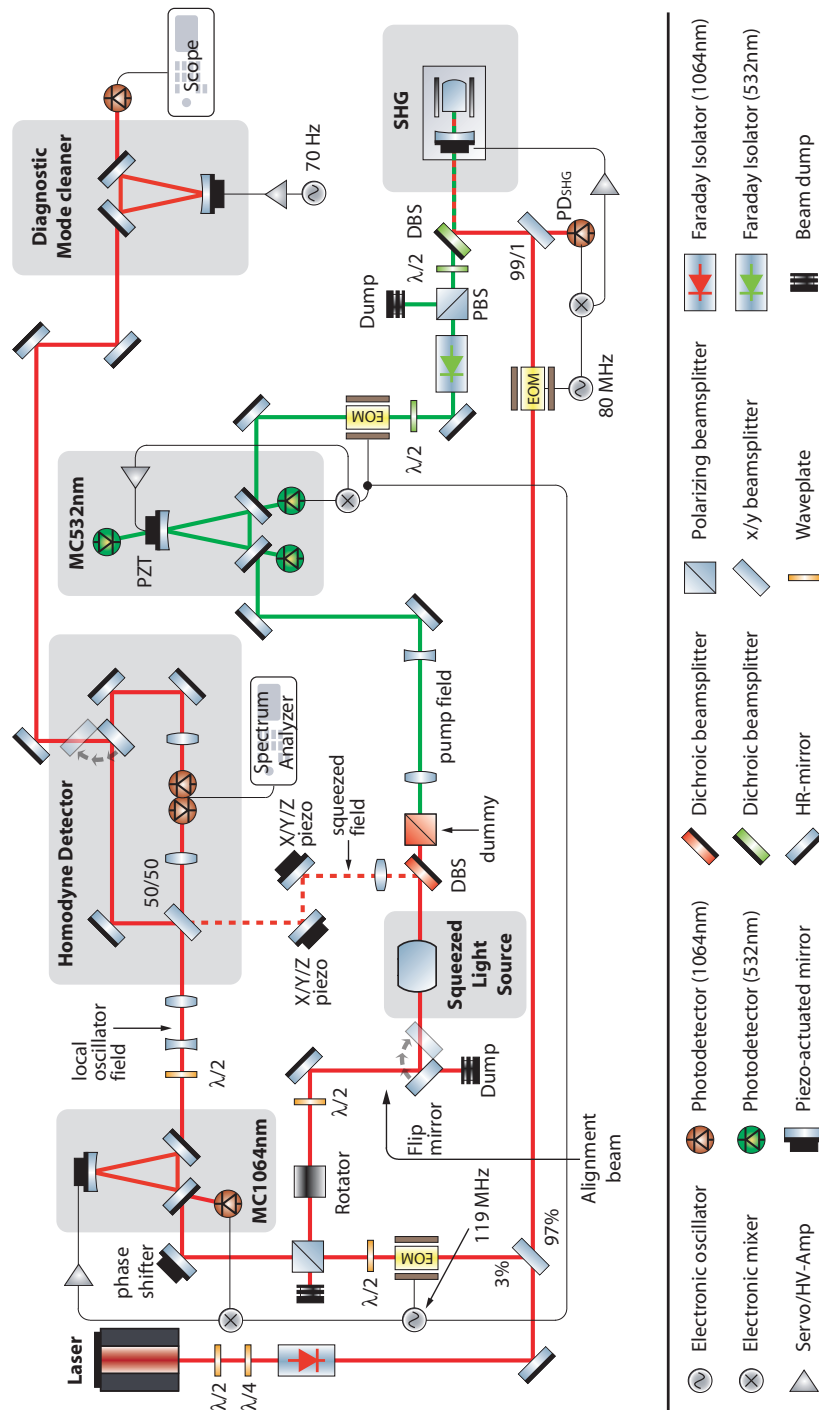


Figure 3.21 — Schematic of the updated experimental setup. Squeezed states of light at 1064 nm were generated inside the squeezed light source via optical parametric oscillation (OPO) below threshold. SHG: second harmonic generation, EOM: electro-optical modulator. An additional ring cavity was implemented as a diagnostic mode cleaner in order to simplify the alignment of the homodyne detector fringe visibility.

- Diagnostic mode cleaner cavity
 - As illustrated in Figure 3.21 one output field of the homodyne beam-splitter could be temporarily injected into an additional ring-cavity. This „diagnostic mode cleaner“ was employed to simplify the alignment of the homodyne detector fringe visibility. Information about the spatial purity and mode-matching quality of either the local oscillator beam or the squeezed beam could be monitored by means of this diagnostic mode cleaner consecutively. Since we achieved a mode matching of 99.99 % for the local oscillator beam into this reference cavity, the diagnostic mode cleaner was an instructive indicator for the alignment of the squeezed beam as well. But since the weak squeezed beam could not be directly used for an reliable adjustment, the auxiliary alignment beam was used as a substitute instead. This guaranteed a constant beam intensity which allowed a more meaningful alignment procedure than the use of a squeezed or anti-squeezed beam with strongly fluctuating intensities. The alignment field transmitted through the squeezed light source also showed a high beam profile quality. Thus, a mode matching of up to 99.9 % into the diagnostic mode cleaner was achieved.

The experimental improvements directly lead to an enhancement of the measured squeezing strength. Figure 3.22 shows zero span measurements at a Fourier sideband frequency of 5 MHz. Trace (a) corresponds to the shot-noise level of uncorrelated photons of approximately 20 mW local oscillator power and was measured with the squeezed light input blocked. Trace (b) shows the quantum noise-reduction when squeezed states were injected into the homodyne detector. The directly observed squeezing level was up to 11.5 dB below the shot-noise level, without any dark noise correction. The electronic detection dark noise is shown in trace (c).

The complete impact of the experimental upgrades can be derived from squeezing and anti-squeezing noise level measurements. Corresponding to a pump power of 570 mW broadband measurements at Fourier frequencies from 3 MHz up to 10 MHz are shown in Figure 3.23. In order to equalize the transfer function of the homodyne detector circuit, each trace was divided by the measured shot-noise reference noise. Trace (b) shows broadband squeezing over a wide bandwidth with an average quantum noise reduction of more than 11 dB. Trace (c) shows the corresponding anti-squeezing measurement. All traces were recorded with a resolution bandwidth of 300 kHz, a video bandwidth of 300 Hz and were averaged 3 times. These measurements can be fitted with a theoretical model assuming a phase jitter free setup but a total optical loss of 4.3 % (shown in trace (d) and (e)). Compared to the 10 dB squeezing measurements

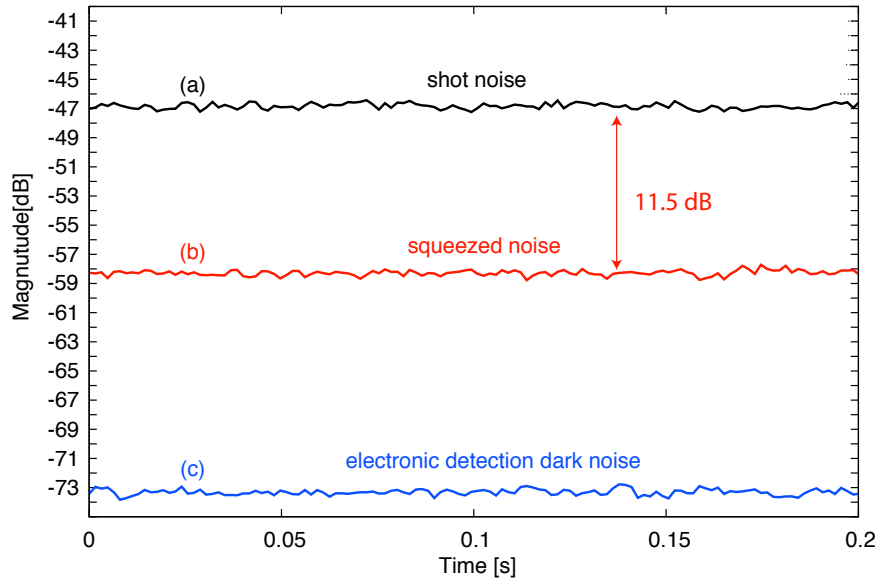


Figure 3.22 — Quantum noise powers at a Fourier frequency of 5 MHz, measured with a resolution bandwidth of 100 kHz and video bandwidth of 100 Hz. Trace (a) shows the vacuum noise level corresponding to 20 mW local oscillator power. Trace (b) shows the noise power of the squeezed vacuum states measured with the same local oscillator power. A nonclassical noise reduction of 11.5 dB below vacuum noise was observed. The electronic detection dark noise is shown in trace (c) and was not subtracted from the data.

it can be derived that the optical loss was reduced by 4.3 % due to the experimental upgrades.

Taking phase noise into account and assuming that the upper limit was still $\phi = 1.2^\circ$ (which was the upper limit we derived from the 10 dB squeezing measurements) we found the minimum value for the total optical loss in our setup to 2.6 %. Compared to the boundary of 5.6 % optical loss obtained from the 10 dB measurement, the upgrades brought out an optical loss reduction of 3.0 %. Please note, that the slight degradation of (anti-)squeezing at higher sideband frequencies as shown in Figure 3.23 was due to the squeezed light source cavity linewidth.

3.6 Conclusion

The direct observation of 11.5 dB squeezing of light's quantum noise, shows that the squeezed light technique has indeed a great application potential as envisaged

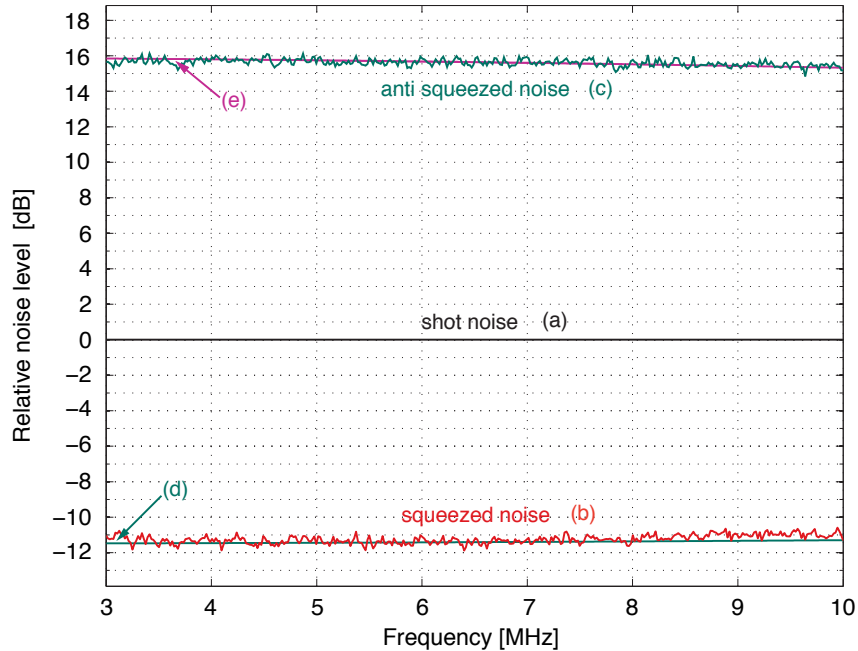


Figure 3.23 — Quantum noise powers at Fourier frequencies from 3 MHz - 10 MHz, measured with a resolution bandwidth of 300 kHz and video bandwidth of 300 Hz. Each trace was averaged three times. The normalized shot-noise reference is shown in trace (a). Trace (b) presents broadband squeezing over a wide bandwidth. Trace (c) shows the corresponding anti-squeezing measurement. These measurements can be fitted with a theoretical model assuming a phase jitter free setup but a total optical loss of 4.3 % (shown in trace (d) and (e)).

more than two decades ago. Injected into a gravitational wave detector, the quantum noise reduction corresponding to an increase of more than a factor of 10 in laser light power will be possible [Caves81]. This is a promising application, since gravitational wave detectors already use the highest single-mode laser powers applicable. Furthermore, our results might enable the generation of strongly entangled states to reach teleportation fidelities well above $2/3$ as already typically achieved in single photon teleportation experiments [Bouwmeester].

To produce even higher levels of squeezing further investigations can be done in the field of alternative nonlinear materials, the effect of green induced infrared absorption and pump power dependent thermal effects in the squeezed light source.

Coherent Control of Vacuum Squeezing in the Gravitational-Wave Detection Band

In this Chapter a coherent control scheme for stable phase locking of squeezed vacuum fields is described and demonstrated. We focus on sideband fields at frequencies within the audio band which is the frequency regime of particular interest in gravitational wave detection and for which conventional control schemes have failed so far. A vacuum field with broadband squeezing covering the entire band from 10 Hz to 10 kHz was produced using optical parametric oscillation and characterized with balanced homodyne detection. The system was stably controlled over long periods utilizing two coherent but frequency shifted control fields. In order to demonstrate the performance of our setup the squeezed field was used for a nonclassical sensitivity improvement of a Michelson interferometer at audio frequencies. The Chapter refers to the following publications

- „*Coherent Control of Vacuum Squeezing in the Gravitational-Wave Detection Band*“,
H.Vahlbruch, S.Chelkowski, B.Hage, A.Franzen, K.Danzmann, and R.Schnabel,
Physical Review Letters, 97, 011101, (2006).

- „*Quantum engineering of squeezed states for quantum communication and metrology*“,
H. Vahlbruch, S. Chelkowski, K. Danzmann, and R. Schnabel,
New Journal of Physics, 9, 371, (2007).
- „*Coherent Control of Broadband Vacuum Squeezing*“,
S.Chelkowski, H.Vahlbruch, K.Danzmann, and R.Schnabel,
Physical Review A, 75, 043814, (2007).

4.1 Introduction

It was first proposed by Caves [Caves81] that injected squeezed states may be used to improve the sensitivity of laser interferometers and might therefore contribute to the challenging effort of direct observation of gravitational waves [Thorne87]. The goal of that proposal was the reduction of the measurement's shot noise. Later Unruh [Unruh82] has found that squeezed light can be used to correlate interferometer shot noise and radiation pressure noise thereby breaking the so-called standard quantum limit and allowing for a quantum nondemolition measurement on the mirror test mass position, for an overview we refer to [Kimbl01]. Harms *et al.* [Harms03] have shown that advanced interferometer recycling techniques [Meers88] that also aim for an improvement of the signal-to-shot-noise-ratio are fully compatible with squeezed field injection. Gravitational wave detectors require squeezing in their detection band from about 10 Hz to 10 kHz. The majority of current squeezing experiments, however, have been performed in the MHz regime. Furthermore the orientation of the squeezing ellipse needs to be designed for every sideband frequency. The transformation from frequency independent squeezing to optimized frequency dependent squeezing can be performed by optical filter cavities as proposed in [Kimbl01] and demonstrated in [Chelk05] for MHz frequencies. Also in the MHz-regime, the combination of squeezed field injection and recycling techniques has been demonstrated [McKen02, Vahlb05]. Squeezing at audio frequencies has been demonstrated for the first time [McKen04, McKen06]. However, the phase of the squeezed vacuum could not be controlled by a coherent field.

Controlling squeezed vacuum fields is the basic problem for squeezed field applications in gravitational wave (GW) detectors. Common control schemes rely on the injection of a weak, phase modulated control field at the carrier frequency into the squeezed light source. It has been shown that even lowest carrier powers introduce large amounts of classical laser noise at audio frequencies and squeezing can no longer be achieved [McKen04]. On the other hand phase modulation sidebands are

not present in a pure vacuum field. For this reason in [McKen04, McKen06] a coherent control field for locking the squeezed quadrature angle to a local oscillator could not be created. The quadrature angle was stabilized instead using so-called noise locking whose stability was found to be significantly less than what can be achieved with coherent modulation locking [McKen05] as used in GW interferometers.

In this Chapter we report on the demonstration of a coherent control scheme for stable phase locking of squeezed vacuum fields. The scheme was used to produce broadband squeezing at audio and sub-audio frequencies, even down to a Fourier frequency of 1 Hz. This frequency regime covers the complete detection band of ground based GW detectors. The measured quantum noise levels were in perfect agreement with theoretical predictions.

The general purpose of an interferometer is to transform an optical phase modulation signal into an amplitude modulation which can be measured by a single photodiode or by a balanced homodyne detector. The observable is described by the time-dependent quadrature operator $\hat{q}_\theta(\Omega, \Delta\Omega, t)$ where Ω denotes the modulation sideband frequency, $\Delta\Omega$ the detection resolution bandwidth (RBW) and θ the quadrature angle. The amplitude quadrature ($\theta = 0$) is usually denoted by subscript 1 and phase quadrature ($\theta = \pi/2$) by subscript 2 [Chelk05]. For the vacuum state the variances of quadrature operators ($\Delta^2 \hat{q}_\theta$) are normalized to unity and, generally, Heisenberg's Uncertainty principle sets a lower bound for the product of the two variances of non-commuting pairs of quadrature operators, e.g.

$$\Delta^2 \hat{q}_1(\Omega, \Delta\Omega, t) \cdot \Delta^2 \hat{q}_2(\Omega, \Delta\Omega, t) \geq 1. \quad (4.1)$$

If an ideal phase-sensitive amplifier such as a loss-less optical parametric oscillator (OPO) acts on the vacuum state the equality still holds but one quadrature variance is squeezed. For a nonclassical improvement of an interferometer's signal-to-noise-ratio the angle of the squeezed quadrature then needs to be aligned to the modulation signal of interest. In realistic situations the degree of squeezing is decreased by optical losses thereby mixing the squeezed with a vacuum state, as well as by noisy classical modulation fields that beat with the same local oscillator, and also by acousto-mechanical disturbances during the squeezed field generation and during its measurement [McKen04].

Noisy modulation fields from the laser source can be completely removed if the squeezed light source is just seeded by a pure vacuum field. To prevent any contamination of the squeezed field, an appropriate control scheme may solely use some additional fields that do not interfere with the squeezed mode. If, nevertheless, such control fields are coherent with the squeezed mode full control capability is possible. The length of the squeezed light source might be controlled by using phase modulation sidebands on a different (frequency shifted) spatial mode or polarization

mode. In the experiment presented here, we used the latter. However, control of the quadrature angle in respect to a homodyning local oscillator or an interferometer is more challenging. Here we propose to use another control field that does sense the OPO nonlinearity but is frequency detuned against the vacuum squeezed mode.

When coupled into the squeezed light source the parametric gain g turns the single sideband field into the following field with amplified and deamplified quadratures, respectively:

$$E(t) \approx e^{-i\omega_0 t} \alpha_\Omega (\sqrt{g} \cos(\Omega t) + i \sin(\Omega t) / \sqrt{g}) + c.c., \quad (4.2)$$

where α_Ω is the complex amplitude of the single sideband field with carrier detuning Ω and with phase set to zero. When $E(t)$ is directly detected with a photo diode and demodulated at 2Ω , an error signal for the quadrature angle can be produced that allows coherent locking of the second harmonic pump field with respect to the control field. Furthermore, when $E(t)$ is overlapped with a local oscillator at the carrier frequency ω_0 and the photo current is demodulated at Ω , another error signal can be derived to lock the control field to the local oscillator thereby locking the squeezed vacuum field to the local oscillator.

4.2 Coherent control theory

In the following the theoretical background of the coherent control scheme is presented [Chelk07]. Most calculations were done using a MATHEMATICA script, which can be found in the Appendix.

An error signal for both

- Phase control between the green pump field (for the squeezed light source) and the injected coherent control field and
- Phase control between the green pump field and a local oscillator field required for homodyne detection

can be derived from a frequency shifted coherent control (quadrature control field, QCF), which has to be injected into the squeezed light source. The first error signal is labeled $S_{\text{Err}}^{\text{QCF/Pump}}$ whereas the second error signal is abbreviated with $S_{\text{Err}}^{\text{QCF/LO}}$.

4.2.1 Coherent control field under nonlinear process

Before the injection of the frequency shifted control field (QCF) into the squeezed light source, the QCF represents a single sideband field at a frequency $\omega_0 + \Omega$ with

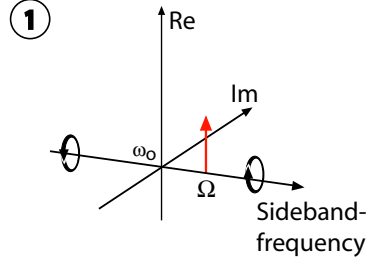


Figure 4.1 — Complex optical field amplitude representing a single sideband field at a frequency $\omega_0 + \Omega$ with respect to the main carrier frequency ω_0 .

respect to the main carrier frequency ω_0 , which is mainly used in the experiment. This is illustrated in Figure 4.1 and can also be found in Figure 4.4 where the marker „①“ indicates this position in the experiment.

This single sideband field can be described by the real-valued amplitude α_Ω . The expectation values of the annihilation operators of the upper and lower sideband fields at frequencies $\omega_0 \pm \Omega$ are

$$\langle \hat{a}_+ \rangle \equiv \langle \hat{a}(\omega_0 + \Omega) \rangle = \alpha_\Omega, \quad (4.3)$$

$$\langle \hat{a}_- \rangle \equiv \langle \hat{a}(\omega_0 - \Omega) \rangle = 0. \quad (4.4)$$

The quadrature amplitudes [Caves85] can be expressed as

$$\hat{a}_1 = \frac{1}{\sqrt{2}}(\hat{a}_+ + \hat{a}_-^\dagger), \quad (4.5)$$

$$\hat{a}_2 = \frac{1}{i\sqrt{2}}(\hat{a}_+ - \hat{a}_-^\dagger). \quad (4.6)$$

After the injection into the squeezed light source, the parametric amplification process amplifies – for example – the phase quadrature at the same time as it de-amplifies the amplitude quadrature, or vice versa. As shown in [Caves85] this (de-)amplification process of the quadratures

$$\bar{\mathbf{a}} = \begin{pmatrix} \hat{a}_1 \\ \hat{a}_2 \end{pmatrix} \quad (4.7)$$

can be described by applying the squeezing operator

$$S(r, \phi) = \exp(r(\hat{a}_+ \hat{a}_- e^{-2i\phi} - \hat{a}_+^\dagger \hat{a}_-^\dagger e^{2i\phi})) \quad (4.8)$$

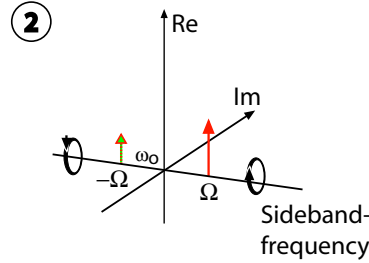


Figure 4.2 — Complex optical field amplitudes. The generated outgoing field from the squeezed light source is composed of two sidebands that are equally separated by Ω from the main carrier frequency ω_0 .

with a squeezing factor r and squeezing angle ϕ . This leads to a squeezed quadrature vector $\bar{\mathbf{b}}$

$$\bar{\mathbf{b}} = \begin{pmatrix} \hat{b}_1(\Omega) \\ \hat{b}_2(\Omega) \end{pmatrix} = S(r, \phi) \bar{\mathbf{a}} S^\dagger(r, \phi) \quad (4.9)$$

$$= \begin{pmatrix} \cosh(r) + \sinh(r)C_{2\phi} & \sinh(r)S_{2\phi} \\ \sinh(r)S_{2\phi} & \cosh(r) - \sinh(r)C_{2\phi} \end{pmatrix} \bar{\mathbf{a}}, \quad (4.10)$$

where $C_{2\phi} = \cos(2\phi)$ and $S_{2\phi} = \sin(2\phi)$. Now the expectation values of the new squeezed quadrature amplitudes $\hat{b}_1(\Omega)$ and $\hat{b}_2(\Omega)$ can be written as

$$\langle \hat{b}_1(\Omega) \rangle = -\frac{i\alpha_\Omega}{\sqrt{2}} S_{2\phi} \sinh(r) + \frac{\alpha_\Omega}{\sqrt{2}} [\cosh(r) + C_{2\phi} \sinh(r)] \quad (4.11)$$

$$\langle \hat{b}_2(\Omega) \rangle = \frac{\alpha_\Omega}{\sqrt{2}} S_{2\phi} \sinh(r) - \frac{i\alpha_\Omega}{\sqrt{2}} [\cosh(r) - C_{2\phi} \sinh(r)]. \quad (4.12)$$

The Fourier transformations at a single frequency of $\hat{b}_1(\Omega)$ and $\hat{b}_2(\Omega)$

$$\hat{b}_1(t) = \hat{b}_1(\Omega)e^{-i\Omega t} + \hat{b}_1^*(\Omega)e^{i\Omega t}, \quad (4.13)$$

$$\hat{b}_2(t) = \hat{b}_2(\Omega)e^{-i\Omega t} + \hat{b}_2^*(\Omega)e^{i\Omega t}. \quad (4.14)$$

is required to obtain the electrical field $E^{\text{QCF}}(t)$ of the coherent control field (QCF) which leaves the squeezed light source

$$E^{\text{QCF}}(t) \propto \langle \hat{b}^{(+)}(t) + \hat{b}^{(-)}(t) \rangle, \quad (4.15)$$

with

$$\hat{b}^{(\pm)}(t) \equiv \frac{1}{2} \left(\hat{b}_1(t) \pm i\hat{b}_2(t) \right) e^{\mp i\omega_0 t}. \quad (4.16)$$

Using $\exp(r) = \sqrt{g}$ this expression can be simplified to

$$\begin{aligned} E^{\text{QCF}}(t) &\propto \frac{1+g}{\sqrt{2g}} \alpha_\Omega \cos(\omega_0 t + \Omega t) \\ &- \frac{1-g}{\sqrt{2g}} \alpha_\Omega \cos(\omega_0 t - \Omega t - 2\phi). \end{aligned} \quad (4.17)$$

Equation 4.17 describes exactly how the parametric (de-)amplification process inside the squeezed light source (de-)amplifies the injected frequency shifted coherent control field. The generated electric field $E^{\text{QCF}}(t)$ (leaving the squeezed light source) is composed of two sidebands that are equally separated by Ω from the main carrier frequency ω_0 . This is illustrated in Figure 4.2 and can also be found in Figure 4.4 where the marker „②“ indicates this section in the experiment.

From this generated electric field $E^{\text{QCF}}(t)$ the two error signals ($S_{\text{Err}}^{\text{QCF/Pump}}$ and $S_{\text{Err}}^{\text{QCF/LO}}$) can be derived, as we will see in the following paragraphs.

4.2.2 Phase control of the second harmonic pump field

Using a single photodiode to detect the outgoing field $E^{\text{QCF}}(t)$ gives the photocurrent

$$\begin{aligned} I^{\text{QCF}} &\propto \frac{\alpha_\Omega^2}{2g} \left[(1+g) \cos(\omega_0 t + \Omega t) \right. \\ &\left. - (1-g) \cos(\omega_0 t - \Omega t - 2\phi) \right]^2. \end{aligned} \quad (4.18)$$

As readable in Figure 4.2, a demodulation of I^{QCF} at 2Ω is required to obtain an error signal $S_{\text{Err}}^{\text{QCF/Pump}}$ for the phase control between the green pump field and the QCF. Choosing the adequate demodulation phase the sinusoidal error signal can be written as

$$S_{\text{Err}}^{\text{QCF/Pump}} \propto \frac{(-1+g^2) \alpha^2 \sin(2\phi)}{4g}. \quad (4.19)$$

This error signal clearly shows the dependency on the squeezing angle ϕ with respect to the QCF. In the experimental setup this relative phase was controlled utilizing an electronic control loop with the error signal fed back onto a phase shifter, which was placed in the green pump path.

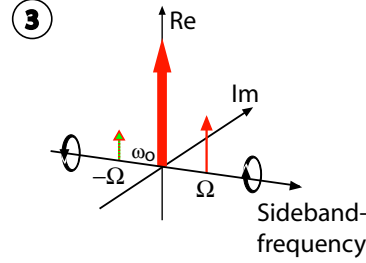


Figure 4.3 — Complex optical field amplitudes. The generated outgoing field from the OPO is composed of two sidebands that are equally separated by Ω from the main carrier frequency ω_0 .

4.2.3 Phase control of the squeezed vacuum field

As a second step of the coherent control scheme, the phase relation between the generated squeezed vacuum field and a homodyning local oscillator field has to be stabilized. Please note that this phase relation can be equally stabilized by using a phase shifter device placed either in the local oscillator beam path or in the squeezed vacuum beam path.

More generally, the phase relation between the generated squeezed vacuum and a homodyning local oscillator field depends on the phase Φ between the green pump field and the local oscillator field. For this control loop the according error signal $S_{\text{Err}}^{\text{QCF/LO}}$ can be generated from the subtracted photocurrents of both homodyne photodiodes $\text{PD}_{\text{HD}1,2}$.

The from the squeezed light source outgoing quadrature control field $E^{\text{QCF}}(t)$ is overlapped with the local oscillator field at the homodyne beam splitter

$$E^{\text{LO}} \propto \alpha^{\text{LO}} e^{-i\omega_0 t} e^{-i\Phi} + \text{c.c.} \quad (4.20)$$

Each output field of the homodyne beamsplitter ($E^{\text{HD}1}$ and $E^{\text{HD}2}$) is detected with a single photodiode, giving the following two complex field amplitudes

$$\begin{aligned} E^{\text{HD}1} &= \frac{1}{\sqrt{2}} (E^{\text{LO}} + E^{\text{QCF}}(t)) \\ &\propto \frac{1}{\sqrt{2}} \left(\alpha^{\text{LO}} e^{-i(\omega_0 t + \Phi)} + \left[\frac{1+g}{\sqrt{2}g} \alpha_{\Omega} \cos(\omega_0 t + \Omega t) \right. \right. \\ &\quad \left. \left. - \frac{1-g}{\sqrt{2}g} \alpha_{\Omega} \cos(\omega_0 t - \Omega t - 2\phi) \right] \right) + \text{c.c.}, \end{aligned} \quad (4.21)$$

$$\begin{aligned}
E^{\text{HD2}} &= \frac{1}{\sqrt{2}} (E^{\text{LO}} - E^{\text{QCF}}(t)) \\
&\propto \frac{1}{\sqrt{2}} \left(\alpha^{\text{LO}} e^{-i(\omega_0 t + \Phi)} - \left[\frac{1+g}{\sqrt{2}g} \alpha_{\Omega} \cos(\omega_0 t + \Omega t) \right. \right. \\
&\quad \left. \left. - \frac{1-g}{\sqrt{2}g} \alpha_{\Omega} \cos(\omega_0 t - \Omega t - 2\phi) \right] \right) + \text{c.c.} . \quad (4.22)
\end{aligned}$$

In Figure 4.3 one of these complex field amplitudes is illustrated. Furthermore in Figure 4.4 the marker „⊗“ indicates this location of the experiment.

Subtraction and subsequent lowpass filtering of both homodyne photocurrents $I^{\text{HD1,2}} = |E^{\text{HD1,2}}|^2$ leads to

$$\begin{aligned}
I_{\text{diff}} &\propto \frac{4\sqrt{2}\alpha^{\text{LO}}\alpha_{\Omega}\cos(\Phi + \omega_0 t)}{\sqrt{g}} \\
&\quad \times \left[(1+g)\cos(\omega_0 t + \Omega t) \right. \\
&\quad \left. - (1-g)\cos(\omega_0 t - \Omega t - 2\phi) \right] \quad (4.23)
\end{aligned}$$

$$\begin{aligned}
&\propto \frac{2\sqrt{2}\alpha^{\text{LO}}\alpha_{\Omega}(-1+g)}{\sqrt{g}} \\
&\quad \times \cos(\Omega t + 2\phi + \Phi) . \quad (4.24)
\end{aligned}$$

Demodulation of I_{diff} at frequency Ω (and additional lowpass filtering) results in the error signal $S_{\text{Err}}^{\text{QCF/LO}}$ for the relative phase Φ between the green pump and the local oscillator

$$S_{\text{Err}}^{\text{QCF/LO}} \propto \frac{\sqrt{2}\alpha^{\text{LO}}\alpha_{\Omega}(-1+g)}{\sqrt{g}} \sin(2\phi + \Phi) . \quad (4.25)$$

This error signal depends on the relative phase Φ between the green pump field and the local oscillator beam but also on the squeezing angle ϕ . However, in the previous paragraph it has been shown that the squeezing angle ϕ can be stabilized independently. Furthermore, it makes no difference for the phase relation between the green pump field and the local oscillator field (Φ) if the local oscillator beam is phase shifted, or – what was done in this experiment – the squeezed beam is phase controlled.

Hence, this scheme enabled the full coherent control of the generated squeezed vacuum states with respect to an external local oscillator beam by using the combination of both error signals according to Equations (4.19) and (4.25).

4.3 Experimental setup

A schematic of the experiment is shown in Figure 4.4. The main laser source (Laser 1) was again a monolithic non-planar Nd:YAG ring laser of 2 W single mode output power at 1064 nm. Approximately 1.4 W was used to pump a second harmonic generation (SHG) cavity. The design of the hemilithic SHG cavity was similar to the one of the squeezed light source described below but with an outcoupling mirror reflectivity of $R=92\%$. For SHG-cavity length stabilization the Pound-Drever-Hall technique was used. Hence, the infrared field was phase modulated at a frequency of 18 MHz before it was injected into the second harmonic generator. As presented in Figure 4.4 the infrared light transmitted through the SHG was detected and subsequently demodulated. The error signal was fed back onto the piezo-actuated SHG-outcoupling-mirror. The unity-gain frequency of this control loop was measured to be approximately 2 kHz. A more detailed description of this frequency doubling setup can be found in [Chelk05]. Only about 100 mW of the second harmonic field was finally used to pump the squeezed light source. The remaining green light (roughly 500 mW) was dumped.

A small fraction of the initial infrared laser light (Laser 1) was guided into a ring cavity for spatial mode cleaning. This cavity was held on resonance with the laser light using the sidebands imprinted at 18 MHz once more. The unity-gain frequency of this electronic servo control loop was about 6 kHz. The mode cleaner was used in the low-finesse mode which showed a finesse of approximately 350. The transmitted light served as a local oscillator beam for downstream homodyne detection of (squeezed-) vacuum states. The beam profile of this local oscillator beam showed a high spacial purity which is a precondition for a high fringe visibility with the squeezed beam at the homodyne beamsplitter.

The squeezed light source was set up as a hemilithic optical resonator consisting of a 7 % doped MgO:LiNbO₃ crystal and a piezo mounted output coupler. The power reflectivity of the coupling mirror was 95.6 % at 1064 nm and 20 % at 532 nm. The curved back surface of the crystal had a high reflection coating ($R = 99.96\%$) for both wavelengths. The cavity's free spectral range was approximately 3.8 GHz. Orientation of the nonlinear crystal was such that s-polarized infrared fields could sense parametric gain.

4.3.1 Squeezed light source cavity length control

For the cavity length control of the squeezed light source we used a phasemodulated p-polarized field which was supplied by another monolithic non-planar Nd:YAG ring

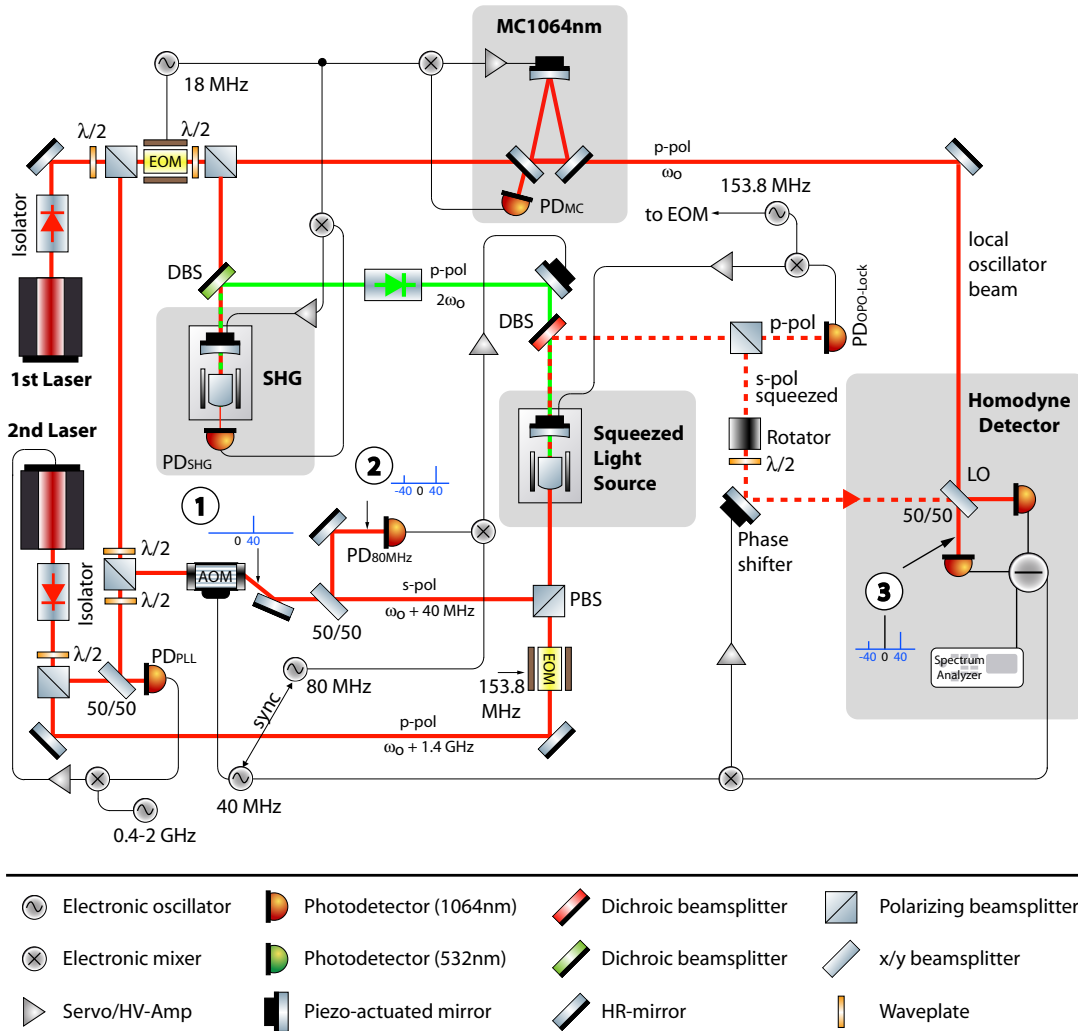


Figure 4.4 — Schematic of the low frequency squeezing experiment. Generation and full coherent control of a broadband squeezed vacuum field at 1064 nm was achieved utilizing two independent but phase locked laser sources. Laser 1 provided the squeezed light source pump field after second harmonic generation (SHG) and the main carrier frequency for the homodyning local oscillator beam. A frequency shifted control field was generated by utilizing an acousto-optical-modulator (AOM). Laser 2 provided another frequency shifted control field. Note: Complex optical field amplitudes at three different locations in the experiment are marked.

laser (Laser 2). We determined a frequency shift of about 1.4 GHz between the two polarization modes for simultaneous resonance inside the squeezer. The frequency offset was controlled via a high bandwidth phase locking loop. The p-polarized locking field was injected through the crystal's back surface and spatially separated

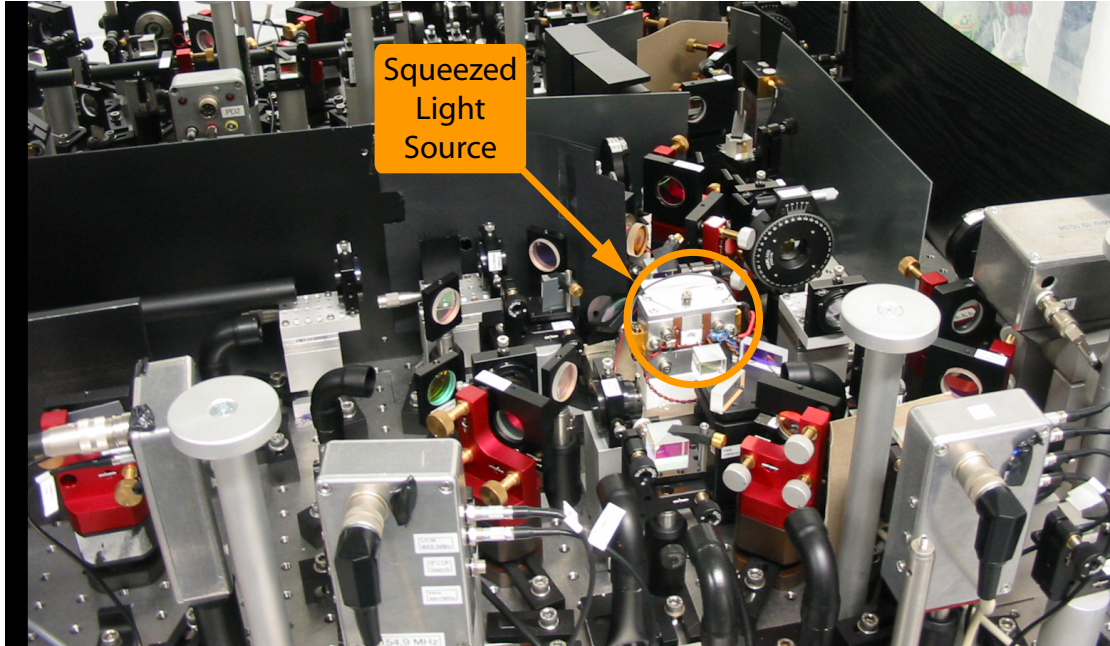


Figure 4.5 — Photograph of the experiment showing parts of the optical setup. In the middle of the picture the squeezed light source (oven construction) is shown. Also several shielding baffles and beam tubes are visible. These were used for reduction of infrared stray light.

from the s-polarized squeezed vacuum with a polarizing beam splitter (PBS). An error signal for cavity length control of the squeezed light source was generated via demodulation of the detected p-polarized light at a sideband frequency of 153.8 MHz without introducing any significant loss to the squeezed field. We measured the optical loss to be less than 0.1% given by the PBS's power reflectivity for s-polarized light of 99.9%. Please note, that the p-polarized control field did not add any significant noise to the squeezed mode, given the low residual power contribution after the PBS and the high frequency offset.

4.3.2 Coherent frequency shifted control field

Phase control with respect to a local oscillator at the fundamental frequency ω_0 is required for both characterization and application of audio-band squeezed vacuum fields. Following our proposal described above we utilized another coherent but frequency shifted control field. Detuned by 40 MHz with respect to the main carrier frequency (ω_0 , Laser 1) utilizing an acousto-optical-modulator (AOM), this s-polarized infrared field ($440 \mu\text{W}$) was also injected into the squeezed light source where its quadratures were parametrically (de-)amplified. This generated a sideband at $\Omega = -40 \text{ MHz}$.

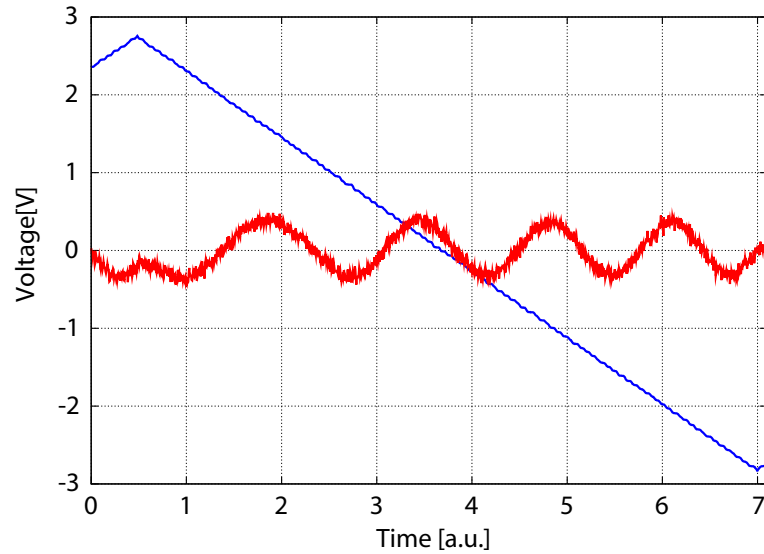


Figure 4.6 — Measured error signal for the phase relation between the coherent control field (40 MHz shifted) and the green pump field. The error signal was obtained by detecting the control field, which was back-reflected from the squeezed light source, and subsequent demodulation of the photocurrent at twice the beat frequency (80 MHz). This sinusoidal error signal (red trace) was recorded while the phase of the green pump beam was varied with an triangle waveform (blue trace).

This mechanism lead to an error signal for the phase relation between the coherent control field and the green pump field. The error signal could be obtained by detecting the control field which was back-reflected from the squeezed light source and subsequently demodulating the photo current at twice the beat frequency (80 MHz). This is illustrated in the sideband scheme in Figure 4.4. By feeding back the error signal to an PZT-mounted mirror in the path of the green pump field stable phase control was realized. In Figure 4.6 the measured sinusoidal error signal is presented. The schematics of the AOM-driver electronics and the phase locked 40 MHz and 80 MHz oscillator electronics are attached in the Appendix. A separate locking loop was required to control the phase between the squeezed vacuum field, given by the phase of the green pump, and the homodyning local oscillator beam. The appropriate error signal was derived at the homodyne detector by taking the difference of both photodiodes and a subsequent demodulation at a frequency of 40 MHz. The error signal was fed back to a phaseshifting PZT-mounted mirror placed in the squeezing path.

For both coherent control loops piezo-actuated HR-mirrors were used as phase shifting devices. A characteristic open-loop gain measurement of these control loops

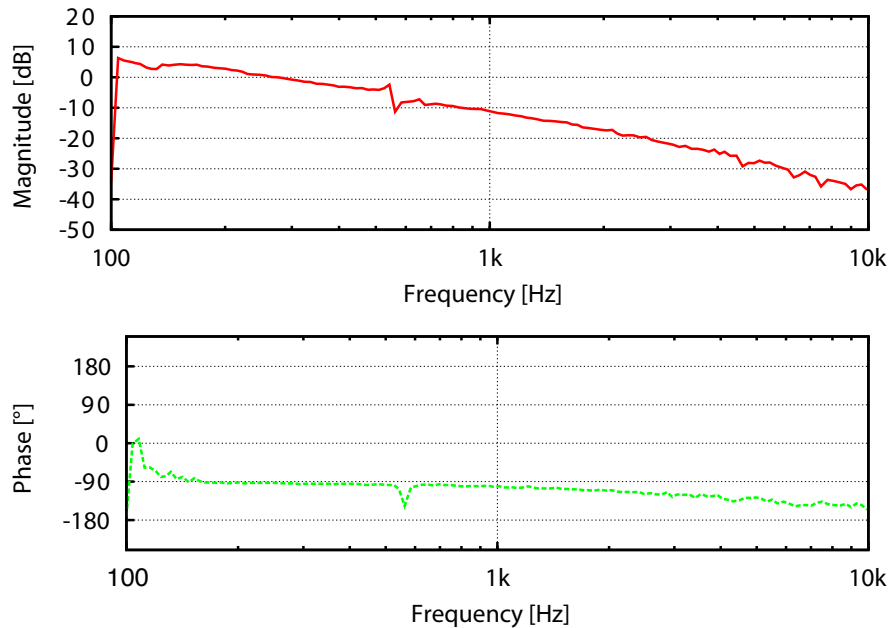


Figure 4.7 — Characteristic open-loop gain measurement of the squeezing angle control locking loops. The unity gain frequency of 250 Hz was mainly limited by a mechanical resonance at roughly 550 Hz.

is presented in Figure 4.7. The unity gain frequency of approximately 250 Hz was mainly limited by a mechanical resonance at roughly 550 Hz. A more rigid mechanical construction of the phase shifting device would help to shift the resonance to higher frequencies but most likely at the expense of the fine steering possibilities. However, the achieved unity gain frequency was sufficient for a stable phase control in our experimental environment.

4.4 Detection of vacuum states and squeezed states of light at audio frequencies

Observation and characterization of squeezed fields at audio frequencies is usually performed with balanced homodyne detection as it is done in the MHz-regime. However, at low frequencies measurement time increases and stable control of all the field's degrees of freedom is essential. In addition homodyne detection at audio frequencies requires a much greater classical noise suppression.

The measurement quantities are the field quadratures, e.g. amplitude or phase

quadratures, and their variances. A rather impressive property of such a detector is its capability to measure even fluctuations of fields that do not contain *any* photons on average, i.e. fields in so-called vacuum states. These vacuum fluctuations contribute to the zero point energy which is a manifestation of quantum physics after which any oscillator, like a single-mode state of light, cannot have zero energy, otherwise Heisenberg's uncertainty relation would be violated [Gerry04]. A balanced homodyne detector is also a perfect device for the detection of squeezed states of light. In this case the variance of a certain field quadrature is found to be *squeezed* below the variance of the corresponding vacuum field.

In balanced homodyne detection dim quantum states of the signal beam are interfered with an intense auxiliary laser beam (local oscillator, LO) on a beam splitter with 50% power reflectivity, as shown in Figure 4.4. The interference with the LO leads to an optical amplification of the measured signal field quadrature by a large factor, which is necessary to reach levels far above electronic noise of photodiodes and subsequent electronic circuits. Each output field from the 50/50 beam splitter is focussed onto a semiconductor photodiode. The final signal is derived from the difference of the two photocurrents, which is spectrally analyzed, for example using a Fast-Fourier-Transformation (FFT). Please note that noise contributions from the LO beam cancel in balanced homodyne detection.

If the signal field and the LO interfere *in phase*, the balanced homodyne detector measures the signal state's *amplitude* quadrature $\hat{q}_1(\Omega, \Delta\Omega, t)$ where $\Omega/2\pi$ is the Fourier frequency and $\Delta\Omega/2\pi$ is the detection resolution bandwidth (RBW). If the LO's optical path length is changed by a quarter wave length the homodyne detector measures the phase quadrature $\hat{q}_2(\Omega, \Delta\Omega, t)$. The amplitude, together with the phase quadrature, form a set of two non-commuting observables. The simultaneous precise knowledge of both their values is limited by Heisenberg's uncertainty relation.

Since the vacuum state sets the reference for squeezed states, we first present measurements of vacuum fluctuations. Vacuum states were produced by carefully blocking the signal input beam of the balanced homodyne detector without introducing scattered fields, while keeping the local oscillator beam. Figure 4.8 shows the spectral noise powers of optically amplified vacuum fluctuations of an optical field mode at 1064 nm for three different LO powers measured with our homodyne detector. We plot the spectral decomposition of the vacuum noise for sideband frequencies $\Omega/2\pi$ between 800 mHz and 3.2 kHz. For all three LO powers the signal port of our homodyne detector was empty and the observation of pure vacuum noise was confirmed in the following way

- Firstly, the measured spectral noise powers scaled linearly with LO power.
- Secondly, the noise spectra were white, i.e. independent of the Fourier frequency

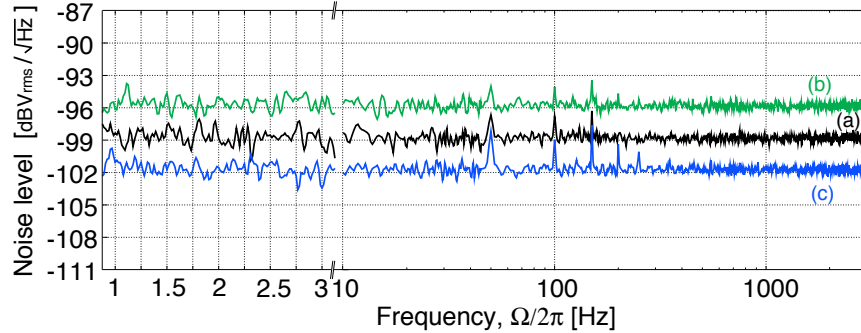


Figure 4.8 — Noise powers (variances) of field quadratures for a spectrum of vacuum states at different sideband frequencies. Three different local oscillator powers were used: (a) $464 \mu\text{W}$, (b) $928 \mu\text{W}$, and (c) $232 \mu\text{W}$. All traces are pieced together from five FFT frequency windows: 0.8–3.2 Hz, 10–50 Hz, 50–200 Hz, 200–800 Hz, 800 Hz–3.2 kHz with resolution bandwidths of $\Delta\Omega/2\pi=15.63$ mHz, 250 mHz, 1 Hz, 2 Hz and 4 Hz, respectively. Each measurement point is the averaged root mean square value of 75, 100, 100, 400 and 400 measurements, again respectively for the five FFT windows. Peaks at 50 Hz and harmonics were due to the electric mains. The electronic dark noise has been subtracted from the data.

$\Omega/2\pi$. Both properties of vacuum noise are predicted from theory and were clearly found in our observations as presented in Figure 4.8.

- Thirdly, independent measurements of the amplification factors of all electronic components used confirmed *quantitatively* within ± 0.5 dB uncertainty, that indeed pure vacuum noise was observed.

Please note, that the measurement of the frequency interval as presented in Figure 4.8 lasted for more than half an hour for each LO power, thereby demonstrating long term stability of our detector-setup. Our results in Figure 4.8 represent the first successful detection of vacuum states at sub-audio and audio frequencies below one kHz with a white (flat) spectrum.

4.5 Squeezed state engineering

We now discuss how an optical field with fluctuations smaller than the fluctuations of vacuum states at sideband frequencies down to 1 Hz was generated.

Since no laser radiation around the frequency ω_0 was injected into the squeezed light source cavity, the parametric process only acted on vacuum fluctuations and produced squeezed vacuum states for all frequencies within the cavity linewidth. The

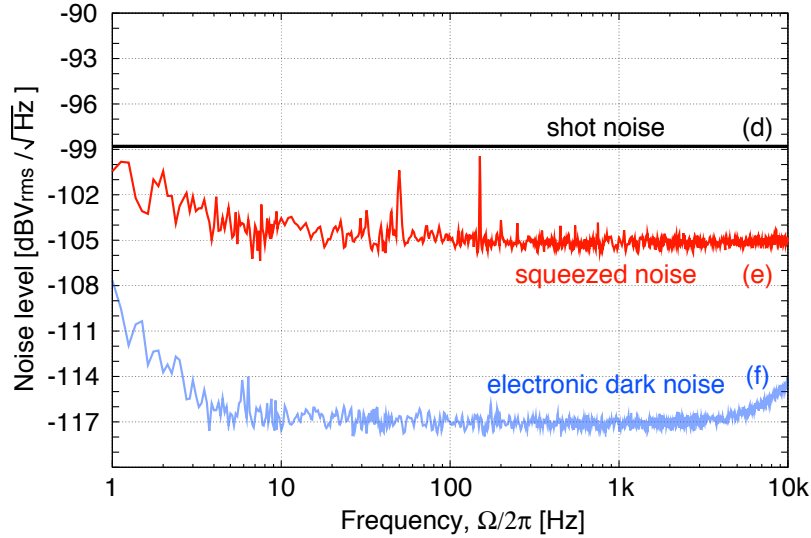


Figure 4.9 — Trace (d) shows the (theoretical) vacuum noise level of our homodyne detector with $464 \mu\text{W}$ local oscillator power as confirmed in Fig. 4.8. Trace (e) shows the noise powers of squeezed states measured with the same local oscillator power. Squeezed vacuum noise was observed throughout the complete spectrum from 1 Hz up to 10 kHz. A nonclassical noise suppression of up to 6.5 dB below vacuum noise was observed here. FFT frequency windows: 1–10 Hz, 10–50 Hz, 50–200 Hz, 200–800 Hz, 800 Hz–3.2 kHz. RBW: 62.5 mHz, 250 mHz, 1 Hz, 2 Hz and 4 Hz. Averages: 30, 100, 100, 400 and 400. The dark noise (f) was not subtracted from the measured data.

squeezed states were coupled out in the counter direction of the injected pump field via a dichroic beamsplitter and were sent to the balanced homodyne detector.

The observed variances of squeezed states between 1 Hz and 10 kHz are presented in Figure 4.9, trace (e). For a significant portion of the spectrum the quantum noise variance was squeezed by an average value of 6.5 dB, i.e. 4.5 times smaller than the vacuum noise variance, trace (d). This value exactly matched the theoretical prediction for our experiment as discussed below. Trace (f) shows the dark-noise contribution of the homodyne detector electronics.

The strength of the observed squeezing was limited by the finite optical parametric gain of the squeezed light source and the total optical loss the squeezed states experienced before (or while) being detected. For the measurements shown in Figure 4.9 a parametric gain of $g = 12 \pm 0.5$ was used which could be achieved with a pump power of 100 mW. Optical losses inside the squeezer, in the propagating beam path and finally in the homodyne detector added up to $l = 0.15 \pm 0.04$. The error bar was mainly due to the uncertainty in the quantum efficiency of the homodyne detector photodiodes (PD1, PD2 in Figure 4.4, model: Epitaxx, ETX500). Both values (g , l) were deduced

from separate measurements. They can be used to estimate the expected strength of squeezing (for Fourier frequencies much smaller than the OPO cavity linewidth) and indeed provide the observed value: $-10 \cdot \log_{10}(l + (1 - l)/g) \approx 6.5$ dB.

Compared with other experiments at audio frequencies, see for example reference [Vahlb06], the squeezing strength reported here has been considerably increased. The improvement was enabled by a spatial mode cleaning cavity in the LO beam path right before the homodyne detector 50/50 beam splitter. With this cavity the spatial overlap, i.e. the interference contrast between LO and signal beam, could be increased up to a fringe visibility of 98.3%.

We note that the squeezed variances shown in Figure 4.9 represent typical results of the setup with high long term stability. With an increased second harmonic pump power the classical OPO gain changed from approximately 12 to 40 ± 4 and up to 7.2 dB of squeezing could be directly observed (7.5 dB when the dark noise was subtracted). In this regime stable operation of the OPO cavity was still possible for several minutes. However, for longer periods thermal fluctuations inside the OPO crystal due to absorption and power fluctuations of the pump beam moved the frequency shift between the fundamental mode and the coherent control beam away from its required value of 1.4 GHz. Long term stable operation with high parametric gain should be possible with an electro-optical stabilization of the second harmonic pump power.

At sub-audio frequencies below 5 Hz, trace (e) shows degraded squeezing strengths. An averaged value of 1.5 dB below vacuum noise was observed at 1 Hz. The degradation was partly due to a rising electronic dark noise level (trace (f)). By subtracting the dark noise, the nonclassical noise suppression recovered to 3.5 ± 0.5 dB which was, however, still significantly lower than 6.5 dB as observed at other frequencies. This degradation was due to remnant parasitic interferences as described in the next Paragraph.

4.6 Parasitic optical interference

The generation and observation of squeezed vacuum states of light at (sub-)audio frequencies, were made possible by a significant reduction of *parasitic interferences*. Parasitic interferences are typically produced by moving surfaces that scatter photons into the low frequency detection band of the homodyne detector as shown below.

Scattered light fields were identified to originate from the micro-roughness of the optical surfaces, non-perfect anti-reflection coatings and residual transmissions of high reflection mirrors. They were partly transmitted through the squeezed light source and

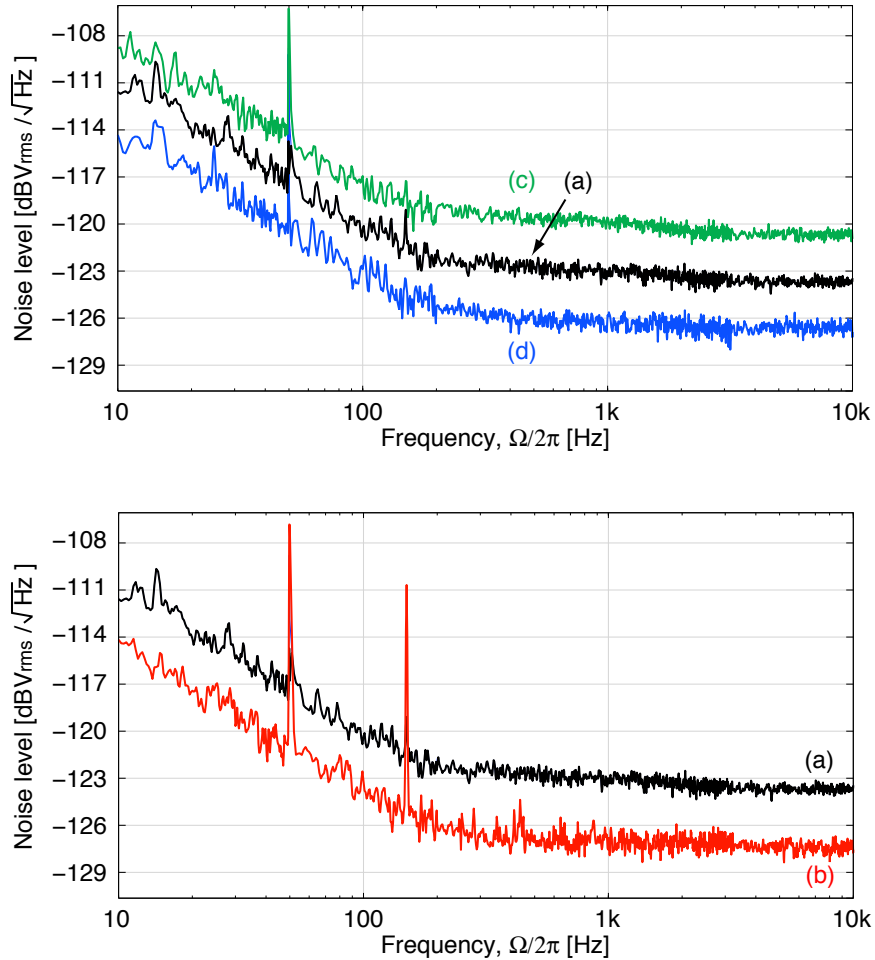


Figure 4.10 — Measured quantum noise spectra corrupted by stray light. Without carefully reduction of scattered light, the white quantum noise spectra show a roll-up below frequencies of approximately 1 kHz. **Top:** Shot noise for three different local oscillator powers, (a) $88\mu\text{W}$, (c) $176\mu\text{W}$, and (d) $44\mu\text{W}$. **Bottom:** (a) Shot noise and (b) squeezed noise with $88\mu\text{W}$ LO power. All traces are pieced together from five FFT frequency windows: 10 Hz-50 Hz, 50 Hz-200 Hz, 200 Hz-800 Hz, 800 Hz-3.2 kHz, and 3.2 kHz-10 kHz. Each point is the averaged rms value of 100, 100, 400, 400 and 800 measurements in the respective ranges. The RBWs of the five windows were 250 mHz, 1 Hz, 2 Hz, 4 Hz and 16 Hz, respectively.

entered our homodyne detector via its signal port. Other scattered fields were found to directly hit the photodiodes of the homodyne detector from other directions. In all cases these fields sensed multiple scattering processes from various optics and optic mounts. The scattering surfaces of these objects continuously moved through thermal expansion and acoustic vibrations. During the scattering processes optical sideband

fields were produced at corresponding Fourier frequencies and higher harmonics.

For any such scattered field which interfered with the homodyne local oscillator the whole setup acted as a sensitive interferometer measuring the motions of the scattering surfaces. These parasitic interferences easily masked the vacuum noise. Given a great number of such sources of scattered light with increasing motion amplitudes towards lower frequencies but low mechanical quality factors, a rather smooth monotonic increase was produced as observed for example in [Vahlb06].

A typical measurement of (squeezed-)vacuum states, which were done without careful shielding of scattered light, is shown in Figure 4.10. As a consequence of stray light effects, a roll-up at frequencies below approximately 1 kHz was measured in the spectra. Note, that these measurements were also done before the implementation of the mode cleaner cavity for the local oscillator beam. Due to a reduced fringe visibility the optical loss was higher for the squeezed beam. This resulted in a reduced squeezing strength.

4.6.1 Potential sources for scattering

Please note, that this squeezing experiment was *not* performed in a clean room ensuring a low density of dust particles. Therefore, additional sources for scattered light apart from the following ones are very likely.

4.6.1.1 Homodyne detector

For the measurement of pure vacuum states only vacuum fluctuations should enter the signal port of the homodyne detector. Unfortunately, this is no longer true if additional photons leak into this port. Scattering, for example, from the homodyne detector photodiodes or non-perfect AR-coatings or dust particles can provide such photons. Additionally, these can also mask the squeezed vacuum states when entering the squeezed light source.

The following list shows the most important issues in our experiment to avoid scattered light.

- Firstly, we removed the protection window from each homodyne Epitaxx ETX500 photodiode. These windows are not, or probably not very efficiently, anti-reflection coated for a wavelength of 1064 nm.
- Usually a high quantum efficiency of the photodetectors is preferred. As a consequence we aligned the homodyne photodiodes under their brewster-angle to raise the quantum efficiency. This also reduced the amount of direct back scattering into the signal port of the homodyne detector and finally helped to

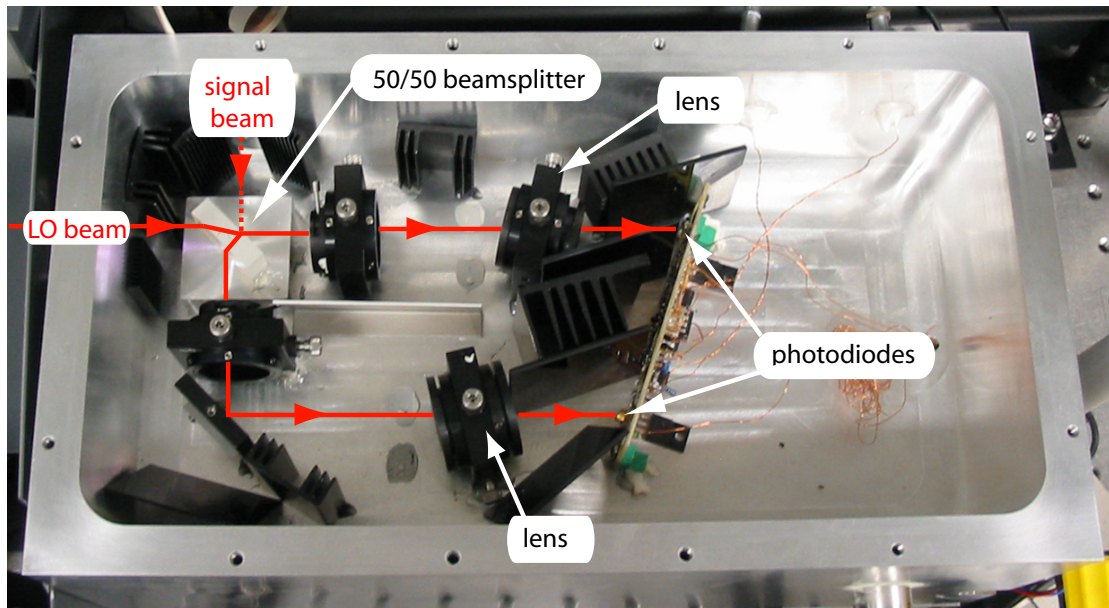


Figure 4.11 — Photograph of the homodyne detector. To avoid stray light all optics were tilted and any residual reflected light was blocked with a combination of black glass filters and black anodized heat sinks. The two Epitaxx ETX500 photodiodes were used without protection windows and were aligned under brewster angle. Finally, the complete homodyne detector setup was shielded against diffuse straylight using an enclosure with only two small ports for the local oscillator and the signal beam.

attenuate the number of photons which are guided towards the squeezed light source.

- The residual light directly reflected from the photodiode surface was carefully dumped using black glass filters. These filters were aligned under their brewster-angle as well. Additionally, black anodized heat sinks made from aluminum were employed to dump remaining light transmitted through the glass filters.
- We used two lenses ($f = 50$ mm) for focusing each output field of the homodyne beamsplitter onto the $500 \mu\text{m}$ ETX500 photo diodes. The anti-reflection coating of the lenses was specified to be better than 0.1 %. Nevertheless, it is advisable to tilt each lens. Again, any residual reflected light was directly blocked with a combination of black glass filters and anodized heat sinks.
- The complete homodyne detector setup was shielded against diffuse stray light illuminating the laboratory using a custom made enclosure with only two small input ports. One port was for the local oscillator beam and the second one was

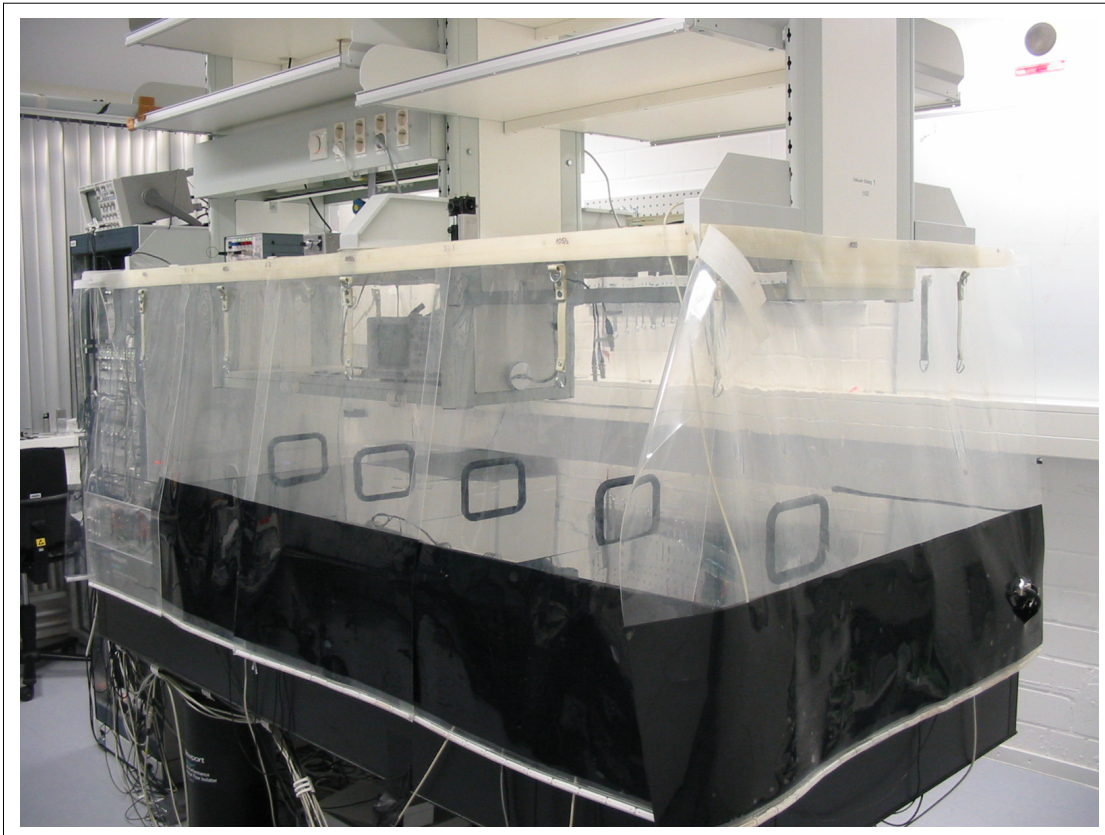


Figure 4.12 — Photograph of the optical table. Using non-transparent coverings the experiment was protected from a „stray-light-background“ which originated from other experiments in the laboratory and the room light, for example.

for the signal input beam. No port-windows were used to avoid any additional scattering. The enclosure contained all optics and electronics necessary for homodyne detection.

A photograph of the homodyne detector setup is shown in Figure 4.11.

4.6.1.2 Frequency shifted control beam

The frequency shifted coherent control beam was generated utilizing an AOM driven at 40 MHz. The angle of divergency, separating the frequency shifted light from the non-frequency shifted one, is proportional to the modulation frequency. Using a frequency of 40 MHz was critical since both beams could hardly be split for the given optical path length. Furthermore, the AOM efficiency is not equal to unity, meaning that not every incoming photon was diverted. Thus, it is very likely that some

remaining – non frequency shifted – infrared photons entered the squeezed light source as stray light. This process can couple high technical laser noise (which is inherent in the infrared laser light at frequency ω_0) into the squeezed light source. This technical noise is than superimposed with the squeezing and can mask the non-classical noise reduction.

4.6.1.3 Green pump beam

Generally, the conversion efficiency of the fundamental 1064 nm field ω_0 into the second harmonic field $2\omega_0$ is in the range of 60-70%. Therefore, some photons at 1064 nm co-propagate with the green pump field, which is injected into the squeezed light source. We used several dichroic beamsplitters to filter out inherent infrared photons in the 532 nm pump field.

4.6.1.4 Lab environment

As a last step, the complete optical table was protected from a „stray-light-background“ which originated from other experiments in the laboratory, the room light and other (unknown) sources. Figure 4.12 shows the non-transparent coverings shielding the experiment.

4.7 Application of squeezed states in a Michelson interferometer

In order to demonstrate how squeezed states can be used to improve high precision optical measurements we performed a table-top experiment according to Figure 4.13. In this experiment the generated squeezed states at audio frequencies were injected into a small Michelson interferometer.

The interferometer had an arm length of 40 mm and was composed of two piezo-mounted flat end mirrors ($R = 99.92\%$). The interferometer laser power was $1.5\ \mu\text{W}$. An error signal for locking the Michelson interferometer to its dark fringe was generated by longitudinal modulation of one end mirror at a frequency of 66 kHz and proper demodulation of the light reflected at the interferometer bright port. A fringe visibility of 99.9% at the 50/50 MI-beamsplitter was achieved. A photograph of the „Mini-Michelson-Interferometer“ is presented in Figure 4.14.

Squeezed vacuum states could be injected into the interferometer's dark port via a polarizing beam splitter and a Faraday rotator, thereby replacing ordinary vacuum states. Since the interferometer was operated at a dark fringe, the (squeezed)

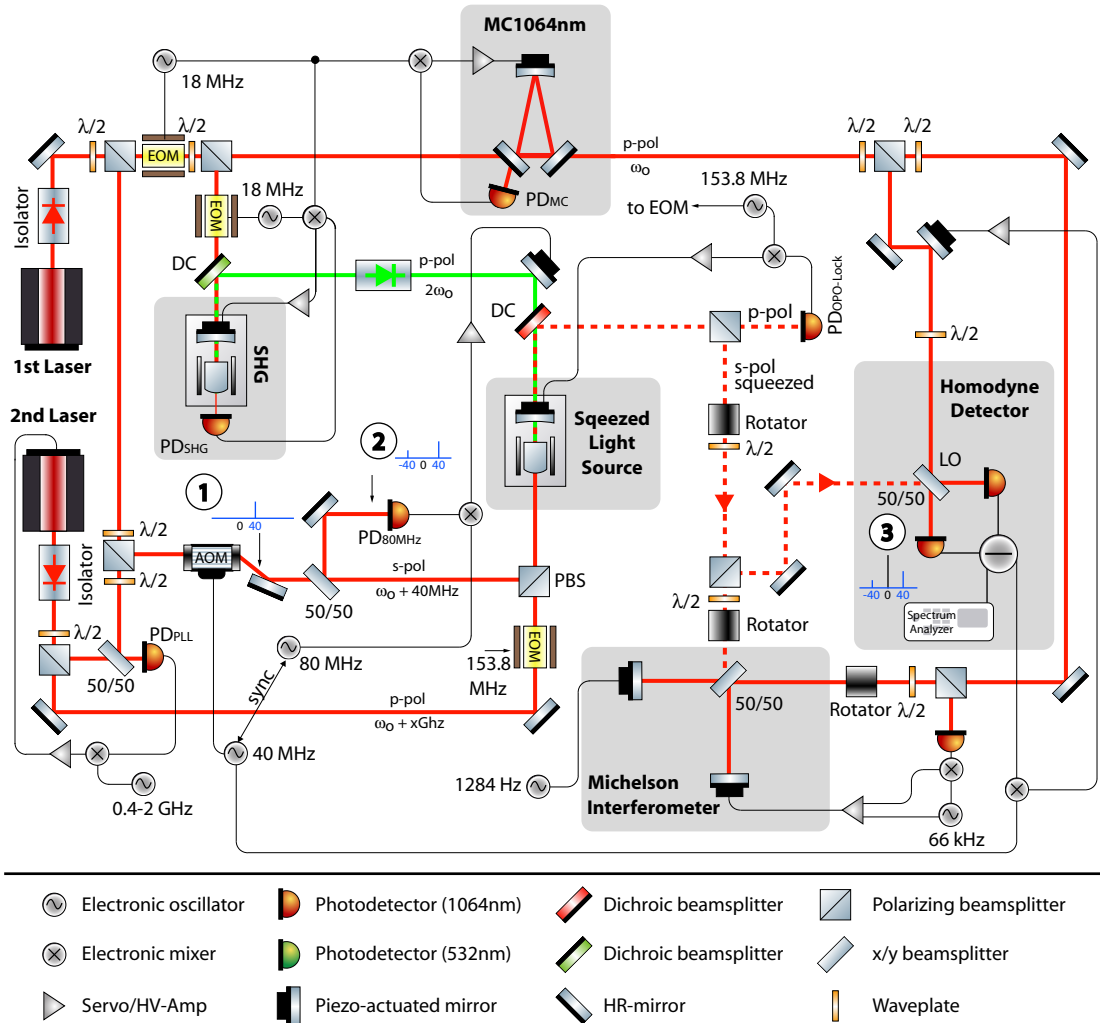


Figure 4.13 — Schematic of the experimental setup for the application of squeezed states in a Michelson interferometer. An interferometer signal at 1284 Hz was artificially generated by dithering one of the interferometer end mirrors.

vacuum noise was reflected and guided towards the homodyne detector together with the interferometer signal. The latter was artificially introduced by continuously dithering one of the interferometer end mirrors at a frequency of 1284 Hz. This frequency represents twice the spin frequency of the prominent millisecond pulsar PSR B1937+21 (PSR J1939+2134) which is the subject of the dedicated search for emission of gravitational waves [Hough83, Aetal05].

The goal of our experiment was to detect the tiny motion of the driven interferometer mirror. For the first measurement the squeezed vacuum input was blocked.

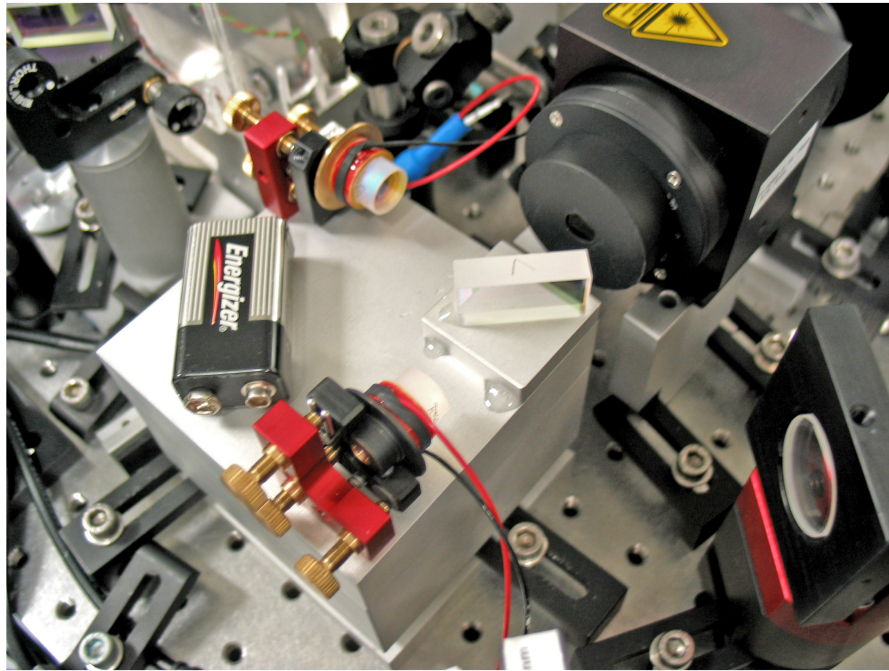


Figure 4.14 — Photograph of the „Mini-Michelson-Interferometer“. In the center of the picture the rectangular 50/50 Michelson beamsplitter can be seen. Both half-inch endmirrors were piezo-actuated. A standard 9 V battery is shown for size comparison.

Hence, the interferometer antisymmetric port was empty, as it is the case for any conventional interferometer. Thus, only vacuum noise entered the measurement device. As shown in trace (a) of Figure 4.15 this vacuum noise completely masked the generated signal. However, *with* the injection of squeezed vacuum states, the quantum noise variance was reduced and the same generated signal amplitude was now clearly visible, as shown in trace (b).

Due to the shorter time scales involved in Figure 4.15 (the measurement time was only a few seconds) an increased parametric gain could be used which resulted in higher initial squeezing of 7.2 dB. This was measured separately before the injection into the Michelson interferometer. Consequently, even with additional optical losses on the squeezed states due to transmissions through the Michelson interferometer and the rotator of about additional 7 %, a non-classical sensitivity improvement of approximately 6.0 dB beyond vacuum noise variance was achieved.

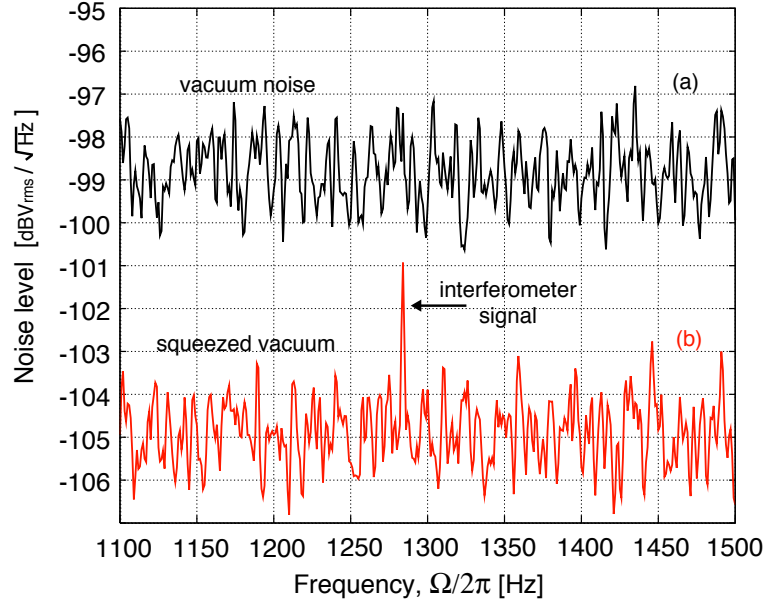


Figure 4.15 — Measurements of the field quadrature variance $\hat{q}_1(\Omega, \Delta\Omega, t)$ in the interferometer's signal output port. When the squeezed vacuum input was blocked, the signal was masked by vacuum noise (a). When squeezed states were injected into the Michelson Interferometer the artificially generated signal at 1284 Hz was clearly visible (b). The vacuum noise variance was squeezed by approximately 6.0 dB.

4.8 Conclusion

In conclusion, we have reported on a new control scheme that allowed stable generation, characterization and application of squeezed fields at audio frequencies. Broadband squeezing in the full gravitational wave detection band and a non-classical interferometer at audio frequencies have been demonstrated for the first time. The coherent control technique reported here provides an important step towards the application of squeezed light in gravitational wave detectors. Based upon our investigations we believe that squeezed states at even lower frequencies with also higher degrees of squeezing can be demonstrated by further protection against parasitic interferences and reduction of optical losses.

Demonstration of a Squeezed Light Enhanced Power- and Signal-recycled Michelson Interferometer

In this Chapter the experimental combination of three advanced interferometer techniques for gravitational wave detection, namely *power-recycling*, *detuned signal-recycling* and *squeezed field injection* is demonstrated. For the first time we experimentally prove the compatibility of especially the latter two. To achieve a broadband non-classical sensitivity improvement we applied a filter cavity for compensation of quadrature rotation. Signal to noise ratio was improved by up to 2.8 dB beyond the coherent state's shot noise. The complete set-up was stably locked for arbitrary times and characterized by injected single-sideband modulation fields. This Chapter refers to the following published papers

- „*Demonstration of a squeezed-light-enhanced power- and signal-recycled Michelson interferometer*“
H.Vahlbruch, S.Chelkowski, B.Hage, A.Franzen, K.Danzmann, and R.Schnabel, *Physical Review Letters*, 95, 211102, (2005).
- „*Squeezed-field injection for gravitational wave interferometers*“
H.Vahlbruch, S.Chelkowski, B.Hage, A.Franzen, K.Danzmann, and R.Schnabel, *Class. Quantum Grav.* 23, S251 - S257, (2006).

5.1 Introduction

Gravitational waves (GWs) have been predicted by Albert Einstein using the theory of general relativity, but so far they have not been observed [Thorne87]. An international array of ground-based, kilometer-scale Michelson interferometers has been set up for their first observation, consisting of GEO 600 [Geo02], LIGO [LIGO], TAMA 300 [TAMA] and VIRGO [Virgo04]. The goal is to measure a gravitational wave induced strain of space-time of the order of 10^{-21} integrated over a bandwidth of a few hundred Hertz at acoustic frequencies. Even for kilometer-scale interferometers the expected signals are that small that several kilowatts of circulating single mode laser radiation are required to push the shot noise below the signal strength. Such high powers cannot be achieved by today's lasers alone. Power-recycling [Dreve83] is an advanced interferometer technique that aims for increased circulating power. Signal-recycling [Meers88] was also invented to improve the signal-to-shot-noise ratio at some detection frequencies. In fact also the injection of squeezed states was first proposed to reduce shot-noise [Caves81]. Later in the 1980s it was realized that squeezed states can also be used to reduce the overall quantum noise in interferometers including radiation pressure noise, thereby beating the standard-quantum-limit [Unruh82, Jaeke90]. Recently it was discovered that at radiation pressure dominated frequencies signal-recycling can also be used to beat the SQL [Buona01]. Gea-Banacloche and Leuchs showed that the techniques of power-recycling and squeezed field injection are fully compatible [GeoBa87]. Chickarmane et al. [Chicka96] found compatibility of signal recycling and squeezed field injection for the shot-noise limited regime. Furthermore the analysis by Harms et al. showed that the same is true for detuned signal-recycling at shot-noise as well as radiation pressure noise dominated frequencies [Harms03] thereby proposing that all the three techniques can simultaneously be used to reduce quantum noise in interferometers.

All of the GW detectors mentioned above use power-recycling, additionally most of them also use arm cavities for further power build up. In both cases additional mirrors form *tuned* cavities. The GEO 600 detector already successfully uses carrier light *detuned* signal-recycling. Signal recycling is established by an additional mirror placed into the interferometer's dark signal port forming a signal tuned cavity. This leads to an optical resonance structure in the interferometer's signal transfer function, whose frequency can be changed and matched to an expected signal, for example emitted by a binary system of two neutron stars or black holes. Signal-recycling in combination with power-recycling is often called dual-recycling and was experimentally demonstrated by Heinzl et al. [Heinze98]. Second-generation detectors currently being planned, for example Advanced LIGO [AdvLi99], are likely to use

this technique. Then in combination with tuned high finesse arm cavities the technique is called resonant sideband extraction [Mizun93, Heinze96]. Squeezed states are envisaged for third generation detectors but so far only a few squeezed light enhanced interferometers have been demonstrated, e.g. table-top Mach-Zehnder and polarization interferometers [Xiao87, Grangi87], respectively. Recently a squeezing enhanced power-recycled Michelson interferometer has been reported already bearing more resemblance to a GW detector [McKen02].

In this letter we report the first power- and signal-recycled Michelson interferometer with broadband sensitivity better than its photon shot-noise. Frequency dependent squeezed light generated in an optical parametric amplifier (OPA) in combination with a detuned filter cavity (FC), as proposed in [Kimbl01], was injected through the signal recycling mirror (SRM) into the interferometer's dark port. The whole setup was stably locked in all its degrees of freedom and characterized by a single-sideband modulation field. Our results generally prove the optical compatibility of the three advanced interferometer techniques described above and also demonstrates a readout and control scheme in which no phase modulation control signals contaminate the detection band.

5.2 Experimental setup

The main laser source of our experiment was a monolithic non-planar Nd:YAG ring laser of 2 W single mode output power at 1064 nm. About 1 W was used for second harmonic generation (SHG) to produce the necessary pump field for the optical parametric amplifier (OPA), see Figure 5.1. The residual beam was transmitted through a mode cleaner ring cavity to reduce laser amplitude noise and spatial fluctuations. The outgoing field was used as a local oscillator for the homodyne detector (50 mW) as well as a seed beam for the OPA (100 mW), filter cavity locking (30 mW) and the Michelson (120 mW). For controlling the OPA cavity length a Pound-Drever-Hall (PDH) locking scheme with a phase modulation sideband frequency of 153.8 MHz was used. The error signal was fed back to the PZT mounted coupling mirror of the hemilithic cavity. A similar locking technique was used for the SHG. Another locking loop stabilized the phase relation between the fundamental and second harmonic field inside the OPA. A more detailed description can be found in [Chelk05]. Locking the OPA to deamplification generates a broadband amplitude quadrature squeezed beam of about 200 μ W at 1064 nm. This beam was then first passed through a Faraday isolator, protecting the OPA from any backscattered light. A $\lambda/4$ -waveplate turned the s-polarized beam into a circularly polarized beam which

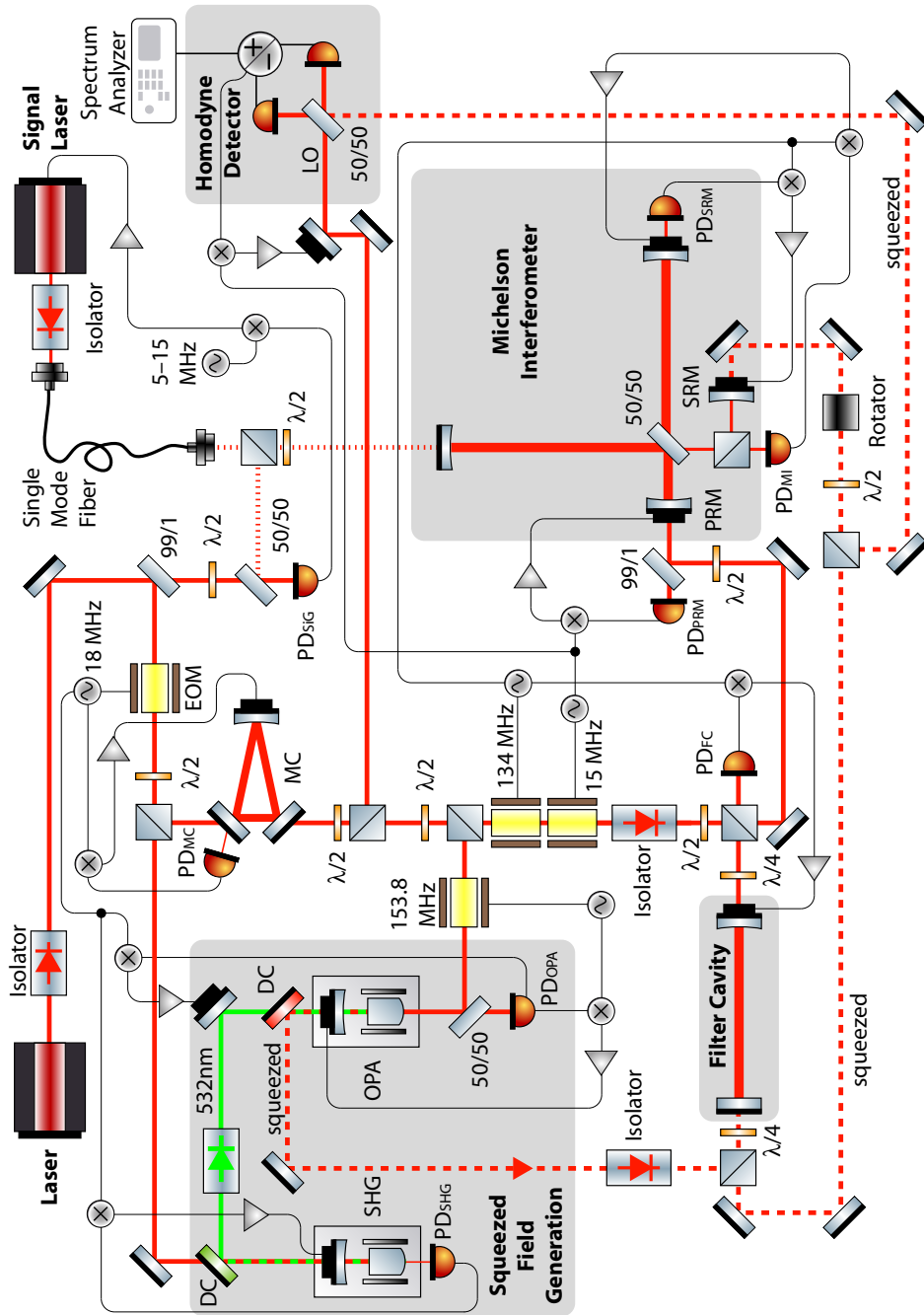


Figure 5.1 — Schematic of the experiment. Amplitude squeezed light is generated in an OPA cavity of controlled length. The detuned filter cavity provides frequency dependent squeezing suitable for a broadband quantum noise reduction of a shot-noise limited dual-recycled Michelson interferometer. SHG: second harmonic generation; OPA: optical parametric amplifier; EOM: electro optical modulator; DC: dichroic mirror; LO: local oscillator; PD: photo diode; MC: mode cleaner; PRM: power recycling mirror; SRM: signal recycling mirror; ■: piezo-electric transducer.

was mode matched into our linear filter cavity (FC). The coupling and end mirrors had reflectivities of 90 % and 99.92 %, respectively. The cavity length was electronically stabilized to about $L=1.21$ m resulting in a free spectral range of 124 MHz. We applied the PDH locking technique utilizing a circularly polarized laser beam that carried 134 MHz phase modulation sidebands and was coupled into the filter cavity from the opposite side. Therefore it was possible to lock the FC stably to a sideband frequency of ± 134 MHz which results in a detuning frequency of ± 10 MHz due to the free spectral range of 124 MHz. This technique avoided unwanted control signals showing up in the detection band. Note that such a signal was present in Figures 3a and 4a of Ref. [Chelk05] at 15 MHz. Locking the filter cavity to either the upper or the lower sideband the squeezed field was then reflected towards the signal recycling mirror of the Michelson interferometer.

The Michelson interferometer was dual recycled; both recycling cavities had lengths of about 1.21 m and the reflectivities of power recycling mirror (PRM) and signal recycling mirror (SRM) were both 90 %, cf. Figure 5.1. The interferometer was stabilized on a dark fringe and the PRM was controlled such that it formed a carrier field resonating cavity together with the two Michelson end mirrors of 99.92 % reflectivity. The finesse of this power recycling cavity (PRC) was measured to 60. The signal recycling cavity that was formed by SRM and the two end mirrors contained no carrier field and could be stably locked to sideband frequencies of ± 10 MHz. All together three electronic control loops were applied to stabilize the interferometer to this operation point utilizing two polarization modes and two modulation frequencies. The phase modulations at 15 MHz and 134 MHz were applied to the carrier field before it entered the interferometer and a $\lambda/2$ -plate in front of the PRM split the incoming beam into 100 mW of s-polarization and 20 mW of p-polarization. The position of the PRM was locked by a PDH technique via the 15 MHz sidebands in the s-polarization. Modulation sidebands at 134 MHz in the s- and p-polarizations were then used to control the dark port and the length of the detuned signal recycling cavity, respectively. The polarization modes were decoupled by a polarizing beam splitter (PBS) that was placed between the 50/50 beamsplitter and the SRM. An arm length difference of the Michelson of 7 mm was sufficient to provide adequate strong error signals.

The squeezed beam from the detuned locked filter cavity was injected into the SRC passing a combination of a PBS, a $\lambda/2$ -plate and a Faraday rotator. This gave spatial degeneracy between the reflected squeezing and the signal output beam of the interferometer. The combined field was guided to a homodyne detector that was built from two electronically and optically matched photodetectors based on Epitaxx ETX1000 photodiodes. All spectra presented in this paper were analyzed in

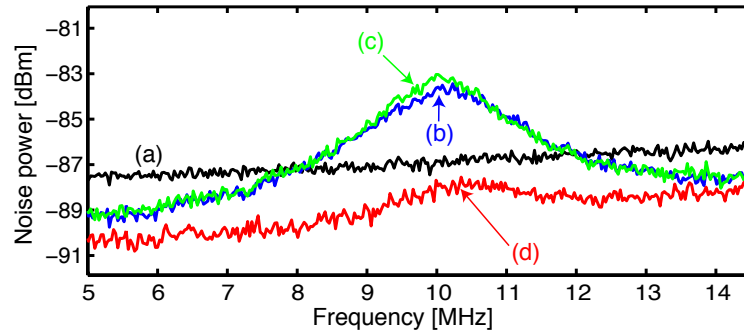


Figure 5.2 — Amplitude quadrature noise power spectra from homodyne detection: (a) shot noise, (b) frequency dependent squeezing after reflection at the +10 MHz detuned signal-recycling cavity (SRC) only, (c) frequency dependent squeezing after reflection at the -10 MHz detuned filter cavity (FC) only and (d) regained broadband squeezed light enhanced performance achieved by reflecting the squeezed light firstly at the FC before it entered the SRC.

a Rohde&Schwarz FSP3 spectrum analyzer with 100 kHz resolution bandwidth and 100 Hz video bandwidth, averaging over 5 subsequent measurements.

The setup described so far facilitate the measurement of the interferometer’s noise transfer function. The measurement of the signal transfer function and therefore the combined signal-to-noise ratio required the generation of a modulation signal of known strength and tunable sideband frequency. We chose to inject a single sideband modulation field into the interferometer, similar in design to [DeVin02]. Such a field is generically different from a phase modulation, for example generated by a gravitational wave. However, it has been shown in [Schna04] that a shot-noise limited signal-recycled interferometer with detuning larger than the SRC bandwidth cannot be significantly improved by frequency dependent homodyning, so-called variational output. The reason is that only a single sideband is supported and injecting a single sideband modulation is therefore a meaningful method to characterize the signal-recycled interferometer. The signal was generated utilizing a second monolithic non-planar Nd:YAG ring laser. This laser was frequency locked to the main laser by a phase lock loop, with tunable beat frequency in the range of 5–15 MHz between both light sources. This signal laser beam was injected through one of the interferometer end mirrors as shown in Figure 5.1.

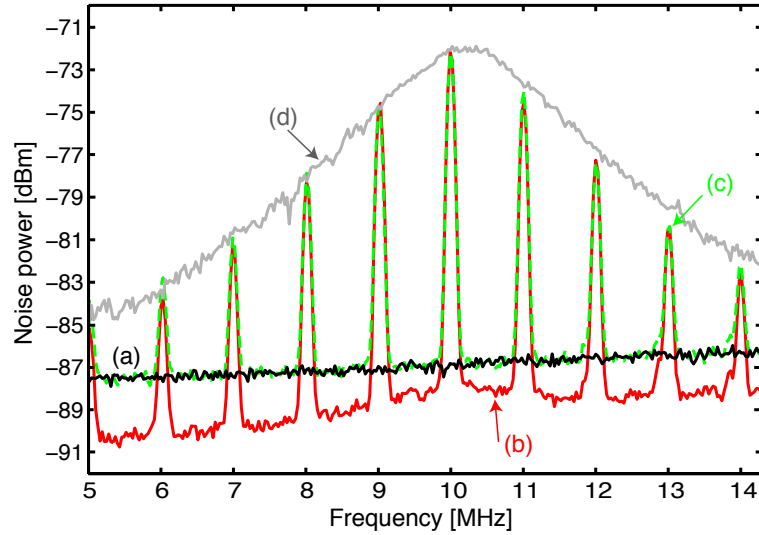


Figure 5.3 — Amplitude quadrature power spectra of the dual recycled Michelson interferometer with and without nonclassical noise reduction. A single sideband modulation was injected at certain frequencies to characterize the signal to noise ratio. (a) Shot-noise measured with a blocked signal beam at the homodyne detector; (b) (dashed line) shot noise limited signals; (c) broadband squeezing enhanced signal-to-noise ratios of up to 2.8 dB below shot-noise. Utilizing the max hold function of the spectrum analyzer the optical transfer function of the SRC was mapped out by continuously sweeping the injected signal (d).

5.3 Results and discussion

Figure 5.2 shows the squeezed light enhanced quantum noise performance of our dual-recycled interferometer. By using frequency dependent squeezed light the quantum noise can be reduced below the shot noise level (a) for all sideband frequencies shown (d). If instead no filter cavity is used the quantum noise is increased at some sideband frequencies (c). This effect is a consequence of a rotation of the field's quadratures when reflected from a detuned cavity [Kimbl01]. While the OPA generated an amplitude squeezed beam the squeezing ellipse is rotated such that antisqueezing is detected around the SRC-detuning frequency by the homodyne detector. This effect has first been observed and characterized in [Chelk05]. The filter cavity compensates this effect while being locked to the same detuning frequency but with opposite sign. The remaining hump around 10 MHz in curve (d) arises from additional losses inside the SRC mainly caused by the PBS. For this reason the squeezing got reduced most

exactly at the detuning frequency.

The mode matchings of the squeezed field into the FC and SRC were 95 % and 97 %, respectively. Additional losses on the squeezing arose from the OPA escape efficiency of 90 %, transmittance of the isolator including double passing the Faraday rotator of 93 %, modematching efficiency at the homodyne detector of 95 % and quantum efficiency of photo diodes of 93 % adding up to an overall efficiency of 65 %. The result was a detected nonclassical noise suppression of 2.8 dB at 5 MHz. The poorer squeezing of about 2.0 dB at 14 MHz was due to the limited bandwidth of the OPA of 20 MHz. In principle the bandwidth can be increased by higher coupler transmission which then in turn requires a higher pump intensity, but since in GW detectors squeezing at acoustic frequencies will apply the OPA bandwidth limitation will not be an issue. We note that all measured spectra were at least 5 dB above the detection dark noise which was taken into account.

Figure 5.3 demonstrates the squeezing enhanced signal to noise ratio of single sideband signals. The Michelson interferometer was stably locked with +10 MHz detuned signal-recycling cavity, while a single sideband was subsequently injected at ten different sideband frequencies and the spectra were measured with and without frequency dependent squeezed field injection. The experimental results show an increase of the SNR over the whole detection bandwidth. In comparison with the shot noise limited signals (c) the SNR was improved by up to 2.8 dB into the nonclassical regime (b).

5.4 Conclusion

In conclusion we have experimentally demonstrated the compatibility of power-recycling, carrier detuned signal-recycling, and squeezed field injection. Broadband nonclassical noise suppression was achieved by employing a detuned filter cavity for compensation of quadrature rotation. The optical layout of our demonstration experiment can directly be applied to improve the sensitivity of large scale signal-recycled interferometers at their shot-noise limited detection frequencies, typically above 1 kHz. The scheme demonstrated also directly applies to the shot-noise limited resonant-sideband extraction topology which is planned for the Advanced LIGO detector (LIGO II) [AdvLi99]. Then the filter cavity needs to be adapted to compensate for the quadrature rotation due to the RSE cavity [Harms03].

After applying classical noise suppression to enable squeezing in the GW band as demonstrated in [McKen04] our squeezed light source would be directly applicable to all current and probably next generation detectors since the same laser wavelength

is used. Future detectors are also expected to be quantum noise limited at lower frequencies due to back-action noise (radiation-pressure-noise). Then the demonstrated experiment can also provide a broadband nonclassical sensitivity improvement if additional filter cavities are used. Then if the initial power- and signal-recycled interferometer is already at the standard-quantum-limit, squeezed field injection can provide QND performance [Harms03, Kimbl01, Buona04]. In our experiment we chose a homodyne readout with external local oscillator. This is in accordance with theoretical investigations that considered a readout scheme that can switch between arbitrary quadrature angles [Buona01, Harms03]. Such a local oscillator might be generated in a large scale GW detector from an unused reflection from the beam splitter anti-reflection coating. We believe that a realistic goal for future GW detectors is a 6 dB improvement of power noise spectral density. This requires the generation of 10 dB squeezed field at detection frequencies and an overall loss of less than 17 %. A detailed estimation of expected individual loss contributions in squeezing enhanced GW detectors will be presented elsewhere [Vahlb05]. However, if loss contributions due to the signal-recycling cavity or the filter cavity lead to an overall loss higher than that, only the performance at the optical resonance is degraded from the 6 dB goal. The performance at neighbouring detection frequencies is then unaffected providing an improved detection bandwidth.

Conceptual Squeezer-design for GEO 600

Most squeezing experiments performed in the field of quantum optics or quantum communication are not explicitly designed for long term stable operations. In general, measurements involving squeezed states only last for a few minutes. However, in order to retain the high duty cycle of gravitational wave detectors a significant higher stability time of a squeezed light source is required.

Some years ago this demand was unrealistic, but the technology of squeezed vacuum generation has progressed rapidly over the past few years and recent low-frequency squeezing experiments have made an important step towards reliable long term operation [Vahlb06, Vahlb07]. Therefore, it is planned to inject squeezed vacuum states into the GEO 600 GW-detector in the year 2009 and only 2 years later the LIGO H1 detector is proposed to surpass the shot noise limit by using squeezed states.

In this Chapter, the conceptual design of a squeezed light source for the GEO 600 GW-detector is presented. Parts of this concept will also be adapted to the LIGO H1-Squeezer design.

It is planned that before being handed out to the GEO 600 site, the complete squeezing experiment will be set up on a custom made breadboard in the clean rooms at the AEI, Hannover. Here, everything will be assembled and initially aligned. Furthermore, an analog control system will be set up for comprehensive electronic stabilization. Finally, after characterization of the experiment, the control scheme is planned to be automated step by step via a real time Linux system. The EPICS (Experimental Physics and Industrial Control System) system will be used for remote control of analog electronics and for data acquisition. Additionally, investigations will be made whether the analog control loops can also be digitalized without degrading

the performance of the squeezing experiment.

In this Chapter the optical layout of the squeezing experiment is presented and requirements for the digital data acquisition system are given. Furthermore, the most appropriate injection port for squeezed vacuum states into the GEO 600 interferometer is discussed.

6.1 Optical GEO 600 squeezer setup

The optical setup is based on the experience gained in the low-frequency squeezing experiment, as described in Chapter 4. Some parts of this experiment were adopted, others have been revised and improved.

In Figure 6.1 a sketch of the general optical setup for the GEO-squeezing experiment is presented. For clarity reasons optics like lenses, wave plates and steering mirrors e.g. were neglected as well as some electronics. The latter topic is addressed in Section 6.3, separately.

6.1.1 Laser preparation stage

For the generation and coherent control of the squeezed vacuum four laser frequencies are required:

- The main laser source at frequency ω_0 , which is frequency locked to the GEO 600 laser source. This main laser (2 W Nd:YAG NPRO, Mephisto, made by Innolight) [Inno] provides the input field for the second harmonic generator and also serves as a local oscillator beam for homodyne detection of the generated squeezed vacuum field. Additionally, a small fraction of this laser beam can be used for the initial alignment of the squeezed light source cavity.
- The main laser frequency is doubled employing a second harmonic generator (SHG). This SHG will produce the necessary pump field for the squeezed light source at the frequency $2\omega_0$. The design of the SHG is planned to be identical to the one already presented in Chapter 3.3.1.
- A second NPRO-laser source (200 mW, Innolight Mephisto OEM Product Line), which is frequency locked to the main laser on the squeezing breadboard, will be used for the cavity length control of the squeezed light source. Using the orthogonal polarization (p-pol.) for locking the cavity length no technical laser noise is introduced to the squeezed beam. Due to the birefringence of the nonlinear crystal inside the squeezed light source, however, this coherent

control beam has to be frequency shifted to be simultaneously resonant with the generated s-polarized squeezed field. Depending on the nonlinear material ($\text{MgO}:\text{LiNbO}_3$ or PPKTP) the frequency offset is supposed to be in the range of 500 - 1500 MHz.

- A third NPRO-laser (again with an output power of 200 mW) will be used for the coherent control of the squeezing ellipse orientation with respect to the diagnostic homodyne detector. This auxiliary laser also has to be frequency locked to the main laser. After the commissioning phase of the squeezing experiment, this coherent control field will be finally used to stabilize the phase relation between the squeezed vacuum field and the GEO 600 interferometer signal output field. Furthermore, this coherent control field will be used to set up an auto alignment system for the squeezed beam into the interferometer.

Using this third laser source instead of an AOM (as described in Chapter 4) to generate the control field offers two important advantages. Firstly, this setup provides a high flexibility for choosing the offset-frequency and secondly the substitution of the AOM will rule out stray light problems as reported in Chapter 4.6.

6.1.2 Squeezed light source design

The squeezed light source will be set up as a linear hemilithic cavity consisting of a HR-coated nonlinear crystal surface and an additional piezo-actuated external out-coupling mirror. The single resonant cavity will have a Finesse of approximately 75 at 1064 nm. The nonlinear material can be chosen from $\text{MgO}:\text{LiNbO}_3$ with 7 % doping, which shows good performance as presented in Chapter 4. But, nevertheless, periodic poled KTP (PPKTP) seems to be also a very promising material [Goda07]. One major advantage of this material is the four times smaller absorption at 532 nm, which reduces the influence of the non-intensity stabilized green pump field to the required PLL-2 offset frequency (see Chapter 6.1.2.3). Furthermore, the phase matching temperature range for PPKTP is approximately 5 K wide, whereas a $\text{MgO}:\text{LiNbO}_3$ -crystal has to be temperature stabilized within some mK interval.

In the following the purpose of the four different laser fields, which will be injected into the squeezed light source, are discussed in more detail.

6.1.2.1 Pump field at frequency $2\omega_0$

This beam is required to initiate the parametric down-conversion process inside the squeezed light source. About 100 mW pump power will be necessary to achieve

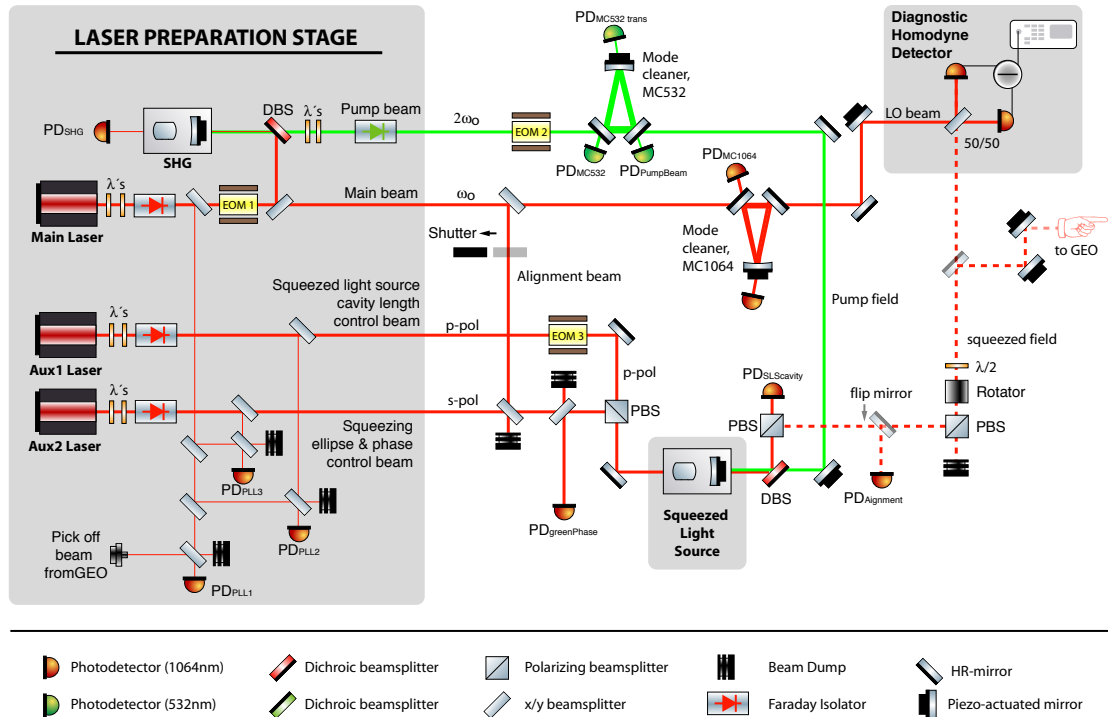


Figure 6.1 — Schematic of the general optical setup for the GEO squeezing experiment utilizing four continuous wave laser beams. Squeezed states at low Fourier frequencies around the carrier frequency ω_0 were produced inside the squeezed light source via the parametric down-conversion process (initiated inside a birefringent nonlinear crystal by pumping the system with a green laser beam at 532 nm). Two auxiliary laser beams are also focussed into the crystal. They serve as control beams for piezo-electric length control of the cavity and phase control of the green light. The fourth laser beam at 1064 nm is used as the local oscillator (LO) to observe the squeezed states using balanced homodyne detection.

sufficiently high parametric gain. After being generated in the SHG, the pump field is guided to a ring-cavity. This mode cleaner will have the same specifications as the one described in Chapter 3.3.2. The purpose of this cavity is to attenuate high frequency phase noise, which is inherent on the green beam due to RF-phase-modulation used for locking the SHG cavity length. It has been shown that phase noise on the green pump beam can deteriorate the squeezing strength. Utilizing the photodiode PD_{MC532} an error signal for the cavity length control can be generated via the Pound-Drever-Hall technique.

6.1.2.2 Alignment beam at frequency ω_0

Temporarily a phase modulated infrared alignment beam at frequency ω_0 will be injected into the squeezed light source. During the assembling phase of the squeezing experiment this field can be used to align the squeezed light source cavity. Once this is adjusted, the cavity length can be stabilized using the light transmitted through the resonator, which is detected on the photodiode $PD_{\text{Alignment}}$ (see Figure 6.1). After demodulation the obtained error signal can be fed back onto the piezo-actuated cavity out-coupling mirror.

If an intense alignment beam (about 100 mW) is injected into the squeezed light source, sufficient amounts of infrared photons at 1064 nm are frequency doubled in order to align the green pump path in the counter direction comfortably. This counter propagating green field can be monitored with either the photodiode PD_{PumpBeam} or $PD_{\text{MC532trans}}$. This procedure offers an ideal alignment of the green pump field, which could otherwise only be adjusted by monitoring the parametric gain inside the squeezed light source, which is quite imprecise. Nevertheless, the parametric gain can be alternatively monitored by using the DC-output of the photodetector $PD_{\text{Alignment}}$.

Please note that during the use of this alignment beam only squeezed states at Fourier frequencies in the MHz regime can be generated due to the technical laser noise carried with this beam at lower Fourier frequencies. Therefore, the alignment beam has to be switched off after the described alignment procedure. It is recommended to avoid any stray light, which is potentially introduced by this required beam dump.

6.1.2.3 Squeezed light source cavity length control beam

For the final cavity length stabilization of the squeezed light source (SLS) the alignment beam will be substituted by a frequency shifted and orthogonally polarized infrared field. This cavity control beam is provided by one of the frequency locked auxiliary NPRO-lasers and is phase modulated before the injection into the squeezer using an EOM. A polarizing beam splitter is placed in the outgoing squeezing path separating the s-polarized squeezed beam from the p-polarized control beam. The latter can be detected with the photodiode $PD_{\text{SLScavity}}$. After proper demodulation at the EOM-modulation frequency, the error signal can be fed back onto the piezo-driven squeezed light source out-coupling mirror.

To ensure that both polarizations are simultaneously resonant inside the cavity, the offset frequency between the two polarizations has to be determined. This can be measured while injecting both, the alignment beam at frequency ω_0 and the frequency shifted cavity length control beam. While scanning the cavity length,

both orthogonally polarized TEM_{00} Airy-peaks must overlap. For metering the simultaneously resonant Airy-peaks the photodetector $PD_{\text{Alignment}}$ can be used again.

6.1.2.4 Squeezing ellipse and phase control beam

As introduced in Chapter 4 a frequency shifted infrared control beam sensing the nonlinear process will be injected into the squeezed light source. Though it has the same polarization as the squeezed vacuum field, the squeezing spectrum is not affected by this control beam due to the frequency offset. Generally, the offset frequency can be chosen over a wide range. The lower limit is given by the claim that no additional laser noise from this control beam should crosstalk into the squeezed beam (approx. 5 MHz), while the upper limit is determined by the SLS-cavity linewidth.

The exact offset frequency has to be matched to the particular experiment. With respect to the GEO 600 GW-detector, the offset frequency has to be adapted to the free spectral range of the signal-recycling cavity, since the control field has to be anti-resonant inside this cavity.

Once the offset frequency is determined, two locking loops have to be set up for a full coherent control of the squeezed vacuum beam. The first loop will stabilize the relative phase between the injected control beam and the green pump field. For this purpose, an error signal can be created by detecting a fraction of the (frequency shifted) light, which is back-reflected from the squeezed light source. Thus the photocurrent of the photodetector $PD_{\text{GreenPhase}}$ has to be demodulated at *twice* the offset frequency (see Chapter 4). The feedback is applied to a phase shifter device placed in the green pump path.

A second control loop has to be set up in order to stabilize the phase relation between the squeezed vacuum field and the local oscillator beam of a homodyne detector. The latter is used for the spectral characterization of the squeezed states. This locking loop is especially important during the assembling and commissioning phase of the experiment. A proper error signal can be extracted from the subtracted photocurrents of both homodyne photo diodes via demodulation at the offset frequency of coherent control beam. A phase shifter device in the local oscillator beam path is used for actuation.

Eventually, when squeezed vacuum states will be injected into the gravitational wave detector, an additional locking loop is required to control the phase (and alignment) between the squeezed states and the GW-detector output signal field coming from the interferometer's antisymmetric port. At first it might be preferable to operate the diagnostic homodyne detector on the squeezing breadboard simultaneously, for a permanent monitor detection of some percentage of the squeezed beam. This squeezing split off can be realized either with an inserted beamsplitter (with a fixed ratio)

or with a combination of a motorized $\lambda/2$ waveplate and a polarizing beam splitter, offering a variable splitting ratio.

Before being injected into the GW-detector via a Faraday Rotator, the squeezed field has to pass phase shifter actuators. It is recommended to decouple these actuators from the actuators used for the homodyne local oscillator field by placing them between the „squeezing beamsplitter“ and the Faraday Rotator.

6.1.3 Diagnostic homodyne detector

The homodyne detector will consist of a polarization dependent 50/50 beamsplitter and two lenses for focusing the beamsplitter output fields onto two photodetectors. In order to achieve a high fringe visibility between the squeezed beam and the local oscillator beam, the latter one will be spatially filtered by means of a mode cleaner ring cavity (MC₁₀₆₄). This cavity will be held on resonance using the phase modulation imprinted by EOM-1 (see Figure 6.1) and subsequent Pound-Drever-Hall locking technique. The error signal feedback is applied to the mode cleaner piezo actuator. The optical layout of the mode cleaner will be comparable to the mode cleaner already employed in the green pump beam.

As discussed in Chapter 4, the homodyne detector optics have to be set up very carefully to ensure that no stray light will enter the signal port of this detector. Hence, baffles for optical shielding and efficient beam blockers are recommended throughout the setup. Additionally, a custom made non-transparent enclosure is intended for optical isolation of the homodyne detector from other parts of the squeezing experiment.

6.2 The GEO 600 squeezer breadboard design

According to the general optical setup as proposed in the previous Chapters, a detailed sketch of the GEO 600 squeezer breadboard layout is shown in Figure 6.2. The custom made breadboard has the dimensions of 135 cm x 113 cm and was made by TMC [TMC]. A thickness of two inch in combination with a steel bottom plate and an aluminum top plate and inner structure guarantees a high mechanical stability at a reasonable weight (approximately 70 kg). The dimensions of the breadboard were adapted to the available space on the GEO 600 detection bench, where the squeezing breadboard will be set up. The assembled squeezer will have an overall weight of approximately 130 kg.

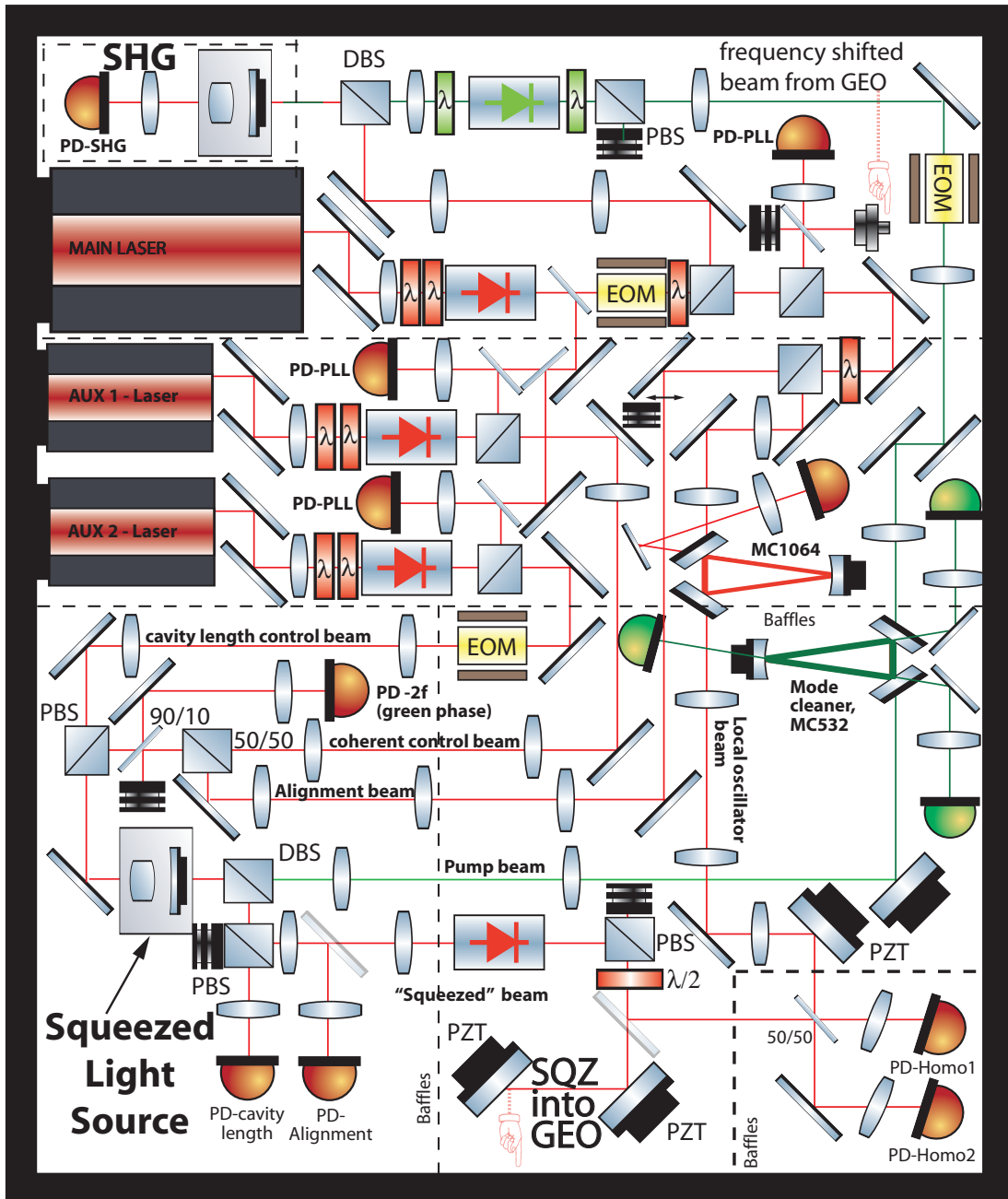


Figure 6.2 — GEO 600 squeezing breadboard layout. The dimensions are 135 cm x 113 cm. A non-transparent box will shield the experiment against stray light. Additionally, baffles will be used inside the setup for further protection. Most components are to scale. The total weight will be approximately 130 kg.

6.3 Control electronics

In the following Chapter the electronic control scheme of the squeezing breadboard is presented. Each experimental section is discussed in detail and an analog scheme with digital remote control and monitor channels is proposed. This Chapter is structured according to the optical alignment sequence of the squeezer setup.

6.3.1 Second harmonic generator control

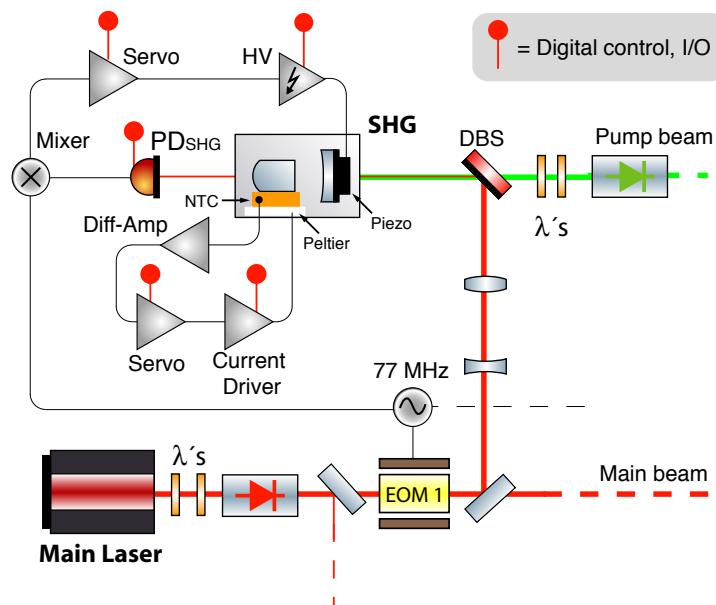


Figure 6.3 — Illustration of the second harmonic generator (SHG) electronic setup. The infrared input field is phase modulated at 77 MHz for cavity length control via PDH locking technique. The optimal phase matching temperature for the nonlinear crystal is regulated via a stabilization circuit.

The second harmonic generation stage requires two independent locking loops. First the crystal temperature has to be stabilized for an efficient conversion process (phase matching condition). As described in Chapter 3.3.1 this control loop is composed of an NTC-thermistor, whose value is compared to the set point in the differential amplifier, servo electronics, a peltier driver stage and finally the peltier itself. Assuming that the non linear crystal will be made from PPKTP, offering a phase matching temperature range of about 5K, it is sufficient to only digitally sample the error point of this control loop for monitoring the long term stability instead of digital

servo remote control. In addition one can think of monitoring the output current of the peltier driver stage with a separate channel.

The second control loop required is the SHG cavity length control loop. Using the Pound-Drever-Hall locking technique, the infrared light experiences a phase modulation via an EOM (driven at 77 MHz) before the injection into the SHG. As shown in Figure 6.3 a fraction of the transmitted infrared light is detected (PD_{SHG}) and demodulated. The offset corrected error signal is processed inside the analog servo before it is fed back onto the piezo-element passing a high-voltage amplifier. For automation of lock acquisition slow digital control of the offset, gain, sign, integrator and ramp is required. Furthermore, the DC-level of the photodetector PD_{SHG} , the error signal as well as the PZT feedback signal are involved in lock acquisition and monitoring. In Table 6.1 a channel list for a digital control of the second harmonic generator is shown.

SHG temperature controller			
Component / Signal	Bandwidth	Purpose	Converter
Error point	slow	monitor	A/D
Peltier current	slow	monitor	A/D
SHG cavity length control			
Component / Signal	Bandwidth	Purpose	Converter
Error signal	fast	monitor	A/D
PD_{SHG} DC level	slow	monitor	A/D
PZT HV	slow	monitor	A/D
Offset	slow	control	D/A
Gain	slow	control	D/A
Integrator	slow	control	TTL or D/A
Sign	slow	control	TTL or D/A
Ramp on/off	slow	control	TTL or D/A

Table 6.1 — Channel list for a digital remote control of the second harmonic generator setup.

6.3.2 Mode cleaner cavity for the green pump beam at frequency $2\omega_0$

Figure 6.4 presents the required electronics for the green mode cleaner (MC_{532}) length control loop. Utilizing an EOM with a modulation frequency of 119 MHz the light at 532 nm is phase modulated before it is injected into the mode cleaner. A resonant photodetector (PD_{MC532}) is placed in the reflection port of the cavity and is used for

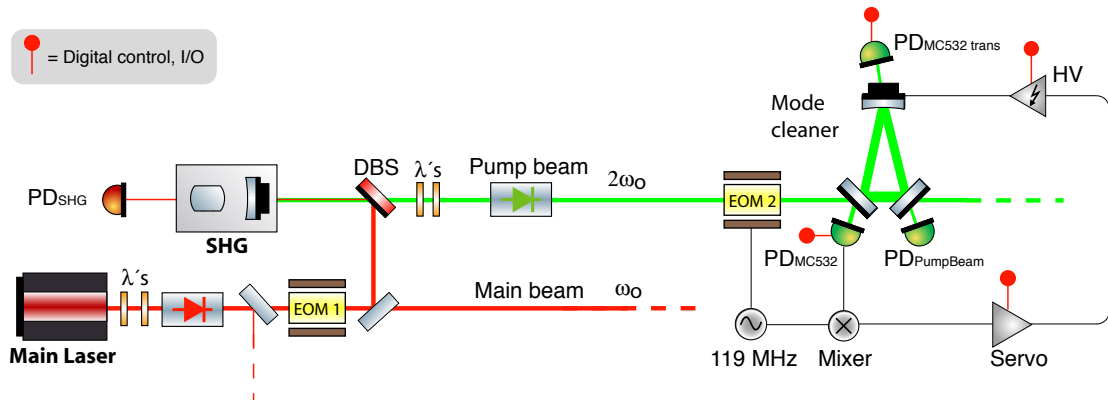


Figure 6.4 — Detailed schematic of the required electronics for the mode cleaner cavity length control loop. An electro optical modulator (EOM 2) imprints a phase modulation at 119 MHz on the green beam ($2\omega_0$). The Pound-Drever-Hall technique is used to hold the ring cavity on resonance.

the error signal generation, while the DC-output of this detector can be used for light intensity monitoring. The error signal processing is comparable to the scheme already described in Chapter 6.3. An out-of-loop photodetector ($PD_{MC532trans}$) can be used for monitoring the intra cavity light intensity independently. Table 6.2 summarizes the for an automated lock acquisition required digital I/O channels.

532 nm mode cleaner cavity length control			
Component / Signal	Bandwidth	Purpose	Converter
Error signal	fast	monitor	A/D
PD_{MC532} DC level	slow	monitor	A/D
PZT HV	slow	monitor	A/D
Offset	slow	control	D/A
Gain	slow	control	D/A
Integrator	slow	control	TTL or D/A
Sign	slow	control	TTL or D/A
Ramp on/off	slow	control	TTL or D/A
$PD_{MC532trans}$ DC level	slow	monitor	A/D

Table 6.2 — Required digital I/O channels for remote controlling the analog MC_{532} cavity length control locking loop.

6.3.3 Squeezed light source and coherent control fields

6.3.3.1 Alignment beam at frequency ω_0

This alignment beam at ω_0 is injected for the adjustment of the green pump path at $2\omega_0$. As previously shown, infrared photons will be frequency doubled and counter propagate the pump beam path. This comfortable alignment procedure requires the squeezed light source cavity length to be stabilized as well as the nonlinear crystal temperature to be controlled. These two Figure loops are comparable to the SHG-setup, as described in Chapter 6.3. For a second time the phase modulation at 77 MHz is used for the Pound-Drever-Hall technique. Using the RF-signal from the photodetector $PD_{\text{Alignment}}$ for demodulation a locking loop can be set up. An electronic block-diagram is presented in Figure 6.5. Since the alignment beam is

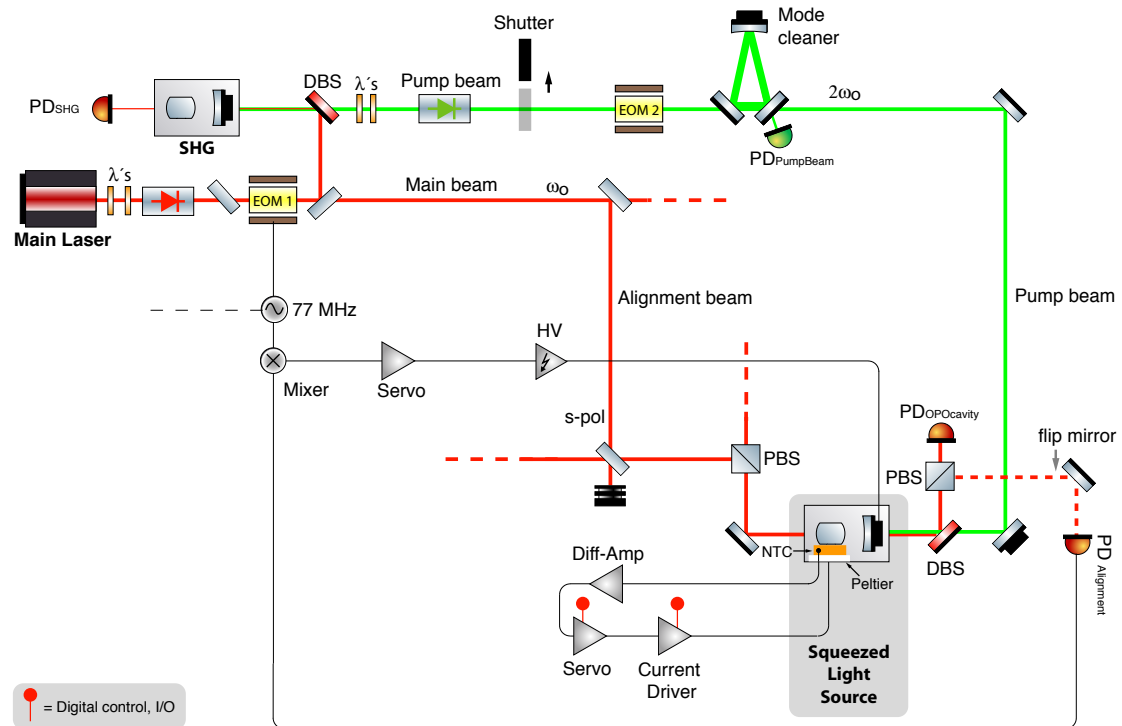


Figure 6.5 — Schematic of the squeezed light source cavity length control loop via the alignment beam at ω_0 . Again the phase modulation at 77 MHz is used for the Pound-Drever-Hall technique. The photons which are converted inside the squeezed light source from the wavelength at 1064 nm to the doubled at 532 nm, can be used for the alignment of the pump field path. Hence, a photodetector PD_{PumpBeam} is placed at a reflection port of the green mode cleaner cavity. The nonlinear crystal inside the squeezer will be temperature stabilized using an additional analog control circuit.

Squeezed light source temperature controller			
Component / Signal	Bandwidth	Purpose	Converter
Error point	slow	monitor	A/D
Peltier current	slow	monitor	A/D

Table 6.3 — Required Digital I/O channels for the squeezed light source crystal temperature stabilization scheme.

exclusively used for optical adjustments, an automated lock acquisition seems not to be necessary, whereas a digital monitoring of the temperature controller error point and peltier current is of a far greater importance. In Table 6.3 the required digital channels are itemized.

6.3.3.2 Auxiliary Laser 1 phase locking loop and SLS cavity length control beam

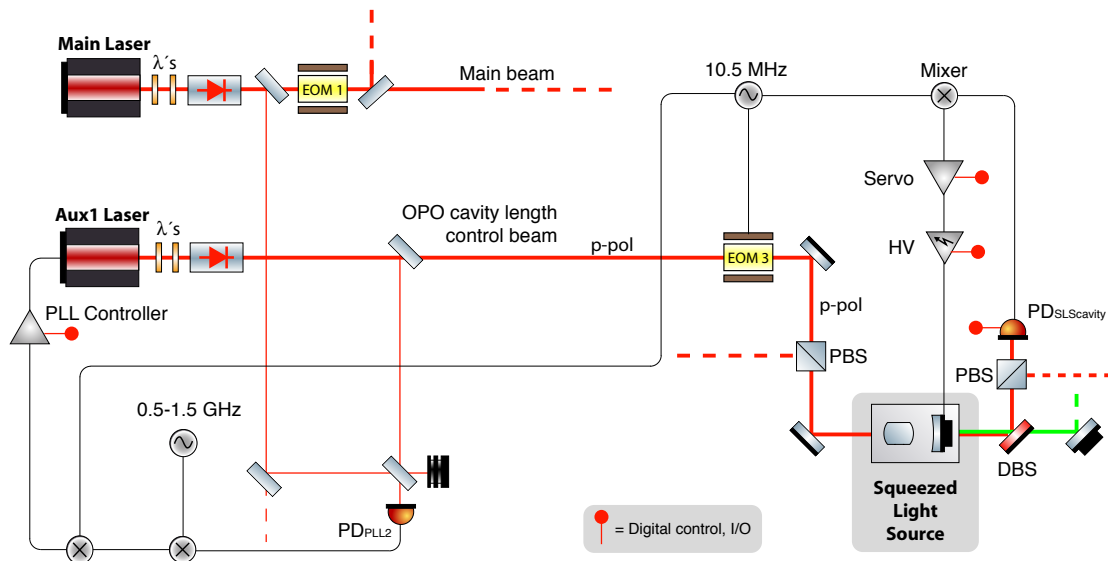


Figure 6.6 — Schematic of the squeezed light source cavity length control loop suitable for the generation of squeezed states in the audio frequency band. This locking loop requires a frequency shifted and orthogonally polarized coherent control, which is provided by an auxiliary laser (Aux1 Laser). This field is phase modulated at 10.5 MHz for the PDH locking technique. A polarizing beam splitter separates this control field from the squeezed beam.

For the generation of squeezed vacuum states in the acoustic frequency band

Auxiliary Laser 1, phase locking loop			
Component / Signal	Bandwidth	Purpose	Converter
Error point	fast	monitor	A/D
PZT feedback	fast	monitor	A/D
Peltier feedback	slow	monitor	A/D
PLL-status	slow / TTL	monitor	A/D
Status reset	slow / TTL	control	D/A
Coherent squeezer cavity length control loop			
Component / Signal	Bandwidth	Purpose	Converter
Error signal	fast	monitor	A/D
PD _{OPOcavity} DC level	slow	monitor	A/D
PZT HV	slow	monitor	A/D
Offset	slow	control	D/A
Gain	slow	control	D/A
Integrator	slow	control	TTL or D/A
Sign	slow	control	TTL or D/A
Ramp on/off	slow	control	TTL or D/A

Table 6.4 — Channel list for digital remote control of the squeezer cavity length control loop and the Auxiliary Laser 1 phase locking loop.

(instead of the squeezing in the MHz regime), the alignment beam must be substituted by an orthogonally polarized and frequency shifted coherent control beam, enabling the squeezed light source cavity length control.

This beam originates from the Auxiliary Laser 1 (Aux1 Laser). The frequency offset, compared to the main laser, will be stabilized via an automated phase locking loop controller circuit [Inno]: The photodetector PD_{PLL2} detects the optical beat signal which is subsequently mixed down with an externally set frequency signal provided by an electronic local oscillator (500-1500 MHz). In a second step this down-converted signal is used for locking the signal to an internal 6 MHz frequency reference (conventionally integrated inside the PLL controller). Please note, that this means that the PLL controller locks the laser beat-frequency to the sum of an externally tunable beat frequency setting plus an internally fixed 6 MHz reference frequency. For an improved long term stability it is recommended to substitute the free drifting internal 6 MHz frequency reference (quarz oscillator) by an externally frequency locked reference signal. For this purpose a copy of the already implemented 10.5 MHz oscillator can be used, as illustrated in Figure 6.6. The output signals of the

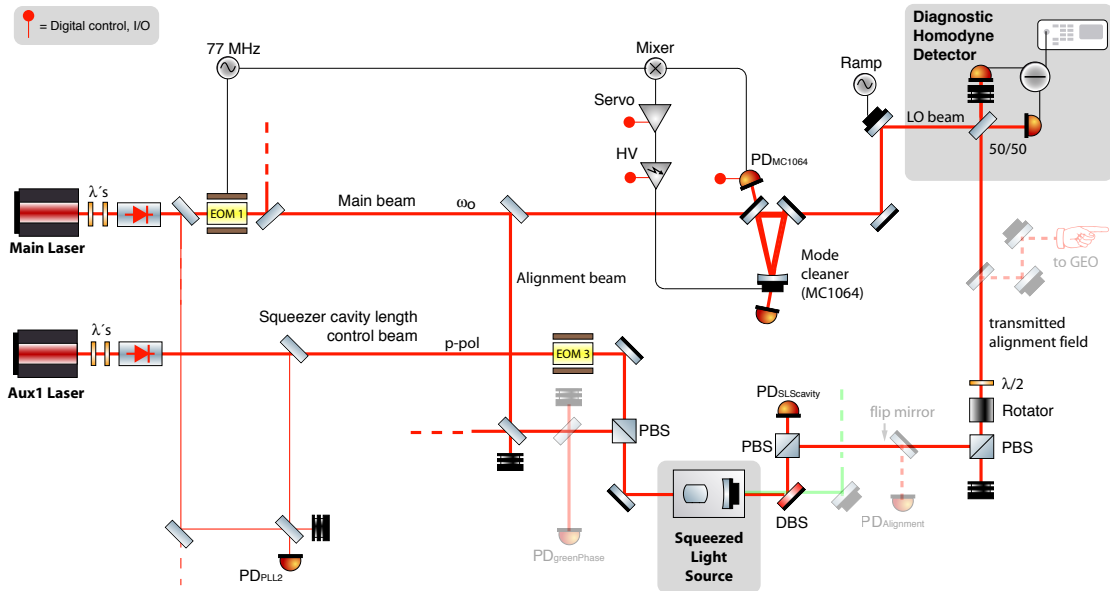


Figure 6.7 — Schematic of the locking loop for the mode cleaner ring cavity (MC1064) placed in the local oscillator beam. For a third time the phase modulation at 77 MHz is used for the Pound-Drever-Hall locking technique.

PLL controller are optimized for the slow and fast laser frequency actuators. Hence, the slow actuator signal acts on the laser crystal temperature and the fast actuator output is applied to the piezo of the laser cavity. All vital information about the PLL controller status can be monitored using the controller diagnostics connector. In Table 6.4 all relevant signals are listed.

As shown in Figure 6.6 the frequency shifted laser light gets phase modulated at 10.5 MHz before being mode matched into the squeezed light source. A polarizing beam splitter separates this control field from the squeezed field. A cavity length control loop is set up by demodulation of the photodetector $PD_{SLS_{cavity}}$ -RF-signal. The obtained error signal is fed back onto the PZT-mounted out-coupling mirror. In addition, the DC-signal can also be used for automated lock acquisition.

6.3.4 Mode cleaner for the homodyne detector LO beam

For the alignment of the homodyne detector fringe visibility, a local oscillator beam is overlapped with the alignment beam on the 50/50 beamsplitter in the diagnostic homodyne detection section. A mode cleaner ring cavity is placed in the LO path for spatial filtering. This cavity is held on resonance with the incoming main laser light by reusing the 77 MHz phase modulation for a third time. As shown in Figure

Mode cleaner for the homodyne detector LO beam			
Component / Signal	Bandwidth	Purpose	Converter
Error signal	fast	monitor	A/D
PD_{MC1064} DC level	slow	monitor	A/D
PZT HV	slow	monitor	A/D
Offset	slow	control	D/A
Gain	slow	control	D/A
Integrator	slow	control	TTL or D/A
Sign	slow	control	TTL or D/A
Ramp on/off	slow	control	TTL or D/A

Table 6.5 — Channel list for digital remote control of the infrared mode cleaner cavity (MC1064) length control loop.

6.7, this locking loop is composed of the photodetector PD_{MC1064} , mixer, servo, high-voltage amplifier and finally the PZT actuated cavity mirror. The relevant channels for digital remote control and monitoring are summarized in Table 6.5. Since the fringe visibility alignment procedure requires the removal of the flip mirror used for the photodetector $PD_{Alignment}$, the squeezer cavity length has to be alternatively controlled via the simultaneous injection of the frequency shifted control beam.

The sinusoidal fringe visibility signal can be obtained by monitoring one homodyne detector photo diode while phase dithering the local oscillator field via a piezo actuated phase shifter device.

6.3.5 Second auxiliary laser phase locking loop and squeezing ellipse and phase control loops

The coherent control scheme for the green pump phase and the local oscillator phase requires a second frequency shifted laser field. This will be provided by auxiliary laser 2, which is also phase locked to the main laser. Comparable to the first auxiliary laser frequency lock, an automated phase locking loop controller will be employed [Inno]. As shown in Figure 6.8 the Photodetector PD_{PLL3} detects the optical beat signal between both laser sources. The useable offset frequency bandwidth of this detector and the subsequent PLL controller ranges from 5 to 50 MHz.

The exact offset frequency was chosen to be 16.72 MHz. For the GEO 600-application this matches even multiples of half the signal-recycling cavity free spectral range (approx. 123 kHz), since the control field has to be anti-resonant inside this cavity. The PD_{PLL3} photocurrent is mixed down with an external frequency signal

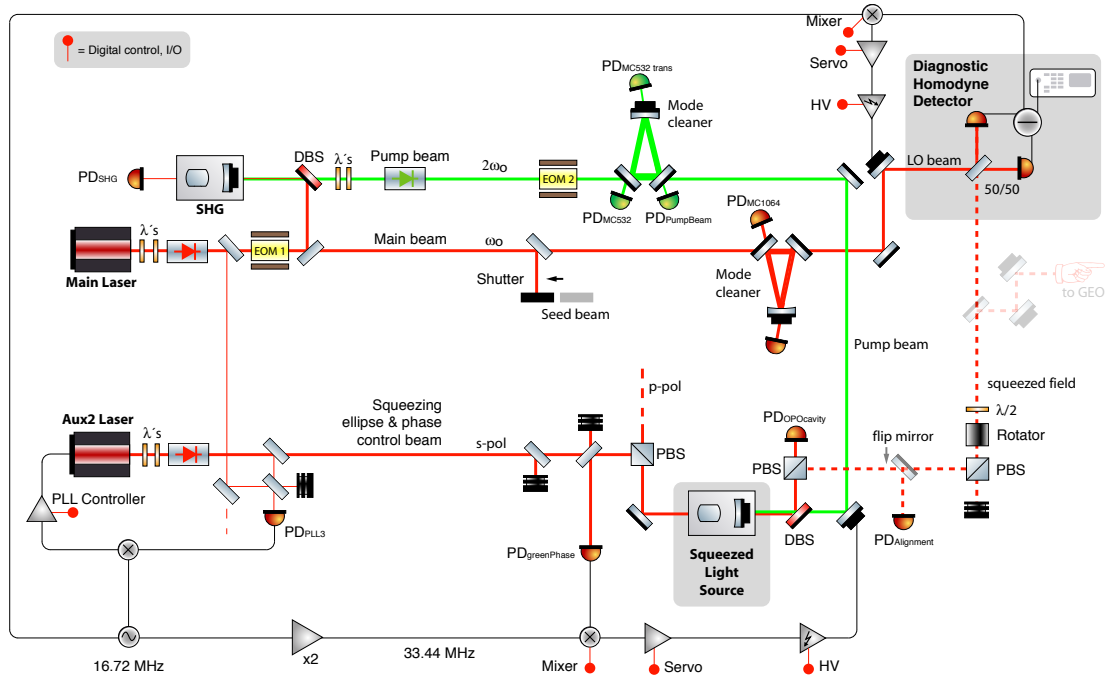


Figure 6.8 — Schematic of the locking loops which are required for the coherent control scheme of the green pump phase and local oscillator phase. A 16.72 MHz frequency shifted field is produced by a second auxiliary laser, which is phase locked to the main one. Two successive locking loops with demodulation frequencies at 16.72 MHz and 33.44 MHz are employed for coherent control of the generated squeezed vacuum states.

provided by an electronic local oscillator (16.72 MHz). The electric output signals of the PLL controller are again slow and fast laser frequency actuator outputs, regulating the Aux 2 - Laser crystal temperature and laser crystal piezo. In Table 6.6 the accessible PLL controller monitor and control channels are summarized.

After the injection of the coherent control beam into the squeezed light source cavity, a fraction of the back-reflected light is detected with $PD_{\text{greenPhase}}$. For a coherent control of the green pump phase this photocurrent has to be demodulated at twice the offset frequency (see chapter 4). Since the demodulation phase is especially important for this locking loop, it is recommended to consider digital control for long term stability. Similar to the other locking loops a servo and a high-voltage amplifier are used to feed back the error signal onto the PZT-driven phase shifter, which is inserted into the green pump path.

For controllable homodyne detection, the phase relation between the squeezed beam and the local oscillator beam can be stabilized by using the subtracted homodyne detector photocurrent. The error signal is obtained via demodulation at 16.72 MHz.

Second auxiliary laser phase locking loop (Aux-2 Laser)			
Component / Signal	Bandwidth	Purpose	Converter
Error point	fast	monitor	A/D
PZT feedback	fast	monitor	A/D
Peltier feedback	slow	monitor	A/D
PLL-status	slow / TTL	monitor	A/D
Status reset	slow / TTL	control	D/A
Coherent green pump phase control			
Component / Signal	Bandwidth	Purpose	Converter
Error signal	fast	monitor	A/D
PZT HV	slow	monitor	A/D
Demod phase	slow	control	D/A
Offset	slow	control	D/A
Gain	slow	control	D/A
Integrator	slow	control	TTL or D/A
Sign	slow	control	TTL or D/A
Ramp on/off	slow	control	TTL or D/A
Coherent local oscillator phase control			
Component / Signal	Bandwidth	Purpose	Converter
Error signal	fast	monitor	A/D
PZT HV	slow	monitor	A/D
Demod phase	slow	control	D/A
Offset	slow	control	D/A
Gain	slow	control	D/A
Integrator	slow	control	TTL or D/A
Sign	slow	control	TTL or D/A
Ramp on/off	slow	control	TTL or D/A
Diagnostic homodyne detector			
Component / Signal	Bandwidth	Purpose	Converter
Subtraction signal (spectrum)	fast	monitor	A/D

Table 6.6 — Channel list for digital remote control of the green pump phase, local oscillator phase and the second laser phase locking loop (Aux2 Laser). A high bandwidth digital input channel can be used for monitoring the squeezing spectrum and strength.

The feedback is applied to a phase shifting device placed in the local oscillator path.

Finally, for the implementation in the GEO 600 environment, a high bandwidth channel should be available to monitor the squeezing spectrum digitally.

6.3.6 Main squeezing laser frequency lock to the GEO 600 laser

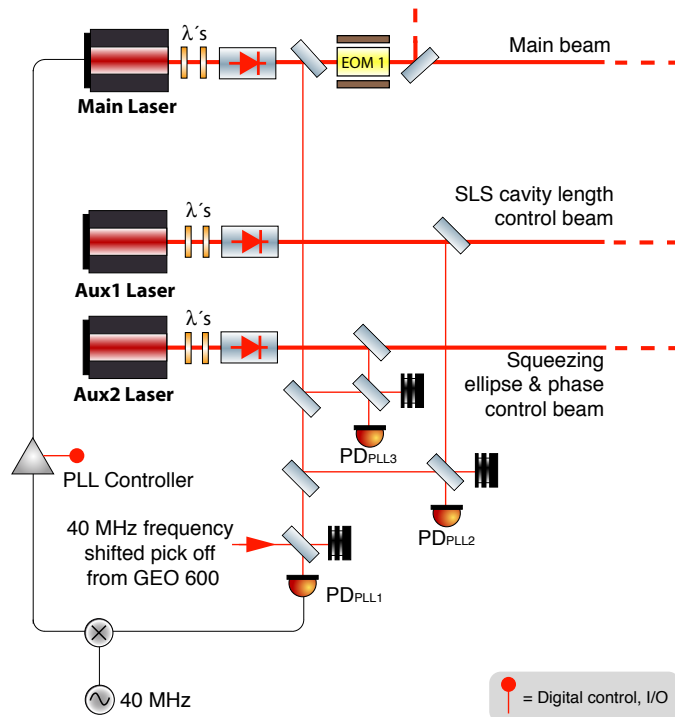


Figure 6.9 — Schematic of a third phase locking loop required to „synchronize“ the squeezing main laser to the GEO 600-laser frequency. Using an AOM, driven at 40 MHz, light from GEO is frequency shifted. This frequency offset is undone via offset locking at -40 MHz.

So far the squeezing breadboard operates independently from the GEO 600 detector. This is sufficient for the alignment and characterization phase of the squeezing experiment. However, for the implementation into the gravitational wave detector, the squeezing laser frequency has to be „synchronized“ with the GEO 600-laser frequency. Hence, a third phase locking loop has to be set up. Using an AOM, driven at 40 MHz, light from GEO 600 is frequency shifted, which allows a „virtual“ frequency offset locking technique, because in the end the frequency offset will be canceled by operating this phase locking loop at exactly the AOM frequency. A scheme of this PLL is presented in Figure 6.9. Depending on the disposable light intensity of the 40 MHz frequency shifted beam either the automated Innolight PLL controller can be

Main squeezing laser phase locking loop			
Component / Signal	Bandwidth	Purpose	Converter
Error point	fast	monitor	A/D
PZT feedback	fast	monitor	A/D
Peltier feedback	slow	monitor	A/D
PLL-Status	slow / TTL	monitor	A/D
Status reset	slow / TTL	control	D/A

Table 6.7 — Channel list for a digital remote control of the main laser phase locking loop.

employed (which requires approximately $800 \mu\text{W}$) or an alternative scheme has to be developed.

6.3.7 Squeezing phase and alignment control for GEO 600

Similar to the homodyne detector local oscillator phase control loop, the phase relation between the squeezed states and the gravitational wave detector output field has to be controlled. Thus, it is required to detect an optical beat of the interferometer output field with the coherent control field from the squeezing breadboard. Demodulation at the coherent control field offset frequency (16.72 MHz) will provide a suitable error signal which can be fed back to both, the suspended GEO-BDO-optics for slow drift compensation, and the piezo-actuated mirrors placed in the squeezed beam path for a faster control.

Additionally, the generation of auto-alignment error signals is under investigation.

6.3.8 Digital I/O channel overview

In Table 6.8 a summary of the described digital control and monitor channels is given. So far 68 I/O channels are required. Additional channels required for an auto-alignment system of the squeezed light injection have not been itemized.

6.3.9 Overview of the modulation frequencies

The control of the squeezing experiment requires several modulation frequencies. These were determined in such way that in the GEO 600 environment the resulting beat frequencies and their harmonics do not contaminate the detection band. Additionally, the beat frequencies are separated by at least 1 MHz. In Table 6.9 a summary of all frequencies involved in the squeezing experiment is given.

Digital I/O channel overview			
Number	Bandwidth	Purpose	Converter
13	fast	monitor	A/D
21	slow	monitor	A/D
35	slow	control	D/A

Table 6.8 — Total number of required digital control and monitor channels.

The already employed modulation frequencies for the GEO 600-operation are 9.017 MHz, 12 MHz, 13 MHz, 14.9 MHz, 25.25 MHz, and 37.16 MHz.

Overview of the modulation frequencies	
Object	Frequency
Second Harmonic Generator	77 MHz
Mode cleaner at 532 nm	119 MHz
Alignment beam	77 MHz
Auxiliary Laser 1	500-1500 MHz
Coherent squeezer cavity length control	10.5 MHz
Mode cleaner at 1064 nm	77 MHz
Auxiliary Laser 2	16.72 MHz
Coherent control beam 2	33.44 MHz
Phase lock to GEO laser	40 MHz

Table 6.9 — Summary of the modulation frequencies required for the squeezing experiment.

6.4 Squeezed light injection into GEO 600

In the following paragraph the most appropriate port for the injection of squeezed states into GEO 600 is discussed. With the gradual transition from GEO to GEO-HF an output mode cleaner (OMC) will be implemented to suppress contributions from higher-order-modes and RF-sidebands to the detected shot noise level [Willk06]. Hence, squeezed vacuum states can be injected „before“ or „after“ this output mode cleaner via a Faraday Rotator, which also has to be implemented into the GEO 600 setup. An optical loss budget for both sequences is calculated and from this an estimation of the expected non-classical sensitivity improvement is derived.

6.4.1 First sequence: Output mode cleaner – Faraday Rotator – Photodetector

In Figure 6.10 a possible arrangement of the optics is illustrated. This sequence has the advantage that after the OMC the mode will obviously be much cleaner, with a lower total intensity. It is very likely that with the upgrade to GEO-HF the circulating light power inside the interferometer will be increased by at least a factor of ten. Probably an additional factor of 2.5 will be gained due to the change of the signal-recycling-mirror (SRM). This means that the „dark port“ intensity will approximately raise from the current 40 mW up to 400 mW. Since back scattered light into the interferometer is a crucial issue, this sequence would help to reduce scattering introduced by the implemented Faraday rotator. However, this argumentation only affects higher order modes since the TEM₀₀-mode is not suppressed by the OMC.

6.4.1.1 Optical loss budget

- The output coupler of the GEO squeezer cavity will have a reflectivity of 92 %. Assuming an intra cavity round trip loss of 0.4 % – which takes into account the AR coating as well as the infrared absorption of the nonlinear crystal – the outcoupling efficiency will be approximately 95 %, resulting in a loss of 5 %.
- The squeezed beam must be protected from backscattered light utilizing a Faraday isolator on the squeezing breadboard. This is necessary to attenuate backscattering from the diagnostic homodyne detector on the squeezing breadboard as well as from GEO 600 into the squeezed light source. A Faraday Rotator – with a tuneable magnetic field – can offer a single pass transmission loss of approximately 2 %.

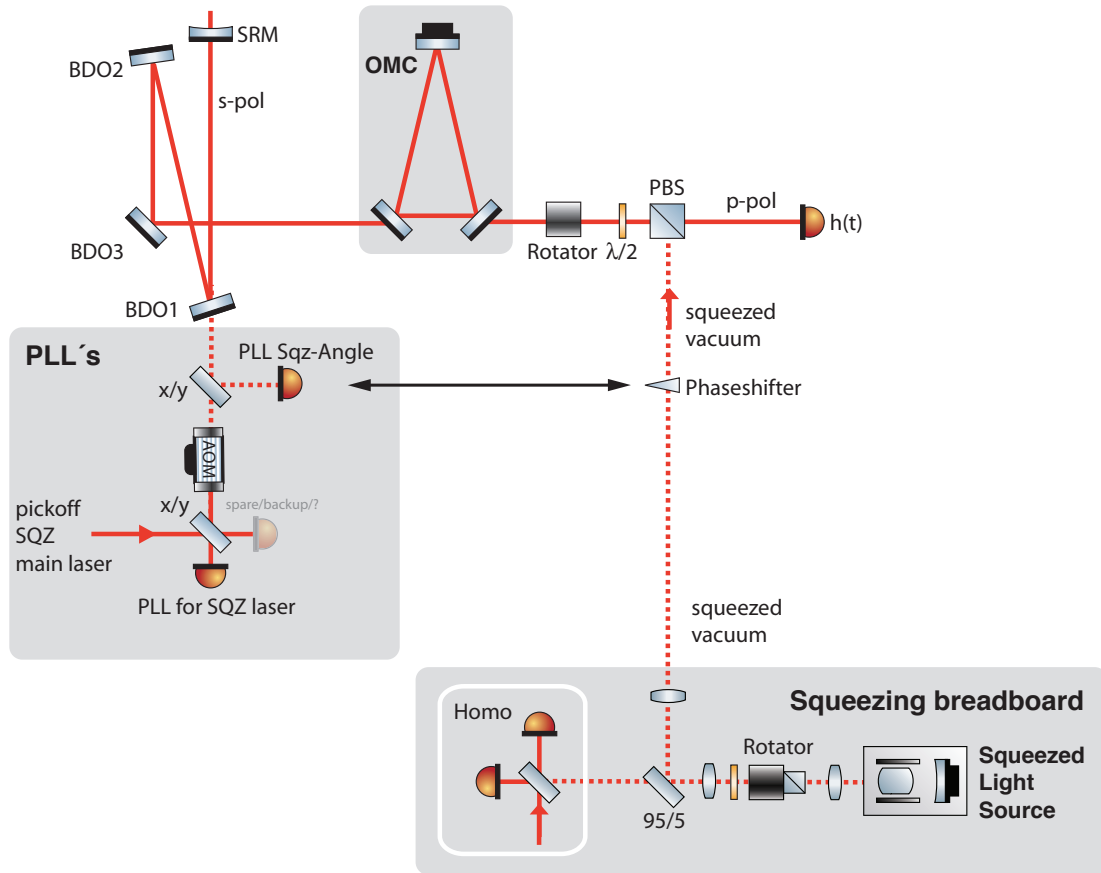


Figure 6.10 — Schematic of the optical configuration for the sequence: OMC – Faraday-Rotator – $PD_{h(t)}$.

- A diagnostic homodyne detector on the squeezing breadboard will permanently monitor the squeezing strength and the spectral purity. For this measurement 5% of the squeezed beam will be picked off. Since this percentage is a major contribution for the overall loss budget, this pick-off can be bypassed after the commissioning phase.
- The squeezed beam has to pass several AR-coated optics, which are required for the mode matching. The upper limit for this loss should be 1%.
- The main Faraday Rotator needed for the squeezed light injection into GEO 600 is specified to have a single pass transmission of 99%. However, a 2% loss has to be assumed since the squeezed beam has to pass this Rotator twice.
- Loss due to mode-mismatch into the OMC is assumed to be maximal 1%.

- A residual transmission of the BDO1 optic can be used among other things for the SQZ-PLL's. The transmission will be lowered from currently 1 % down to 0.5%. Since the squeezing has to pass twice, the loss for this optical component adds up to 1 %.
- The squeezing has to be mode matched into the GEO 600 signal-recycling cavity. A maximum loss of 1 % seems feasible.
- After backreflection at the signal-recycling cavity, the squeezed beam is mode matched into the OMC together with the interferometer local oscillator and signal field. A loss of 1 % seems feasible but has to be doubled since this mode matching is comparable to the fringe visibility of the homodyne detector. Therefore, the total loss adds up to 2 %.
- Finally detected, the squeezing level will be degraded by the quantum efficiency of the photodetector. Recent measurements lead to the assumption that a quantum efficiency of min. 98 % should be achievable.

In summary, this sequence leads to a total loss of 22 % with an operating diagnostic homodyne detector, or to a loss of 17 % without.

6.4.2 Second sequence: Faraday Rotator – OMC - Photodetector

As illustrated in Figure 6.11 the squeezed states are injected into the interferometer via the Faraday Rotator which is placed between the signal-recycling mirror and the OMC. The main difference compared to the first sequence is the fact that the light which is guided back towards the squeezer will have a higher intensity. Assuming GEO-HF will use the full laser light input power, about 400 mW will exit the dark port. Hence, determined by the Faraday Rotator attenuation (approx. 40 dB) a significant fraction (also containing the higher order modes) will be guided towards the squeezing breadboard. This may require an additional Faraday Rotator to protect the squeezed light source. When the Faraday rotator is placed „after“ the OMC this intensity will be reduced by a factor of 10 and the transmitted light will be only in the TEM₀₀ mode.

6.4.2.1 Optical loss budget

- As described in Chapter 6.4.1.1 the inherent optical loss on the squeezing breadboard plus additional mode matching optics is 13 %. This percentage also includes a 5 % loss for the diagnostic homodyne detector pick-off.

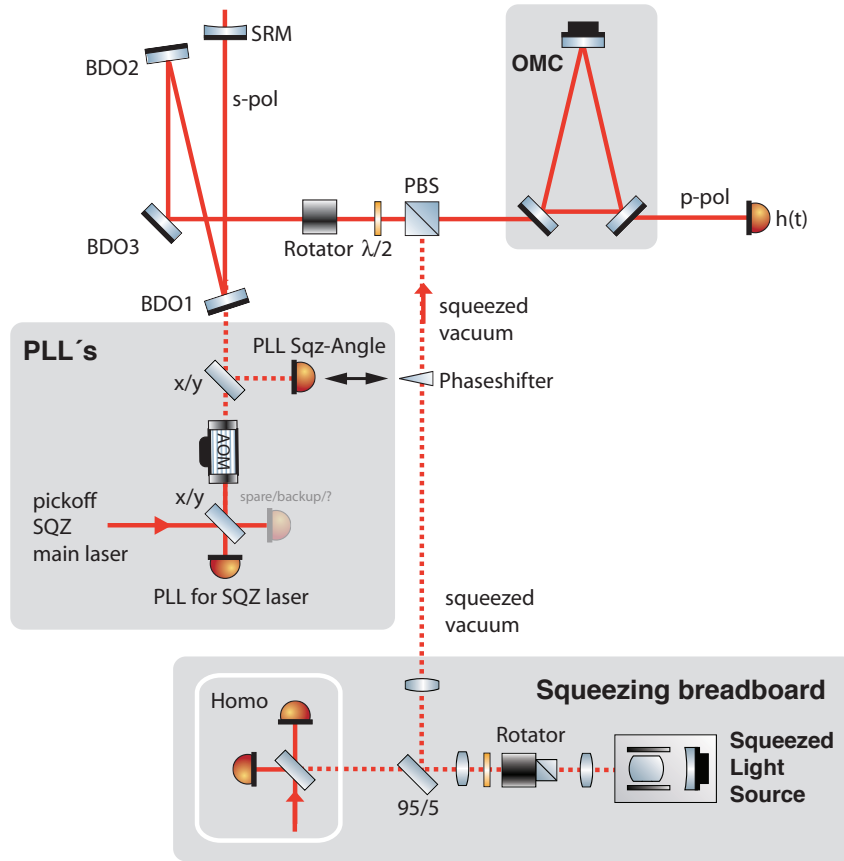


Figure 6.11 — Schematic of the optical configuration for the sequence: Faraday Rotator – OMC – $PD_{h(t)}$.

- Doublepassing the main Faraday Rotator, a loss of 2 % has to be taken into account.
- The estimated loss for the mode matching of the squeezed beam into the signal-recycling cavity is 1 %.
- Another 1 % loss is introduced by the residual transmission of the BDO1 optic (double pass).
- The squeezing has to be mode matched into the OMC together with the interferometer fields. A maximum loss of 1 % seems possible. Again this number has to be doubled due to the homodyne visibility. Therefore, a total loss of 2 % seems to be realistic.

- Finally, the quantum efficiency of the h(t) photodiode will give another 2 % loss.

Thus, this sequence ends up with a total loss of 21 % for the squeezed beam. When the diagnostic homodyne detector is bypassed the loss can be reduced down to 16 %.

6.4.3 Estimated squeezing strength

In Figure 6.12 the squeezing level versus the optical loss is plotted. The initial (anti-) squeezing level was defined to a reasonable value which is determined by the parametric (de-)amplification factor inside the squeezed light source. This parameter mainly depends on the finesse of the squeezer-cavity at 1064 nm and the intensity

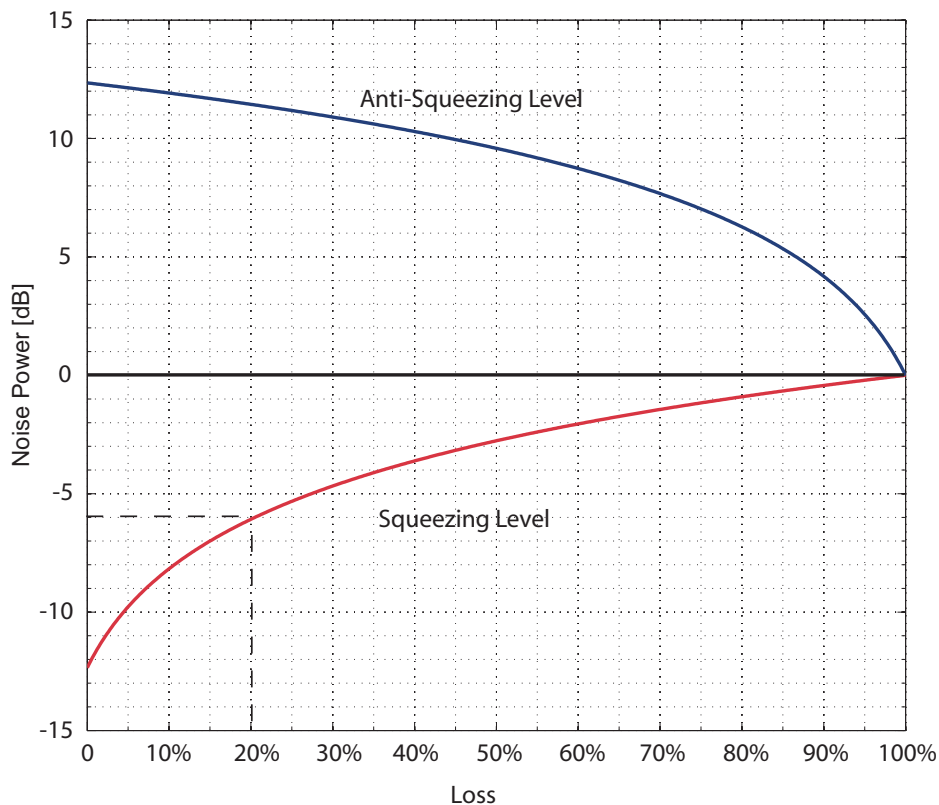


Figure 6.12 — Degree of squeezing versus optical loss. For the GEO squeezer setup an initial squeezing level of 13 dB is plausible leading to a detected squeezing level of approximately 6 dB after 21 % or 22 % optical loss. Bypassing the diagnostic homodyne detector would increase the detected squeezing level to about 7 dB.

of the pump beam at 532 nm. For the GEO squeezer setup an initial squeezing level of 13 dB is plausible. As one can see, after optical losses in the range of 21 % or 22 % one would end up with a detected squeezing level of nearly 6 dB. In this case the diagnostic homodyne detector on the squeezing breadboard would permanently monitor about 0.25 dB of squeezing. If this homodyne detector is bypassed the finally detected squeezing level will increase up to 6.5 - 7 dB.

Based on the optical loss budget the positioning of the Faraday Rotator seems not to introduce any significant differences. Only for the sequence OMC – Faraday Rotator – Photodetector the subcarrier field (16.72 MHz frequency shifted) is attenuated during transmission through the OMC (due to the OMC-linewidth of about 3 MHz). However, this should be compensable by increasing the laser intensity of the frequency shifted subcarrier beam on the squeezing breadboard. In Figure 6.13 the theoretical frequency

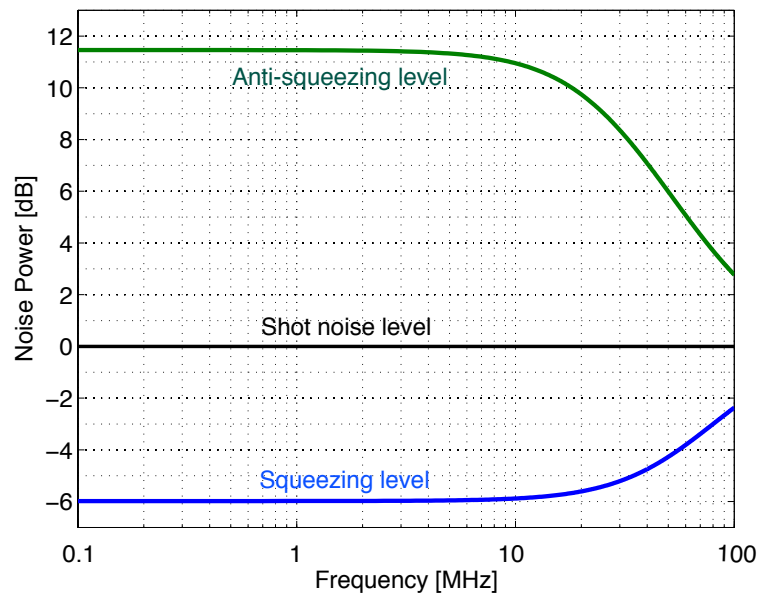


Figure 6.13 — Theoretical plot of the detected (anti-)squeezing strength in dependence of the sideband-frequency. An overall optical loss of 20 % degraded the squeezing level down to 6 dB and even further in the MHz-regime due to a limited squeezer cavity linewidth.

dependent squeezing strength is illustrated. An overall optical loss of 20 % degraded the initial squeezing level down to 6 dB within the detection band of earth-based GW-detectors. In the MHz-regime the squeezing level gets further reduced due to the limited cavity linewidth of the squeezed light source.

Summary and Outlook

The purpose of this thesis was the experimental investigation and optimization of squeezed light generation, especially in the view of application to laser-interferometric gravitational wave detectors.

The direct observation of 11.5 dB squeezing of light's quantum noise at a wavelength of 1064 nm, as described in Chapter 3, shows that the squeezed light technique has indeed a great application potential as envisaged more than two decades ago [Caves81]. Injected into a gravitational wave detector, the quantum noise reduction corresponding to an increase of more than a factor of 4 in laser light power will now be possible (see Chapter 6). This is a promising application, since gravitational wave detectors already use the highest single-mode laser powers applicable. For example, it is proposed for the advanced LIGO detectors to store up to a megawatt of laser light power inside the interferometer. Optical waveform distortion due to absorption and the excitation of parametric instabilities, however, both have a risk to limit the maximum light power [Dambr03], [Shaug04].

Considering the literature to date on squeezed light generation, such as the observation of 7 dB squeezed states at 1064 nm [Lam99] and 9 dB squeezing at 860 nm [Furus07], indicates that even the generation of 11.5 dB squeezing at 1064 nm is most likely not the limit. In order to produce still higher squeezing levels further investigations in the field of alternative nonlinear crystal materials, the effect of green induced infrared absorption and pump power dependent thermal effects inside the squeezed light source should be performed.

Controlling squeezed vacuum fields was a basic problem for squeezed field applications in gravitational wave (GW) detectors. Common control schemes rely on the injection of a weak, phase modulated control field at the carrier frequency into the squeezed light source. It has been shown that even the lowest carrier powers

introduce large amounts of classical laser noise at audio frequencies and squeezing can no longer be achieved [McKen04]. However, in Chapter 4 of this thesis, a novel coherent control scheme was proposed for a comprehensive phase control of squeezed vacuum states. Based on this scheme the generation of up to 6.5 dB broadband vacuum squeezing at Fourier-frequencies from 1 Hz up to 10 kHz, thus covering the entire detection band of ground-based GW-detectors, was demonstrated. Furthermore, this coherent control scheme is directly applicable to large-scale GW-detectors.

On the basis of the squeezed light sources developed in this thesis and the experimental results achieved a conceptional design of a squeezed light source – optimized for a high duty cycle application in GW-detectors – was proposed and elaborated upon in Chapter 6. In particular, the ideal port for the injection of squeezed states into the GEO 600 GW-detector has been discussed and theoretical analyses determined the feasibility of a shot noise level reduction by 6 dB using non-classical states of light. As a result, it is planned to inject squeezed states into the large-scale GEO 600 GW-detector in the year 2009 and also for the LIGO H1-detector it is proposed to surpass the shot noise limited sensitivity in the year 2011 by the use of squeezed states.

Source Codes

A.1 Homodyne detection

The following GNUPLOT script was used to investigate the influence of a slightly unbalanced homodyne detector as described in the Chapter 2.

```

1 set term aqua
# Simulation of an slightly , ,unbalanced ' homodyne detector
6 # Parameters
G = 1.          # Electronic gain
R = .5         # Reflectivity of the beamsplitter (
               power)
K = 1.         # Visibility
S = -10.       # Squeezing in dB
11 # Some calculations
V(sqz) = 10**(sqz/10.0) # Variance of the squeezed quadrature
r(R) = sqrt(R)         # Reflectivity (amplitude)
t(R) = sqrt(1-R)      # Transmission (amplitude)
16 K(R) = t(R)/r(R)*K  # Kontrast / Visibility

# Definition of the measured variance

numerator(G,R,K,S) = (t(R)**2 - G*r(R)**2)**2 +
21 → → → ((1 + G)*r(R)*t(R))**2*(1 - K**2 + K**2*V(S))

```

```

denominator(G,R,K,S) = (t(R)**2 + G*r(R)**2)**2 +
→ → → ((1 - G)*r(R)*t(R))**2*(1 - K**2 + K**2*V(S))
26
V_meas(G,R,K,S) = numerator(G,R,K,S)/denominator(G,R,K,S)

# Definition
V_plot(G,R,K,S) = 10*log10(V_meas(G,R,K,S)/V(S))
31
# Graphix
#set terminal postscript landscape color solid
#set output 'SingleModeSQZ_equalPDpos.ps'
set ylabel 'V_real_□_V_meas_□[dB]'
36 set grid
set yrange [0:∗]

set multiplot
set size .5,.5
41

# Variation of the gain

set origin .0, .5
46 set xlabel 'Gain'
set title 'K_□=□1.0;□R_□=□0.5'
plot [G=.9:1.1] V_plot(G,0.5,1.0, -10.0) title '-10_dB',\
                V_plot(G,0.5,1.0, -13.0) title '-13_dB',\
                V_plot(G,0.5,1.0, -20.0) title '-20_dB'
51

set origin .5, .5
set title 'K_□=□0.998;□R_□=□0.5'
56 plot [G=.9:1.1] V_plot(G,0.5,0.998, -10.0) title '-10_dB',\
                V_plot(G,0.5,0.998, -13.0) title '-13_dB',\
                V_plot(G,0.5,0.998, -20.0) title '-20_dB'

61 # Variation of the reflectivity

set origin .0, .0
set xlabel 'Reflectivity'
set title 'K_□=□1.0;□G_□=□1.0'

```

```

66 plot [R=.48:.52] V_plot(1.0,R,1.0,-10.0) title '-10_dB',\
      V_plot(1.0,R,1.0,-13.0) title '-13_dB',\
      V_plot(1.0,R,1.0,-20.0) title '-20_dB'

71 set origin .5, .0
set title 'K=0.998;G=1.0'
plot [R=.48:.52] V_plot(1.0,R,0.998,-10.0) title '-10_dB',\
      V_plot(1.0,R,0.998,-13.0) title '-13_dB',\
      V_plot(1.0,R,0.998,-20.0) title '-20_dB'

76
unset multiplot
pause -1

```

A.2 Squeezing simulations

The following MATLAB script was used to simulate squeezing levels and spectra. The influence of phase noise and optical loss is included and experimentally measured data can be directly imported for comparison with the simulation.

```

%Resonator mit Squeezer
4 clear data
clear out

set(0,'DefaultAxesFontSize',14);
9 set(0,'DefaultTextFontSize',14);
set(gcf,'DefaultLineMarkerSize',14);

%Lichtgeschwindigkeit
14 c=299792458;

L=c/10.5e9;
%Reflektivität der Amplitude am 1. Spiegel
r1=0.88;
19 %Reflektivität der Amplitude am 2. Spiegel

```

140 SOURCE CODES

```
r2=1;
%Verstimmung des Resonators (in Radian)
phi=0.00;
%Homodynwinkel
24 zeta2 = pi/2
zetaVar=0.0
zeta = 0*pi/2 + zetaVar/180*pi;

%%
29 zetaX2 = pi/2
zetaXVar=1.3
zetaX = 0*pi/2 + zetaXVar/180*pi;
%%

34 %Verluste der Leistng im Resonator
alpha=0.0013;
eta=.94;
%Squeezingfactor
%cg=40;
39 cg=11.0;
gain=cg;
g=(cg*r1*r2-sqrt(cg*r1^2*r2^2-2*cg*r1^3*r2^3+cg*r1^4*r2^4))/(
cg*r1^2*r2^2);
r=log(g);

44 %Transmittivitaeten
t1=sqrt(1-r1^2);
t2=sqrt(1-r2^2);

%Minimale und maximale Seitenbandfrequenz
49 min=0.01e6;
max=100e6;

Ein=[1 0; 0 1];
54 %Datenvektor
data=[];
out=[];
data2=[];
59 out2=[];

%%
dataX=[];
```



```

outX = [];
64 dataX2 = [];
outX2 = [];
%%%%%%%%%%%%%%%%

%Modulations-Frequenzen
69 f=linspace (min,max,500);
for x=f

%Relative Phasenverschiebung der Seitenbaender bezogen auf
den Traeger
%entlang der Strecke M1-M2-M1 (Abstand L)
74 phase=(2*pi*x)*(L/c);

%Transfermatrix des Feldes im Resonator (M1-M2-M1)
%Der Squeezer (1. Matrix) quetscht immer die
Amplitudenquadratur
RES=r2*sqrt(1-alpha)*exp(2*i*phase)*[exp(-r) 0; 0 exp(r)]*[
cos(2*phi) ...
79 -sin(2*phi); sin(2*phi) cos(2*phi)];

%Transfer des reflektierten Feldes
REF=inv (Ein-r1*RES)*(RES-Ein*r1);

84 %Transfer des Verlustfeldes aus dem Resonator
LOSS=inv (Ein-r1*RES)*sqrt(alpha)*t1;

%Spektrale Rauschdichtematrizen der einzelnen Felder
S1=1/2*(REF*transpose (conj (REF))+conj (REF)*transpose (REF));
89 S2=1/2*(LOSS*transpose (conj (LOSS))+conj (LOSS)*transpose (
LOSS));

%Spektrale Rauschdichte
%Amplitudenquadratur: zeta=0
%Phasenquadratur: zeta=pi/2
94 N1 = [cos(zeta) sin(zeta)]*S1*[cos(zeta); sin(zeta)];
N2 = [cos(zeta) sin(zeta)]*S2*[cos(zeta); sin(zeta)];
N=N1+N2;

N12 = [cos(zeta2) sin(zeta2)]*S1*[cos(zeta2); sin(zeta2)];
99 N22 = [cos(zeta2) sin(zeta2)]*S2*[cos(zeta2); sin(zeta2)];
N2=N12+N22;

%%%%%%%%%%%%%%%%

```

142 SOURCE CODES

```

104   N1X = [cos(zetaX) sin(zetaX)]*S1*[cos(zetaX); sin(zetaX)];
      N2X = [cos(zetaX) sin(zetaX)]*S2*[cos(zetaX); sin(zetaX)];
      NX=N1X+N2X;

      N12X = [cos(zetaX2) sin(zetaX2)]*S1*[cos(zetaX2); sin(zetaX2
          )];
      N22X = [cos(zetaX2) sin(zetaX2)]*S2*[cos(zetaX2); sin(zetaX2
          )];
109   N2X=N12X+N22X;
      %%%%%%%%%%%

%Konstruktion eines Vektors, der die spektralen Rauschdichten
      enthaelt
      data=[data; [sqrt(N1) sqrt(N2) sqrt(N)]];
114   out=[out;N];
      data2=[data2; [sqrt(N12) sqrt(N22) sqrt(N2)]];
      out2=[out2;N2];
      dataX=[dataX; [sqrt(N1X) sqrt(N2X) sqrt(NX)]];
      outX=[outX;NX];
119   dataX2=[dataX2; [sqrt(N12X) sqrt(N22X) sqrt(N2X)]];
      outX2=[outX2;N2X];
      end
      out=10*log10(eta*out+(1-eta));
      out2=10*log10(eta*out2+(1-eta));
124   outX=10*log10(eta*outX+(1-eta));
      outX2=10*log10(eta*outX2+(1-eta));
      %%%%%%%%%%%

%IMPORT DER MESSDATEN
129 %anti = importdata('BBANTIavg5.txt',';',26)
      %vac = importdata('BBVACavg5.txt',';',26)

      %sqz1 = importdata('BBSQZ1.txt',';',26)
      %sqz2 = importdata('BBSQZ2.txt',';',26)
134 %sqz3 = importdata('BBSQZ3.txt',';',26)
      %sqz4 = importdata('BBSQZ4.txt',';',26)
      %sqz5 = importdata('BBSQZ5.txt',';',26)

      %dark = importdata('BBDARKavg5.txt',';',26)
139 %freq = anti.data(:,1);
      %anti = anti.data(:,2);
      %vac = vac.data(:,2);
      %sqz1 = sqz1.data(:,2);

```

```

144 %%sqz2 = sqz2.data(:,2);
    %sqz3 = sqz3.data(:,2);
    %sqz4 = sqz4.data(:,2);
    %sqz5 = sqz5.data(:,2);

149 %sqz = [sqz1,sqz2,sqz3,sqz4,sqz5];

    %dark = dark.data(:,2);

    % antiLin = 10.^(anti/10);
154 % vacLin = 10.^(vac/10) ;
    % sqzLin = 10.^(sqz./10) ;
    % darkLin = 10.^(dark/10) ;

    %for n=1:5
159 %sqzLinAVG= (sqzLin(:,1)+sqzLin(:,2)+sqzLin(:,3)+sqzLin(:,4)
        +sqzLin(:,5))/5;

    % sqzLinDarkCorr = sqzLinAVG - darkLin;
    % antiLinDarkCorr= antiLin - darkLin;
    % vacLinDarkCorr = vacLin - darkLin;

164 % NormVac = 10*log10( vacLinDarkCorr./vacLinDarkCorr );
    % NormSqz = 10*log10( sqzLinDarkCorr ./ vacLinDarkCorr);
    % NormAnti= 10*log10( antiLinDarkCorr ./ vacLinDarkCorr);
    % plot(freq, NormAnti, freq, NormVac, freq, NormSqz)
169 freq=freq/1e6;

    %plot(f/1e6,[out],f/1e6,[out2],...
        %freq, NormAnti, freq, NormVac, freq, NormSqz)

174 plot(f/1e6,[out],f/1e6,[outX],f/1e6,[out2],f/1e6,[outX2],...
        freq, NormAnti, freq, NormVac, freq, NormSqz)

179 xlim([1.2 100]);
    % plot(f/1e6,[out],f/1e6,[out2], 'LineWidth',2.5)
    grid on
    set(gca, 'YMinorGrid', 'on')
    %set(gca, 'YTick',[-12 -11 -10 -9 -8 -7 -6 -5 -4 -3 -2 -1 0 1
        2 3 4 5 6 7 8 9 10 11 12 13 14 15 16 17 18 19 20])

184 %legend('reflected_vacuum','intracavity_loss','total_noise')

```

144 SOURCE CODES

```
189 %legend( 'total_noise' )  
    xlabel( 'Frequency_[MHz]' );  
    ylabel( 'Noise_Power_[dB]' );  
    title ( [ 'phase=' , num2str(zetaVar) , ',_eta=' , ...  
            num2str(eta) , ',_cg=' num2str(cg) ] )
```

Electronics

In the following schematics of electronics are presented. This includes

- AOM driver electronics. Up to 1 W output power was generated at a modulation frequency of 40 MHz. Additionally a phase locked $2f$ output is provided. This circuit was used for the coherent control scheme of squeezed vacuum states at sideband frequencies in the audio band.
- Schematics of servo electronics. This generic design was optimized each time depending on the specific application.
- A peltier driver stage used for temperature control of mode cleaner cavities made from aluminum.
- Schematic of the homodyne detector circuit used for the low-frequency squeezing experiment. This circuit provides an additional resonant high frequency output, which is required for the coherent control scheme of squeezed vacuum states.
- Schematic of the resonant photodiode circuit used for the Pound-Drever-Hall locking technique.
- Schematic of a generic temperature controller circuit employed for second harmonic generator and squeezed light source ovens.

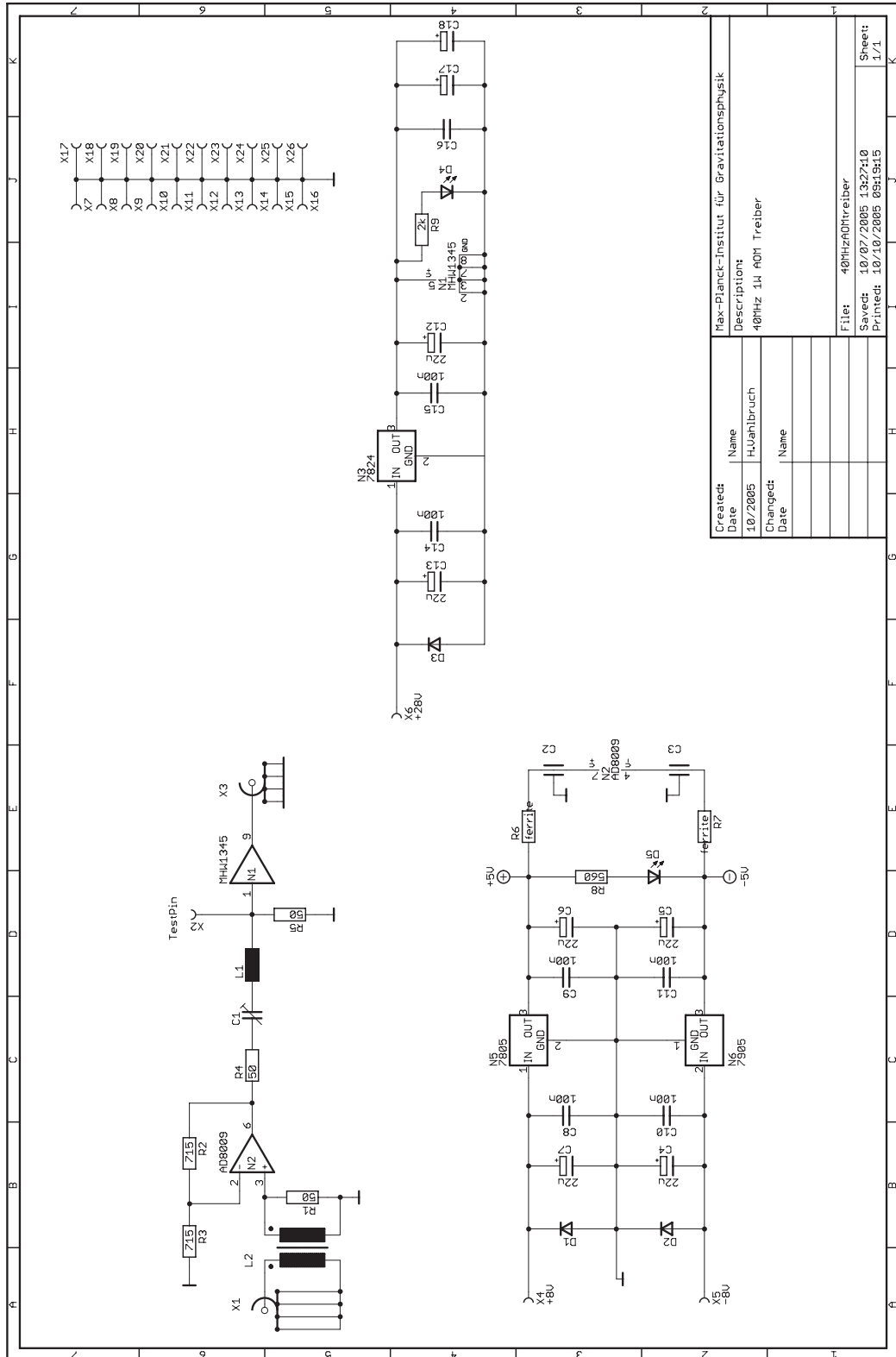
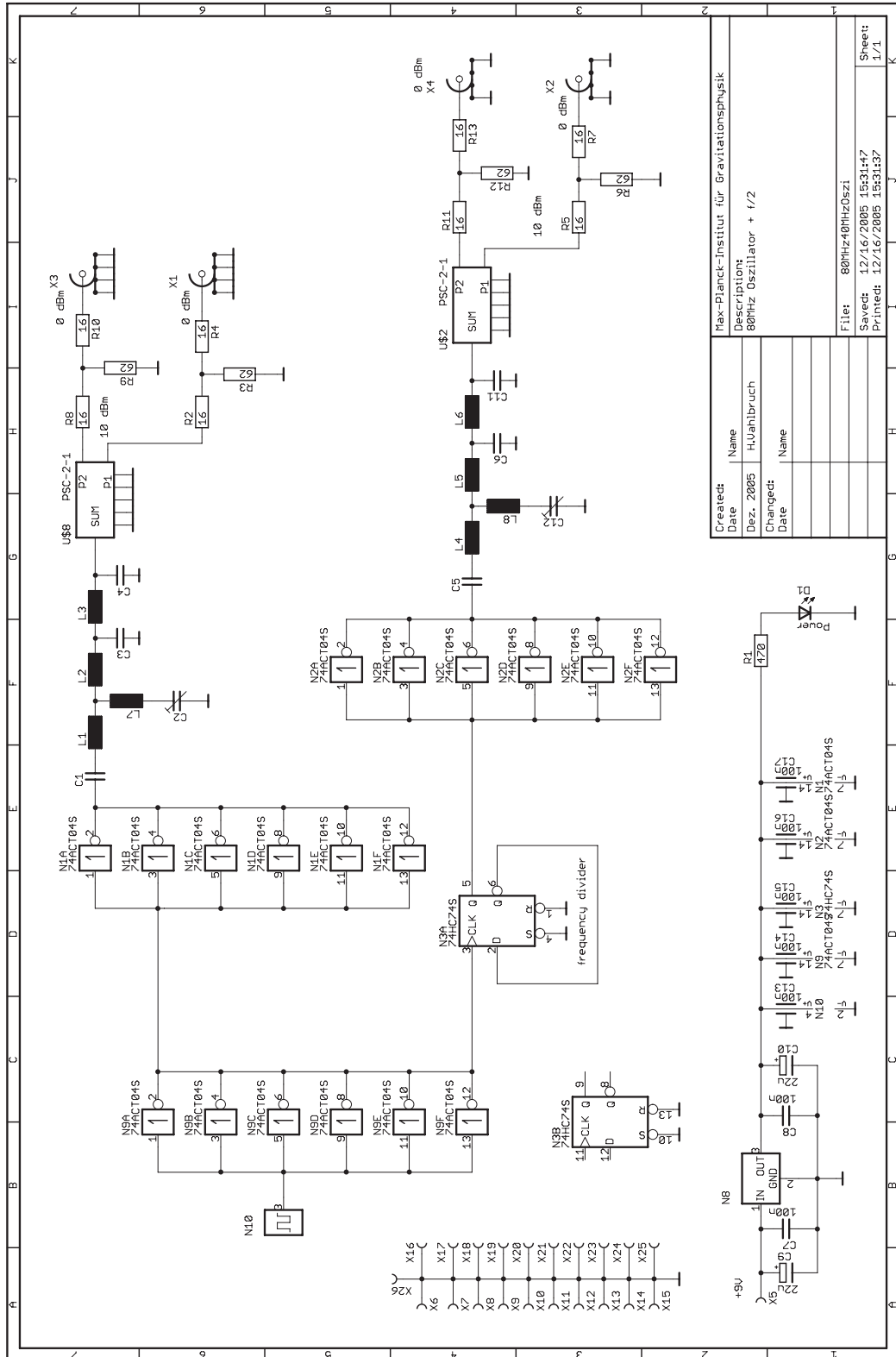


Figure B.1 — Schematic of the 40 MHz AOM-Driver circuit.



Created:	Name
Date	HJahnbruch
Description	
Dez. 2005	80MHz Oszillator + 1/2
Changed:	Name
Date	
File: 80MHz40MHzOsz	
Saved: 12/16/2005 15:31:47	
Printed: 12/16/2005 15:31:37	
Sheet: 1/1	

Figure B.2 — Schematic of a 80 MHz frequency generator plus frequency divider. This circuit is used for the coherent control scheme, driving the AOM stage.

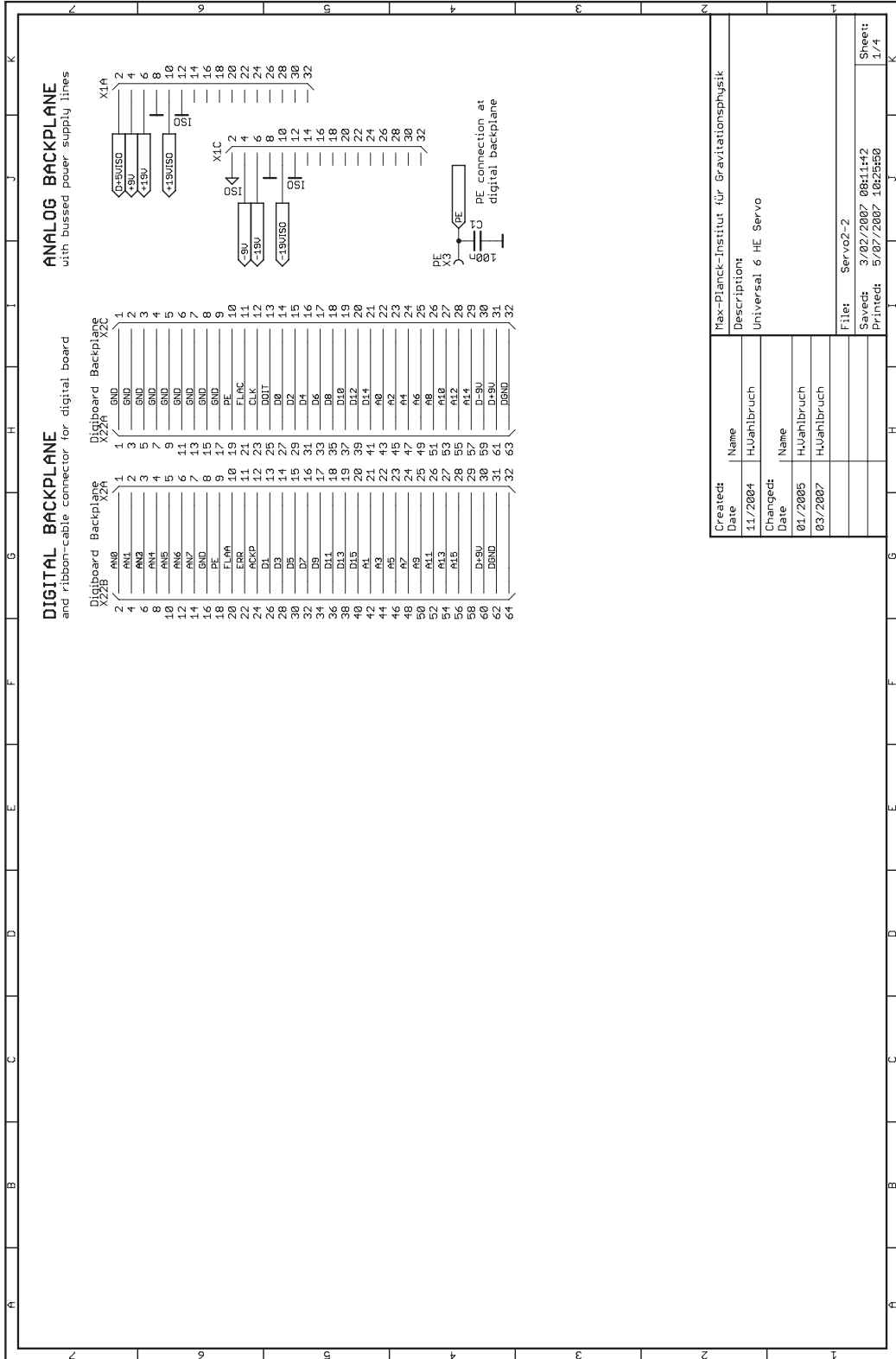


Figure B.3 — Schematic of the generic Servo circuit (page 1).

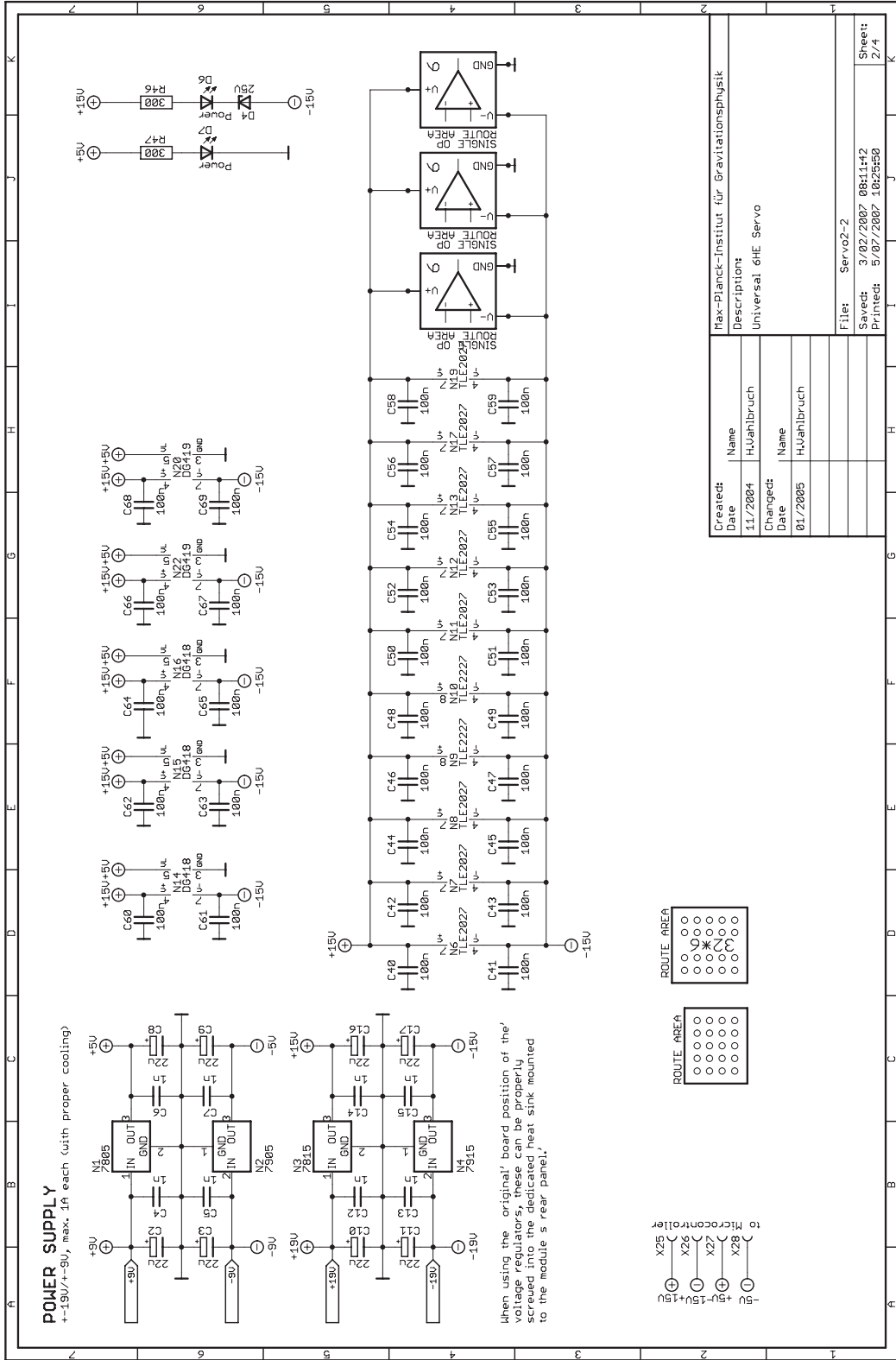
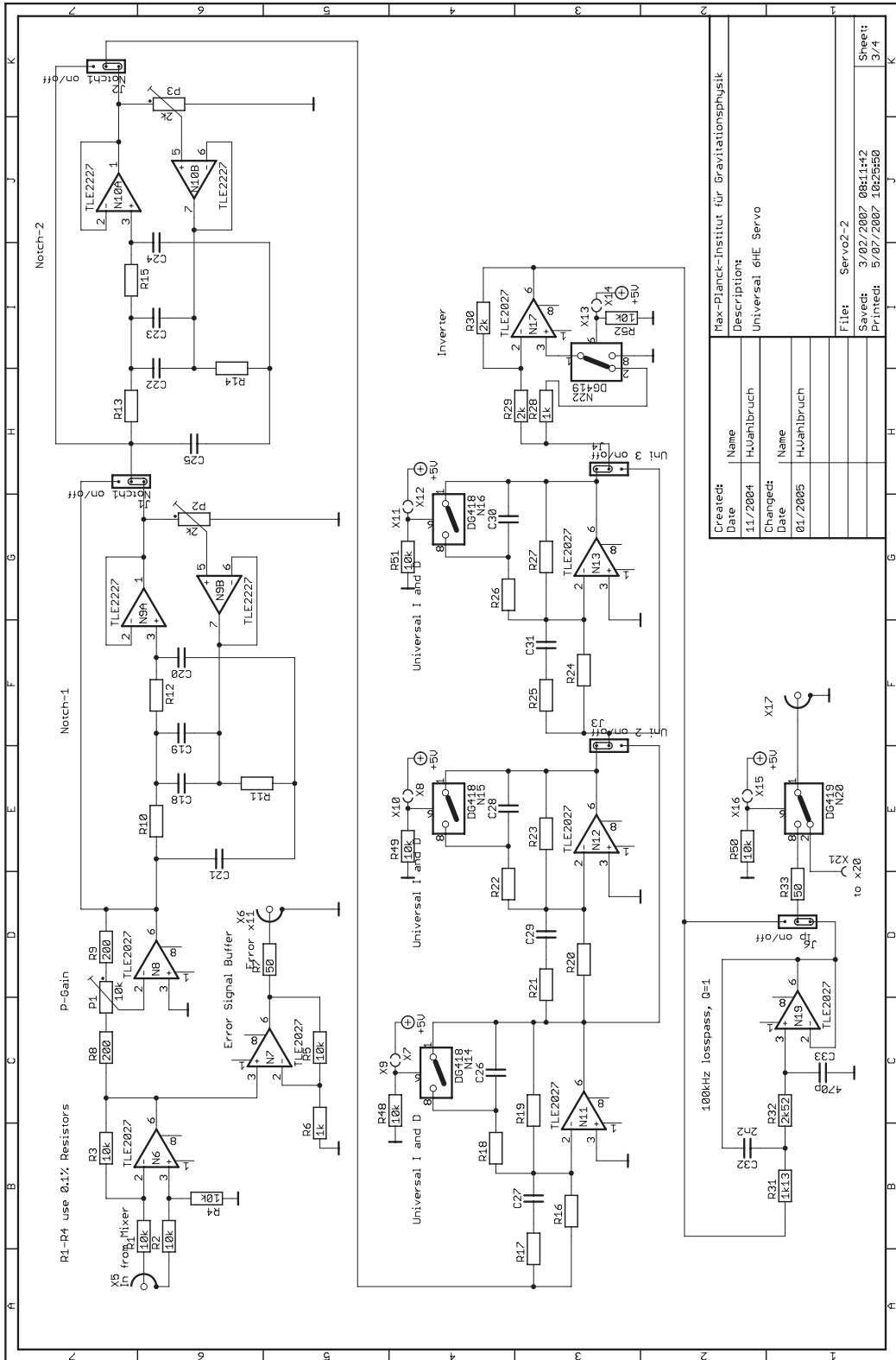


Figure B.4 — Schematic of the generic Servo circuit (page 2).



Created#	Name	Max-Planck-Institut für Gravitationsphysik
Date	Description	Universal 6HE Servo
Changed#	Name	
Date		
File:	Servo2-2	
Saved:	3/02/2007 08:11:42	Sheet: 3/4
Printed:	5/07/2007 10:25:50	

Figure B.5 — Schematic of the generic Servo circuit (page 3).

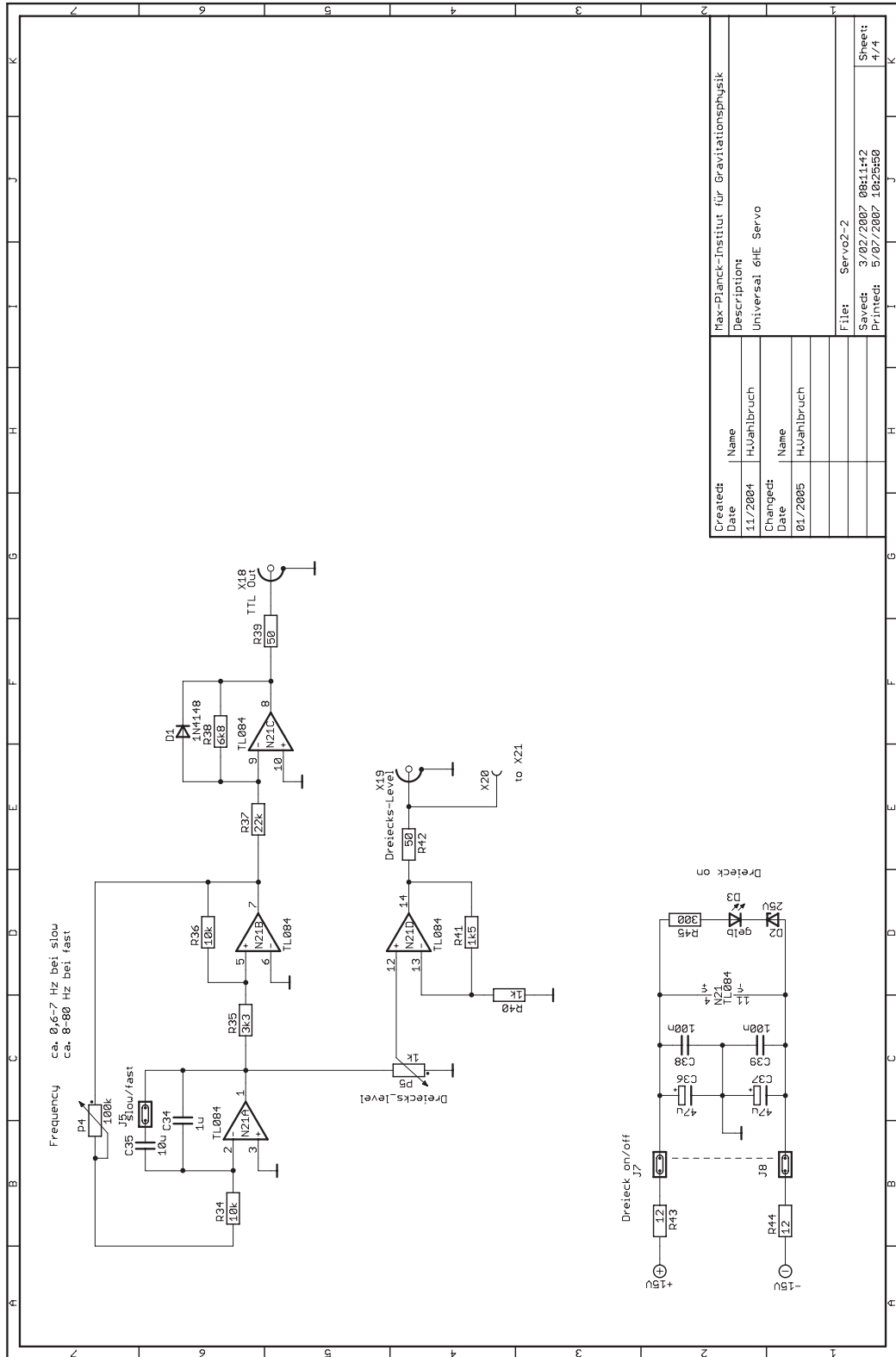


Figure B.6 — Schematic of the generic Servo circuit (page 4).

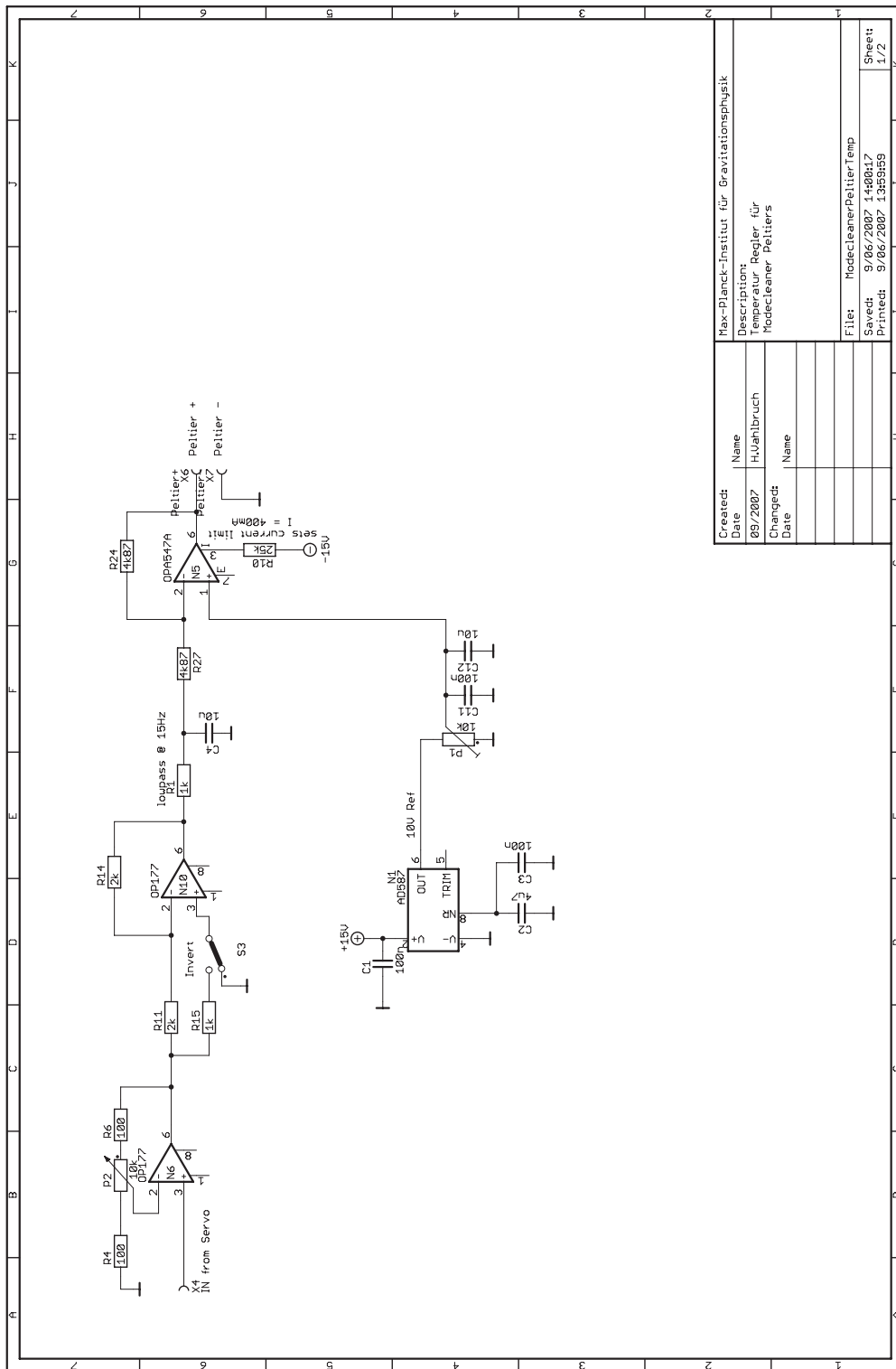


Figure B.7 — Schematic of the modecleaner Peltier circuit.

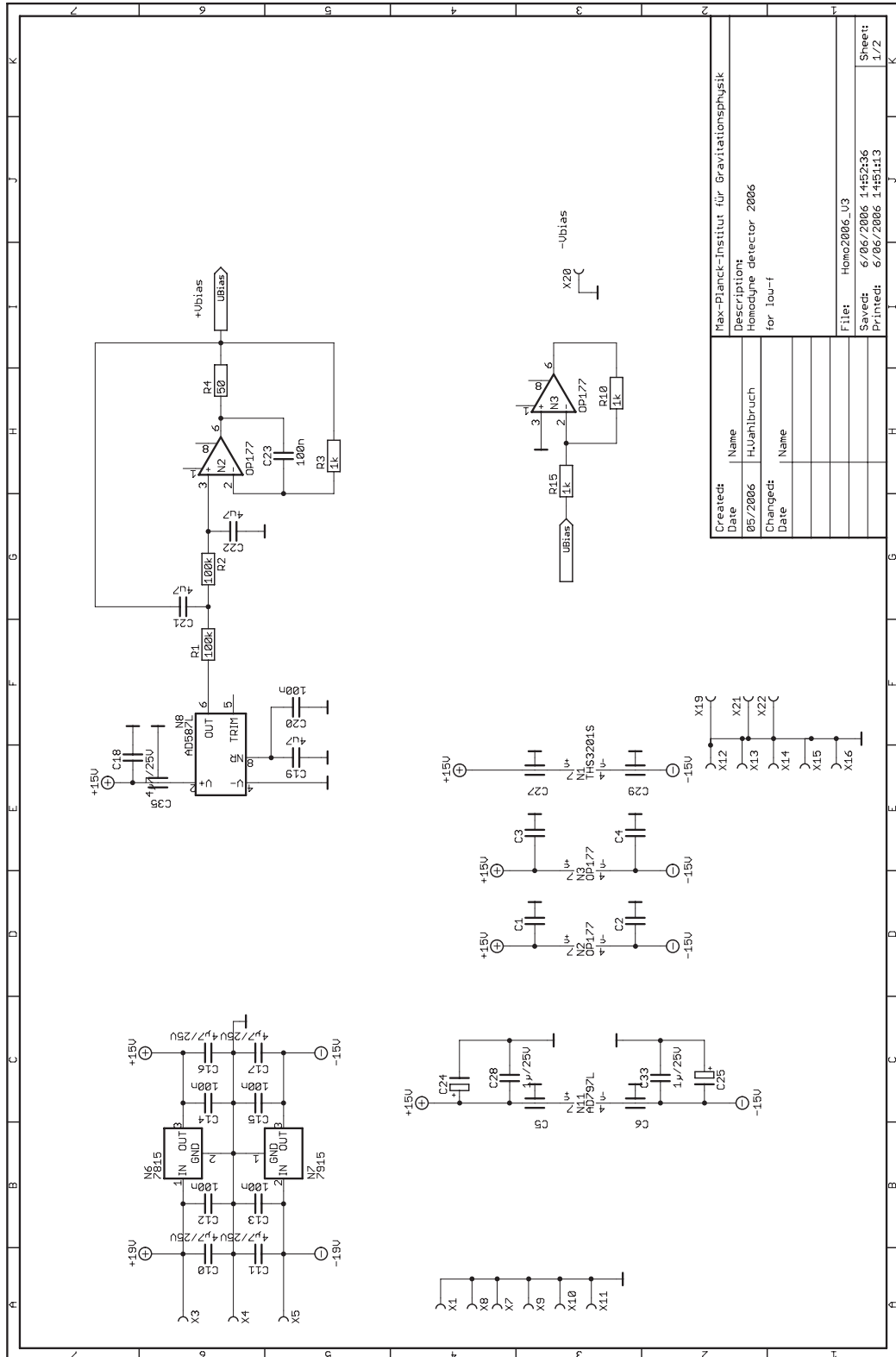


Figure B.8 — Schematic of the homodyne detector circuit (page1).

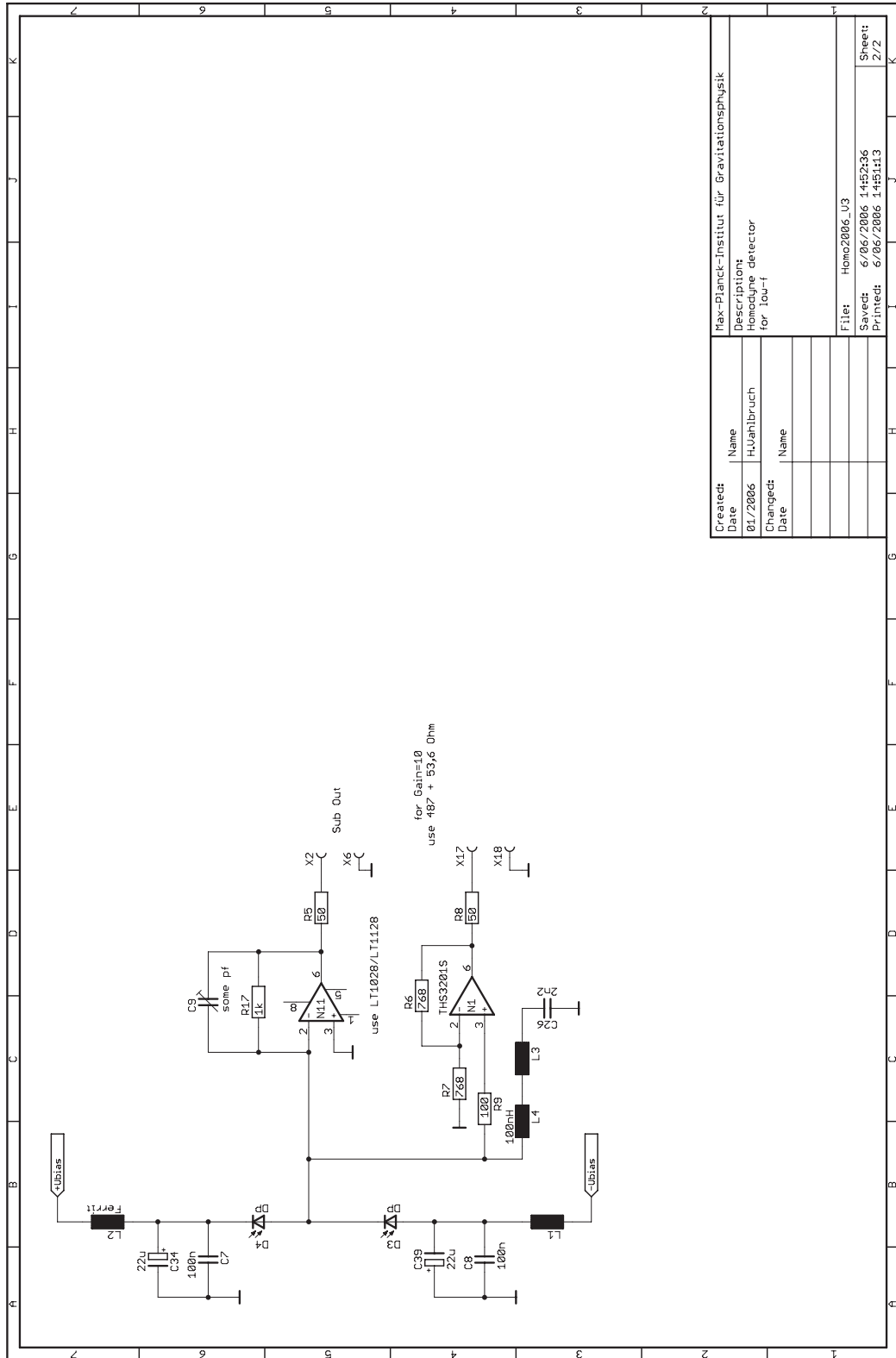


Figure B.9 — Schematic of the homodyne detector circuit (page 2).

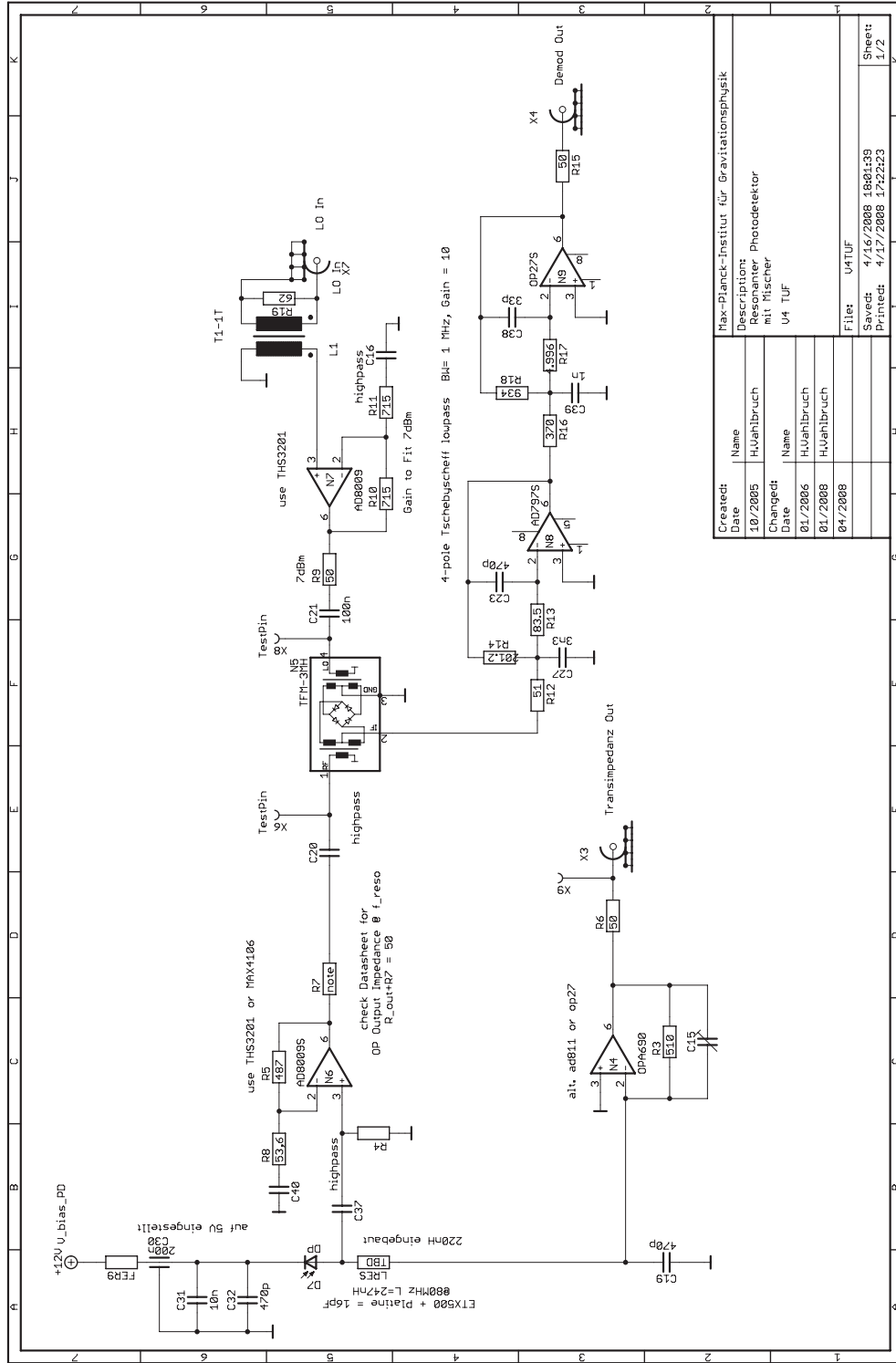


Figure B.10 — Schematic of the resonant photodiode circuit (page 1).

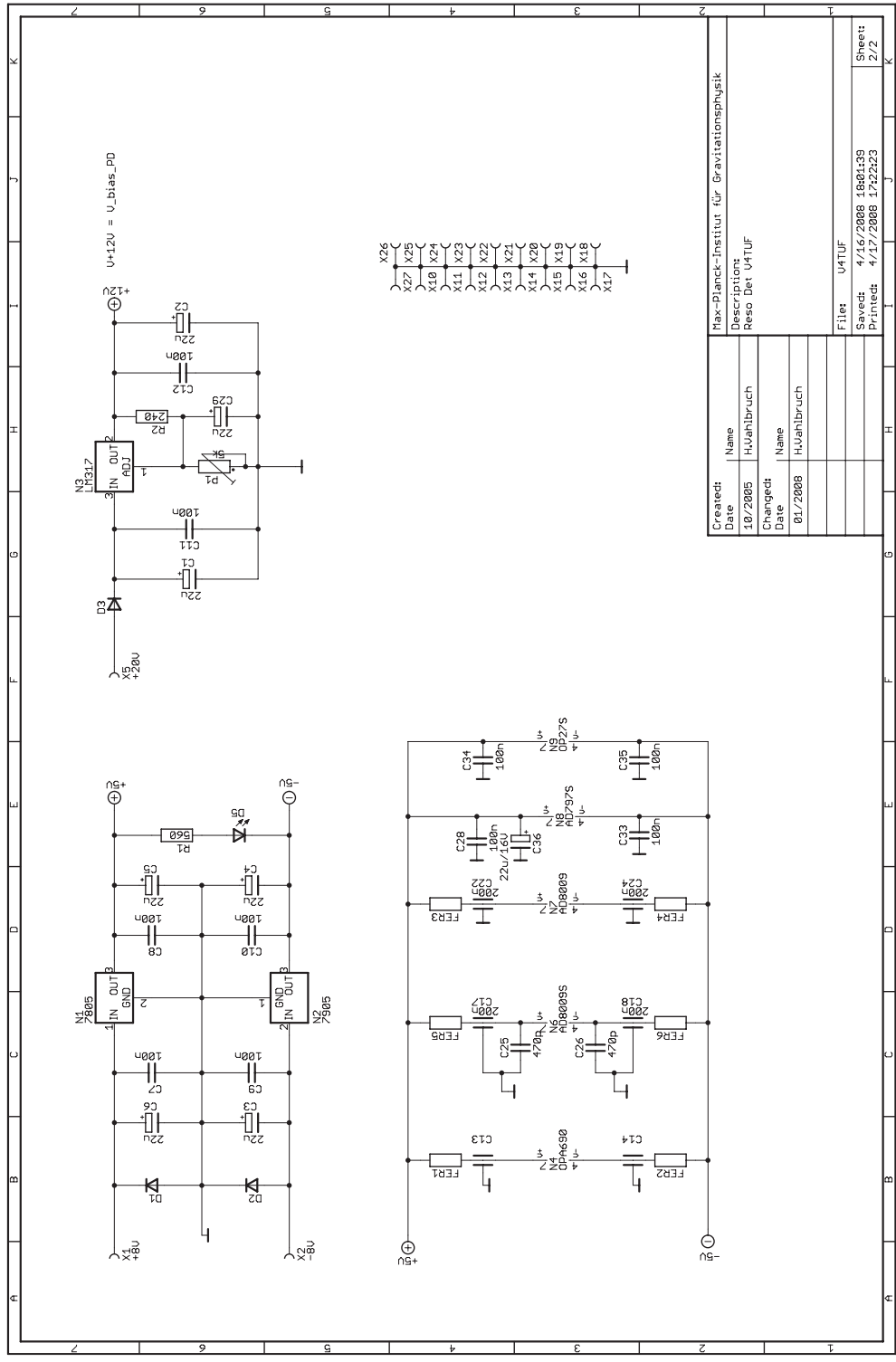
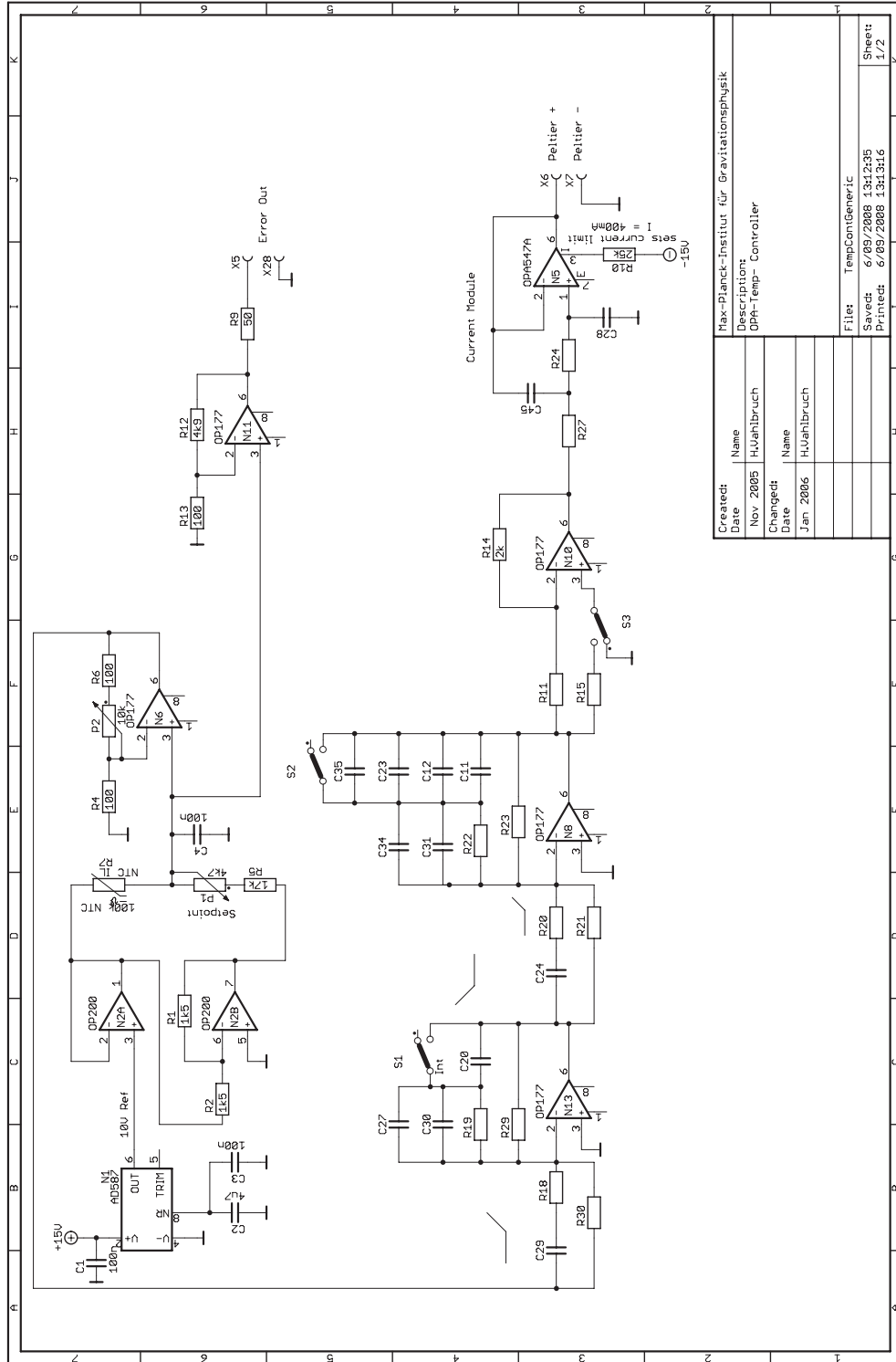


Figure B.11 — Schematic of the resonant photodiode circuit (page 2).



Created:	Name	Max-Planck-Institut für Gravitationsphysik
Date	Description:	OPA-Temp- Controller
Nov 2005	Author:	H.Wahlbruch
Changed:	Name	
Date	File:	TempCon1Generic
Jan 2006	Saved:	6/08/2008 13:12:05
	Printed:	6/08/2008 13:13:16
	Sheet:	1/2
		1/2

Figure B.12 — Schematic of the generic OPA/SHG temperature controller.

Bibliography

- [Aetal05] B. Abbott et.al for the LSC, *Limits on Gravitational-Wave Emission from Selected Pulsars Using LIGO Data*, *Phys. Rev. Lett.* **94**, 181103, (2005).
- [AdvLi99] E. Gustafson, D. Shoemaker, K. Strain, and R. Weiss, LIGO Document No. T990080-00-D, Caltech/MIT, 1999. See also www.ligo.caltech.edu/
- [Mario06] O.D. Aguiar et.al, *Class. Quantum Grav.* **23**, S239 (2006).
- [Akama04] D. Akamatsu, K. Akiba, M. Kozuma, *Phys. Rev. Lett.* **92**, 20 (2004).
- [EXPLO06] P. Astone et.al, *Class. Quantum Grav.* **23**, S57 (2006).
- [Aufmu05] P. Aufmuth, K. Danzmann, *New J. Phys.* **7**, 202 (2005).
- [Bouwme] D. Bouwmeester et al., *Nature* **390**, 575 (1997); D. Boschi et al., *Phys. Rev. Lett.* **80**, 1121 (1998); I. Marcikic et al., *Nature* **421**, 509 (2003); R. Ursin et al., *Nature* **430**, 849 (2004).
- [Bowen03] W. P. Bowen, N. Treps, B. C. Buchler, R. Schnabel, T. C. Ralph, H.-A. Bachor, T. Symul, and P. K. Lam, *Phys. Rev. A* **67**, 032302 (2003).
- [Boyd92] R.W. Boyd, *Nonlinear Optics*, Academic Press, 1992.
- [Bragi92] V. B. Braginsky and F. Ya. Khalili *Quantum Measurements* Cambridge University Press, Cambridge, 1992.
- [Bragi99] V. B. Braginsky, M. L. Gorodetsky and S. P. Vyatchanin, *Physics Letters A* **264**, 1-10 (1999).
- [Bragi01] V. B. Braginsky, and S. P. Vyatchanin *Physics Letters A* **279**, 154-162 (2001).
- [Braun00] S. L. Braunstein and H. J. Kimble, *Phys. Rev. A* **61**, 042302 (2000).

- [Braun05] S. L. Braunstein and P. van Loock, *Rev. Mod. Phys.* **77**, 513 (2005).
- [Breite97] G. Breitenbach, S. Schiller, J. Mlynek, *Nature* **387**, 471 (1997).
- [Breite98] G. Breitenbach, F. Illuminati, S. Schiller, J. Mlynek, *Europhys. Lett.* **44**, 192 (1998).
- [Buona01] A. Buonanno and Y. Chen, *Class. Quantum Grav.* **18**, L95 (2001).
- [Buona04] A. Buonanno, Y. Chen, *Phys. Rev. D* **69**, 102004 (2004).
- [Caves81] C. M. Caves, *Phys. Rev. D* **23**, 1693 (1981).
- [Caves85] C. M. Caves and B. L. Schumaker, *Phys. Rev. A* **31**, 3068 (1985).
- [Chelk05] S. Chelkowski, H. Vahlbruch, B. Hage, A. Franzen, N. Lastzka, K. Danzmann, and R. Schnabel, *Phys. Rev. A* **71**, 013806 (2005).
- [Chelk07] S. Chelkowski, H. Vahlbruch, K. Danzmann, R. Schnabel, *Phys. Rev. A* **75**, 043814 (2007).
- [Chicka96] V. Chickarmane and S. V. Dhurandhar, *Phys. Rev. A* **54**, 786 (1996).
- [Cho03] A. Cho, *Science* **299**, 36 (2003).
- [Crook04] D.R.M. Crooks, G. Cagnoli, M. M. Fejer, A. Gretarsson, G. Harry, J. Hough, N. Nakagawa, S. Penn, R. Route, S. Rowan and P. H. Sneddon *Class. Quantum Grav.* **21**, S1059–S1065 (2004).
- [Dambr03] E. D'Ambrosio, *Phys. Rev. D* **67**, 102004 (2003).
- [DeVin02] G. de Vine, D. A. Shaddock, D. E. McClelland, *Class. Quantum Grav.* **19**, 1561 (2002).
- [Dodon02] V. V. Dodonov, *J. Opt. B: Quantum Semiclass. Opt* **4**, R1 (2002).
- [Drever83] R. W. P. Drever and J. L. Hall, *Applied Physics B.*, 31:97, (1983).
- [Dreve83] R. W. P. Drever *et al.* in *Quantum Optics, Experimental Gravitation, and Measurement Theory*, edited by P. Meystre and M. O. Scully (Plenum, New York, 1983), p. 503–514.
- [Eckha91] R.C. Eckhardt, C.D. Nabors, W.J.Kozlowsky, and R.L.Byer, *J.Opt.Soc.Am.B*, 8:646, (1991).

- [Einst16] A. Einstein *Sitzungsbericht Preuss. Akad. Wiss. Berlin* **688** (1916).
- [Einst18] A. Einstein *Sitzungsbericht Preuss. Akad. Wiss. Berlin* **154** (1918).
- [ESA] Website: <http://lisa.esa.int/science-e/www/area/index.cfm?fareaid=27>
- [Fiura98] A. Furusawa, J. L. Sørensen, S. L. Braunstein, C. A. Fuchs, H. J. Kimble, and E. S. Polzik, *Science* **282**, 706 (1998).
- [Franze06] A. Franzen, B. Hage, J. DiGuglielmo, J. Fiurášek, and R. Schnabel, *Phys. Rev. Lett.* **97**, 150505 (2006).
- [Franze08] A. Franzen, Präparartion von destillierten und purifizierten gequetschten Zuständen, Ph.D. Thesis (2008).
- [Furus07] Y. Takeno, M. Yukawa, H. Yonezawa, A. Furusawa, *Optics express* **7**, 15, 4321 (2007).
- [Garci06] R. García-Patrón and N. J. Cerf, *Phys. Rev. Lett.* **97**, 190503 (2006).
- [GeoBa87] J. Gea-Banacloche and G. Leuchs, *Journal of Modern Optics* **34**, 793 (1987).
- [GEO600] <http://www.geo600.uni-hannover.de>
- [Geo02] B. Willke et al., *Class. Quantum Grav.* **19**, 1377 (2002).
- [Gerry04] C. C. Gerry, P. L. Knight, *Introductory quantum optics* (Cambridge University Press, Cambridge, UK, 2004).
- [Goda07b] , K.Goda Development of Techniques for Quantum-Enhanced Laser-Interferometric Gravitational-Wave Detectors, Ph.D. Thesis, 2007.
- [Goda07] K.Goda, E.E. Mikhailov, O.Miyakawa, S. Saraf, S.Vass, A.Weinstein, and N. Mavalvala , *arXiv:quant-ph/0703001v1*.
- [Goda08] K. Goda, O. Miyakawa, E .E. Mikhailov, S. Saraf, R. Adhikari, K. McKenzie, R. Ward, S. Vass, A. J. Weinstein and N. Mavalvala *Nature physics* **4**, 472 (2008).
- [Grangi87] P. Grangier, R. E. Slusher, B. Yurke and A. LaPorta, *Phys. Rev. Lett.* **59**, 2153 (1987).
- [Gross01] F. Grosshans and P. Grangier, *Phys. Rev. A* **64**, 010301 (2001).

- [Haine06] S. A. Haine, M. K. Olsen, J. J. Hope, *Phys. Rev. Lett.* **96**, 4 (2006).
- [Harms03] J. Harms, Y. Chen, S. Chelkowski, A. Franzen, H. Vahlbruch, K. Danzmann, and R. Schnabel, *Phys. Rev. D* **68**, 042001 (2003).
- [Heinze96] G. Heinzl, J. Mizuno, R. Schilling, A. Rüdiger, W. Winkler and K. Danzmann, *Phys. Lett. A* **217**, 305 (1996).
- [Heinze98] G. Heinzl, K. A. Strain, J. Mizuno, K. D. Skeldon, B. Willke, W. Winkler, R. Schilling, A. Rüdiger, and K. Danzmann, *Physical Review Letters* **81**, 5493 (1998).
- [HHI] Website: <http://www.hhi.fraunhofer.de>
- [Holle79] J. N. Hollenhorst, *Phys. Rev. D* **19**, 1669 (1979).
- [Hough83] J. Hough and Drever, R. W. P. and Ward, H. and Munley, A. J. and Newton, G. P. and Meers, B. J. and Hoggan, S. and Kerr, G. A., *Nature* **303**, 202 (1983).
- [Mthsu06] M. T. L. Hsu, G. Hétet, O. Glöckl, J. J. Longdell, B. C. Buchler, H.-A. Bachor, and P. K. Lam, *Phys. Rev. Lett.* **97**, 183601 (2006).
- [Hulse94] R. A. Hulse, *Rev. Mod. Phys.* **66**, 699-710 (1994).
- [Inno] <http://www.innolight.de>
- [Jaeke90] M. T. Jaekel and S. Reynaud, *Europhys. Lett.* **13**, 301 (1990).
- [Kimbl01] H. J. Kimble, Y. Levin, A. B. Matsko, K. S. Thorne and S. P. Vyatchanin, *Phys. Rev. D* **65**, 022002 (2001).
- [Kurod06] K. Kuroda and the LCGT Collaboration *Class. Quantum Grav.* **23**, S215–S221 (2006).
- [Lam99] P. K. Lam, T. C. Ralph, B. C. Buchler, D. E. McClelland, H.-A. Bachor and J. Gao, *J. Opt. B.* **1**, 469 (1999).
- [Lastz07] N. Lastzka and R. Schnabel, *Opt. Express*, **15**, 7211-7217 (2007).
- [LIGO] <http://www.ligo.caltech.edu>
- [Ligo92] A. Abramovici et al., *Science* **256**, 325 (1992).

- [LigoG04] B. Abbott, et al., *Nuclear Instruments and Methods in Physics Research A* **517**, 26 (2004).
- [Liu00] Y. T. Liu and Kip S. Thorne *Physical Review D* **62**, 122002 (2000).
- [McKen02] K. McKenzie, D. A. Shaddock, D. E. McClelland, B. C. Buchler, and P. K. Lam, *Phys. Rev. Lett.* **88**, 231102 (2002).
- [McKen04] K. McKenzie, N. Grosse, W. P. Bowen, S. E. Whitcomb, M. B. Gray, D. E. McClelland, and P. K. Lam, *Phys. Rev. Lett.* **93**, 161105 (2004).
- [McKen05] K. McKenzie, E. E. Mikhailov, K. Goda, P. K. Lam, N. Grosse, M. B. Gray, N. Mavalvala, and D. E. McClelland, *J. Opt. B* **7**, 421 (2005).
- [McKen06] K. McKenzie, M. B. Gray, S. Goßler, P. K. Lam and D. E. McClelland, *Class. Quantum Gravity* **23**, S245-250 (2006).
- [Meers88] B. J. Meers, *Phys. Rev. D* **38**, 2317 (1988).
- [Menic06] N. C. Menicucci, P. van Loock, M. Gu, C. Weedbrook, T. C. Ralph, and M. A. Nielsen, *Phys. Rev. Lett.* **97**, 110501 (2006).
- [Mizun93] J. Mizuno, K. A Strain, P. G. Nelson, J. M. Chen, R. Schilling, A. Rüdiger, W. Winkler and K. Danzmann, *Phys. Lett. A* **175**, 273 (1993).
- [Navas06] M. Navascués, F. Grosshans, and A. Acín, *Phys. Rev. Lett.* **97**, 190502 (2006).
- [Neerg06] J. S. Neergaard-Nielsen, B. Melholt Nielsen, C. Hettich, K. Mølmer, E. S. Polzik, *Phys. Rev. Lett.* **97**, 4 (2006).
- [Niels06] J. S. Neergaard-Nielsen, B. Melholt Nielsen, C. Hettich, K. Mølmer, E. S. Polzik, *Phys. Rev. Lett.* **97**, 4 (2006).
- [Ourjo06] A. Ourjoumtsev, R. Tualle-Brouiri, J. Laurat, P. Grangier, *Science* **312**, 83 (2006).
- [Param] Plot parameters: $m = 5.6$ kg, $L = 1200$ m, $P_{in} = 7$ W
- [Pinar05] M. Pinard, et al., *Europhys. Lett.* **72**, 747 (2005).
- [Roukes06] M. Roukes, *Nature* **443**, 154 (2006).
- [Rowan05] S. Rowan, J. Hough, D.R.M. Crooks *Physics Letters A* **347**, 25-32 (2005).

- [Schill98] K. Schneider, M. Lang, J. Mlynek, and S. Schiller, *Optics express* **2**, 3, 59 (1998).
- [Shaug04] R. O’Shaughnessy, S. Strigin, S. Vyatchanin, *arXiv:gr-qc / 0409050v1*, (2004).
- [Schna04] R. Schnabel, J. Harms, K. A. Strain, and K. Danzmann, *Class. Quantum Grav.* **21**, S1045 (2004).
- [Slush85] R. E. Slusher, L. W. Hollberg, B. Yurke, J. C. Mertz, J. F. Valley, *Phys. Rev. Lett.* **55**, 2409 (1985).
- [Takei05] N. Takei, H. Yonezawa, T. Aoki, and A. Furusawa, *Phys. Rev. Lett.* **94**, 220502 (2005).
- [Taken07] Y. Takeno, M. Yukawa, H. Yonezawa, and A. Furusawa, *Optics Express* **15**, 4321 (2007).
- [TAMA] <http://tamago.mtk.nao.ac.jp>
- [Tama01] M. Ando *et al.*, *Phys. Rev. Lett.* **86**, 3950 (2001).
- [Taylor94] J.H. Taylor, *Rev. Mod. Phys.* **66**, 711-719 (1994).
- [Thorne87] K.S. Thorne, in *300 Years of Gravitation*, edited by S.W. Hawking and W. Isreal (Cambridge University Press, Cambridge, England, 1987), pp. 330–458.
- [TMC] <http://www.technicalmanufacturing.com>
- [Trep03] N. Treps, N. Grosse, W. P. Bowen, C. Fabre, H.-A. Bachor, and P. K. Lam, *Science* **301**, 940 (2003).
- [Unruh82] W. G. Unruh, in *Quantum Optics, Experimental Gravitation, and Measurement Theory*, edited by P. Meystre and M. O. Scully (Plenum, New York, 1983), p. 647–660.
- [Vahlb05] H. Vahlbruch, S. Chelkowski, B. Hage, A. Franzen, K. Danzmann, and R. Schnabel, *Phys. Rev. Lett.* **95**, 211102 (2005).
- [Vahlb06] H. Vahlbruch, S. Chelkowski, B. Hage, A. Franzen, K. Danzmann, and R. Schnabel, *Phys. Rev. Lett.* **97**, 011101 (2006).

- [Vahlb07] H. Vahlbruch, S. Chelkowski, K. Danzmann, R. Schnabel *New J. Phys.* **9** (2007) 371.
- [AURIGA] A. Vinante et.al, *Class. Quantum Grav.* **23**, S103 (2006).
- [VIRGO] <http://wwwcascina.virgo.infn.it>
- [Virgo04] F. Acernese *et al.*, *Class. Quantum Grav.* **21**, S709 (2004).
- [GRAIL06] A. de Waard et.al, *Class. Quantum Grav.* **23**, S79 (2006).
- [Walls83] D. F. Walls, *Nature* **306**, 141 (1983).
- [Weber69] J. Weber *Phys. Rev. Letters*, **22**, 1320 (1969).
- [Willk06] B. Willke et. al. *Class. Quantum Grav.* **23**, S207-S214, (2006).
- [Yuen76] H. P. Yuen *Phys. Rev. A.* **13**, 2226 (1976).
- [Yuen78] H. P. Yuen and J. H. Shapiro, *IEEE Transactions On Information Theory* **24**, 657 (1978).
- [Xiao87] M. Xiao, L.-A. Wu and H. J. Kimble, *Phys. Rev. Lett.* **59**, 278 (1987).

Acknowledgments

It is my pleasure to thank the many people how have contributed to this work in many different ways.

I would like to thank Karsten Danzmann for creating and leading an institute where I found ideal working conditions. Not only the friendly atmosphere but also the impressive technical support and financial reserves to buy everything needed for the experiments made the daily work very enjoyable.

Being part of a young and ambitious research team was exciting. I want to thank Roman Schnabel for his superb mentoring. He always took time for discussion and his scientific input as well as his humor enriched my work. With you I was lucky to have a dedicated advisor.

Almost none of my research was accomplished by me alone. From the beginning of my studies until now I worked together with Alexander Franzen, Simon Chelkowski, André Thüring, Nicolai Große, Boris Hage, Nico Lastzka, Oliver Burmeister, Moritz Mehmet, Christian Gräf, Alexander Khalaidovski, and many more. I hope they had as much fun working with me as I had working with them.

For proofreading of parts of this manuscript I am truly grateful to James DiGuglielmo, Alexander Khalaidovski, Nico Lastzka, Moritz Mehmet and André Thüring. Of course, all remaining errors are in my own responsibility.

I thank my parents for supporting and encouraging me all the years. I´m proud to share this with you.

Special thanks go to Kerstin and Hannes!

Henning Vahlbruch, Oktober 2008

Curriculum vitae

Henning Vahlbruch
Zum Johannisbruch 42
31832 Springe

Born on July 29th, 1976 in Frankfurt am Main, Germany

University studies

- | | |
|-------------------|--|
| 04/2004 - present | Scientific Assistant,
Max-Planck Institut für Gravitationsphysik (AEI), Hannover |
| 04/2004 - present | Doctoral studies in Physics, University of Hannover |
| 04/2004 | Diploma thesis, University of Hannover, <i>Gequetschtes Licht bei kleinen Seitenbandfrequenzen</i> |
| 10/1997 - 04/2004 | Physics studies, University of Hannover |

Community service

- | | |
|-----------|--|
| 1996-1997 | Civil service. DRK-Sozialstation Springe |
|-----------|--|

Education

- | | |
|------|-------------------------------------|
| 1996 | Abitur, Otto-Hahn-Gymnasium Springe |
|------|-------------------------------------|

Publications

— 2008 —

- 1 | H. Vahlbruch, M. Mehmet, S. Chelkowski, B. Hage, A. Franzen, N. Latstzka, S. Gossler, K. Danzmann, and R. Schnabel
„*Observation of Squeezed Light with 10 dB Quantum-Noise Reduction*“,
Physical Review Letters, **100**, 033602, (2008).
- 2 | B. Abbott, . . . , H. Vahlbruch, . . . , J. Zweizig,
„*Search of S3 LIGO data for gravitational wave signals from spinning black hole and neutron star binary inspirals*“,
Phys. Rev. D **78**, 042002 (2008).
- 3 | B. Abbott, . . . , H. Vahlbruch, . . . , J. Zweizig,
„*Search for gravitational waves associated with 39 gamma-ray bursts using data from the second, third, and fourth LIGO runs*“,
Phys. Rev. D **77**, 062004 (2008).
- 4 | B. Abbott, . . . , H. Vahlbruch, . . . , J. Zweizig,
„*Search for gravitational waves from binary inspirals in S3 and S4 LIGO data*“,
Phys. Rev. D **77**, 062002 (2008).
- 5 | B. Abbott, . . . , H. Vahlbruch, . . . , J. Zweizig,
„*All-sky search for periodic gravitational waves in LIGO S4 data*“,
Phys. Rev. D **77**, 022001 (2008).
- 6 | B. Abbott, . . . , H. Vahlbruch, . . . , J. Zweizig,
„*Implications for the Origin of GRB 070201 from LIGO Observations*“,
The Astrophysical Journal, 681:1419–1430, 2008.

— 2007 —

- 7 | H. Vahlbruch, S. Chelkowski, K. Danzmann, R. Schnabel,
„Quantum engineering of squeezed states for quantum communication and metrology“,
New Journal of Physics **9**, 371 (2007).
- 8 | S. Chelkowski, H. Vahlbruch, K. Danzmann, R. Schnabel,
„Coherent control of broadband vacuum squeezing“,
Physical Review A **75**, 043814 (2007).
- 9 | B. Abbott, . . . , H. Vahlbruch, . . . , J. Zweizig,
„Searches for periodic gravitational waves from unknown isolated sources and Scorpius X-1: Results from the second LIGO science run“,
Phys. Rev. D **76**, 082001 (2007).
- 10 | B. Abbott, . . . , H. Vahlbruch, . . . , J. Zweizig,
„Search for gravitational wave radiation associated with the pulsating tail of the SGR 1806-20 hyperflare of 27 December 2004 using LIGO“,
Phys. Rev. D **76**, 062003 (2007).
- 11 | B. Abbott, . . . , H. Vahlbruch, . . . , J. Zweizig,
„Search for gravitational-wave bursts in LIGO data from the fourth science run“,
Class. Quantum Grav. **24**, 5343-5369.
- 12 | B. Abbott, . . . , H. Vahlbruch, . . . , J. Zweizig,
„Upper limits on gravitational wave emission from 78 radio pulsars“,
Phys. Rev. D **76**, 042001 (2007).
- 13 | B. Abbott, . . . , H. Vahlbruch, . . . , J. Zweizig,
„Searching for a Stochastic Background of Gravitational Waves with the Laser Interferometer Gravitational-Wave Observatory“,
The Astrophysical Journal, 659:918–930, 2007.
- 14 | B. Abbott, . . . , H. Vahlbruch, . . . , J. Zweizig,
„Upper limit map of a background of gravitational waves“,
Phys. Rev. D **76**, 082003 (2007).
- 15 | B. Abbott, . . . , H. Vahlbruch, . . . , J. Zweizig,
„First cross-correlation analysis of interferometric and resonant-bar gravitational-wave data for stochastic backgrounds“,
Phys. Rev. D **76**, 022001 (2007).

— 2006 —

- 16 | H. Vahlbruch, S. Chelkowski, B. Hage, A. Franzen, K. Danzmann, R. Schnabel,
„*Coherent Control of Vacuum Squeezing in the Gravitational-Wave Detection Band*“,
Physical Review Letters **97**, 011101 (2006).
- 17 | H. Vahlbruch, S. Chelkowski, B. Hage, A. Franzen, K. Danzmann, R. Schnabel,
„*Squeezed-field injection for gravitational wave interferometers*“,
Classical Quantum Gravity **23**, S251 - S257 (2006).
- 18 | H. Lück, M. Hewitson, . . . , H. Vahlbruch, . . . , R. Zhu,
„*Status of the GEO600 detector*“,
Classical Quantum Gravity **23**, S71–S78 (2006).
- 19 | B. Willke, P. Ajith, . . . , H. Vahlbruch, . . . , R. Zhu,
„*The GEO-HF project*“,
Classical Quantum Gravity **23**, S207–S214 (2006).

— 2005 —

- 20 | H. Vahlbruch, S. Chelkowski, B. Hage, A. Franzen, K. Danzmann, and R. Schnabel,
„*Demonstration of a squeezed-light-enhanced power- and signal-recycled Michelson interferometer*“,
Physical Review Letters **95**, 211102 (2005).
- 21 | S. Chelkowski, H. Vahlbruch, B. Hage, A. Franzen, N. Lastzka, K. Danzmann, and R. Schnabel,
„*Experimental characterization of frequency-dependent squeezed light*“,
Physical Review A **71**, 013806 (2005).
- 22 | H. Grote, B. Allen, . . . , H. Vahlbruch, . . . , I. Zawischa,
„*The status of GEO600*“,
Classical Quantum Gravity **22**, S193–S198 (2005).

— 2004 —

- 23 | H. Vahlbruch, „*Gequetschtes Licht bei kleinen Seitenbandfrequenzen*“,
Diplomarbeit Universität Hannover (2004).

- 24 | R. Schnabel, H. Vahlbruch, A. Franzen, S. Chelkowski, N. Grosse, H.-A. Bachor, W. P. Bowen, P. K. Lam, and K. Danzmann,
„*Squeezed light at sideband frequencies below 100 kHz from a single OPA*“,
Optics Communication **240**, 185–190 (2004).

— 2003 —

- 25 | J. Harms, Y. Chen, S. Chelkowski, A. Franzen, H. Vahlbruch, K. Danzmann,
and R. Schnabel,
„*Squeezed-input, optical-spring, signal-recycled gravitational-wave detectors*“,
Phys. Rev. A **67**, 012316 (2003).

Index

A	
Annihilation operator	12
AOM	82
Auxiliary laser frequency lock . . .	102
B	
Balanced homodyne detection	84
C	
Coherent control theory	74
Coherent state	17
Conversion efficiency	48
Correspondence rule	12
Creation operator	12
Custom made photodiodes	63
D	
Dark noise clearance	41
Detection efficiency	41
Detuned filter cavity	102
Diagnostic homodyne detector . . .	113
Diagnostic mode cleaner	67
Dichroic beamsplitter	56
Displacement operator	18, 21
Dual recycling	99
E	
Eigenstate	12
Eigenvalue	12
EPICS	108
Epitaxx ETX500	63
Escape efficiency	39
Extra-ordinary axis	29
F	
Field quantization	11
Filter cavity	97
Finesse	54
Fock states	14
Frequency dependent squeezing . .	102
Frequency lock	125
Fringe visibility	31
G	
GEO squeezer	107
GEO 600 squeezer breadboard design	113
GEO 600 squeezer electronics . . .	115
Ground-state	13
H	
Hamiltonian	12
Holevo capacity	38
Homodyne detection	31
Homodyne detector	57
Homodyne efficiency	40
I	
Intra cavity loss	39

M

Maxwell equations	11
MgO:LiNbO ₃	53
MI signal transfer	102
Minimum uncertainty state	18
Mode cleaner	49
Mode mismatch	40
Monolithic squeezer	53

N

Number operator	12, 13
---------------------------	--------

O

Open loop gain	46
Ordinary axes	29

P

Parametric down conversion	28
Parasitic interferences	88
Phase Jitter	41
Phase matching	56
Phase matching condition	29
Phase space	21
Photon number	22
Photon probability distribution	24
Photon shot noise	4
Photon statistics	22
Pound-Drever-Hall	80
Power recycling	97
Propagation loss	40

Q

Quadrature control field	74
Quadrature operators	15
Quadrature rotation	104
Quantum efficiency	41
Quantum information storage	38
Quantum noise	4

R

Radiation pressure noise	5
------------------------------------	---

S

Scattering source	90
Second harmonic generation	28, 44, 80
Seismic noise	4
Sellmeier equation	29
Shot noise	4
Signal laser	102
Signal recycling	97
Squeezed light injection	99
Squeezed state	18
Squeezing angle	76
Squeezing factor	76
Squeezing operator	19, 75
Squeezing parameter	20
Standard Quantum Limit	5

T

Temperature stabilization	56
Thermal noise	4
Thermal transfer function	46
Type II phase matching	30

U

Up-conversion	28
-------------------------	----

V

Vacuum fluctuations	14
Vacuum-state	13
Variational output	102
Visibility	40

W

Wigner function	24
---------------------------	----

Z

Zero-point energy	13
-----------------------------	----